DEVELOPMENT OF NANOPARTICLE RATE-MODULATING AND SYNCHROTRON PHASE CONTRAST-BASED ASSESSMENT TECHNIQUES FOR CARDIAC TISSUE ENGINEERING

A Thesis Submitted to the College of

Graduate Studies and Research in Partial

Fulfillment of the Requirements for the

Degree of Doctor of Philosophy

in the Division of

Biomedical Engineering

University of Saskatchewan Saskatoon, Saskatchewan

By

MOHAMMAD IZADIFAR

PERMISSION TO USE

In presenting this thesis in partial fulfillment of the requirements for a Postgraduate degree from the University of Saskatchewan, I agree that the Libraries of this University may make it freely available for inspection. I further agree that permission for copying of this thesis in any manner, in whole or in part, for scholarly purposes may be granted by Prof. Daniel Chen and Prof. Michael E. Kelly, who supervised my thesis work or, in their absence, by the Head of the Division of Biomedical Engineering or the Dean of the College of Engineering in which my thesis work was done. It is understood that any copying or publication or use of this thesis or parts thereof for financial gain shall not be allowed without my written permission. It is also understood that due recognition shall be given to me and to the University of Saskatchewan in any scholarly use which may be made of any material in my thesis.

Requests for permission to copy or to make other uses of materials in this thesis in whole or part should be addressed to:

Head of the Division of Biomedical Engineering

57 Campus Drive, University of Saskatchewan

Saskatoon, Saskatchewan S7N 5A9

Canada

ABSTRACT

Myocardial infarction (MI) is the most common cause of heart failure. Despite advancements in cardiovascular treatments and interventions, current therapies can only slow down the progression of heart failure, but not tackle the progressive loss of cardiomyocytes after MI. One aim of cardiac tissue engineering is to develop implantable constructs (e.g. cardiac patches) that provide physical and biochemical cues for myocardium regeneration. To this end, vascularization in these constructs is of great importance and one key issue involved is the spatiotemporal control of growth-factor (GF)-release profiles. The other key issue is to non-invasively quantitatively monitor the success of these constructs *in-situ*, which will be essential for longitudinal assessments as studies are advanced from *ex-vivo* to animal models and human patients. To address these issues, the present research aims to develop nanoparticles to modulate the temporal control of GF release in cardiac patches, and to develop synchrotron X-ray phase contrast tomography for visualization and quantitative assessment of 3D-printed cardiac patch implanted in a rat MI model, with four specific objectives presented below.

The first research objective is to optimize nanoparticle-fabrication process in terms of particle size, polydispersity, loading capacity, zeta potential and morphology. To achieve this objective, a comprehensive experimental study was performed to examine various process parameters used in the fabrication of poly(lactide-co-glycolide) (PLGA) nanoparticles, along with the development of a novel computational approach for the nanoparticle-fabrication optimization. Results show that among various process parameters examined, the polymer and the external aqueous phase concentrations are the most significant ones to affect the nanoparticle physical and release characteristics. Also, the limitations of PLGA nanoparticles such as initial burst effect and the lack of time-delayed release patterns are identified.

The second research objective is to develop bi-layer nanoparticles to achieve the controllable release of GFs, meanwhile overcoming the above identified limitations of PLGA nanoparticles. The bi-layer nanoparticle is composed of protein-encapsulating PLGA core and poly(L-lactide) (PLLA)-rate regulating shell, thus allowing for low burst effect, protein structural integrity and time-delayed release patterns. The bi-layer nanoparticles, along with PLGA ones, were successfully fabricated and then used to regulate simultaneous and/or sequential release of multiple angiogenic factors with the results demonstrating that they are effective to promote angiogenesis in fibrin matrix.

The third objective is to develop novel mathematical models to represent the controlled-release of bioactive agents from nanoparticles. For this, two models, namely the mechanistic model and geno-mechanistic model, were developed based on the local and global volume averaging approaches, respectively, and then validated with experiments on both single- and bi-layer nanoparticles, by which the ovalbumin was used as a protein model for the release examination. The results illustrates the developed models are able to provide insight on the release mechanism and to predict nanoparticle transport and degradation properties of nanoparticles, thus providing a means to regulate and control the release of bioactive agents from the nanoparticles for tissue engineering applications.

The fourth objective of this research is to develop a synchrotron-based phase contrast non-invasive imaging technique for visualization and quantitative assessment of cardiac patch implanted in a rat MI model. To this end, the patches were created from alginate strands using the three-dimensional (3D) printing technique and then surgically implanted on rat hearts for the assessment based on phase contrast tomography. The imaging of samples was performed at various sample-to-detector distances, CT-scan time, and areas of the region of interest (ROI) to

examine their effects on imaging quality. Phase-retrieved images depict visible and quantifiable structural details of the patch at low radiation dose, which, however, are not seen from the images by means of dual absorption-phase and a 3T clinical magnetic resonance imaging.

Taken together, this research represents a significant advance in cardiac tissue engineering by developing novel nano-guided approaches for vascularization in myocardium regeneration as well as non-invasive and quantitative monitoring techniques for longitudinal studies on the cardiac patch implanted in animal model and eventually in human patients.

ACKNOWLEDGMENTS

I would like to record my gratitude to my supervisors, Dr. Daniel Chen and Dr. Michael Kelly, for their guidance and unflinching supports during my Ph.D. program. I also extend my appreciation to the other members of the Advisory Committee, Dr. Paul Babyn, Dr. Eric McNair, and Dr. Dean Chapman, for their valuable advice and suggestions towards the completion of this thesis.

I gratefully acknowledge Mrs. Leona Boyer and Dr. Melanie Gibbons for their assistance with anesthesia and intubation, and Mr. Shawn J. Kisch for his help with MRI at the Royal University Hospital. I wish to thank Mrs. Karen Yuen and Mrs. Eiko Kawamura for their help with the scanning electron microscopy. Special thanks are due to Dr. Mark Adam Webb and Dr. George Belev for their help on sample imaging at the Biomedical Imaging and Therapy (BMIT) beamline at the Canadian Light Source (CLS), where all synchrotron-based imaging experiments were performed. I would like to acknowledge the BMIT facility at the CLS, which is supported by the Canada Foundation for Innovation (CFI), Natural Sciences and Engineering Research Council of Canada (NSERC), the University of Saskatchewan, the Government of Saskatchewan, Western Economic Diversification Canada, the National Research Council Canada, and the Canadian Institutes of Health Research (CIHR). I also appreciate the support from the Bio-Fabrication Lab at the University of Saskatchewan, where the 3D-printing of cardiac patches was performed.

I would like to acknowledge the financial support to the present study from the CIHR (through the research grant to my supervisors), Saskatchewan Innovation and Opportunity Scholarship (to me), and the University of Saskatchewan Graduate Research Scholarship (to me).

Finally, I would like to express a deep gratitude to my parents for their constant love and support. My gratitude also goes to all my family members as well as my friends who supported me in this journey.

TABLE OF CONTENTS

LIST OF FIGURES

LIST OF TABLES

CHAPTER 1

BACKGROUND

Notes: Sections 1.1 – 1.6 of this chapter are adopted from the publication of “M. Izadifar, M. Kelly and X. B. Chen, 2014, Engineering Angiogenesis for Myocardial Infarction Repair: Recent Developments, Challenges, and Future Directions, *Cardiovascular Engineering and Technology*, 5(4), 281-307” According to the Copyright Agreement, "the authors retain the right to include the journal article, in full or in part, in a thesis or dissertation".

1.1. Introduction

Cardiovascular diseases including myocardial infarction are leading causes of death that account for nearly 40% of all fatalities, more than all cancers combined [1]. Each year, an estimated ~620,000 Americans are hospitalized or die due to coronary heart diseases, and ~295,000 have a recurrent coronary attack [2]. Heart defects are also the leading cause of death in the first year of life [3]. Recognized as a critical public health issue worldwide, heart failure is caused by various cardiovascular diseases including acute myocardial infarction, ischemic cardiomyopathy, and idiopathic cardiomyopathy [4]. Despite recent achievements in drug-eluting stents [5], off-pump cardiac surgery includuing coronary artery bypass grafting [6], mitral valve repair and left ventricular reconstruction surgery [7], and permanent pacemakers with left ventricle resynchronization devices [8], millions of people continue to suffer from heart failure [9-12]. The heart is a terminally differentiated organ that fails to repair itself because of the intrinsic inability of damaged heart tissue to regenerate [13-15], so the large number of patients worldwide who survive myocardial infarction and develop advanced heart failure face largely unresolvable issues [16]. At present, heart transplantation is the best solution for patients with end-stage heart failure. However, donor supply is declining and creating an increasing gap

between supply and demand for heart replacement therapies. Left ventricular assist devices may provide a temporary therapeutic option for patients with pump failure but do not provide a definitive therapy [17]. Thus, there has been great interest in alternative therapeutic strategies to reverse this common and deadly disease.

Regenerative medicine and tissue engineering are rapidly growing areas that aim to maintain, replace, restore, or enhance the functionality of damaged, lost, or degenerated tissues/ organs using combinations of cells, biomaterials, and/ or biologically active molecules [18]. Cardiac regeneration therapy is a promising approach to revolutionize current therapies for myocardial infarction and heart failure towards any successes that can significantly improve the quality of life for millions of patients. Although cardiac tissue engineering could be the most valuable approach for the regeneration of failing hearts, there are significant challenges associated with the complexity of the damaged cardiac tissue. Among the different challenges faced by cardiac tissue engineering, angiogenesis and timely connection to the host blood supply are the most substantial.

This chapter presents an overview for cardiac tissue engineering strategies and associated challenges, with emphasis on angiogenesis as the major challenge in cardiac tissue engineering. Strategies for myocardial infarction repair are examined and recent advances and developments in engineering vascularization and inosculation approaches towards the rapid integration of cardiac scaffolds, once implanted, with the host tissue are presented.

1.2. Atherosclerosis

Atherosclerosis is the major cause of cardiovascular diseases [19]. Arterial wall, which consists of intima (endothelium), media (smooth muscle cells (SMCs)) and adventitia, is a dynamic and regulated system, but several risk factors can disturb its normal homeostasis and cause

atherogenesis. Smoking, aging, hypercholesterolemia, hypertension, hyperglycemia, genetics (family history) [20], high levels of reactive oxygen species (ROS) and low density lipid (LDL) [21, 22], dyslipidemia [23] and diabetes [20] are among various traditional and novel risk factors that can cause endothelial dysfunction. Such endothelial dysfunction allows the permeation of LDL into the subendothelial space where LDL accumulates by binding to proteoglycans in the extra cellular matrix (ECM). In addition, hypertension may contribute to the LDL retention in intima by promoting the production of LDL-binding proteoglycans by SMCs. The trapped LDL in the subendothelial space is oxidized by the ROS and continues to promote inflammation by triggering the expression of proinflamatory cytokines (chemoattractant signals). The cytokines at the endothelial luminal surface direct mainly monocytes to the forming lesion. The monocytes role and adhere to the luminal surface and penetrate in the intima, and then differentiate into macrophages under the influence of macrophage colony stimulating factor. Mature macrophages then engulf oxidized LDL and form foam cells. Immobile foam cells stuck at the focus of the lesion form the early atherosclerotic streak. The local accumulation of foam cells fuels foam cell apoptosis in the lipid-rich center of the plaque (necrotic core) and augments the release of proinflammatory cytokines that promote atherosclerotic plaque progression and SMC migration into the intima. During decades of development, the plaque accumulates a distinct thrombogenic lipid core surrounded by a protective fibrous cap. In the early stage of the plaque growth, a compensatory outward remodeling of the arterial wall preserves the lumen diameter. This early stage of plaque growth produces no ischemic symptoms and can evade the detection by angiography. In later stages, plaque growth narrows the vessel diameter and impedes the blood flow, leading to tissue ischemia and tissue injury. Meanwhile, the extracellular matrix plays a pivotal role in fortifying the fibrous cap that isolates the plaque thrombogenic core from the

blood circulation. If the fibrous cap of the plaque ruptures due to an unstable ECM and the release of matrix metaloproteinases, the exposure of the procoagulants within the plaque to the circulating blood causes platelet aggregation and which leads to thrombus formation which can occlude the vessel and results in infarction of the involved myocardium [24].

1.3. Myocardial infarction

The progression of vascular disease, which can cause myocardial infarction, is intimately related to the dysfunction of the endothelial cells (ECs) of blood vessels. Blood vessels are basically composed of three layers: the intima (endothelium), an intermediate layer of media (muscle cells), and an outer layer of adventitia (connective tissue). The inner layer, consisting of a thin layer of ECs, provides a smooth and protective surface preventing toxic and blood-borne substances from penetrating into the media. However, factors including high levels of low-density lipoprotein (LDL) cholesterol, high levels of triglycerides, hypertension, a high omega-6:omega-3 ratio, excess insulin, insufficient vitamin D and K, and nitric oxide deficit in the blood can cause endothelial dysfunction, ultimately resulting in lipids and toxics permeating to the intermediate layer (media) [25-29]. The accumulation of lipids and toxics in the media along with oxidative and inflammatory cascades leads to the development of plaque deposits that slowly grow and locally narrow the blood vessel. This slow process is known as atherosclerosis. Over time, the plaques calcify and become susceptible to rupture. If a plaque in the artery breaks, a blood clot forms around the plaque and can eventually block the blood flow. If this process happens in a coronary artery of the heart, the blood flow that supplies oxygen to the heart muscle is severely reduced or cut off such that the heart muscle is starved for oxygen and nutrients. This occurrence is called ischemia. Because the heart wall is composed of tightly packed myocytes and fibroblasts with high metabolic demand, the myocardium requires large amounts of oxygen

and cannot tolerate ischemia. Thus, ischemia can lead to the serious damage or death of part of the heart muscle in a process known as heart attack or myocardial infarction.

When myocardial infarction occurs, the myocardium reacts to the ischemia with a series of changes in cellular and extracellular matrix (ECM) components that lead to left ventricular remodelling [30]. The lack of oxygen in the myocardium causes cardiomyocyte necrosis and a subsequent inflammatory response. The inflammatory response consists of upregulation of a series of cytokines, chemokines, and cell adhesion molecules that triggers the recruitment of neutrophils and monocytes to the infarct region [31]. Monocyte adherence to ECM initiates conversion to macrophages, in part by inducing the expression of cytokines including macrophage colony stimulating factor (M-CSF) that is necessary for macrophage survival [32]. The primary role of the macrophage in the post-myocardial infarction is to facilitate wound healing through phagocytosis of necrotic cells and secretion of angiogenic factors for angiogenesis, fibroblast activation and proliferation, and collagen metabolism [33, 34]. Activated macrophages in the myocardial infarction zone are key angiogenic effector cells and influence each phase of the angiogenic process, including local ECM destabilization; induction of ECs to differentiate, migrate, and proliferate; and maturation of new microvessels [35]. Induction of EC sprouting requires the dissolution of the local extracellular matrix. Macrophages secrete matrix metalloproteinases (MMPs) that degrade the ECM and liberate extracellular matrix-bound growth factors to facilitate new blood capillary formation [36]. Macrophages are also a major source of initiating factors that activate fibroblasts that secrete collagen to form scar tissue in the myocardial infarction zone [37]. During the healing process, post-myocardial infarction, central necrosis, infiltration of inflammatory cells, and secretion of MMPs by macrophages weaken the infarcted myocardium for several weeks until the end of scar formation [38]. Over subsequent

weeks to months, a granulation tissue is created and ultimately becomes a thick and stiff collagenous scar [39]. The fibrotic scar tissue formed is unable to actively contract thus imposing an extra burden on the remaining healthy myocardium, reducing the contractile function of the heart, and leading to ventricle wall thinning [40]. When the infarct is large, infarct expansion is promoted such that the progressive increase in left ventricle volume can lead to chronic heart failure [38]. Although the inflammatory response modulated by macrophages is a necessary component of the post-myocardial infarction healing process [41], post-infarction inflammation can be a double-edged sword as excessive inflammation can play an important role in infarct expansion [38]. The role of macrophages following myocardial infarction has been well reviewed by Lambert et al. (2008) [42]. Cardiac ECM also plays a very important role during infarct healing. Beyond the mechanical support, ECM proteins perform as regulators by modulating cellular interactions that are involved in the inflammatory response including angiogenesis. An excellent review on the role of ECM as a modulator of the inflammatory response post-myocardial infarction was published by Dobaczewski et al. (2010) [43].

1.4. Strategies for myocardial infarction repair

Regeneration of heart tissue through direct cell transplantation, scaffold-based tissue engineering, and mobilization of heart progenitor cells with active biomolecules holds tremendous potential for the treatment of myocardial infarction and other forms of heart injury although this has remained an elusive goal for over a decade. Classical treatments for heart diseases continue to evolve; cell therapy combined with tissue engineering techniques now offer novel therapeutic concepts for myocardial repair [44]. Cardiac regeneration therapy strategies can be classified into two general categories: cardiac graft engineering and *in situ* cell-based cardiac regeneration therapy.

1.4.1. Graft-based cardiac tissue engineering

The goal of graft-based cardiac tissue engineering is to repair the myocardial infarction area using a supporting scaffold/ sheet/ gel containing functional cells and signaling molecules. The strategy is based on growing selected cells (e.g., progenitor cardiac cells) on a three-dimensional (3-D) scaffold or patch in bioreactors followed by implanting the graft to direct new cardiac cell formation and maturation in the damaged area. The critical elements of a successful cardiac tissue engineered construct include the graft biomaterial that serves as a mechanical and biological support for cells, progenitor cells that must be differentiated into cardiac cells, and inductive growth factors that instruct cellular activities.

A successful cardiac tissue construct must demonstrate functional and morphological properties of native heart muscle, mechanically/ electrically integrate into the heart muscle after implantation, and improve systolic and diastolic function of the damaged myocardium over time [45]. Therefore, a cardiac tissue engineered graft should be contractile, mechanically robust but flexible, electrophysiologically stable, non-immunogenic, and quickly vascularized after implantation in order to mimic the functionality and properties of native heart muscle. Different 3-D myocardial tissue constructs have been developed by a number of research groups [46-49]. Despite numerous efforts devoted to scaffold-based cardiac tissue engineering, a tissue engineered substitute suitable for replacing non-functioning myocardium is not on the horizon; however, adding cardiac-engineered patches to the damaged heart muscle rather than replacing part of the heart muscle seems more pragmatic. Table 1.1 provides a summary of the biodegradable and biocompatible materials used for graft-based cardiac tissue engineering. High mechanical stability, which is required for any cardiac scaffold to withstand systolic pressure, is one of the significant characteristics that biomaterials fail to offer.

Table 1.1. Biodegradable and biocompatible materials used in graft-based cardiac tissue engineering.

Material	Research objective	Ref.
Collagen	Development of contractile bioartificial myocardial tissue	[50]
Collagen-glycosaminoglycan (GAG)	Evaluation of the tissue response to collagen-GAG scaffolds	[51]
Alginate	Stimulation of neovascularization and attenuate left ventricle dilation	[52]
PGA[a] copolymerized with PLA[b]	Development of contractile bioartificial myocardial tissue	[53]
PLLA[b]	Formation of synchronously contracting engineered human cardiac tissue	[54]
PCL[c] copolymerized with PLA	Development of contractile cardiac grafts *in vitro*	[55]
Polyurethane coated with gelatine/ laminin/ collagen	Development of contracting films	[56]
Collagen/ Matrigel	Engineering cardiac muscle constructs with functional and morphological properties similar to native cardiac muscle	[57]

[a]poly(glycolic acid), [b]poly(lactic acid), [c]poly(L-lactic acid), [d]poly(ε-caprolacton)

1.4.2. *In situ* cardiac regeneration therapy

A second approach to cardiac tissue engineering is based on *in vivo* myocardium regeneration with the aim to repair myocardial infarction by regenerating the heart muscle *in situ*. *In situ* cardiac regeneration therapy can be further categorized into: i) cell suspension direct injection, ii) biomolecule/ biomaterial-enhanced myocardium self-repair, and iii) cell-containing hydrogel injection. Although scaffold-based cardiac tissue engineering allows for good control over the cardiac tissue engineered construct size, shape, development, and *in vitro* function, it has been unable to create a robust and stable heart muscle-like tissue construct; thus, the risk of tissue necrosis after implantation remains.

1.4.2.1. Cell suspension direct injection

This approach aims to repopulate cardiac cells in the damaged myocardium by injecting cell suspensions with a syringe or the minimally invasive approach of cardiac catheterization. Fetal cardiomyocytes, skeletal myoblasts, and bone marrow stem cells have been employed in this method; however, restoring damaged heart muscle has met with limited success. Due to inflammation, fibrosis, and the lack of blood supply, a major challenge in cell therapy approaches is maintaining the survival of newly implanted cells [58]. Cell survival rates range from 1 to 32% within one week post-injection into injured hearts [59], with three major causes of cell death being the loss of ECM support, ischemia, and inflammation. Preparation of cell suspensions to be injected into the site of therapy inevitably leads to decreased ECM adhesion-related survival signals that are important for cell survival; specifically, the loss of cell contacts with the extracellular environment eliminates protective signalling pathways [60]. A recent study suggests that inhibition of Rho-associated kinase can improve the viability of human embryonic stem cells possibly due to the prevention of anoikis [61]. Ischemia that increases the production

of reactive oxygen species and mitochondrial dysfunction is followed by inflammation that causes a harsh environment leading to cell death. Improved cell survival rates can be achieved by stimulating cell protective mechanisms against oxidative stress and inflammation with insulin-like growth factor-1 (IGF-1) [62-64].

In addition to the challenges associated with cell death following cell injection, EC-cardiomyocyte crosstalk plays a very important role in the context of ischemia/ infarction injuries and reperfusion. Crosstalk modulates vascular tone and stimulates proliferation of neighbouring cells during cell stresses due to ischemia, where ECs might promote the survival of cardiomyocytes [65]. Paracrine function of ECs enhances signaling in cardiomyocytes that secrete factors affecting EC functionality [66]. The secretion of paracrine and autocrine factors may contribute to endogenous and pharmacological cardioprotective pathways during ischemia-induced cell stresses [67]. In a recent study by Thorsten et al. (2011), observations support the hypothesis that ECs contribute to isoflurane-enhanced protection of cardiomyocytes against hypoxia, with such protection dependent on a hypoxia-inducible factor and nitric oxide [66]. Recent insights in the paracrine modulation of cardiomyocyte contractility by cardiac ECs are well reviewed by Noireaud et al. (2014) [68].

1.4.2.2. Biomolecule/ biomaterial-induced myocardium self-repair

In this second approach, bioactive materials and growth factors are injected into the damaged myocardium to stimulate heart muscle self-regeneration. Biomaterials such as hyaluronan [69], fibronectin, vitronectin, laminin, and collagen [70] enable cell matrix crosstalk that enhances cell proliferation in the damaged tissue. In addition, biomaterials can be administered with several bioactive molecules (e.g., growth factors, cytokines) that stimulate cells to produce additional growth factors that regulate cell proliferation and differentiation in order to potentially stimulate

myocardial self-repair [71, 72]. The heart contains progenitor cells that can differentiate to cardiomyocytes [73, 75]. In the presence of biomaterials and bioactive molecules that can stimulate and instruct the progenitor cells, these cardiac progenitors can potentially differentiate into cardiomyocytes for myocardial infarction repair. This strategy of growth factor-mediated cardiac regeneration therapy is evolving dramatically by means of catheter-based injection, as this therapeutic approach can avoid the need for surgery. Table 1.2 summarizes important cytokines and their roles in stimulating myocardial repair.

Table 1.2. Potential bioactive molecules for stimulating myocardial infarction repair.

Biomolecule	Activity	Ref.
Granulocyte colony-stimulating factor (G-CSF)	- Critical role in regulation of proliferation, differentiation, and survival of myeloid progenitor cells - Hematopoietic stem cell mobilization - Improving cardiac function after myocardial infarction - Reducing mortality after acute myocardial infarction	[76-79]
Stromal derived growth factor (SDG)	- Important role in trafficking and survival of hematopoietic, endothelial progenitor, and mesenchymal stem cells - Augmenting endothelial progenitor cells	[80-82]
Insulin-like growth factor (IGF)	- Enhancing nuclear phospho-Akt and telomerase and delaying cardiomyocyte aging and death - Improving stem cell homing, healing, and regeneration of the injured muscle	[83-85]
Erythropoietin (EPO)	- Important for erythrocyte survival and differentiation - Maintaining vascular auto-regulation and attenuating primary (apoptotic) and secondary (inflammatory) causes of	[86, 87]

	cell death - Recruitment of stem cells into the region of damage	
Leukemia inhibitory factor (LIF)	- Increasing cardiac L-type Ca^{2+}channel current - Inducing endothelial differentiation in cardiac stem cells	[88-90]
Bone morphogenic protein (BMP)	- Regulation of cardiomyocyte differentiation from mesoderm in the heart-forming region - Formation of the ventricular chambers and septovalvulogenesis in the atrioventricular canal and outflow tract	[91]

1.4.2.3. Cell-containing hydrogel injection for cardiac regeneration therapy

Hydrogels offer great advantages including shielding cells from the harsh environment of ischemic areas, having the ability to be polymerized *in situ* after injection, mediating growth factor delivery to enhance the vasculogenic and myogenic capacity of encapsulated cells, and improving cell retention in the heart [92]. Three therapeutic approaches involving injectable hydrogels are epicardial, endocardial, and intracoronary injection (Fig. 1.1). Epicardial hydrogel injection can be performed through direct injection or can use a catheter to puncture and inject the hydrogel into the damaged heart wall. Direct epicardial injection is the most controllable injection technique, with the surgeon able to precisely control the location of injection as well as the amount of the hydrogel injected via syringe into the ischemic/ infarcted area; however, this approach requires an invasive surgical procedure. Because patients with recent myocardial infarction are typically at higher risk for conventional surgical approaches, efforts have been devoted to employ minimally invasive catheter-based injection approaches to deliver the hydrogel into the ischemic/ infarcted myocardium. One such approach is catheter-based

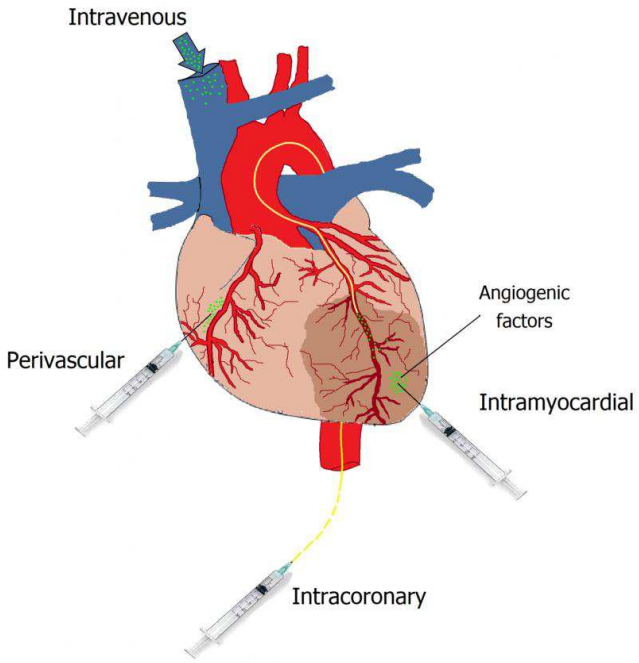

Figure 1.1. Schematic diagram of intravenous, intracoronary, and intramyocardial delivery of angiogenic factors.

epicardial injection, in which the coronary system is used as a roadmap to the heart and a composite catheter system allows for stable access to the remote myocardium with intravascular ultrasound and fluoroscopic guidance. Catheter-based transendocardial injection is another alternative for minimally invasive hydrogel injection, guided by endoscopic surgical techniques to deliver hydrogel into the myocardial infarction region in the left ventricle. Catheter-based transendocardial injection may be unstable in the mobile ventricular wall. Contrary to epicardial and transendocardial injection approaches that puncture the heart wall, intracoronary injection utilizes a percutaneous transluminal coronary angioplasty balloon to deliver the liquid form of the hydrogel into the cardiac tissue from the blood stream [93]. This delivery method is unique as it uses leaky vessels of the myocardial infarction region rather than puncture injection. In

terms of therapeutic yield, intracoronary and catheter-based injection approaches are generally less specific than the direct injection method and may potentially decrease the therapeutic yield. Considering that catheter technology and endoscopic techniques have been extensively used, minimally invasive surgery procedures have been well established, and the safe use of these approaches has been demonstrated, many cell and growth factor delivery strategies to maintain and repair the infarcted myocardium are moving towards transendocardial injection. This delivery method avoids the risk of open chest surgery, reduces the time of treatment post-myocardial infarction, provides quicker patient recovery, and facilitates clinical translations of achievements in cardiac regeneration therapy. Table 1.3 summarizes the advantages and disadvantages associated with each of the three clinical hydrogel delivery approaches for myocardial infarction repair. The hydrogels used to date for injectable hydrogel-based myocardial infarction repair include fibrin, chitosan, alginate, collagen, hyaluronic acid, Matrigel, polyethylene glycol, and poly(N-iso-propylacrylamide) [94]. Efforts need to be devoted to developing/ improving new biomaterials with unique properties suitable for transendocardial injection that have been found promising for *in vivo* cardiac regeneration.

1.5. Challenges in myocardial infarction repair

Despite advances in graft-based and *in situ* cardiac tissue engineering, cardiac regeneration therapy still faces significant challenges associated with cells, biomaterials, and angiogenesis. Increasing evidence shows promising results in the area of *in vivo* regeneration of functional myocardium, but issues in this area need to be identified and addressed in future studies. Below, the major challenges in the area of cardiac regeneration therapy are outlined.

Table 1.3. Pros and cons of epicardial, endocardial, and intracoronary injection approaches.

Injection approach	Pros	Cons
Intracoronary	- Uses standard, routine, and well-established interventional cardiology techniques - No direct puncturing of the heart wall required	- Material must be non-thrombogenic - Gel must set only once delivered to the tissue (not in bloodstream) - No precise control over the delivered volume of the material - Limited material delivery to the entire infarct due to inadequate vasculature - Spatially less specific compared to direct epicardial injection
Direct epicardial	- Precise control over the volume of material delivery into the myocardial infarction region - Clear visual delivery and good control over the location of injection - Double-barrel syringes can be used to mix polymerizable hydrogel materials right before injection	- Surgical procedure required - Relatively long patient recovery time needed
Catheter-based epicardial	- Short and flexible time for injection post-myocardial infarction - Minimally invasive - Stable access to the remote myocardium - Precise control over the volume of the	- Spatially less specific compared to direct epicardial injection - Needs to be combined with an imaging modality - Accuracy of localization of ischemic/ infarcted area and injection location relies

	delivered hydrogel - No general anesthesia	on the imaging technique - Special training for catheter injection use and imaging required - Hydrogel biomaterial must remain in liquid form during the injection - Gel must not set in the catheter
Catheter-based transendocardial	- Minimally invasive - Short and flexible time for injection post-myocardial infarction - Short patient recovery time -Well established endoscopic surgery procedures and catheter-based techniques used - Precise control over the volume of the delivered hydrogel - No general anesthesia	- Needs to be combined with an imaging modality - Localization of injections relies on the imaging technique - Very hard to control the injection into the constantly moving ventricle wall - Special training for catheter injection use and imaging required - Biomaterial must be in a liquid form during the injection - Gel must not set in the catheter

1.5.1. Cell source

Regardless of cardiac tissue engineering strategy used for myocardial infarction repair, cardiac muscle regeneration relies on the source of cells used. Ideally, the cells employed should be able to easily expand, proliferate, and differentiate into mature and functional cardiomyocytes. Many studies have been performed to evaluate a wide variety of cells for this purpose, including stem cells and cardiac progenitor cells, to find an optimal cell source for myocardium regeneration [95-98]. Potential cell sources for cardiac tissue engineering are crude bone marrow [99],

endothelial progenitor cells [100], umbilical cord cells [101], skeletal myoblasts [102], human embryonic stem cells [103], smooth muscle cells [104], fibroblasts [105], fetal cardiomyocytes [106], adipose-derived adult stem cells [107], and resident cardiac stem cells [108, 109]. Of these, resident cardiac stem cells are known to be endogenous myogenic progenitors; however, their numbers are too limited to be reliable in cell-based cardiac regeneration therapy. Induced pluripotent stem cells, which are genetically modified adult cells, also have demonstrated potential to differentiate into the cardiovascular lineage [110]. Studies show that human embryonic-stem-cell-derived cardiomyocytes (hESC-CMs) can result in favourable effects of cardiac regeneration therapy in animal models [111, 112]. Recently, Chong et al. showed that cryopreservation and intra-myocardial delivery of one billion hESC-CMs can generate extensive remuscularization of infarcted monkey heart with a progressive but incomplete maturation within 3 months [113]. Cardiomyocytes derived from pluripotent stem cells are currently the most attractive exogenous myogenic cell source for cardiac tissue engineering although the use of undifferentiated cells carries the risk of uncontrolled differentiation [114]. Non-myogenic cell sources are also used for vascularization although they do not increase new cardiomyocytes [115].

A variety of ECs including human dermal microvascular ECs, human umbilical vein ECs (HUVECs), bovine aortic ECs (BAECs), and bovine capillary ECs (BCEs) [116] have been used as sources of endothelial cells; however, low proliferation rates, limited availability, and heterogeneity in EC genotype and phenotype are disadvantages [117]. In addition, HUVECs are of macrovascular origin whereas the cells most involved in inflammation, wound healing, and vascularization *in vivo* are microvascular ECs [118]. Human blood outgrowth ECs demonstrate stronger contractive function on malleable substrates compared to HUVECs [119]. Furthermore,

although HUVECs have been widely used in numerous experimental models for human macrovascular ECs, they are incapable of fully representing the metabolic properties and interactions of the ECs distributed in the entire organism [120]. These disadvantages have led to the use of other sources of cells. Human pluripotent stem cells including embryonic stem cells (hESCs) and induced pluripotent stem cells (hiPSCs) are promising sources for the generation of healthy ECs [121, 122]. Although hiPSCs and hESCs can unlimitedly self-renew and differentiate into various lineages, hiPSCs can be used to derive autologous ECs for regenerative medicine applications [123]. Several studies that investigated the therapeutic efficacy of pluripotent stem cell-derived ECs in pre-clinical models of ischemic cardiovascular disease have shown that these cells can enhance angiogenesis, tissue perfusion, and organ function [124-127]. iPSC-derived ECs exhibit the rich functional phenotypic plasticity of mature primary vascular endothelium, can be directed to an atheroprotective phenotype via pharmacological stimulus, undergo endothelial activation, and maintain dynamic permeability [128]. Furthermore, ECM can differentially promote iPSC differentiation into ECs, possibly through binding to various types of integrins [129]. Endothelial progenitor cells (EPCs) from peripheral blood or cord blood can be also a potential cell source to enhance neovascularization of tissue engineered constructs or ischemic tissues. EPCs have been studied for their role in endogenous maintenance and for their therapeutic potential in vascular regenerative medicine; despite their obvious potential in clinical practice, however, many questions still remain regarding how EPCs actually enhance endothelial repair and neovascularization [130]. Furthermore, the number of EPCs in bone marrow or peripheral blood is limited and, unlike hESCs which possess the capacity for unlimited self-renewal, EPCs usually have limited expansion ability [131].

1.5.2. Biomaterials

Biomaterials are one of the major components of tissue engineering. In addition to biocompatibility and biodegradability, they should support cell attachment, differentiation, and proliferation; provide mechanical support to cells during ECM synthesis; have an interconnected porous structure to allow for tissue ingrowth and vascularization; and possess the desired dispensability (e.g., for 3D-printed scaffolds), fluidity (e.g., for injectable hydrogels), and thermal sensitivity (e.g., for *in situ* polymerizing hydrogels). The selection and design of biomaterials for myocardial infarction repair strongly depends on the cardiac tissue engineering approach adopted.

In classical scaffold-based cardiac tissue engineering, which aims to reconstruct heart muscle tissue using a cell-incorporated construct, the biomaterials must be able to imitate the ECM of the myocardium to support the cells, provide mechanical support to the cells, and develop contractile functionality while withstanding expansion loads associated with diastolic events. Yet, no example of an engineered myocardium made of scaffolds has been reported. In fact, no biomaterial is able to beat without cardiomyocytes. Assuming the scaffold contains a sufficient population of cardiomyocytes, the transfer of a beating signal from cells to the scaffold strongly relies on the softness of the scaffold. If the scaffold is stiff enough to withstand the required mechanical loads and stresses, beating signals from cells cannot be adequately transferred. On the other hand, if the scaffold is soft enough to beat, it may fail to withstand systolic/ diastolic loads. Thus, efforts to build a functional myocardium construct have so far been disappointing [132].

One graft-based cardiac tissue engineering approach applies heart patches made of cell/ bioactive molecule-incorporated biomaterials to the infarct region to deliver healthy and functional

cardiomyocytes to the damaged area while the patch degrades with time. When using stiffer biomaterials, the patches can also serve as a mechanical support to the damaged muscle of the left ventricle. Despite successes and promising results with this approach, the most significant challenge is associated with designing biomaterials with nonlinear elasticity similar to that of heart muscle so the patch and heart can beat together. Some studies indicate promising paths towards achieving nonlinear elastic biomaterials for patch-based cardiac tissue engineering [133-135]. In addition to nonlinear elasticity, another challenge is that the biomaterial stiffness must be close to ~50 kPa in normal hearts or 200-300 kPa in congestive heart failure cases at the end of diastole.

Minimally invasive transendocardial injection of hydrogels that contain cells and growth factors is potentially the most promising strategy to be translated into clinical practice. As mentioned earlier (see §3.2.3), hydrogels injected to the infarct region via image-guided catheter technology must be fluidic enough to be easily injected and have a gelling behavior that avoids clogging the catheter during multiple injections but results in *in situ* polymerization once injected. *In situ* copolymerization of two polymeric biomaterials is not an alternative because no double-barreled catheter system can facilitate multiple injections without clogging [92]. Thermo-responsive polymers and self-assembly polymers with optimized properties can be good candidates for *in situ* polymerization post-injection. Fibrin properties can be adjusted to provide different gelation rates [136]; however, due to the multiple injections that last up to an hour, more studies need to be done to optimize fibrin properties. Only alginate has reached Phase II clinical trials for minimally invasive endocardial hydrogel injection-based cardiac regeneration therapy [137].

1.5.3. Vascularization

Despite great advances in tissue engineering, much still needs be learned about translating *in vitro* achievements into clinically relevant successes. One major hurdle challenging clinical implementation of tissue engineering is vascularization.

In vitro perfusion bioreactors are often used to supply nutrients and oxygen to cells seeded onto tissue engineered constructs; however, creation of an oxygen and nutrient supply from the host tissue to the implanted tissue construct or injected hydrogel remains the most challenging issue in tissue engineering. Following the injection or implantation of a scaffold, blood circulation is the only source of oxygen and nutrients for the cells.

The issue of vascularization is very critical in cardiac tissue engineering because the ischemic and infarct area have already undergone a blood vessel shortage, thus reducing the blood supply for the survival of cardiomyocytes and the rate of potential angiogenesis during cardiac regeneration therapy. Thus, the success of any cardiac tissue engineering scenario including graft- or *in situ* injectable hydrogel-based approaches requires a timely and effective connection to the blood network of the healthy myocardium surrounding the infarcted region. In particular, the cardiomyocytes in the center of the hydrogel injected into the infarcted region will require a vascular supply of their own because the hydrogel can only supply nutrients for a short period of time. Angiogenesis is currently considered the most pressing obstacle for the implementation of cardiac tissue engineering and myocardial infarction repair. Due to the high metabolic rate of cardiomyocytes within the injected hydrogel at the infarcted region, timely vascularization with an intercapillary distance of 19 to 20 μm [138, 139] within the injected scaffold or implanted cardiac engineered graft is crucial for cardiomyocyte survival. In the past two decades, many studies have been conducted on angiogenesis to promote reperfusion to improve the function of

ischemic/ infarcted heart tissue; however, vascularization in a damaged heart muscle or in engineered cardiac patches/ injected hydrogels is still a central and unresolved problem for myocardial infarction repair [140].

Stimulating angiogenesis and inosculation [141-146] are principal strategies of vascularization within cardiac tissue engineered constructs or hydrogels that are implanted or injected at the infarcted region. The first strategy is based on stimulating and guiding the ingrowth of newly formed blood vessels into the injected/ implanted scaffold from the surrounding vascular network of the host tissue (Fig. 1.2a); the second approach focuses on prevascularization of the engineered cardiac graft or injectable hydrogels and interconnection with the host microvasculature within a short period of time (Fig. 1.2b). When angiogenesis is the only mechanism of vascularization within the injected hydrogel, the physiologically slow blood vessel ingrowth (Fig. 1.2a) prevents the timely supply of oxygen and nutrients to myocytes in the center. In contrast, inosculation can lead to the rapid establishment of an adequate blood supply to the center of the injected hydrogel (Fig. 1.2b).

1.6. Strategies for engineering microvascular networks

As previously discussed, new blood vessels are formed by either angiogenesis, which is the sprouting of new vessels from pre-existing ones, or vasculogenesis, which is the assembly of undifferentiated EPCs. *In vitro* tube formation by capillary ECs was first reported in 1980 by Folkman and Haudenschild, who developed a microvascular network on a gelatin substrate within several weeks of culture [147]. Since then, critical factors that affect vascularization have been better identified and methods for blood vessel formation have been significantly refined as the understanding of vascularization mechanisms has evolved.

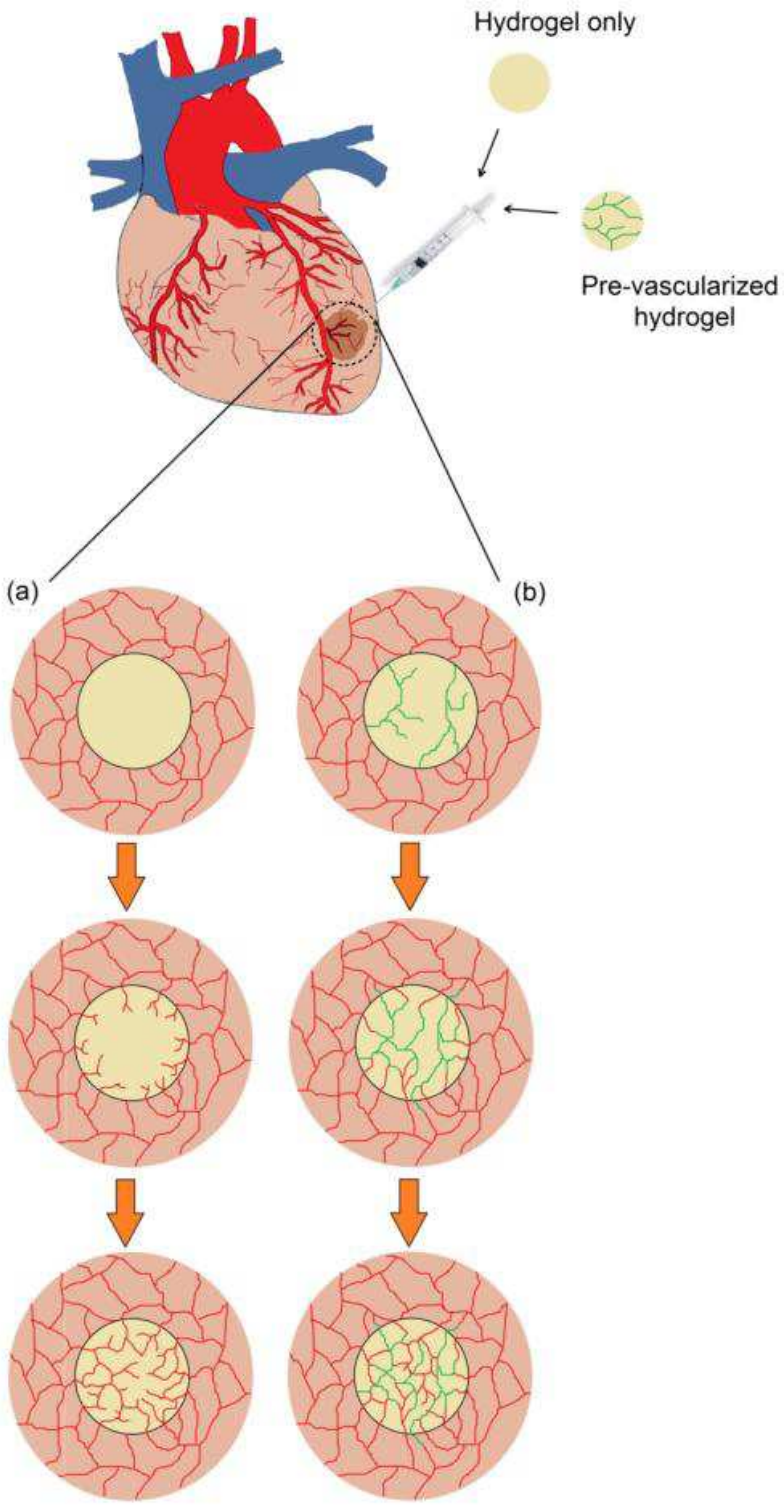

Figure 1.2. Schematic of principal vascularization strategies: (a) angiogenesis only and (b) inosculation within the hydrogel injected into the myocardial infarcted region.

It is now well known that insoluble components of ECM including fibrin, fibronectin, hyaluronan, and laminin have very critical roles in many events during blood vessel formation [148]. The regulation of EC growth, differentiation, migration, pericyte recruitment, and vessel formation are largely influenced by cell-cell interactions and growth factors. ECs from human tissues behave differently than those from rat or bovine aorta; contrary to ECs from animals that spontaneously differentiate into capillary structures, ECs from human tissue require growth factor-based regulation and may degenerate in some basic culture conditions [149]. Although microvascular cells are mostly involved in inflammation, wound healing, and vascularization, the commonly used ECs for vascularization studies are HUVECs isolated from macrovascular origins [150]. Endothelial progenitor cells have been also used for capillary formation in neovascularization studies [151, 152]. The physicochemical and biological properties of cardiac engineered patches or injectable hydrogels have a significant role in regulating vascularization. Porosity, morphology, interconnectivity, and size of pores; ability to facilitate localized and sustained delivery of growth factors; inclusion of ECM components; cell attachment properties; and biodegradability significantly influence vascularized tissue ingrowth.

In cardiac tissue engineering, speedy establishment of vascularization that provides a high microvascular network density is crucial for long-term cardiomyocyte survival; however, it still remains a major challenge. Engineering of microvascular networks ranges from controlling vascular signalling pathways and cellular interactions to direct assembly of engineered blood vessels using microfabrication techniques. Numerous strategies have been proposed in recent years to stimulate vascularization within implanted cardiac scaffolds based on the two principal mechanisms of endogenous stimulation (angiogenesis only and inosculation, Fig. 1.2), and here we highlight those involving different levels of engineering guidance.

1.6.1. Stimulating angiogenesis at the implantation site

Several approaches have been under investigation for improving vascularization of infarcted myocardium based on stimulating angiogenesis at the implantation site. These strategies include: i) direct angiogenic factor delivery, ii) stem cell-based vascularization at the implantation site, iii) scaffold and biomaterial-guided vascular ingrowth, iv) functionalized cardiac scaffolds and injectable hydrogels, and v) micro-patterning of bioactive ligands. Direct angiogenic factor delivery approaches including intravenous, intracoronary, or intramyocardial delivery of angiogenic factors to induce vascularization in ischemic areas have been investigated in recent decades; however, many challenges must be overcome before this strategy advances to a clinical angiogenesis therapy for humans. Table 1.4 presents important angiogenic factors, their roles, associated critical issues, and desired release criteria for angiogenesis stimulation. Recent progress in delivery strategies of angiogenic factors and targeting neovascular maturation as well as critical challenges in this area have been recently reviewed by Chu and Wang (2012) as well as Said et al. (2013) [162, 163]. Stem cell-based approaches for vascular regeneration have demonstrated the capacity to replicate, differentiate, and form new blood vessels in a directed fashion; however, clinical translations of this strategy have been very limited. Recent advances in stem cell-based strategies for vascular regeneration have been reviewed and presented in recent articles by Hutton and Grayson (2014), Silvestre (2012), and Leeper et al. (2010) [164-166].

1.6.1.1. Scaffold architecture and biomaterial support guidance

Conceptually, the easiest way to stimulate angiogenesis is to use scaffolds with appropriate structures to allow for blood vessel penetration into the scaffold, such as porous collagen scaffolds and decellularized porcine myocardial matrix [167, 168]. Recent studies indicate that

Table 1.4. Summary of important angiogenic factors, roles critical issues and release characteristics.

Growth factor	Roles	Issues	Release criteria	Ref.
VEGF[a]	• Motivates proliferation, migration, differentiation, and survival of ECs • Promotes vascular permeability	• Short half-life • Excessive dose causes tumor, leaky and congested vessels	• Tightly controlled dose • Slow and sustained release	[153-157]
bFGF[b]	• Stimulates proliferation, migration, and survival of ECs • Motivates collagenase and plasminogen activator	• Rapid diffusion • Mitogen for variety of cells	• Simultaneous release with VEGF desired	[155, 158]
HGF[c]	• Promotes motility, survival, and invasion of ECs	• Rapid diffusion • Short half-life	• High level of dose and sustained release	[159]
PDGF[d]	• Promotes vascular maturation by regulating recruitment and proliferation of pericytes and SMCs[e] • Regulates the integrity and survival of ECs	High dose causes vessel destabilization	• Controlled dose • Temporally and sequentially controlled release	[160, 161]

[a]vascular endothelial growth factor, [b]basic fibroblast growth factor, [c]hepatocyte growth factor, [d]platelet-derived growth factor, [e]smooth muscle cells

scaffolds with pore sizes smaller than 200 μm facilitate shallow ingrowth of small-diameter blood vessels, whereas those with pore diameters larger than 200 μm allow for deeper ingrowth of larger blood vessels [169-171]. Pore interconnectivity is a critically important factor for the formation of a hierarchical blood vessel structure. A technique involving salt fusion, porogen, and foaming poly(lactic-co-glycolic acid) (PLGA) has been used for increasing the interconnectivity of cardiac scaffolds; however, nondirectional high humidity of the fusion causes an unpredictable geometry of connecting pores [172]. Modification of these physical characteristics of cardiac scaffolds can now be made using micro-biofabrication techniques that enable full control over the 3D configuration [173]. Recently, microstructured ice templates have been used to fabricate silk fibroin-chitosan (SF-CS) scaffolds with predefined microfluidic channels, open-pore surface, and oriented porous structures to enhance cell growth and nutrient delivery [174]. A sprayed phase separation technique has been also used for patterning polyurethane sheets laminated together to form micro-channeled scaffolds [175]. Fabrication of 3-D branching and interconnected flow-channel networks comprising multiple tetrahedral units using a micro-fabrication technique has provided control over pore size and interconnectivity as well as architectural and geometrical characteristics of scaffolds [176]. Another study fabricated micropores at different length scales in cell-laden hydrogels by micromolding fluidic channels and leaching sucrose crystals [177]. In addition to structural characteristics that can promote blood vessel ingrowth into scaffolds, different biomaterial chemical compositions can result in different angiogenic responses after scaffold implantation. Recent studies reveal that PLGA hydrogel can markedly promote vascular ingrowth, guaranteeing more adequate engraftment with the host tissue than collagen, chitosan, and hydroxyapatite hydrogels [178, 179]. Scaffolds

made of isogeneic acellular dentin also promote angiogenesis and neovascularization to rapidly incorporate the scaffold into the host tissue [180].

1.6.1.2. Functionalized cardiac scaffolds and injectable hydrogels

Endogenous blood vessel formation can be stimulated by chemoattractants, such as stromal cell-derived factor-1, granulocyte monocyte colony-stimulating factor, granulocyte colony-stimulating factor, vascular endothelial growth factor (VEGF), placental growth factor, erythropoietin, and angiopoietin-1 to mobilize EPCs *in vivo* [181]. Preclinical and clinical investigations indicate that therapeutic administration of angiogenic factors, such as VEGF and basic fibroblast growth factor (bFGF), to sites of ischemia in the heart can improve regional blood flow [182, 183]. Thus, functionalization of injectable and implantable cardiac scaffolds with biologically active motifs offers many possibilities for stimulating vascularization *in vivo*. Biologically functionalized scaffolds can be achieved by direct incorporation of growth factors into the scaffold, immobilization of GFs onto biomaterials, or encapsulation of GFs within nano/ micro-particulate delivery systems that are subsequently incorporated with scaffolds. As direct incorporation can reduce the half-life of GFs due to oxidation and proteolysis within the scaffold microenvironment, particularly for prolonged release, this approach may be less desirable. Some studies have used angiogenic factors covalently immobilized onto biomaterials to promote EC proliferation and tube formation of primary rat aortic ECs *in vitro* [184-186]. Immobilized GF-based bioactive scaffolds for engineered vascularized cardiac tissues are reviewed by Chiu et al. (2010) [187]. Although covalently immobilized angiogenic factors promote localized EC proliferation for vasculogenesis, the lack of mobility of the immobilized angiogenic factors prevents VEGF diffusion and induction of the VEGF concentration gradient that is considered crucial for navigating tip cells in angiogenesis *in vivo* [188]. Critical regulatory factors of a

functionalized cardiac scaffold include the dose, timing, sequence, and sustainability of release of angiogenic factors. These factors can be well controlled by hybrid delivery systems consisting of particulate delivery vehicles incorporated into injectable or implantable scaffolds, thus providing high flexibility in modulating release profiles of multiple angiogenic factors [189]. In this context, micro- and nano-particulate delivery systems have pivotal roles in regulating the timing, dose, and sequence of release of angiogenic factors for spatiotemporal control of angiogenesis stimulation. Table 1.5 summarizes recent studies on micro/ nano-particulate delivery systems used for controlled release of different angiogenic factors to stimulate angiogenesis or vasculogenesis *in vivo* or *in vitro* in cardiac tissue engineering.

Sequential release of VEGF and platelet derived growth factor (PDGF) through an alginate hydrogel in the myocardial infarction region results in blood vessel maturation and stabilization as well as improved systolic function of the heart [201]. Prolonged release of VEGF from a nanofibrous scaffold functionalized by heparin-binding domain sequence LRKKLGKA and self-assembling peptide RADA16 promoted angiogenesis, reduced scar size, and improved cardiac function [202]. Sequential delivery of VEGF and TAT-HSP27 within 7 and 28 days, respectively, to the ischemic heart through a hybrid scaffold consisting of VEGF-loaded PLGA microspheres and TAT-HSP27-incorporated alginate reduced muscle degeneration and fibrosis and promoted new blood vessel formation in the ischemic site [203]. Sustained release of engineered VEGF and immobilized VEGF for myocardial repair through functionalized and biodegradable collagen cardiac patches decreased fibrosis and increased vasculature density in the infarction site [204, 205]. Sustained release of hepatocyte growth factor (HGF) alone and simultaneous release of HGF and IGF at the site of myocardial infarction through an injectable *in situ* forming alginate hydrogel led to significant improvements in angiogenesis post-infarction

[206]. Injection of collagen-chitosan hydrogel containing thymosin β4 (Tβ4) to myocardial infarcted rat models significantly reduced scar size and improved blood vessel density [207]. Reis et al. (2012) developed a thermoresponsive hydrogel made of chitosan conjugated with the angiopoietin-1 derived peptide, QHREDGS, and mixed with collagen type I; subcutaneous injection of the hydrogel with cardiomyocytes in the back of Lewis rats illustrated its ability to

Table 1.5. Recent *in vivo* and *in vitro* studies on nano/ micro-particulate angiogenic factor delivery systems for myocardial infarction and ischemia repair.

Delivery system	Composition	Angiogenic factor	Type of study	Study conclusion	Ref.
Liposome	Anti-P-selectin-conjugated	VEGF	*In vivo* (targeted delivery to rat infarcted myocardium)	Improved systolic function	[190]
Core-shell lipid-based nanoparticles	Lecithin containing VEGF in core, Pluronic-127[a] in shell	VEGF	*In vitro* (aqueous solution at body temperature)	Minimally improved vascularization compared to single gel only	[191]
Polymeric microsphere	PLGA	VEGF	*In vivo* (ischemic rat model)	Increased angiogenesis, arteriogenesis, greater left ventricle wall thickness	[192]
Polymeric	Trehalose and rat	VEGF	*In vivo*	Significant blood	[193]

microsphere	serum albumin in succinate buffer		(subcutaneous injection into dorsal area of Wistar rats)	vessel formation	
Functionalized polymeric nanosphere	Heparin- chitosan and γ-PGA[b]	FGF	*In vivo* (human foreskin fibroblasts)	Enhanced angiogenic tube formation	[194]
Hybrid microsphere	Combined alginate gel and PLGA	VEGF	*In vivo* (hindlimb ischemia rat model)	Enhanced angiogenesis	[195]
Functionalized nanosphere	Heparin-functionalized fibrin gel	VEGF	*In vivo* (rabbit model of hindlimb ischemia)	Increased angiographic score	[196]
Nanospheres	Dex-GMA and gelatine	VEGF	*In vivo* (rabbit model of hindlimb ischemia)	Significant increase in blood perfusion and capillary density	[197]
Microsphere	PLGA	FGF and NRG1[c]	*In vivo* (myocardial infarction rat model)	Significant improvement in cardiac function	[198]
Nanosphere	PLGA	VEGF	*In vivo* (mouse femoral artery ischemia model)	Increased blood vessel volume	[199]
Microsphere	Collagen	VEGF	*In vitro*	Induction of capillary formation of human umbilical vein ECs	[200]
Hybrid microsphere	PLGA and alginate	Sequential delivery of PDGF and VEGF	*In vivo* (myocardial infarcted rat model)	Higher density of α-actin positive	[201]

[a]poly(ethylene oxide)-poly(propylene oxide)-poly(ethylene oxide), [b]poly(γ-glutamic acid), [c]neuregulin-1

localize at the site of injection and retain cells [208]. The hydrogel was more suitable for the survival and maturation of transplanted cardiomyocytes *in vitro* compared to chitosan-collagen hydrogel alone.

1.6.1.3. Micro-patterning of bioactive ligands

Micro-patterning and bioprinting offer the possibility to organize cells and bioactive molecules in three dimensions *in vitro* with desired density, functionality, and shape. Considering that an intermediate density of ECM components (100-500 ng/cm^2) can significantly promote EC tube networks (within 1-2 days) [209], it is very important to precisely control the density and geometry of ECM-coated substrates for stimulation of vascularization. Micro-patterning of self-assembled monolayers of alkanethiolates to form islands of fibronectin with various geometries on gold led to formation of EC tubular structures on 10-μm wide lines of fibronectin [210]. Micro-patterning of chitosan and gelatine also resulted in capillary morphogenesis of ECs on 20-μm lines of gelatine [210]. In other studies, poly(ethylene glycol) diacrylate hydrogels incorporated with various cell adhesion ligands (e.g., Arg-Gly-Asp-Ser (RGDS)) were used for two-dimensional and 3D micropatterning of these ligands using photolithographic techniques to guide cell adhesion and migration [210-214]. Based on HUVEC adhesion on 50- and 200-μm wide hydrogel laser-printed strips, micro-patterning of various concentrations of poly(ethylene glycol)-RGDS indicated that tubular formation significantly increased at 100 μg/cm^2 after one day [209]. Patterned micro-scale regions of poly(ethylene glycol) hydrogels covalently bound with RGDS and VEGF accelerated tubulogenesis, forming EC tubes with lumens within two days, whereas tubule-like structures formed in two days on RGDS-only control patterns and had no observable lumens [215]. Quantification of the effect of pattern size on tubule formation revealed that all patterned strips smaller than 35 μm promoted tubule formation; however, the percentage of patterns that promoted tubule formation decreased as the pattern size increased [215].

1.6.2. Prevascularization and inosculation strategies

Although widely investigated, angiogenesis is a time-consuming process, as slow as ~5 μm/h [216]; thus, angiogenesis-only strategies are unable to prevent the death of cardiomyocytes in the center of infarcted myocardium in the initial days after implantation. This pivotal issue has led to the emerging field of engineering preformed microvascular networks within injectable or implantable scaffolds. Prevascularization of cardiac scaffolds or injectable hydrogels can be performed by either *in vitro* or *in vivo* approaches. For *in vitro* prevascularization, different combinations of ECs, EPCs, pericytes, smooth muscle cells, and stem cells along with angiogenic factors and ECM compounds are incorporated within injectable hydrogels or implantable scaffolds to form EC tubular structures in the scaffolds or hydrogels within several days to weeks of culturing *in vitro*. Microvascular networks and branching patterns of ECs can be micropatterned using bioprinting within cardiac patches prior to implantation. For *in vivo* prevascularization, both the arteriovenous loop method and avascular grafts in peritoneal cavity have been used to vascularize scaffolds prior to explanation and transferring to the defect site. The prevascularization approach offers the major advantage of anastomosis of a preformed microvascular network to the existing blood vessels of the host tissue in the defect area after implantation. This process is termed inosculation and can significantly accelerate vascularization of the implanted or injected scaffold in the infarcted and ischemic myocardium.

1.6.2.1. In vitro spontaneous microvascular network formation

Coculture of ECs with other cell types, such as pericytes, smooth muscle cells, mural cells, and even stem cells, in relevant ECM and angiogenic factors results in the formation of a spontaneous capillary-like network [217-220]. *In vitro* microvascular network formation in injectable hydrogels and cardiac patches can increase the chance of inosculation after

implantation. Zimmerman et al. (2002) developed a preformed microvascularized and functional cardiac hydrogel by seeding cardiac myocytes within collagen type I mixed with Matrigel [221]. Anastomosis with host tissue vasculature was accelerated when a fibrin hydrogel containing fibroblasts was prevascularized with HUVECs, leading to rapid perfusion and enhanced cell proliferation within the transplant [222]. Comparing the abilities of HUVECs and cord blood EPC-derived ECs (EPC-ECs) to form a microvascular network and inosculation within fibrin gel revealed the better potential of EPC-ECs to anastomose with host vasculature [222]. Co-culture of pericytes and a higher density of fibroblasts also accelerated inosculation [222, 223]. Stevens et al. (2009) developed cardiac patches containing hESC-derived cardiomyocytes, HUVECs, and stromal mouse embryonic fibroblasts that led to the formation of a human EC network resembling a vascular plexus [224]. The microvascularized disc-shaped patches formed significantly larger cardiomyocyte patches that contained more microvascular networks compared to cardiomyocyte-only patches, suggesting the clinical potential of human cardiomyocyte microvascularized patches for myocardial infarction repair.

1.6.2.2. *In-vivo* prevascularization

Because spontaneous microvascular formation methods demand complex and time-consuming cell isolation, seeding, and cultivation procedures and might not necessarily lead to interconnected functional microvessels, *in vivo* prevascularization has been introduced. This approach involves multiple surgeries or an arteriovenous loop to exploit the natural angiogenic potential of an organism to vascularize cardiac scaffolds or patches within the body. The scaffold is implanted into a well-vascularized host tissue or next to an artery, inducing a random ingrowth of microvessels from the host tissue to the scaffold due to angiogenesis that results in functional blood-perfused microvessels in the scaffold. The explanted scaffold is then transferred to the

defect area for faster inosculation. Using this approach, a 2-mm thick cardiac patch made of alginate and proangiogenic factors was implanted on the omentum to generate a microvascular network within the scaffold *in vivo* [225]. The vascularized patch was then explanted after 3 weeks and implanted onto infarcted myocardium. In another study, the same approach was used to generate cardiac patches without the use of exogenous biomaterials [226]. In a recent study, Laschke et al. (2011) demonstrated that short-term cultivation of *in situ* prevascularized scaffold accelerated inosculation of preformed microvascular networks after implantation into the host tissue [227]. They prevascularized a hydroxyapatite/ poly(ester-urethane) scaffold for 20 days by implanting the scaffold in the flank of transgenic mice followed by fractionally destabilizing the preformed microvessels for 3 and 10 days by cultivating the prevascularized scaffold in Dulbecco's modified Eagle's medium (DMEM). They then implanted the cultivated scaffolds into dorsal skinfold chambers of FVB/N wild-type mice for inosculation. Ten days after implantation, the scaffolds that were non-cultivated or cultivated for 10 days contained many preformed non-perfused blood vessels whereas the scaffold cultivated for only 3 days exhibited a dense network of red blood cell-perfused microvessels indicating good inosculation [227]. This experiment clearly indicated that short-term destabilization of preformed microvessels of the scaffold can lead to rapid inosculation with the host tissue.

Alternatively, cardiac patches or scaffolds can be vascularized by implanting scaffolds into an isolation chamber containing an arteriovenous loop [228-230]. In a recent study, a vascular pedicle with intact vessels (or using a constructed arteriovenous loop) and flow-through chamber were placed into an isolated chamber containing a mixture of cells and hydrogel (Matrigel) followed by implantation of the chamber into the groin region of rats [230]. The arteriovenous loop was perfused by the femoral vessels for 4-6 weeks. Blood microvascular ingrowth from

surrounding tissues vascularized the chamber within 4-6 weeks of implantation [230]. This prevascularization approach facilitates the generation of a 2-mm thick vascularized cardiac construct with neonatal rat cardiomyocytes [229, 230]; however, the 3-4 day delay in establishing the new vascular network causes significant cell death immediately post-implantation [229]. This issue has been addressed in rats using a flow-through chamber containing an intact vascular pedicle [231]. Due to the appropriate-sized inflow and outflow conduits (e.g., femoral vessels) for anastomosis, this vascularization approach is very attractive for myocardial infarction repair. One disadvantage is the multiple surgeries required for implantation, explantation, and re-implantation of the cardiac patch or construct.

1.6.2.3. Modular assembly and microvascular fragments incorporation

Modular tissue engineering is a bottom-up approach that aims to create building blocks of tissues to then recreate larger tissues. Self-assembled aggregation, micro-patterning of cell-laden hydrogels, and direct bioprinting of tissues are different methods of bottom-up tissue engineering. The building blocks created are assembled into larger tissues by random packing, stacking of layers, or direct assembly. The random packing approach has been used for assembling tissue modules to create capillary networks. Microtissues composed of cell-embedded hydrogels (e.g., collagen) are prepared and confluent layers of ECs are grown on the module surface [232]. The tissue modules are packed together to form a macrotissue with interconnected tortuous channels, allowing for blood flow in a perfusion bioreactor while confluent ECs perform as antithrombogenic factors to prevent clotting [232-234]. The interconnection of confluent ECs of modules eventually results in a perfusable and non-coagulative tissue to be used for implantation [232]. Although modular tissue assembly allows for quick assembly of a working microvessel network from a premature vascular network, the

initial vasculature is unstable and demands extensive remodeling of parenchymal cells within the tissue to stabilize the vessels [235]. Kunz-Schugart et al. (2006) developed 3-D spheroids containing fibroblasts and ECs as building blocks to create a microvascular network [236]. The packed bed of the spheroids resulted in a complex 3-D network of EC tubular structures with extensions of up to 400 μm, lumen formation, pinocytotic activity, and tight junctions [236]. Kelm et al. (2010) demonstrated the feasibility of biofabrication of engineered vascularized grafts from the tissue spheroids [237]. In a recent attempt to accelerate prevascularization and inosculation, vital microvascular fragments (as the biological building blocks of vascular tissue) isolated from adipose tissue and seeded onto scaffolds under dynamic conditions significantly increased functional microvessel density and interconnections with the host tissue after implantation [238]. This finding indicates that vascularization and inosculation of cardiac patches and injectable hydrogels can be markedly improved by incorporation of microvascular fragments.

1.6.2.4. Tubulogenesis micro-patterning and micro-fluidic microvessels

To further control the assembly of building blocks of microvascular networks, omnidirectional printing has been used to construct 3-D microvascular networks composed of hierarchical and branching topology with microchannel diameters ranging from 200 to 600 μm [239]. A scaffold-free approach has been also used for assembling tissue spheroids with precisely controlled diameter in tubular structures. In this approach, straight agarose rods and uniform multicellular spheroids were initially deposited layer-by-layer with a wall thickness of 300 μm [240]. Once the tubular structure was assembled, multicellular spheroids can fuse within 5-7 days, resulting in a fused tubular structure. The branched pattern of 300 μm spheroids and 0.9-1.2 mm branch diameter fused after 6 days of deposition [240]. Although this approach provides accurate control

of tube diameter and wall thickness, the absence of a functional endothelium was a shortcoming. In another study, ECs embedded within collagen and micro-patterned into 100-μm wide and 50- to 100-μm high strips self-assembled into tubular structures that anastomosed with host vasculature within 3 days of implantation [241]. The microvessel structures that were initially immature with open lumens recruited pericytes and stabilized 28 days post-implantation [242]. Microgroove patterns between an explanted artery and a vein with culturing cardiac cells on the top of the capillary bed have been used to direct capillary sprouting and generate a beating cardiac sheet [243]. Combining photocrosslinking and self-assembled monolayer-based cell deposition techniques, a robust 3-D hydrogel scaffold composed of endothelialized hollow vascular structures was produced [244]. The endothelialized microchannels provide shear conditions associated with flow in the hollow vascular structure that can promote endothelium sustainability [245]. Furthermore, anastomosis points can be well defined in the construct to enhance the connection between the hollow vascular structures and blood microvessels at the implantation site. Thus, micro-fluidic networks designed to mimic human vascular networks show promise for rapid *in vivo* integration with the host tissue.

Control over spatial patterns of vascular networks using microfabrication techniques allows for precise design of anastomosis points, microvascular geometry, tubular diameters, and branching direction and angle in fabricated cardiac scaffolds for rapid inosculation. In addition, co-culture of parenchymal cells embedding vascular cells in precisely defined patterns has been performed using a layer-by-layer biofabrication technique in a tissue engineered construct with limited interactions between the populations of the two cell layers [246]. Fabrication of prevascularized and functional cardiac constructs and patches by bioprinting techniques allows for rapid inosculation of the construct after implantation for effective myocardial infarction repair. Table

1.6 highlights the advantages, disadvantages, and challenges associated with vascularization strategies in tissue engineering.

1.7. Challenges

Despite intense efforts to improve cardiac tissue vascularization, the ability to achieve vascularized cardiac scaffolds to provide mature, stable, and functional microvascular networks capable of rapid integration with the host tissue remains a major challenge. Sophisticated methods based on stimulation of angiogenesis have been developed; however, angiogenesis is a time-consuming process and cardiac cells survival relies on rapid blood supply, so these approaches alone may not prevent the death of cardiac myocytes in the initial days after implantation.

Recent studies indicate that, in many cases of prevascularized scaffolds, inosculation is observed within 4 days of implantation while the ingrowth of new blood vessels into large tissue engineered scaffolds can take several weeks via angiogenesis alone. Despite the fact that prevascularization promotes inosculation, even this approach is incapable of providing adequate blood perfusion to prevent the death of cardiomyocytes in the initial days after implantation [265, 266]. This is most likely due to the fact that effective inosculation can only occur when preformed microvessels of the implanted scaffold and the pre-existing blood vessels of the host tissue simultaneously grow toward each other to form interconnections. Therefore, directed sprouting in both the scaffold and the host tissue has a pivotal role in accelerating inosculation after implantation. To achieve directed cardiac tissue regeneration and vascularization, spatiotemporal control over biochemical and microstructural characteristics of the cardiac patch is very crucial.

Table 1.6. Advantages, disadvantages, and challenges associated with common tissue engineered scaffold vascularization strategies.

Vascularization approach	Pros	Cons	Challenges	Ref.
Delivery of pro-angiogenic factors	• Well and widely investigated • Profound effects of VEGF alone on angiogenesis • Significant vascularization using multiple angiogenic factor delivery • Minimally invasive delivery through injectable hydrogels into the ischemic region • Clinically efficient and cost effective via transendocardial hydrogel injection	• Overdose of angiogenic factors (e.g., VEGF) can lead to aberrant vessels and hemangiomas • Short half-life of angiogenic factors dramatically reduces their efficacy and retention in the target zone • Microenvironmental dose is critical and delivery of a single angiogenic factor is not always the best strategy	• Characterization of optimal release kinetics and profiles, and dose of vital angiogenic factors • Development and optimization of sophisticated delivery systems to provide sequential and spatio-temporally controlled release of multiple angiogenic factors • Determination of the most effective angiogenic factor combinations	[247-250]
Injection of transfected cells and EPCs within hydrogels	• Genetic alterations could improve the effectiveness of cell transplantation	• Over-expression of angiogenic factors can cause destabilized	• Optimization of quantity/ number of cells injected to the ischemic area • Isolation of subsets of	[247, 251-, 255]

	• Expressions of multiple angiogenic factors improve vascularization • Transfected MSCs support their survival in addition to angiomyogenic response post-transplantation • Released angiogenic factors from transfected cells facilitate angiogenesis • The ability of EPCs to differentiate into ECs and to initiate new vessel formation • EPCs can also secret angiogenic factors and differentiate into cardiomyocytes • ECs can form complex vascular network	vascularization or massive blood vessels (tumor) • Uncontrolled angiogenic factor release by the transfected cells after injection • EPC-mediated vasculogenesis essential for malignant growth of tumours • Apoptosis rate of ECs in injected gels is high • Limited proliferative potential of mature ECs reduces the clinical applicability	EPCs due to the lack of consensus on EPC-defining markers and standardized protocols for their detection	
Functionalized and	• Stimulating vessel	• Slow vascularization	• Sophisticated delivery	[201,

injectable scaffolds	ingrowth into scaffolds *in vivo* • Synergistic effect of multiple factors including biomaterial support, GFs, ECM components promote angiogenesis *in vivo*	due to endogenous angiogenesis-only • Slow inosculation • Loss of GF biological functionality if GFs remain unprotected in the scaffold	systems are required to regulate dose, timing, sequence, and profile of GF release	231, 235, 236]
Spontaneous vascularization in biomaterials of injectable scaffolds and cardiac patches	• The most close-to-nature vascularization • Functional anastomosis based on numerous studies • Easy to play with scaffold/ hydrogel composition for optimization • Ability to use co-culture of multiple cells (e.g., ECs with fibroblasts)	• Reduced EC-to-EC connections • Formation of fibrous tissues during scaffold degradation • Potential host inflammatory reactions to the scaffold polymer/ monomers • Extremely difficult to control due to many factors (e.g., multiple angiogenic factors, scaffold ingredients, type of cells) involved	• Vasculogenesis mechanism controls the vascularization and is not well understood • Identifying the subsets of EPC leading to effective vascularization • Vessel maturation followed by tubular formation • Adjusting scaffold porosity for oxygen transfer in bioreactor	[149, 221, 222, 256-258]
Modular tissue	• A prominent	• Randomized vascular	• Presence of ECs alone	[235, 259,

assembly	engineering approach for vascularization • Easily scalable • Structurally controlled endothelium assembly	networks • Lack of components for immediate anastomosis • Extensive tissue remodeling essential for successful engraftment • Isolated tissue modules may be problematic for contractive cardiac muscle regeneration	leads to a significant vessel regression due to immune response • Long inosculation time (~20 days) to integrate with host tissue	260]
In vivo prevascularization	• Prevascularization of thick (2 mm) cardiac patches • Fast inosculation • Fully functional vascular network formation	• Multiple surgeries required • Cardiac cell death due to delay in new vessel network formation (3-4 days)	• Large and thick scaffolds (cms) require appropriate anatomical sites on the patient • Large scaffolds leave wound behind on the patient after vascularization	[227-230]
Tubulogenesis micro-patterning	• Organized ECs, SMCs, and molecules in scaffold • ECs can self-organize into tubular structures	• Microvessels have initially immature structures with open lumens • Weak mechanical	• Tubular channels need to rapidly evolve into stable vascular networks • Efficient bioreactors to accelerate tissue	[240, 241, 261-263]

	in 2 days • Desired local cell density and anatomical shape • Defined topology and tubular structure • Promoting angiogenesis	properties of microvessel networks	maturation are required • Micro-patterning of combinational cells (ECs, pericytes) to improve vascular maturation	
3D-Bioprinting and micro-fluidic microvessels	• Precisely controlled geometry of 3D complex vasculatures in micron • Ability to create complex hierarchical macro- to micro-vascular trees • Forming confluent linings • Lower chance of contaminating substrates due to contactless printing • Defined anastomosis points for fast inosculation	• Resolution lower than microfluidic technique • Cell damage due to high shear stress during ejection and the impact of fluid drops • Potential changes in bioactive molecules during the inkjet delivery process • Costly • Weak mechanical properties of bioprinted constructs • Potential damage to cells and DNA during printing	• Retention of biological activity of printed bioinks • Retention of printed patterns over time • Biopaper removal after bioprinting • Scalability • Combinational printing of functional ECs, SMCs, and fibroblasts to mimic intima, media, and adventitia	[256, 263, 264]

With rapid development in micro-fabrication technologies including bio-printing of engineered tissue scaffolds, it becomes increasingly possible to precisely fabricate 3D cardiac constructs with spatially well defined microstructural properties to provide physical and biochemical cues essential for guided vascularization and cardiac regeneration. To this end, spatiotemporal control of GF release is of critical importance and yet remains unachievable. Also, 3D-printing of cardiac patches made of soft hydrogels (>98% water) is challenging and needs to be optimized. Furthermore, due to low density and weak X-ray absorption coefficient of the hydrogels, conventional radiography and X-ray μ-CT provide little or no information of microstructural features of the implanted hydrogel-based cardiac patches; thus, development of non-invasive and quantitative imaging methods with no contrast agents for visualization and longitudinal assessment of the implanted hydrogel-based cardiac patches is strategic priority in cardiac tissue engineering.

1.8. Research objectives

In overall, this research aims to develop polymeric nanoparticle for regulating GF release and non-invasive quantitative imaging techniques for cardiac tissue engineering. Accordingly, specific objectives of this research are set as follows:

- Optimization of nanoparticle fabrication variables that affect the size, polydispersity, loading capacity, zeta potential and morphology of the nanoparticles through comprehensive experimental and computational studies.
- Regulation of the release of multiple growth factors to promote angiogenesis in fibrin matrix through the development of biologically active bi-layer nanoparticles for time-delayed release and single polymer nanoparticles for zero-order release kinetics.

- Mathematical modeling of release behavior of bi-layer nanoparticles to have a better insight into the release mechanism and provide a powerful and efficient tool for developing nanoparticles for cardiovascular tissue engineering.
- Development of a low-dose synchrotron-based in-line phase contrast computed tomography for non-invasive visualization and quantitative assessment of an implanted 3D-printed hydrogel cardiac patch towards monitoring patch degradation as well as vascularization and cardiac regeneration guided by the nanoparticles in the patch *in-situ*.

1.9. Organization of the dissertation

The dissertation is organized into seven chapters, including this introductory chapter.

A literature review on rate-programming of nanoparticulate delivery systems for bioactive tissue engineered constructs is presented in Chapter 2. GF release strategies in tissue engineering are reviewed, critical factors in release behavior of polymeric nanoparticles are discussed, and the role of mathematical modeling of controlled release for designing smart tissue engineered scaffolds is elaborated. Moreover, spatiotemporal control of GF release in tissue engineered scaffolds is introduced as a challenge in cardiac tissue engineering.

Chapter 3 presents a comprehensive experimental study, along with the development of a novel Geno-Neural model, on the optimization of the nanoparticle fabrication variables, which affect nanoparticle characteristics including size, polydispersity, zeta potential, protein loading capacity, and morphology. Physical, morphological and release characteristics of the polymeric nanoparticles are evaluated at different fabrication conditions. Moreover, the effect of the fabrication variables on the structural integrity of the encapsulated protein is investigated.

In Chapter 4, the development and characterization of bi-layer nanoparticles are explored, the structural integrity of the encapsulated protein in the bi-layer nanoparticles is examined, and the

performance of the nanoparticles to regulate simultaneous and sequential release of multiple angiogenic GFs is assessed in the context of angiogenesis in fibrin matrix hydrogel through an *ex-vivo* study. Furthermore, a validated hybrid computational approach is presented for pre-programming of release rates of the nanoparticles.

In Chapter 5, two novel mathematical modeling approaches which are validated by experimental data are presented to explore the release mechanisms of the bi-layer nanoparticles. The models are implemented to identify and predict critical parameters of the bi-layer nanoparticles involved in the polymer degradation and protein release mechanisms for time-delayed release patterns. The predictability of the models is discussed by comparing the estimated release parameters to measured values and those in literature.

Chapter 6 presents a comprehensive study on the development of the synchrotron in-line PCI-CT that includes 3D-printing of a dual-component hydrogel-based cardiac patch, surgical and patch implantation procedure in a rat MI model. The optimum imaging parameters are presented and the procedure for lowering the radiation dose is given in details. The imaging performance of phase retrieved PCI-CT is compared to that of phase non-retrieved phase contrast imaging and magnetic resonance imaging (MRI) for the same sample. The visualized patch microstructural features are quantitatively compared to the measured values from stereomicroscope images. Moreover, image quality criteria of the developed low dose PCI-CT is evaluated and statistically compared to the standard PCI-CT to evaluate the potentials of the PCI-CT for cardiac tissue engineering studies.

Finally, Chapter 7 presents the conclusions drawn from this research. The first section of Chapter 7 concludes the achievements of this research associated with the development of the rate-modulated nanoparticles as well as the presented computational models to design and pre-

program polymeric nanoparticles for cardiac tissue engineering. The second section of Chapter 7 presents the conclusion drawn from the development of the low-dose synchrotron-based PCI-CT for non-invasive quantitative visualization of implanted cardiac patch and cardiac tissues for cardiac tissue engineering studies.

1.10. Contributions of the primary investigator

The manuscripts included in this thesis are co-authored; however it is the mutual understanding of all authors that Mohammad Izadifar, as the first author, is the primary investigator of the research work. The contributions of other authors are greatly appreciated and acknowledged in this thesis.

References

[1] Roger VL, Go AS, Lloyd-Jones DM, Benjamin EJ, Berry JD, Borden WB, Bravata DM, Dai S, Ford ES, Fox CS, Fullerton HJ, Gillespie C, Hailpern SM, Heit JA, Howard VJ, Kissela BM, Kittner SJ, Lackland DT, Lichtman JH, Lisabeth LD, Makuc DM, Marcus GM, Marelli A, Matchar DB, Moy CS, Mozaffarian D, Mussolino ME, Nichol G, Paynter NP, Soliman EZ, Sorlie PD, Sotoodehnia N, Turan TN, Virani SS, Wong ND, Woo D, Turner MB 2012 Heart disease and stroke statistics-2012 update: a report from the American Heart Association. Circulation. **125** e2-220.

[2] Go AS, Mozaffarian D, Roger VL, Benjamin EJ, Berry JD, Blaha MJ, Dai S, Ford ES, Fox CS, Franco S, Fullerton HJ, Gillespie C, Hailpern SM, Heit JA, Howard VJ, Huffman MD, Judd SE, Kissela BM, Kittner SJ, Lackland DT, Lichtman JH, Lisabeth LD, Mackey RH, Magid DJ, Marcus GM, Marelli A, Matchar DB, McGuire DK, Mohler ER 3rd, Moy CS, Mussolino ME, Neumar RW, Nichol G, Pandey DK, Paynter NP, Reeves MJ, Sorlie PD, Stein J, Towfighi A, Turan TN, Virani SS, Wong ND, Woo D, Turner MB 2014 Heart disease and stroke statistics-2014 update: a report from the American Heart Association. Circulation. **129** e28-292.

[3] Rosamond W., Flegal K., Furie K., Go A, Greenlund K, Haase N, Hailpern SM, Ho M, Howard V, Kissela B, Kittner S, Lloyd-Jones D, McDermott M, Meigs J, Moy C, Nichol G, O'Donnell C, Roger V, Sorlie P, Steinberger J, Thom T, Wilson M, Hong Y 2008 Heart disease and stroke statistics-2008 update: a report from the American Heart Association. Circulation. **117** e25-146.

[4] Ripa RS, Nilsson JC, Wang Y, Sondergaard L, Jorgensen E, Kastrup J 2007 Short- and long-term changes in myocardial function, morphology, edema, and infarct mass after ST-segment

elevation myocardial infarction evaluated by serial magnetic resonance imaging. Am Heart J. **154** 929-36.

[5] Morice MC, Serruys PW, Kappetein AP, Feldman TE, Stahle E, Colombo A, Mack MJ, Holmes DR, Torracca L, van Es GA, Leadley K, Dawkins KD, Mohr F 2010 Outcomes in patients with de novo left main disease treated with either percutaneous coronary intervention using paclitaxel-eluting stents or coronary artery bypass graft treatment in the Synergy Between Percutaneous Coronary Intervention with TAXUS and Cardiac Surgery (SYNTAX) trial. Circulation. **121** 2645-2653.

[6] Parolari A, Pesce LL, Trezzi M, Loardi C, Kassem S, Brambillasca C, Miguel B, Tremoli E, Biglioli P, Alamanni F 2009 Performance of EuroSCORE in CABG and off-pump coronary artery bypass grafting: single institution experience and meta-analysis. Eur Heart J. **30** 297-204.

[7] Athanasuleas CL, Buckberg GD, Stanley AW, Siler W, Dor V, Di Donato M, Menicanti L, Almeida de Oliveira S, Beyersdorf F, Kron IL, Suma H, Kouchoukos NT, Moore W, McCarthy PM, Oz MC, Fontan F, Scott ML, Accola KA 2004 Surgical ventricular restoration in the treatment of congestive heart failure due to post-infarction ventricular dilation. J Am Coll Cardiol. **44** 1439-1445.

[8] Van Bommel RJ, Delgado V, Schalij MJ, Bax JJ 2010 Critical appraisal of the use of cardiac resynchronization therapy beyond current guidelines. J Am Coll Cardiol. **56** 754-762.

[9] Bonow RO, Maurer G, Lee KL, Holly TA, Binkley PF, Desvigne-Nickens P, Drozdz J, Farsky PS, Feldman AM, Doenst T, Michler RE, Berman DS, Nicolau JC, Pellikka PA, Wrobel K, Alotti N, Asch FM, Favaloro LE, She L, Velazquez EJ, Jones RH, Panza JA 2011 Myocardial viability and survival in ischemic left ventricular dysfunction. N Engl J Med. **364** 1617-1625.

[10] Cohen DJ, Van Hout B, Serruys PW, Mohr FW, Macaya C, den Heijer P, Vrakking MM, Wang K, Mahoney EM, Audi S, Leadley K, Dawkins KD, Kappetein AP 2011 Quality of life after PCI with drug-eluting stents or coronary-artery bypass surgery. N Engl J Med. **364** 1016-1026.

[11] Jones RH, Velazquez EJ, Michler RE, Sopko G, Oh JK, O'Connor CM, Hill JA, Menicanti L, Sadowski Z, Desvigne-Nickens P, Rouleau JL, Lee KL 2009 Coronary bypass surgery with or without surgical ventricular reconstruction. N Engl J Med. **360** 1705-1717.

[12] Velazquez EJ, Lee KL, Deja MA, Jain A, Sopko G, Marchenko A, Ali IS, Pohost G, Gradinac S, Abraham WT, Yii M, Prabhakaran D, Szwed H, Ferrazzi P, Petrie MC, O'Connor CM, Panchavinnin P, She L, Bonow RO, Rankin GR, Jones RH, Rouleau JL 2011 Coronary artery bypass surgery in patients with left ventricular dysfunction. N Engl J Med. **364** 1607-1616.

[13] Deb A, Wang S, Skelding KA, Miller D, Simper D, Caplice NM 2003 Bone marrow-derived cardiomyocytes are present in adult human heart: A study of gender-mismatched bone marrow transplantation patients. Circulation. **107** 1247-1249.

[14] Laflamme MA, Myerson D, Saffitz JE, Murry CE 2002 Evidence for cardiomyocyte repopulation by extracardiac progenitors in transplanted human hearts. Circ Res. **90** 634-640.

[15] Quaini F, Urbanek K, Beltrami AP, Finato N, Beltrami CA, Nadal-Ginard B, Kajstura J, Leri A, Anversa P 2002 Chimerism of the transplanted heart. N Engl J Med. **346** 5-15.

[16] Jessup M, and Brozena S. Heart failure. N Engl J Med. 2003;348,2007-18.

[17] Copeland JG, Smith RG, Arabia FA, Nolan PE, Sethi GK, Tsau PH, McClellan D, Slepian MJ 2004 Cardiac replacement with a total artificial heart as a bridge to transplantation. N Engl J Med. **351** 859-867.

[18] Le Huu A, Paul A, Xu L, Prakash S, Shum-Tim D 2013 Recent advancements in tissue engineering for stem cell-based cardiac therapies. Ther Deliv. **4** 503-516.

[19] Libby P, Ridker PM, Hansson GK 2011 Progress and challenges in translating the biology of atherosclerosis. Nature.**473** 317-325.

[20] HAR Hadi, CS Carr, J Al-Suwaidi 2005 Endothelial Dysfunction: Cardiovascular Risk Factors, Therapy, and Outcome. Vasc Health Risk Manag. **1** 183–198.

[21] Rodford JL, Torrens C, Siow RC, Mann GE, Hanson MA, Clough GF 2008 Endothelial dysfunction and reduced antioxidant protection in an animal model of the developmental origins of cardiovascular disease. J Physiol. **586** 4709-4720.

[22] Bahorun T, Soobrattee MA, Luximon-Ramma V, Aruoma OI 2006 Free Radicals and Antioxidants in Cardiovaskular Health and Disease. Internet J Med Update. **1** 1–17.

[23] Kustiyah I, Prasetyo A. Sarjadi. Pengaruh B, Variasi D, Ekstrak M, et al. 2003 Lipid Serum dan Perkembangan Lesi Atherosklerotik pada Aorta Abdominalis Tikus Wistar. Media Medika Indonesiana.**38** 193–202.

[24] Lilly SL. Pathophysiology of heart diseases: a collaborative project of medical students and faculty. Wolters Kluwer; 5th edition, Baltimore, MD (2011).

[25] Nitenberg A 2006 Hypertension, endothelial dysfunction and cardiovascular risk. Arch Mal Coeur Vaiss. **99** 915-921.

[26 Beulens JW, Bots ML, Atsma F, Bartelink ML, Prokop M, Geleijnse JM, Witteman JC, Grobbee DE, van der Schouw YT 2009 High dietary menaquinone intake is associated with reduced coronary calcification. Atherosclerosis **203** 489-493.

[27] Dobnig H, Pilz S, Scharnagl H, Renner W, Seelhorst U, Wellnitz B, Kinkeldei J, Boehm BO, Weihrauch G, Maerz W 2008 Independent association of low serum 25-hydroxyvitamin d

and 1,25-dihydroxyvitamin d levels with all-cause and cardiovascular mortality. Arch Intern Med. **168** 1340-1349.

[28] Bonora E, Kiechl S, Willeit J, Oberhollenzer F, Egger G, Meigs JB, Bonadonna RC, Muggeo M 2007 Insulin Resistance as Estimated by Homeostasis Model Assessment Predicts Incident Symptomatic Cardiovascular Disease in caucasian subjects from the general population the bruneck study. Diabetes Care. **30** 318-324.

[29] Wan JB, Huang LL, Rong R, Tan R, Wang J, Kang JX 2010 Endogenously decreasing tissue n-6/n-3 fatty acid ratio reduces atherosclerotic lesions in apolipoprotein E-deficient mice by inhibiting systemic and vascular inflammation. Arterioscler Thromb Vasc Biol. **30** 2487-2494.

[30] Opie LH, Commerford PJ, Gersh BJ, Pfeffer MA 2006 Controversies in ventricular remodelling. Lancet. **367** 356-367.

[31] Frangogiannis NG, Smith CW, Entman ML 2002 The inflammatory response in myocardial infarction. Cardiovasc Res. **53** 31-47.

[32] Frangogiannis NG, Mendoza LH, Ren G, Akrivakis S, Jackson PL, Michael LH, Smith CW, Entman ML 2003 MCSF expression is induced in healing myocardial infarcts and may regulate monocyte and endothelial cell phenotype. Am J Physiol Heart Circ Physiol. **285** H483-92.

[33] Ren G 2003 Inflammatory mechanisms in myocardial infarction. Curr Drug Targets Inflamm Allergy. **2** 242-256.

[34] Luikart SD, Levay-Young B, Hinkel T, Shearer J, Mills C, Caldwell MD, Gyetko MR, Oegema TR 2006 Mactinin treatment promotes wound-healing-associated inflammation in urokinase knockout mice. Wound Repair Regen. **14** 123-128.

[35] Moldovan NI, Goldschmidt-Clermont PJ, Parker-Thornburg J, Shapiro SD, Kolattukudy PE 2000 Contribution of Monocytes/Macrophages to Compensatory Neovascularization: The Drilling of Metalloelastase-Positive Tunnels in Ischemic Myocardium. Circ Res. **87** 378-384.

[36] Sunderkotter C, Steinbrink K, Goebeler M, Bhardwaj R, Sorg C 1994 Macrophages and angiogenesis. J Leukoc Biol. **55** 410-422.

[37] Camelliti P, Borg TK, Kohl P 2005 Structural and functional characterisation of cardiac fibroblasts. Cardiovasc Res. **65** 40-51.

[38] Anzai T 2013 Post-Infarction Inflammation and Left Ventricular Remodeling: A Double-Edged Sword. Circ J. **77** 580-587.

[39] Nian M, Lee, P, Khaper N, Liu P 2004 Inflammatory cytokines and postmyocardial infarction remodeling. Circ Res. **94** 1543-1553.

[40] Novakovic GV, Tandon N, Godier A, Maidhof R, Marsano A, Martens TP, Radisic M 2010 Challenges in cardiac tissue engineering. Tissue Eng Part B. **16** 169-187.

[41] Kakio T, Matsumori A, Ono K, Ito H, Matsushima K, Sasayama S 2000 Roles and relationship of macrophages and monocyte chemotactic and activating factor/monocyte chemoattractant protein-1 in the ischemic and reperfused rat heart. lab invest. **80** 1127-1136.

[42] Lambert JM, Lopez EF, Lindsey ML 2008 Macrophage roles following myocardial infarction. Int J Cardiol. **130** 147-158.

[43] Dobaczewski M, Gonzalez-Quesada C, Frangogiannis NG 2010 The extracellular matrix as a modulator of the inflammatory and reparative response following myocardial infarction. J Mol Cell Cardiol. **48** 504-511.

[44] Etzion S, Kedes LH, Kloner RA, Leor J 2001 Myocardial regeneration: Present and future trends. Am J Cardiovasc Drugs. **1** 233-244.

[46] Papadaki M, Bursac N, Langer R, Merok J, Vunjak-Novakovic G, Freed LE 2001 Tissue engineering of functional cardiac muscle: Molecular, structural, and electrophysiological studies. Am J Physiol Heart Circ Physiol. **280** H168-178.

[47] Carrier RL, Rupnick M, Langer R, Schoen FJ, Freed LE, Vunjak-Novakovic G 2002 Perfusion improves tissue architecture of engineered cardiac muscle. Tissue Eng. **8** 175-188.

[48] Dar A, Shachar M, Leor J, Cohen S 2002 Optimization of cardiac cell seeding and distribution in 3D porous alginate scaffolds. Biotechnol Bioeng. **80** 305-312.

[49] Shimizu T, Yamato M, Isoi Y, Akutsu T, Setomaru T, Abe K, Kikuchi A, Umezu M, Okano T 2002 Fabrication of pulsatile cardiac tissue grafts using a novel 3-dimensional cell sheet manipulation technique and temperature-responsive cell culture surfaces. Circ Res. **90** e40.

[50] Kofidis T, Akhyari P, Wachsmann B, Boublik J, Mueller-Stahl K, Leyh R, Fischer S, Haverich A 2002 A novel bioartificial myocardial tissue and its prospective use in cardiac surgery. Eur J Cardio-Thorac Surg. **2** 238-243.

[51] Xiang Z, Liao RL, Kelly MS, Spector M 2006 Collagen-gag scaffolds grafted onto myocardial infarcts in a rat model: a delivery vehicle for mesenchymal stem cells. Tissue Eng. **12** 2467-2478.

[52] Leor J, Aboulafia-Etzion S, Dar A, Shapiro L, Barbash IM, Battler A, Granot T, Cohen S 2000 Bioengineered cardiac grafts: A new approach to repair the infarcted myocardium. Circulation. **102** 56-61.

[53] Radisic M, Vunjak-Novakovic G 2005 Serbian. Cardiac tissue engineering. J Chem Soc. **70** 541-556.

[54] Caspi O, Lesman A, Basevitch Y, Gepstein A, Arbel G, Huber I, Gepstein L, Levenberg S 2007 Tissue Engineering of Vascularized Cardiac Muscle From Human Embryonic Stem Cells. Circ Res. **100** 263-272.

[55] Shin M, Ishii O, Sueda T, Vacanti JP 2004 Contractile cardiac grafts using a novel nanofibrous. Biomaterials. **25** 3717-3723.

[56] Alperin C, Zandstra PW, Woodhouse KA 2005 Polyurethane films seeded with embryonic stem cell-derived cardiomyocytes for use in cardiac tissue engineering. Biomaterials. **26** 7377-7386.

[57] Zimmermann WH, Melnychenko I, Eschenhagen T 2004 Engineered heart tissue for regeneration of diseased hearts. Biomaterials. **25** 1639-1647.

[58] Siminiak T, Burchardt P, Kurpisz M 2006 Postinfarction heart failure: surgical and trans-coronary-venous transplantation of autologous myoblasts. Nat Clin Pract Cardiovasc Med. **3** S46-S51.

[59] Zhang M, Methot D, Poppa V, Fujio Y, Walsh K, Murry CE 2001 Cardiomyocyte grafting for cardiac repair: graft cell death and anti-death strategies. J Mol Cell Cardiol. **33** 907-921.

[60] Discher DE, Mooney DJ, Zandstra PW 2009 Growth factors, matrices, and forces combine and control stem cells. Science. **324** 1673-1677.

[61] Watanabe K, Ueno M, Kamiya D, Nishiyama A, Matsumura M, Wataya T, Takahashi JB, Nishikawa S, Muguruma K, Sasai Y 2007 A rock inhibitor permits survival of dissociated human embryonic stem cells. Nat Biotechnol. **25** 681-686.

[62] Padin-Iruegas ME, Misao Y, Davis ME, Segers VFM, Esposito G, Tokunou T, Urbanek K, Hosoda T, Rota M, Anversa P, Leri A, Lee RT, Kajstura J 2009 Cardiac progenitor cells and

biotinylated insulin-like growth factor-1 nanofibers improve endogenous and exogenous myocardial regeneration after infarction. Circulation.**120** 876-887.

[63] Torella D, Rota M, Nurzynska D, Musso E, Monsen A, Shiraishi I, Zias E, Walsh K, Rosenzweig A, Sussman MA, Urbanek K, Nadal-Ginard B, Kajstura J, Anversa P, Leri A 2004 Cardiac stem cell and myocyte aging, heart failure, and insulin-like growth factor-1 overexpression. Circ Res. **94** 514-524.

[64] Santini MP, Tsao L, Monassier L, Theodoropoulos C, Carter J, Lara-Pezzi E, Slonimsky E, Salimova E, Delafontaine P, Song YH, Bergmann M, Freund C, Suzuki K, Rosenthal N 2007 Enhancing repair of the mammalian heart. Circ Res. **100** 1732-1740.

[65] Brutsaert DL 2003 Cardiac endothelial-myocardial signalling: its role in cardiac growth, contractile performance, and rhythmicity. Physiol Rev. **83** 59-115.

[66] Leucker TM, Bienengraeber M, Muravyeva M, Baotic I, Weihrauch D, Brzezinska AK, Warltier DC, Kersten JR, Pratt PF Jr 2011 Endothelial-cardiomyocyte crosstalk enhances pharmacological cardioprotection. J Mol Cell Cardiol. **51** 803-811.

[67] Teng R, Calvert JW, Sibmooh N, Piknova B, Suzuki N, Sun J, Martinez K, Yamamoto M, Schechter AN, Lefer DJ, Noguchi CT 2011 Acute erythropoietin cardioprotection is mediated by endothelial response. Basic Res Cardiol. **106** 343-354.

[68] Noireaud J, Andriantsitohaina R 2014 Recent insights in the paracrine modulation of cardiomyocyte contractility by cardiac endothelial cells Biomed Res Int. **2014** 923805.

[69] Nguyen H, Qian JJ, Bhatnagar RS, Li S 2003 Enhanced cell attachment and osteoblastic activity by P-15 peptide-coated matrix in hydrogels. Biochem Biophys Res Commun. **311** 179-186.

[70] Ventre M, Causa F, Netti PA 2012 Determinants of cell-material crosstalk at the interface: towards engineering of cell instructive materials. J R Soc Interface. **9** 2017-2032.

[71] Nian M, Lee P, Khaper N, Liu P 2004 Inflammatory cytokines and postmyocardial infarction remodeling. Circ Res. **94** 1543-1553.

[72] Hench LL, Polak JM 2004 Third-generation biomedical materials. Science. **95** 1014-1017.

[73] Beltrami AP, Barlucchi L, Torella D, Baker M, Limana F, Chimenti S, Kasahara H, Rota M, Musso E, Urbanek K, Leri A, Kajstura J, Nadal-Ginard B, Anversa P 2003 Adult cardiac stem cells are multipotent and support myocardial regeneration. Cell. **114** 763-776.

[74] Oh H, Bradfute SB, Gallardo TD, Nakamura T, Gaussin V, Mishina Y, Pocius J, Michael LH, Behringer RR, Garry DJ, Entman ML, Schneider MD 2003 Cardiac progenitor cells from adult myocardium: homing, differentiation, and fusion after infarction. Proc Natl Acad Sci USA. **100** 12313-12318.

[75] Matsuura K, Nagai T, Nishigaki N, Oyama T, Nishi J, Wada H, Sano M, Toko H, Akazawa H, Sato T, Nakaya H, Kasanuki H, Komuro I 2004 Adult cardiac Sca-1-positive cells differentiate into beating cardiomyocytes. J Biol Chem. **279** 11384-11391.

[76] Takano H, Ohtsuka M, Akazawa H, Toko H, Harada M, Hasegawa H, Nagai T, Komuro I 2003 Pleiotropic effects of cytokines on acute myocardialinfarction: G-CSF as a novel therapy for acute myocardial infarction. Curr Pharm Des. **9** 1121-1127.

[77] Minatoguchi S, Takemura G, Chen XH, Wang N, Uno Y, Koda M, Arai M, Misao Y, Lu C, Suzuki K, Goto K, Komada A, Takahashi T, Kosai K, Fujiwara T, Fujiwara H 2004 Acceleration of the healing process and myocardial regeneration may be important as a mechanism of improvement of cardiac function and remodeling by postinfarction granulocyte colony stimulating factor treatment. Circulation. **109** 2572-2580.

[78] Orlic D, Kajstura J, Chimenti S, Limana F, Jakoniuk I, Quaini F, Nadal-Ginard B, Bodine DM, Leri A, Anversa P 2001 Mobilized bone marrow cells repair the infarcted heart, improving function and survival. Proc Natl Acad Sci USA. **98** 10344-10349.

[79] Ohtsuka M, Takano H, Zou Y, Toko H, Akazawa H, Qin Y, Suzuki M, Hasegawa H, Nakaya H, Komuro I 2004 Cytokine therapy prevents left ventricular remodeling and dysfunction after myocardial infarction through neovascularization. FASEB J. **18** 851-853.

[80] Hiasa K, Ishibashi M, Ohtani K, Inoue S, Zhao Q, Kitamoto S, Sata M, Ichiki T, Takeshita A, Egashira K 2004 Gene transfer of stromal cell-derived factor-1{alpha} enhances ischemic vasculogenesis and angiogenesis via vascular endothelial growth factor/endothelial nitric oxide synthase-related pathway: Next-generation chemokine therapy for therapeutic neovascularization. Circulation. **109** 2454-2461.

[81] Askari AT, Unzek S, Popovic ZB, Goldman CK, Forudi F, Kiedrowski M, Rovner A, Ellis SG, Thomas JD, DiCorleto PE, Topol EJ, Penn MS 2003 Effect of stromal-cell-derived factor 1 on stem-cell homing and tissue regeneration in ischaemic cardiomyopathy. Lancet. **362** 697-603.

[82] Yamaguchi J, Kusano KF, Masuo O, Kawamoto A, Silver M, Murasawa S, Bosch-Marce M, Masuda H, Losordo DW, Isner JM, Asahara T 2003 Stromal cell-derived factor-1 effects on exvivo expanded endothelial progenitor cell recruitment for ischemic neovascularization. Circulation. **107** 1322-1328.

[83] Musaro A, Giacinti C, Borsellino G, Dobrowolny G, Pelosi L, Cairns L, Ottolenghi S, Cossu G, Bernardi G, Battistini L, Molinaro M, Rosenthal N 2004 Stem cell-mediated muscle regeneration is enhanced by local isoform of insulin-like growth factor 1. Proc Natl Acad Sci USA. **101** 1206-1210.

[84] Torella D, Rota M, Nurzynska D, Musso E, Monsen A, Shiraishi I, Zias E, Walsh K, Rosenzweig A, Sussman MA, Urbanek K, Nadal-Ginard B, Kajstura J, Anversa P, Leri A 2004 Cardiac stem cell and myocyte aging, heart failure, and insulin-like growth factor-1 overexpression. Circ Res. **94** 514-524.

[85] Winn N, Paul A, Musaro A, Rosenthal N 2002 Insulin-like growth factor isoforms in skeletal muscle aging, regeneration, and disease. Cold Spring Harbor Symp Quant Biol. **67** 507-518.

[86] Calvillo L, Latini R, Kajstura J, Leri A, Anversa P, Ghezzi P, Salio M, Cerami A, Brines M 2003 Recombinant human erythropoietin protects the myocardium from ischemia-reperfusion injury and promotes beneficial remodeling. Proc Natl Acad Sci USA. **100** 4802-4806.

[87] Heeschen C, Aicher A, Lehmann R, Fichtlscherer S, Vasa M, Urbich C, Mildner-Rihm C, Martin H, Zeiher AM, Dimmeler S 2003 Erythropoietin is a potent physiological stimulus for endothelial progenitor cell mobilization. Blood. **102** 1340-1346.

[88] Zou Y, Takano H, Mizukami M, Akazawa H, Qin Y, Toko H, Sakamoto M, Minamino T, Nagai T, Komuro I 2003 Leukemia inhibitory factor enhances survival of cardiomyocytes and induces regeneration of myocardium after myocardial infarction. Circulation.**108** 748-753.

[89] Takahashi E, Fukuda K, Miyoshi S, Murata M, Kato T, Ita M, Tanabe T, Ogawa S 2004 Leukemia Inhibitory Factor Activates Cardiac L-Type Ca^{2+} Channels via Phosphorylation of Serine 1829 in the Rabbit Ca_v 1.2 Subunit. Circ Res. **94** 1242-1248.

[90] Mohri T, Fujio Y, Maeda M, Ito T, Iwakura T, Oshima Y, Uozumi Y, Segawa M, Yamamoto H, Kishimoto T, Azum J 2006 Leukemia Inhibitory Factor Induces Endothelial Differentiation in Cardiac Stem Cells. J Biol Chem. **281** 6442-6447.

[91] Van-Wijk B, Moorman AFM, van den Hoff MJB 2007 Role of bone morphogenetic proteins in cardiac differentiation. Cardiovasc Res. **74** 244-255.

[92] Hwang NS, Varghese S, Elisseeff J 2008 Controlled differentiation of stem cells. Adv Drug Deliv Rev. **60** 199.

[93] Leor J, Tuvia S, Guetta V, Manczur F, Castel D, Willenz U, Petneházy O, Landa N, Feinberg MS, Konen E, Goitein O, Tsur-Gang O, Shaul M, Klapper L, Cohen S 2009 Intracoronary injection of in situ forming alginate hydrogel reverses left ventricular remodeling after myocardial infarction in swine. J Am Coll Cardiol. **54** 1014-1023.

[94] Johnston TD, Christman KL 2013 Injectable hydrogel therapies and their delivery strategies for treating myocardial infarction. Expert Opin. Drug Deliv. **10** 59-72.

[95] Passier R, van Laake LW, Mummery CL 2008 Stem-cell based therapy and lessons from the heart. Nature. **453** 322-329.

[96] Laugwitz KL, Moretti A, Caron L, Nakano A, Chien KR 2008 Islet1 cardiovascular progenitors: a single source for heart lineages. Development. **135** 193-205.

[97] Orlic D, Kajstura J, Chimenti S, Jakoniuk I, Anderson SM, Li B, Pickel J, McKay R, Nadal-Ginard B, Bodine DM, Leri A, Anversa P 2001 Bone marrow cells regenerate infarcted myocardium. Nature. **410** 701-705.

[98] Yang L, Soonpaa MH, Adler ED, Roepke TK, Kattman SJ, Kennedy M, Henckaerts E, Bonham K, Abbott GW, Linden RM, Field LJ, Keller GM 2008 Human cardiovascular progenitor cells develop from a KDR+ embryonic-stem-cell derived population. Nature. **453** 524-528.

[99] Ryu JH, Kim IK, Cho SW, Cho MC, Hwang KK, Piao H, Lim SH, Hong YS, Choi CY, Yoo KJ, Kim BS 2005 Implantation of bone marrow mononuclear cells using injectable fibrin matrix enhances neovascularization in infarcted myocardium. Biomaterials. **26** 319-326.

[100] Wu X, Rabkin-Aikawa E, Guleserian KJ, Perry TE, Masuda Y, Sutherland FW, Schoen FJ, Mayer JE Jr, Bischoff J 2004 Tissue-engineered microvessels on three-dimensional biodegradable scaffolds using human endothelial progenitor cells. Am J Physiol Heart Circ Physiol. **287** H480-H487.

[101] Kadner A, Zund G, Maurus C, Breymann C, Yakarisik S, Kadner G, Turina M, Hoerstrup SP 2004 Human umbilical cord cells for cardiovascular tissue engineering: A comparative study. Eur J Cardiothorac Surg. **25** 635-641.

[102] Kamelger FS, Marksteiner R, Margreiter E, Klima G, Wechselberger G, Hering S, Piza H 2004 A comparative study of three different biomaterials in the engineering of skeletal muscle using a rat animal model. Biomaterials. **25** 1649-1655.

[103] Levenberg S, Huang NF, Lavik E, Rogers AB, Itskovitz-Eldor J, Langer R 2003 Differentiation of human embryonic stem cells on three-dimensional polymer scaffolds. Proc Natl Acad Sci USA. **100** 12741-12746.

[104] Matsubayashi K, Fedak PW, Mickle DA, Weisel RD, Ozawa T, Li RK 2003 Improved left ventricular aneurysm repair with bioengineered vascular smooth muscle grafts. Circulation. **108** II219-II225.

[105] Li RK, Yau TM,Weisel RD, Mickle DA, Sakai T, Choi A, Jia ZQ 2000 Construction of a bioengineered cardiac graft. J Thorac Cardiovasc Surg. **119** 368-375.

[106] Leor J, Aboulafia-Etzion S, Dar A, Shapiro L, Barbash IM, Battler A, Granot Y, Cohen S 2000 Bioengineered cardiac grafts: A new approach to repair the infarcted myocardium?. Circulation. **102** III56-III61.

[107] Planat-Benard V, Menard C, Andre M, Puceat M, Perez A, Garcia-Verdugo JM, Pénicaud L, Casteilla L 2004 Spontaneous cardiomyocyte differentiation from adipose tissue stroma cells. Circ Res. **94** 223-229.

[108] Evans SM, Mummery C, Doevendans PA 2007 Progenitor cells for cardiac repair. Semin Cell Dev Biol. **18** 153-160.

[109] Smith RR, Barile L, Cho HC, Leppo MK, Hare JM, Messina E, Giacomello A, Abraham MR, Marban E 2007 Regenerative potential of cardiosphere-derived cells expanded from percutaneous endomyocardial biopsy specimens. Circulation. **115** 896-908.

[110] Narazaki G, Uosaki H, Teranishi M, Okita K, Kim B, Matsuoka S, Yamanaka S, Yamashita JK 2008 Directed and systematic differentiation of cardiovascular cells from mouse induced pluripotent stem cells. Circulation. **18** 498-506.

[111] Shiba Y, Fernandes S, Zhu WZ, Filice D, Muskheli V, Kim J, Palpant NJ, Gantz J, Moyes KW, Reinecke H, Biber BV, Dardas T, Mignone JL, Izawa A, Hanna R, Viswanathan M, Gold JD, Kotlikoff MI, Sarvazyan N, Kay MW, Murry CE, Laflamme MA 2012 Human ES-cell-derived cardiomyocytes electrically couple and suppress arrhythmias in injured hearts. Nature. **489** 322-325.

[112] Fernandes S, Naumova AV, Zhu WZ, Laflamme MA, Gold J, Murry CE 2010 Human embryonic stem cell-derived cardiomyocytes engraft but do not alter cardiac remodeling after chronic infarction in rats. J Mol Cell Cardiol. **49** 941-949.

[113] Chong JJH, Yang X, Don CW, Minami E, Liu YW, Weyers JJ, Mahoney WM, Biber BV, Cook SM, Palpant NJ, Gantz JA, Fugate JA, Muskheli V, Gough GM, Vogel KW, Astley CA, Hotchkiss CE, Baldessari A, Pabon L, Reinecke H, Gill EA, Nelson V, Kiem HP, Laflamme MA, Murry CE 2014 Human embryonic-stem-cell-derived cardiomyocytes regenerate non-human primate hearts. Nature. **510** 273-277.

[114] Laflamme MA, Chen KY, Naumova AV, Muskheli V, Fugate JA, Dupras SK, Reinecke H, Xu C, Hassanipour M, Police S, O'Sullivan C, Collins L, Chen Y, Minami E, Gill EA, Ueno S, Yuan C, Gold J, Murry CE 2007 Cardiomyocytes derived from human embryonic stem cells in pro-survival factors enhance function of infarcted rat hearts. Nat Biotechnol. **25** 1015-1024.

[115] Passier R, van Laake LW, Mummery CL 2008 Stem-cellbased therapy and lessons from the heart. Nature. **453** 322-329.

[116] Vailhe B, Vittet D, Feige JJ 2001. In vitro models of vasculogenesis and angiogenesis, Lab Invest. **81** 439-452.

[117] Santos MI, Reis RL 2010 Vascularization in bone tissue engineering: physiology, current strategies, major hurdles and future challenges, Macromol Biosci. **10** 12-27.

[118] Bramfeldt H, Sabra1 G, Centis V, Vermette P 2010 Scaffold Vascularization: A Challenge for Three-Dimensional Tissue Engineering. Curr Med Chem. **17** 3944-3967.

[119] Sieminski AL, Hebbel RP, Gooch KJ 2004 The relative magnitudes of endothelial force generation and matrix stiffness modulate capillary morphogenesis in vitro. Exp Cell Res. **297** 574-584.

[120] Lo Vasco VR, Pacini L, Di Raimo T, D'arcangelo D, Businaro R 2011 Expression of phosphoinositide-specific phospholipase C isoforms in human umbilical vein endothelial cells. J Clin Pathol. **64** 911-915.

[121] Leeper NJ, Hunter AL , Cooke JP 2010 Stem cell therapy for vascular regeneration: adult, embryonic, and induced pluripotent stem cells. Circulation. **22** 517-526.

[122] Volz KS, Miljan E, Khoo A, Cooke JP 2012 Development of pluripotent stem cells for vascular therapy. Vascular Pharmacol. **56** 288-296.

[123] Rufaihah AJ, Huang NF, Kim J, Herold J, Volz KS, Park TS, Lee JC, Zambidis ET, Reijo-Pera R, Cooke JP 2013 Human induced pluripotent stem cell-derived endothelial cells exhibit functional heterogeneity. Am J Transl Res. **5** 21-35.

[124] Rufaihah AJ, Huang NF, Jame S, Lee JC, Nguyen HN, Byers B, De A, Okogbaa J, Rollins M, Reijo-Pera R, Gambhir SS, Cooke JP 2011 Endothelial cells derived from human iPSCS increase capillary density and improve perfusion in a mouse model of peripheral arterial disease. Arterioscler Thromb Vasc Biol. **31** e72-e79.

[125] Cho SW, Moon SH, Lee SH, Kang SW, Kim J, Lim JM, Kim HS, Kim BS, Chung HM 2007 Improvement of postnatal neovascularization by human embryonic stem cell derived endothelial-like cell transplantation in a mouse model of hindlimb ischemia. Circulation. **116** 2409-2419.

[126] Huang NF, Niiyama H, Peter C, De A, Natkunam Y, Fleissner F, Li Z, Rollins MD, Wu JC, Gambhir SS, Cooke JP 2010 Embryonic stem cell-derived endothelial cells engraft into the ischemic hindlimb and restore perfusion. Arterioscler Thromb Vasc Biol. **30** 984-991.

[127] Li Z, Wilson KD, Smith B, Kraft DL, Jia F, Huang M, Xie X, Robbins RC, Gambhir SS, Weissman IL, Wu JC 2009 Functional and transcriptional characterization of human embryonic stem cell-derived endothelial cells for treatment of myocardial infarction. PloS one **4** e8443.

[128] Adams WJ, Zhang Y, Cloutier J, Kuchimanchi P, Newton G, Sehrawat S, Aird WC, Mayadas TN, Luscinskas FW, Garcia-Cardena G 2013 Functional Vascular Endothelium Derived from Human Induced Pluripotent Stem Cells. Stem Cell Reports. **1** 105-113.

[129] Hou L, Huang N 2014 Extracellular matrix-mediated endothelial differentiation of human induced pluripotent stem cells. FASEB J. **28** 1152-1154.

[130] Kalka C, Masuda H, Takahashi T, Kalka-Moll WM, Silver M, Kearney M, Li T, Isner JM, Asahara T 2000 Transplantation of ex vivo expanded endothelial progenitor cells for therapeutic neovascularisation. Proc Natl Acad Sci USA. **97** 3422-3427.

[131] Yamahara K, Itoh H 2009 Potential use of endothelial progenitor cells for regeneration of the vasculature. Ther Adv Cardiovasc Dis. **3** 17-27.

[132] Chen QZ. Harding SE, Ali NN, Lyon AR, Boccaccini AR 2008 Biomaterials in cardiac tissue engineering: ten years of research survey. Mater Sci Eng. **59** 1-37.

[133] Chen QZ. Harding SE, Ali NN, Lyon AR, Boccaccini AR. Myocardial tissue engineering. In: Boccaccini AR, Gough J, editors. Tissue Engineering Using Ceramics and Polymers. Woodhead Publishing Limited; 2008.

[134] Luo ZP, Sun YL, Fujii T, An KN 2004 Single molecule mechanical properties of type II. Biorheology. **41** 247-254.

[135] Storm C, Pastore JJ, MacKintosh FC, Lubensky TC, Janmey PA 2005 Nonlinear elasticity in biological gels. Nature. **435** 191-194.

[136] Martens TP, Godier AFG, Parks JJ, Wan LQ, Koeckert MS, Eng GM, Hudson BI, Sherman W, Vunjak-Novakovic G 2009 Percutaneous cell delivery into the heart using hydrogels polymerizing in situ. Cell Transplant. **18** 297-204.

[137] Holdings I Inc. IK-5001 for the prevention of remodeling of the ventricle and congestive heart failure after acute myocardial infarction. In: Clinical Trial Detail. 2010. http://clinicaltrials.gov/show/NCT01226563.

[138] Carmeliet P, Jain RK 2000 Angiogenesis in cancer and other diseases. Nature. **407** 249-257.

[139] Rakusan K, Flanagan MF, Geva T, Southern J, Van-Praagh R 1992 Morphometry of human coronary capillaries during normal growth and the effect of age in left ventricular pressure-overload hypertrophy. Circulation. **86** 38-46.

[140] Tongers J, Losordo DW, Landmesser U 2011 Stem and progenitor cell-based therapy in ischaemic heart disease: promise, uncertainties, and challenges. Eu Heart J. **32** 1197-1206.

[141] Carmeliet P, Jain RK 2011 Molecular mechanisms and clinical applications of angiogenesis. Nature. **473** 298-307.

[142] Richardson TP, Murphy WL, Mooney DJ 2001 Polymeric delivery of proteins and plasmid DNA for tissue engineering and gene therapy. Crit Rev Eukaryot Gene Expr. **11** 47-58.

[143] Laschke MW, Rücker M, Jensen G, Carvalho C, Mülhaupt R, Gellrich NC, Menger MD 2008 Incorporation of growth factor containing Matrigel promotes vascularization of porous PLGA scaffolds. J Biomed Mater Res A. **85** 397-407.

[144] Laschke MW, Vollmar B, Menger MD 2009 Inosculation: connecting the life-sustaining pipelines. Tissue Eng Part B Rev. **15** 455-465.

[145] Defilippi P, Olivo C, Venturino M, Dolce L, Silengo L, Tarone G 1999 Actin cytoskeleton organization in response to integrin-mediated adhesion. Microscopy Res Tech. **47** 67-78.

[146] Tremblay PL, Hudon V, Berthod F, Germain L, Auger FA 2005 Inosculation of tissue-engineered capillaries with the host's vasculature in a reconstructed skin transplanted on mice. Am J Transplant. **5** 1002-1010.

[147] Folkman J, Haudenschild C 1980 Angiogenesis in vitro. Nature. **288** 551-556.

[148] Sottile J 2004 Regulation of angiogenesis by extracellular matrix. Biochim Biophys Acta. **1654** 13-22.

[149] Black AF, Berthod F, L'Heureux N, Germain L, Auger FA 1998 In vitro reconstruction of a human capillary-like network in a tissue-engineered skin equivalent. FASEB J. **12** 1331-1340.

[150] Unger RE, Peters K, Wolf M, Motta A, Migliaresi C, Kirkpatrick CJ 2004 Endothelialization of a non-woven silk fibroin net for use in tissue engineering: growth and gene regulation of human endothelial cells. Biomaterials. **25** 5137-5146.

[151] Wu X, Rabkin-Aikawa E, Guleserian KJ, Perry TE, Masuda Y, Sutherland FW, Schoen FJ, Mayer JE, Bischoff J 2004 Tissue-engineered microvessels on three-dimensional biodegradable scaffolds using human endothelial progenitor cells. Am J Physiol Heart Circ Physiol. **287** H480-H487.

[152] Yamamoto K, Takahashi T, Asahara T, Ohura N, Sokabe T, Kamiya A, Ando J 2003 Proliferation, differentiation, and tube formation by endothelial progenitor cells in response to shear stress. J Appl Physiol. **95** 2081-2088.

[153] Eppler SM, Combs DL, Henry TD, Lopez JJ, Ellis SG, Yi JH, Annex BH, Mccluskey ER, Zioncheck TF 2002 A target-mediated model to describe the pharmacokinetics and hemodynamic effects of recombinant human vascular endothelial growth factor in humans. Clin Pharmacol Ther. **72** 20-32.

[154] Zisch AH, Lutolf MP, Hubbell JA 2003 Biopolymeric delivery matrices for angiogenic growth factors. Cardiovasc Pathol. **12** 295-310.

[155] Zisch AH, Lutolf MP, Ehrbar M, Raeber GP, Rizzi SC, Davies N, Schmokel H, Bezuidenhout D, Djonov V, Zilla P, Hubbell JA 2003 Cell-demanded release of VEGF from synthetic, biointeractive cell ingrowth matrices for vascularized tissue growth. FASEB J. **17** 2260-2262.

[156] Bauer SM, Bauer RJ, Liu ZJ, Chen H, Goldstein L, Velazquez OC 2005 Vascular endothelial growth factor-C promotes vasculogenesis, angiogenesis, and collagen constriction in three-dimensional collagen gels. J Vasc Surg. **41** 699-707.

[157] Huang YC, Kaigler D, Rice KG, Krebsbach PH, Mooney DJ 2005 Combined angiogenic and osteogenic factor delivery enhances bone marrow stromal cell-driven bone regeneration. J Bone Miner Res. **20** 848-857.

[158] Marra KG, Defail AJ, Clavijo-Alvarez JA, Badylak SF, Taieb A, Schipper, B, Bennett J, Rubin JP 2008 FGF-2 enhances vascularization for adipose tissue engineering. Plast Reconstr Surg. **121** 1153-1164.

[159] Zhao W, Han Q, Lin H, Gao Y, Sun W, Zhao Y, Wang B, Chen B, Xiao Z, Dai J 2008 Improved neovascularisation and wound repair by targeting human basic fibroblast growth factor (bFGF) to fibrin. J Mol Med. **86** 1127-1138.

[160] Andrae J, Gallini R, Betsholtz C 2008 Role of platelet derived growth factors in physiology and medicine. Genes Dev. **22** 1276-1312.

[161] Perets, A., Baruch Y, Weisbuch F, Shoshany G, Neufeld G, Cohen S 2003 Enhancing the vascularization of three dimensional porous alginate scaffolds by incorporating controlled release basic fibroblast growth factor microspheres. J Biomed Mater Res A. **65** 489.

[162] Chu H. Wang Y 2012 Therapeutic angiogenesis: controlled delivery of angiogenic factors. Ther Deliv. **3** 693-714.

[163] Said SS, Pickering JG, Mequanint K 2013 Advances in growth factor delivery for therapeutic angiogenesis. J Vasc Res. **50** 35-51.

[164] Hutton DL, Grayson WL 2014 Stem cell-based approaches to engineering vascularised bone. Curr Opin Chem Biol. **3** 75-82.

[165] Silvestre JS 2012 Pro-angiogenic cell-based therapy for the treatment of ischemic cardiovascular diseases. Thromb Res. **130** S90-S94.

[166] Leeper NJ, Hunter AL, Cooke JP 2010 Stem cell therapy for vascular regeneration: Adult, Embryonic, and Induced Pluripotent Stem Cells. Circulation. **122** 517-526.

[167] Singelyn JM, DeQuach JA, Seif-Naraghi SB, Littlefield RB, Schup-Magoffin PJ, Christman KL 2009 Naturally derived myocardial matrix as an injectable scaffold for cardiac tissue engineering. Biomaterials. **30** 5409-5416.

[168] Manning MC, Patel K, Borchardt RT 2010 Stability of protein pharmaceuticals: an update. Pharm Res. **27** 544-5475.

[169] Choi SW, Zhang Y, Macewan MR, Xia Y 2013 Neovascularization in biodegradable inverse opal scaffolds with uniform and precisely controlled pore sizes. Adv Healthc Mater. **2** 145-154.

[170] Mehdizadeh H, Sumo S, Bayrak ES, Brey EM, Cinar A 2004 Three-dimensional modeling of angiogenesis in porous biomaterial scaffolds. Biomaterials. 2013;4:2875-87.

[171]Kotov NA, Liu Y, Wang S, Cumming C, Eghtedari M, Vargas G, Motamedi M, Nichols J, Cortiella J. Inverted colloidal crystals as three-dimensional cell scaffolds. Langmuir. **20** 7887-7892.

[172] Murphy WL, Dennis RG, Kileny JL 2002 Mooney DJ. Salt fusion: an approach to improve pore interconnectivity within tissue engineering scaffolds. Tissue Eng. **8** 43-52.

[173] Culver JC, Hoffmann JC, Poche RA, Slater JH, West JL, Dickinson ME 2012 Three dimensional biomimetic patterning in hydrogels to guide cellular organization. Adv Mater. **24** 2344-2348.

[174] Mao M, He J, Liu Y, Li X, Li D 2012 Icetemplate-induced silk fibroin-chitosan scaffolds with predefined microfluidic channels and fully porous structures. Acta Biomater. **8** 2175-2184.

[175] Kennedy JP, McCandless SP, Rauf A, Williams LM, Hillam J, Hitchcock RW 2011 Engineered channels enhance cellular density in perfused scaffolds. Acta Biomater. **7** 3896-3804.

[176] Huang H, Oizumi S, Kojima N, Niino T, Sakai Y 2007 Avidin-biotin binding-based cell seeding and perfusion culture of liverderived cells in a porous scaffold with a three-dimensional interconnected flow channel network. Biomaterials. **28** 3815-3823.

[177] Park JH, Chung BG, Lee WG, Kim J, Brigham MD, Shim J, Lee S, Hwang CM, Durmus NG, Demirci U, Khademhosseini A 2010 Microporous cell-laden hydrogels for engineered tissue constructs. Biotechnol Bioeng. **106** 138-148.

[178] Rücker M, Laschke MW, Junker D, Carvalho C, Schramm A, Mulhaupt R, Gellrich NC, Menger MD 2006 Angiogenic and inflammatory response to biodegradable scaffolds in dorsal skinfold chambers of mice. Biomaterials. **27** 5027-5038.

[179] Tavassol F, Schumann P, Lindhorst D, Sinikovic B, Voss A, von See C, Kampmann A, Bormann KH, Carvalho C, Mülhaupt R, Harder Y, Laschke MW, Menger MD, Gellrich NC, Rücker M 2010 Accelerated angiogenic host tissue response to poly(L-lactide-co-glycolide) scaffolds by vitalization with osteoblast-like cells. Tissue Eng Part A. **16** 2265-2279.

[180] Rücker M, Laschke MW, Junker D, Carvalho C, Tavassol F, Mülhaupt R, Gellrich NC, Menger MD 2008 Vascularization and biocompatibility of scaffolds consisting of different calcium phosphate compounds. J Biomed Mater Res A. **86** 1002-1011.

[181] Aicher A, Zeiher AM, Dimmeler S 2005 Mobilizing endothelial progenitor cells. Hypertension. **45** 321-325.

[182] Henry TD, Rocha-Singh K, Isner JM, Kereiakes DJ, Giordano FJ, Simons M, Losordo DW, Hendel RC, Bonow RO, Eppler SM, Zioncheck TF, Holmgren EB, McCluskey ER 2001 Intracoronary administration of recombinant human vascular endothelial growth factor to patients with coronary artery disease. Am Heart J. **142** 872-880.

[183] Lazarous DF, Unger EF, Epstein SE, Stine A, Arevalo JL, Chew EY, Quyyumi AA 2000 Basic fibroblast growth factor in patients with intermittent claudication: results of a phase I trial. J Am Coll Cardiol. **36** 1239-1244.

[184] Chiu LL, Radisic M, Vunjak-Novakovic G 2010 Bioactive scaffolds for engineering vascularized cardiac tissues. Macromol Biosci. **10** 1286-1301.

[185] Chiu LL, Radisic M 2010 Scaffolds with covalently immobilized VEGF and Angiopoietin-1 for vascularization of engineered tissues. Biomaterials. **31** 226-241.

[186] Chiu LL, Weisel RD, Li RK, Radisic M 2011 Defining conditions for covalent immobilization of angiogenic growth factors onto scaffolds for tissue engineering. J Tissue Eng Regen Med. **5** 69-84.

[187] Chiu LL, Radisic M, Vunjak-Novakovic G 2010 Bioactive scaffolds for engineering vascularized cardiac tissues. Macromol Biosci. **10** 1286-1301.

[188] Gerhardt H, Golding M, Fruttiger M, Ruhrberg C, Lundkvist A, Abramsson A, Jeltsch M, Mitchell C, Alitalo K, Shima D, Betsholtz C 2003 VEGF guides angiogenic sprouting utilizing endothelial tip cell filopodia. J Cell Biol. **161** 1163-1177.

[189] Izadifar M, Haddadi A, Chen XB 2014 Rate-programming of nano-particulate delivery systems for smart bioactive scaffolds in tissue engineering. Nanotechnology. **26** 12001.

[190] Scott RC, Rosano JM, Ivanov Z, Wang B, Chong PL, Issekutz AC, Crabbe DL, Kiani MF 2009 Targeting VEGF-encapsulated immunoliposomes to MI heart improves vascularity and cardiac function. FASEB J **23** 3361-3367.

[191] Oh KS, Song JY, Yoon SJ, Park Y, Kim D, Yuk SH 2010 Temperature-induced gel formation of core/shell nanoparticles for the regeneration of ischemic heart. J Control Release. **146** 207-211.

[192] Formiga FR, Pelacho B, Garbayo E, Abizanda G, Gavira JJ, Simon-Yarza T, Mazo M, Tamayo E, Jauquicoa C, Ortiz-de-Solorzano C, Pro´sper F, Blanco-Prieto MJ 2010 Sustained release of VEGF through PLGA microparticles improves vasculogenesis and tissue remodeling in an acute myocardial ischemia-reperfusion model. J Control Release. **147** 30-37.

[193] Amsden BG, Timbart L, Marecak D, Chapanian R, Tse MY, Pang SC 2010 VEGF-induced angiogenesis following localized delivery via injectable, low viscosity poly(trimethylene carbonate). J Control Release. **145** 109-115.

[194] Tang DW, Yu SH, Ho YC, Mi FL, Kuo PL, Sung HW 2010 Heparinized chitosan/poly(gamma-glutamic acid) nanoparticles for multi-functional delivery of fibroblast growth factor and heparin. Biomaterials. **31** 9320-9332.

[195] Sun Q, Silva EA, Wang A, Fritton JC, Mooney DJ, Schaffler MB, Grossman PM, Rajagopalan S 2010 Sustained release of multiple growth factors from injectable polymeric system as a novel therapeutic approach towards angiogenesis. Pharm Res. **27** 264-271.

[196] Chung YI, Kim SK, Lee YK, Park SJ, Cho KO, Yuk SH, Tae G, Kim YH 2010 Efficient revascularization by VEGF administration via heparin-functionalized nanoparticle-fibrin complex. J Control Release. **143** 282-289.

[197] Xie J, Wang H, Wang Y, Ren F, Yi W, Zhao K, Li Z, Zhao Q, Liu Z, Wu H, Gu C, Yi D 2013 Induction of angiogenesis by controlled delivery of vascular endothelial growth factor using nanoparticles. Cardiovasc Ther. **31** e12-e18.

[198] Formiga FR, Pelacho B, Garbayo E, Imbuluzqueta I, Díaz-Herráez P, Abizanda G, Gavira JJ, Simón-Yarza T, Albiasub E, Tamayoa E, Prósper F, Blanco-Prieto MJ 2014 Controlled delivery of fibroblast growth factor-1 and neuregulin-1 from biodegradablemicroparticles promotes cardiac repair in a rat myocardial infarction model through activation of endogenous regeneration. J Control Release. **73** 132-139.

[199] Golub JS, Kim YT, Duvall CL, Bellamkonda RV, Gupta D, Lin AS, Weiss D, Robert Taylor W, Guldberg RE 2010 Sustained VEGF delivery via PLGA nanoparticles promotes vascular growth. Am J Physiol Heart Circ Physiol. **298** H1959-H1965.

[200] Nagai N, Kumasaka N, Kawashima T, Kaji H, Nishizawa M, Abe T 2010 Preparation and characterization of collagen microspheres for sustained release of VEGF. J Mater Sci Mater Med. **21** 1891-198.

[201] Hao X, Silva EA, Mansson-Broberg A, Grinnemo KH, Siddiqui AJ, Dellgren G, Wa¨rdell E, Brodin LA, Mooney DJ, Sylve´n C 2007 Angiogenic effects of sequential release of VEGF-

A165 and PDGF-BB with alginate hydrogels after myocardial infarction. Cardiovasc Res. **75** 178-185.

[202] Guo HD, Cui GH, Yang JJ, Wang C, Zhu J, Zhang LS, Jiang J, Shao SJ 2012 Sustained delivery of VEGF from designer self-assembling peptides improves cardiac function after myocardial infarction. Biochem Biophys Res Commun. **424** 105-111.

[203] Shin SH, Lee J, Lim KS, Rhim T, Lee SK, Kim YH, Lee KY 2013 Sequential delivery of TAT-HSP27 and VEGF using microsphere/hydrogel hybrid systems for therapeutic angiogenesis. J Controll Release. **166** 38-45.

[204] Gao J, Liu J, Gao Y, Wang C, Zhao Y, Chen B, Xiao Z, Miao Q, Dai J 2011 A myocardial patch made of collagen membranes loaded with collagen-binding human vascular endothelial growth factor accelerates healing of the injured rabbit heart. Tissue Eng Part A. **17** 2739-2747.

[205] Miyagi Y, Chiu LL, Cimini M,Weisel RD, Radisic M, Li RK 2011 Biodegradable collagen patch with covalently immobilized VEGF for myocardial repair. Biomaterials. **32** 1280-1290.

[206] Ruvinov E, Leor J, Cohen S 2011 The promotion of myocardial repair by the sequential delivery of IGF-1 and HGF from an injectable alginate biomaterial in a model of acute myocardial infarction. Biomaterials. **32** 565-578.

[207] Chiu LL, Reis LA, Momen A, Radisic M 2012 Controlled release of thymosin beta4 from injected collagen-chitosan hydrogels promotes angiogenesis and prevents tissue loss after myocardial infarction. Regen Med. **7** 523-533.

[208] Reis LA, Chiu LL, Liang Y, Hyunh K, Momen A, Radisic M 2012 A peptide-modified chitosan-collagen hydrogel for cardiac cell culture and delivery. Acta Biomater.**8** 1022-1036.

[209] Moon JJ, Hahn MS, Kim I, Nsiah BA, West JL 2009 Micropatterning of poly(ethylene glycol) diacrylate hydrogels with biomolecules to regulate and guide endothelial morphogenesis. Tissue Eng Part A. **15** 579.

[210] Co CC, Wang YC, Ho CC 2005 Biocompatible micropatterning of two different cell types. J Am Chem Soc.**127** 1598-1599.

[211] Hahn MS, Miller JS, West JL 2005 Laser scanning lithography for surface micropatterning on hydrogels. Adv Mater. **17** 2939-2942.

[212] Hahn MS, Taite LJ, Moon JJ, Rowland MC, Ruffino KA, West JL 2006 Photolithographic patterning of polyethylene glycol hydrogels. Biomaterials. **27** 2519-2524.

[213] Hahn MS, Miller JS, West JL 2006 Three-dimensional biochemical and biomechanical patterning of hydrogels for guiding cell behavior. Adv Mater. **18** 2679-2684.

[214] Lee SH, Moon JJ, West JL 2008 Three-dimensional micropatterning of bioactive hydrogels via two-photon laser scanning photolithography for guided 3D cell migration. Biomaterials. **29** 2962-2968.

[215] Leslie-Barbick JE, Shen C, Chen C, West JL 2010 Micron-Scale Spatially Patterned, Covalently Immobilized Vascular Endothelial Growth Factor on Hydrogels Accelerates Endothelial Tubulogenesis and Increases Cellular Angiogenic Responses. Tissue Eng Part A. **17** 221-229.

[216] Orr AW, Elzie CA, Kucik DF, Murphy-Ullrich JE 2003 Thrombospondin signaling through the alreticulin LDL receptor-related protein co-complex stimulates random and directed cell migration. J Cell Sci.**116** 2917.

[217] Koike N, Fukumura D, Gralla O, Au P, Schechner JS, Jain RK 2004 Tissue engineering: creation of long-lasting blood vessels. Nature. **428** 138-139.

[218] Levenberg S, Rouwkema J, Macdonald M, Garfein ES, Kohane DS, Darland DC, Marini R, van Blitterswijk CA, Mulligan RC, D'Amore PA, Langer R 2005 Engineering vascularized skeletal muscle tissue. Nat Biotechnol. **23** 879-884.

[219] Shepherd BR, Hoying JB, Williams SK 2007 Microvascular transplantation after acute myocardial infarction. Tissue Eng. **13** 2871-2879.

[220] Wang ZZ, Au P, Chen T, Shao Y, Daheron LM, Bai H, Arzigian M, Fukumura D, Jain RK, Scadden DT 2007 Endothelial cells derived from human embryonic stem cells form durable blood vessels in vivo. Nat Biotechnol. **25** 317-318.

[221] ZimmermannWH, Schneiderbanger K, Schubert P, Didie M, Munzel F, Heubach JF, Kostin S, Neuhuber WL, Eschenhagen T 2002 Tissue engineering of a differentiated cardiac muscle construct. Circ Res. **90** 223-230.

[222] Chen X, Aledia AS,Ghajar CM, Griffith CK, Putnam AJ, Hughes CC, George SC 2009 Revascularization of a fibrin-based tissue construct accelerates the formation of functional anastomosis with host vasculature. Tissue Eng Part A. **15** 1363-1371.

[223] Berthod F, Symes J, Tremblay N, Medin JA, Auger FA 2012 Spontaneous fibroblast-derived pericyte recruitment in a human tissue-engineered angiogenesis model in vitro. J Cell Physiol. **227** 2130-2137.

[224] Stevens KR, Kreutziger KL, Dupras SK, Korte FS, Regnier M, Muskhelib V, Nourseb M B, Bendixenb K, Reineckeb H, Murrya CE 2009 Physiological function and transplantation of scaffold-free and vascularized human cardiac muscle tissue. Proc Natl Acad Sci USA. **106** 16568-16573.

[225] Dvir T, Kedem A, Ruvinov E, Levy O, Freeman I, Landad N, Holbovad R, Feinbergd MS, Drore S, Etzione Y, Leord J, Cohena S 2009 Prevascularization of cardiac patch on the omentum improves its therapeutic outcome. Proc Natl Acad Sci USA. **106** 14990-14995.

[226] Shimizu T, Sekine H, Yang J, Isoi Y, Yamato M, Kikuchi A, Kobayashi E, Okano T 2006 Polysurgery of cell sheet grafts overcomes diffusion limits to produce thick, vascularized myocardial tissues. FASEB J. **20** 708-710.

[227] Laschke MW, Mussawy H, Schuler S, Kazakov A, Rucker M, Eglin D, Alini M, Menger MD 2011 Short-term cultivation of in situ prevascularized tissue constructs accelerates inosculation of their preformed microvascular networks after implantation into the host tissue. Tissue Eng Part A. **17** 841-852.

[228] Tee R, Lokmic Z, Morrison WA, Dilley RJ 2010 Strategies in cardiac tissue engineering. ANZ J Surg. **80** 683-693.

[229] Lokmic Z, Stillaert F, Morrison WA, Thompson EW, Mitchell GM 2007 An arteriovenous loop in a protected space generates a permanent, highly vascular, tissue-engineered construct. FASEB J. **21** 511-522.

[230] Morritt AN, Bortolotto SK, Dilley RJ, Han X, Kompa AR, McCombe D. Cardiac tissue engineering in an in vivo vascularized chamber. Circulation. 2007;115:353-60.

[231] Lim SY, Hernández D, Dusting GJ 2013 Growing Vascularized Heart Tissue From Stem Cells. J Cardiovasc Pharmacol. **62** 122-129.

[232] McGuigan AP, Sefton MV 2006 Vascularized organoid engineered by modular assembly enables blood perfusion. Proc Natl Acad Sci. **103** 1461-1466.

[233] McGuigan AP, Sefton MV 2008 The thrombogenicity of human umbilical vein endothelial cell seeded collagen modules. Biomaterials. **29** 2453-2463.

[234] She M, McGuigan AP, Sefton MV 2007 Tissue factor and thrombomodulin expression on endothelial cell-seeded collagen modules for tissue engineering. J Biomed Material Res Part A. **80** 497-504.

[235] Leung B, Sefton M 2007 A modular tissue engineering construct containing smooth muscle cells and endothelial cells. Ann Biomed Eng. **35** 2039-2049.

[236] Kunz-Schughart LA, Schroeder JA, WondrakM, van Rey F, Lehle K, Hofstaedter F, Wheatley DN 2006 Potential of fibroblasts to regulate the formation of three-dimensional vessel-like structures from endothelial cells in vitro. Am.J. Physiol. Cell Physiol. **290** C1385-C1398.

[237] Kelm JM, Lorber V, Snedeker JG, Schmidt D, Broggini-Tenzer A, Weisstanner M, Odermatt B, Mol A, Zünd G, Hoerstrup SP 2010 A novel concept for scaffold-free vessel tissue engineering: self-assembly of micro tissue building blocks. J Biotechnol. **148** 46-55.

[238] Laschke MW, Kleer S, Scheuer C, Schuler S, Garcia P, Eglin D, Alini M, Menger MD 2012 Vascularization of porous scaffolds is improved by incorporation of adipose tissue-derived microvasculature fragments. Eur Cell Mater. **24** 266-277.

[239] Wu W, DeConinck A, Lewis JA 2011 Omnidirectional printing of 3D microvascular networks. Adv Mater. **23** H178-H183.

[240] Norotte C, Marga FS, Niklason LE, Forgacs G 2009 Scaffold-free vascular tissue engineering using bioprinting. Biomaterials. **30** 5910-5917.

[241] Raghavan S, Nelson CM, Baranski JD, Lim E, Chen CS 2010 Geometrically controlled endothelial tubulogenesis in micropatterned gels. Tissue Eng Part A. **16** 2255-2263.

[242] Baranski JD, Chaturvedi RR, Stevens KR, Eyckmans J, Carvalho B, Solorzano RD, Yang MT, Miller JS, Bhatia SN, Chen CS 2013 Geometric control of vascular networks to enhance engineered tissue integration and function. Proc Natl Acad Sci USA. **110** 7586-7591.

[243] Chiu LL, Montgomery M, Liang Y, Liu H, Radisic M. Perfusable branching microvessel bed for vascularization of engineered tissues. Proc Nat Acad Sci USA. 2012 **109** E3414-E3423.

[244] Sadr N, Zhu M, Osaki T, Kakegawa T, Yang Y, Moretti M, Fukuda J, Khademhosseini A 2011 SAM-based cell transfer to photopatterned hydrogels for microengineering vascular- like structures. Biomaterials. **32** 7479-7490.

[245] Chrobak KM, Potter DR, Tien J 2006 Formation of perfused, functional microvascular tubes in vitro. Microvasc Res. **71** 185-196.

[246] Bettinger CJJ,Weinberg EJJ, Kulig KM, Vacanti JP, Wang Y, Borenstein JT, Langer R 2006 Three-dimensional microfluidic tissue-engineering scaffolds using a flexible biodegradable polymer. Adv Mater. **18** 165-169.

[247] Chung JCY, Shum-Tim D 2012 Neovascularization in tissue engineering. Cells. **1** 1246-1260.

[248] Ozawa CR, Banfi A, Glazer, NL, Thurston G, Springer ML, Kraft PE, McDonald DM, Blau HM 2004 Microenvironmental VEGF concentration, not total dose, determines a threshold between normal and aberrant angiogenesis. J Clin Invest. **113** 516-527.

[249] Richardson TP, Peters MC, Ennett AB, Mooney DJ 2001 Polymeric system for dual growth factor delivery. Nat Biotechnol. **19** 1029-1034.

[250] Freeman I, Cohen S 2009 The influence of the sequential delivery of angiogenic factors from affinity-binding alginate scaffolds on vascularization. Biomaterials. **30** 2122-2131.

[251] Kocher AA, Schuster MD, Szabolcs MJ, Takuma S, Burk-hoff D, Wang J, Homma S, Edwards NM, Itescu S 2001 Neovascularization of ischemic myocardium by human bone-marrow-derived angioblasts prevents cardiomyocyte apoptosis, reduces remodeling and improves cardiac function. Nat Med. **7** 430-436.

[252] Leri A, Kajstura J, Anversa P 2011 Role of cardiac stem cells in cardiac pathophysiology: a paradigm shift in human myocardial biology. Circ Res. **109** 941-961.

[253 Beltrami AP, Barlucchi L, Torella D, Baker M, Limana F, Chimenti S, Kasahara H, Rota M, Musso E, Urbanek K, Leri A, Kajstura J, Nadal-Ginard B, Anversa P 2003 Adult cardiac stem cells are multipotent and support myocardial regeneration. Cell. **114** 763-776.

[254] Geiger F, Lorenz H, Xu W, Szalay K, Kasten P, Claes L, Augat P, Richter W. 2007 VEGF producing bone marrow stromal cells (BMSC) enhance vascularization and resorption of a natural coral bone substitute. Bone. **41** 516-522.

[255] Hur J, Yoon CH, Kim HS, Choi JH, Kang HJ, Hwang KK, Oh BH, Lee MM, Park YB 2004 Characterization of two types of endothelial progenitor cells and their different contributions to neovasculogenesis. Arterioscler Thromb Vasc Biol. **24** 288-293.

[256] Campbell PG, Weiss LE 2007 Tissue engineering with the aid of inkjet printers. Expert Opin Biol Ther. **7** 1123-1127.

[257] Montano I, Schiestl C, Schneider J, Pontiggia L, Luginbuhl J, Biedermann T, Böttcher-Haberzeth S, Braziulis E, Meuli M, Reichmann E 2010 Formation of human capillaries in vitro: the engineering of prevascularized matrices. Tissue Eng Part A. **16** 269-282.

[258] Stevens KR, Pabon L, Muskheli V, Murry CE 2009 Scaffold-free human cardiac tissue patch created from embryonic stem cells. Tissue Eng Part A. **15** 1211-1222.

[259] Chamberlain MD, Gupta R, SeftonMV 2011 Chimeric vessel tissue engineering driven by endothelialized modules in immunosuppressed Sprague-Dawley rats. Tissue Eng Part A. **17** 151-160.

[260] Gupta R, Sefton MV 2011 Application of an endothelialized modular construct for islet transplantation in syngeneic and allogeneic immunosuppressed rat models. Tissue Engineering Part A. **17** 2005-2015.

[261] Marga F, Jakab K, Khatiwala C, Shephard B, Dorfman S, Hubbard B, Colbert S, Gabor F 2012 Toward engineering functional organ modules by additive manufacturing. Biofabrication. **4** 22001.

[262] Mironov V, Kasyanov V, Markwald RR 2011 Organ printing: from bioprinter to organ biofabrication line. Curr Opin Biotechnol. **22** 667-673.

[263] Auger FA, Gibot L, Lacroix D 2013 The pivotal role of vascularization in tissue engineering. Annu Rev Biomed Eng. **15** 177-200.

[264] Cui X, Boland T 2009 Human microvasculature fabrication using thermal inkjet printing technology. Biomaterials. **30** 6221-6227.

[265] Laschke MW, Rucker M, Jensen G, Carvalho C, Mulhaupt R, Gellrich NC, Menger MD 2008 Improvement of vascularization of PLGA scaffolds by inosculation of in situ-preformed functional blood vessels with the host microvasculature. Ann Surg. **248** 939-948.

[266] Tremblay PL, Hudon V, Berthod F, Germain L, Auger FA **2005** Inosculation of tissue-engineered capillaries with the host's vasculature in a reconstructed skin transplanted on mice. Am J Transplant. **5** 1002-1010.

CHAPTER 2

RATE-PROGRAMMING OF NANO-PARTICULATE DELIVERY SYSTEMS FOR BIOACTIVE SCAFFOLDS IN CARDIAC TISSUE ENGINEERING

“This chapter has been published as “M. Izadifar, A. Haddadi, X. B. Chen and M. Kelly, 2015, Rate-Programming of Nano-Particulate Delivery Systems for Smart Bioactive Scaffolds in Tissue Engineering, *Nanotechnology*, 26(1), 012001” According to the Copyright Agreement, "the authors retain the right to include the journal article, in full or in part, in a thesis or dissertation".

2.1 Abstract

Development of smart bioactive scaffolds is of importance in tissue engineering, where cell proliferation, differentiation and migration within scaffolds can be regulated by the interactions between cells and scaffold through the use of growth factors (GFs) and extra cellular matrix peptides. One challenge in this area is to spatiotemporally control the dose, sequence and profile of release of GFs so as to regulate cellular fates during tissue regeneration. This challenge would be addressed by rate-programming of nano-particulate delivery systems, where the release of GFs via polymeric nanoparticles is controlled by means of the methods of, such as externallycontrolled and physicochemically/architecturally-modulated so as to mimic the profile of physiological GFs. Identifying and understanding such factors as the desired release profiles, mechanisms of release, physicochemical characteristics of polymeric nanoparticles, and externally-triggering stimuli are essential for designing and optimizing such delivery systems.

This review surveys the recent studies on the desired release profiles of GFs in various tissue engineering applications, elucidates the major release mechanisms and critical factors affecting release profiles, and overviews the role played by the mathematical models for optimizing nanoparticulate delivery systems. Potentials of stimuli responsive nanoparticles for spatiotemporal control of GF release are also presented, along with the recent advances in strategies for spatiotemporal control of GF delivery within tissue engineered scaffolds. The recommendation for the future studies to overcome challenges for developing sophisticated particulate delivery systems in tissue engineering is discussed prior to the presentation of conclusions drawn from this paper.

2.2 Introduction

One goal of tissue engineering is to maintain, replace, restore or enhance the functionality of a damaged/degenerated tissue/organ by controlling its biological environment [1, 2]. Generally, tissue engineering strategies include (i) injection of functional cells into a non-functional tissue, (ii) implantation of three dimensional (3D) tissue structures, which are formed in bioreactors, to the damaged/degenerated tissue/organ; and (iii) scaffold-based cell delivery to defected tissues for an *in-situ* tissue regeneration. Furthermore, stem cells with tremendous potentials of differentiations are opening new avenues for tissue engineering applications [3].

For all tissue engineering strategies, cellular differentiation, proliferation, and migration are all critical processes and must be well regulated. Such controls and regulations are performed by growth factors (GFs), which have pivotal roles in instructing specific cellular responses during the tissue regeneration process [4]. The specific cellular response trigged by GFs can result in a wide range of cell functions, depending on the dose, type, release rate and timing of GF presented. The role of GF release profile becomes more critical when multiple GFs are used for

regenerative therapy. As such, the dose, release rate, and concentration gradients of different GFs need to be spatiotemporally controlled by GF delivery systems to mimic the native release patterns of GFs. Particulate delivery systems can perform critical roles in controlling the GF presentation patterns. Achieving a successful controlled GF release demands particulate delivery systems being well-designed and even optimized. This requires one to understand the release mechanisms and critical factors involved, as well as their relationships with GF release profiles. This paper presents an overview on recent developments in the field of smart bioactive scaffolds and GF delivery strategies in tissue engineering with an emphasis on the rate-programmed nano-particulate delivery systems in order to mimic natural presentation patterns of GFs. Factors that are critical to the rate-programming of nanoparticles are discussed, along with the role played by mathematical models for optimizing nano-particulate delivery systems. This review reveals that actively controlled nano-particulate delivery systems, triggered by either external stimuli or internal microenvironment conditions, can be of importance in the rate-programming of GF release in scaffolds. Strategies for spatiotemporal control of GF release are presented, along with their challenges and opportunities for the development of sophisticated delivery systems in tissue engineering.

2.3. Smart bioactive tissue engineering scaffolds

Tissue engineering generally requires an artificial extra cellular matrix (ECM) to facilitate cell adhesion, mechanical stimuli and cell-cell signals for tissue regeneration. In addition, the presence of signalling molecules including GFs and cytokines in the microenvironment is essential. In fact, the success of cell proliferation, differentiation and migration, leading to tissue regeneration, relies on the functionality of the matrix scaffolding cells. Interactions between cell receptors (e.g. integrin) and scaffold components (e.g. GFs, ECM peptides, mechanical stimuli)

lead to sequential biochemical cascades controlling gen expressions to regulate cellular activities. In this regard, the role of bio-functional scaffolds behaving as a natural microenvironment for cells in instructing cells for tissue regeneration is inevitable. The concept of smart scaffolds is referred to the functionality of biomaterial-based scaffolds to properly supply ECM components, deliver signalling molecules, and provide required electrical or mechanical stimuli to guide cells for tissue regeneration.

Generally tissue engineered scaffolds can be made of natural or synthetic biomaterials. Although natural biomaterials possess some remarkable properties such as cell adhesion, biodegradability and biocompatibility, they suffer from several deficiencies including limited flexibility for customizing physical properties of scaffold (e.g. porosity, stiffness), sourcing and inconsistent properties from material supplies, antigenicity and possible disease transmission, processing and deterioration. In contrast, synthetic biomaterials provide customizable scaffolds with reproducible and controllable physical and mechanical properties, degradation time and microstructural characteristics that can be manipulated according to particular applications. Despite numerous advantages, the lack of cell recognition signals is the major disadvantage of synthetic biomaterials. In recent years, there has been a significant increase in the number of studies on combining synthetic biomaterials as the frameworks with cell-recognition sites and GFs, aimed to facilitate cell proliferation, differentiation, and migration for tissue regeneration. In addition, a new trend has emerged in scaffold design to combine different scaffold fabrication techniques and different biomaterials to provide cells with mechanical and biological cues at the micro- and nano-scales. Combination of these two strategies in development of bioactive biomaterials and micro-fabrication of electrically/mechanically cell-stimulating scaffolds can

lead to smart tissue engineered scaffolds mimicking the natural cellular environment for tissue engineering.

Fabrication of bioactive scaffolds with properly designed mechanical properties and architecture mimicking natural ECM can be achieved using biofabrication techniques such as bioprinting, micro-fabrication, electro-spinning, self-assembly, and freeze drying methods. The scaffold characteristics are further improved to provide cell adherence properties, present signalling molecules, and deliver chemical cues to guide cells towards their proliferation, differentiation and migration. In a recent study, using electro-spinning technique Schulte et al. (2014) fabricated a 3D scaffold made of functionalized fibers incorporated into hydrogel possessing cell adhesive and spreading properties to mimic ECM microenvironment [5]. Shevach et al. (2014) biochemically and mechanically manipulated a double sheet of peritoneum as a natural scaffold, which was then seeded with cardiac cells and populated with endothelial cells in order to achieve a functional and vascularized cardiac tissue patch [6]. The emerging modular approach, also called bottom-up approach, is based on the generation of microscale tissue building blocks that resemble micro- and nano-architecture of native tissue to be assembled to form a functional tissue. Adopting modular strategy, Lee et al. (2014) successfully printed alginate hydrogel containing adipocytes and chondrocytes into an ear tissue construct mimicking ear shape and composition allowing for both adipogenesis and chondrogenesis [7]. Using capillary force lithography, Kim et al. (2014) fabricated nanopatterned cell culture substrates for vascular tissue engineering, in which endothelial cells showed better attachment, rapid EC migration and tubular morphology compared to non-patterned substrates [8]. Galler et al. (2011) incorporated basic fibroblast GF (bFGF), transforming GF (TGF) and vascular endothelial GF (VEGF) into a cell adhesive and enzyme-cleavable hydrogel made of self-assembling peptide nanofibers to

encapsulate dental pulp stem cells for dental pulp tissue engineering [9]. Implantation of the scaffold led to the formation of a vascularized soft connective tissue similar to dental pulp [9]. Hussain et al. (2013) coated chitosan fibers with fibronectin to enhance cell adhesion and migration properties and then fabricated an electrospun chitosan scaffold resembling the scale and architecture of natural ECM for cardiac tissue engineering [10]. They demonstrated that the chitosan nanofibers in the presence of fibronectin resulted in good cellular attachment and spreading as well as spatial organization [10]. The biologically active chitosan scaffolds for regenerative medicine have been well reviewed by Jiang et al. (2008) and Hyashi et al. (2012) [11, 12]. Several studies have shown that degradation rate [13], pore gradient and interconnectivity [14] and surface topography [15] of scaffolds have significant regulatory impact on cell fates. In addition, the role of ECM components in the scaffold matrix is crucially important for regulating cell fates mainly through integrins, substrate-specific receptors on cell surface. Among ECM components, fibronectin, collagen type I, II, VI, laminin, vitronectin, and osteopontin are typically important ECM proteins which regulate cell proliferation, survival, differentiation, and migration within scaffolds by activating several intracellular signalling pathways and focal adhesion formation [16-18]. GFs are also critical signalling molecules that instruct cells during development. GF-based tissue engineering is an attractive field in tissue engineering aiming to control the tissue regeneration process by precise control of GF delivery in a local area within the scaffold. An overview on the recent developments of this field has been provided by Kangwon et al. (2011) [19]. Despite the important roles of GFs in instructing cells, these signalling molecules need to act systematically to exert spectrum effects for tissue regeneration. Furthermore, GFs have a short half-life once they are presented to the cellular microenvironment. Although most often the precursors of GFs are more stable than active

molecules, upon presentation and binding to ECM molecules, the GFs are activated and rapidly degraded with a biological half-life of minutes [20, 21].

Although numerous studies have shown the potential of GF-based tissue engineering, there are several major issues that must be addressed before reliable human applications can be considered. Table 2.1 shows the most important GFs and the delivery approaches as well as the associated biopolymers used in tissue engineering. In the context of GF delivery, the control of dose remains one of challenging issues. For example, in a study in which a liposomal delivery system containing TGF and a fibrinogen/thrombin/TGF solution were added to porcine full-thickness defects, liposomal TGF concentrations between 200 and 900 ng/ml stimulated chondrogenesis while concentrations above 900 ng/ml caused osteophyte formation [44]. In addition to dose, a precise control of sequence (co-delivery or sequential delivery) and timing of

Table 2.1. Most commonly used polymers for GF delivery in tissue engineering.

Regenerative therapy	Delivered GF	Polymer	Delivery system	Ref.
Angiogenesis	VEGF	PLGA[1]	Scaffold	[22]
	VEGF and Ang-1[2]	Collagen	Scaffold	[23]
	VEGF	PLGA	Microparticles	[24]
	VEGF	PCL	Scaffold	[25]
	VEGF and bFGF	PLGA	Nanoparticles	[26]
	VEGF	PEG[3]	Scaffold	[27]
	VEGF	Alginate	Scaffold	[28]
	VEGF	Collagen	Microparticles	[29]

	VEGF and bFGF	PEG	Scaffold	[27]
	VEGF and PDGF[4]	HA[5]/chitosan	Nanoparticle	[30]
Bone	TGF-β	PLA	scaffold	[31]
	PDGF	Chitosan/ PLA	Scaffold	[32]
	rhBMP-2[7] and rhIGF-1[8]	PLGA	Microspheres	[33]
	PDGF	PCL[9]	Scaffold	[34]
Cartilage	TGF-β	Alginate	Beads	[35]
	TGF- β	Chitosan	Scaffold	[36, 37]
	BMP and TGF- β	Chitosan	Hydrogel	[38]
Dermis	EGF[10]	Gelatin	Bilayer scaffold	[39]
	bFGF	Chitosan	Scaffold	[40]
Mesenchymal stem cell therapy	BMP-2	Chitosan	Microspheres	[41]
Ligament	PDGF	Fibrin	Scaffold	[42]
Spinal bone	rhBMP-7	HAC[11]	Hydrogel scaffold	[43]

[1]Poly(lactide-co-glycolide), [2]angiopoietin-1, [3]poly(ethylene glycol), [4]platelet-derived growth factor, [5]hydroxyapatite, [6]poly(lactic acid), [7]recombinant human bone morphogenetic protein-2, [8]recombinant human Insulin-like growth factor-1, [9]poly(ε-caprolactone), [10]epidermal growth factor,[11]hydroxyapatite carrier

release as well as local concentration gradient of GFs is significantly challenging. Although studies have shown that the delivery of multiple GFs can improve tissue regeneration [45], most studies have used single GF delivery because of extremely little knowledge about optimum sequence and concentration of delivered GFs. These types of information are essentially critical for designing and optimizing nano-particulate delivery systems. Table 2.2 summarizes some of recent studies on determination of desired release characteristics of GFs for angiogenesis, cartilage and bone tissue engineering.

Despite of the rapid progress, further investigations in developing more sophisticated bioactive scaffolds are required. Improvements in smart scaffolds must include spatiotemporal control of

Table 2.2. Desired doses and release profiles of GFs reported by some studies on angiogenesis, cartilage, and bone regeneration.

Regenetive therapy	Type of study	GFs	Total dose	Desired Release profile	Delivery system	Ref.
Angiogenesis	*in-vivo*	VEGF	0.04 µg/g	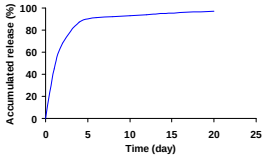	Alginate/ PLGA microspheres	[46]
Angiogenesis	*in-vivo* & *in-vitro*	VEGF	0.1 µg/g	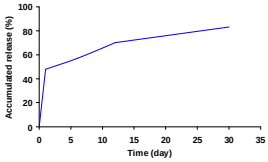	Alginate hydrogel	[47]

Angiogenesis	*in-vivo* & *in-vitro*	VEGF and S1P	100 µg/ml and 1.8 mg/ml	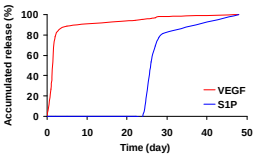	Cellulose hollow fiber	[48]
Cartilage regeneration	*in-vitro*	TGF-β1 and BMP-7	10 ng/ml and 22.7 ng/ml	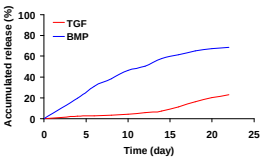	Chitosan hydrogel	[38]
Bone regeneration	*in-vitro*	bFGF and VEGF and BMP-7	10 ng/ml and 1 ng/ml and 50 ng/ml	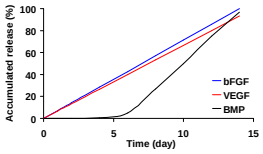	Direct administration to the culture medium	[49]

review, important aspects of smart delivery systems for controlled release of GFs are overviewed. The emphasis will be placed on critical parameters in rate-programming of polymeric nanoparticles and potentials of externally triggerable nanoparticles to control GF release in tissue engineered scaffolds.

2.4. GF release strategies in tissue engineering

Strategies for GF delivery in tissue engineering can be generally classified into two categories: i) chemical immobilization of GFs into the scaffold biomaterial and ii) physical encapsulation of GFs in the delivery system. In the first delivery approach, GFs are first conjugated with the

scaffold biomaterial, which may be mixed with cells for the subsequent scaffold fabrication (Fig. 2.1a). The presentation of the GFs is regulated based on the extent of binding of GFs to the scaffold biopolymeric matrix. The chemical binding and affinity interaction between the GFs and the scaffold biomaterial binding domains determine the release rate of GFs. The GF conjugation with the scaffold matrix can be either non-covalent or covalent, thereby affecting the release rate of GFs from the scaffold.

In non-covalent incorporation, electrostatic (charge-charge) interaction or indirect interactions via intermediate proteins are the major mechanisms for immobilizing GFs in their place within scaffolds. Hydrogels containing intermediate proteins such as fibronectin, laminin, collagen, elastin or the glycosaminoglycans heparin sulphate, chondroitin sulphate, fibrin, and hyaluronic acid can be used to link GFs into the scaffold matrix [50-57]. Due to the affinity of GFs to heparin, the surface of extracellular matrix components has been modified by grafting heparin in

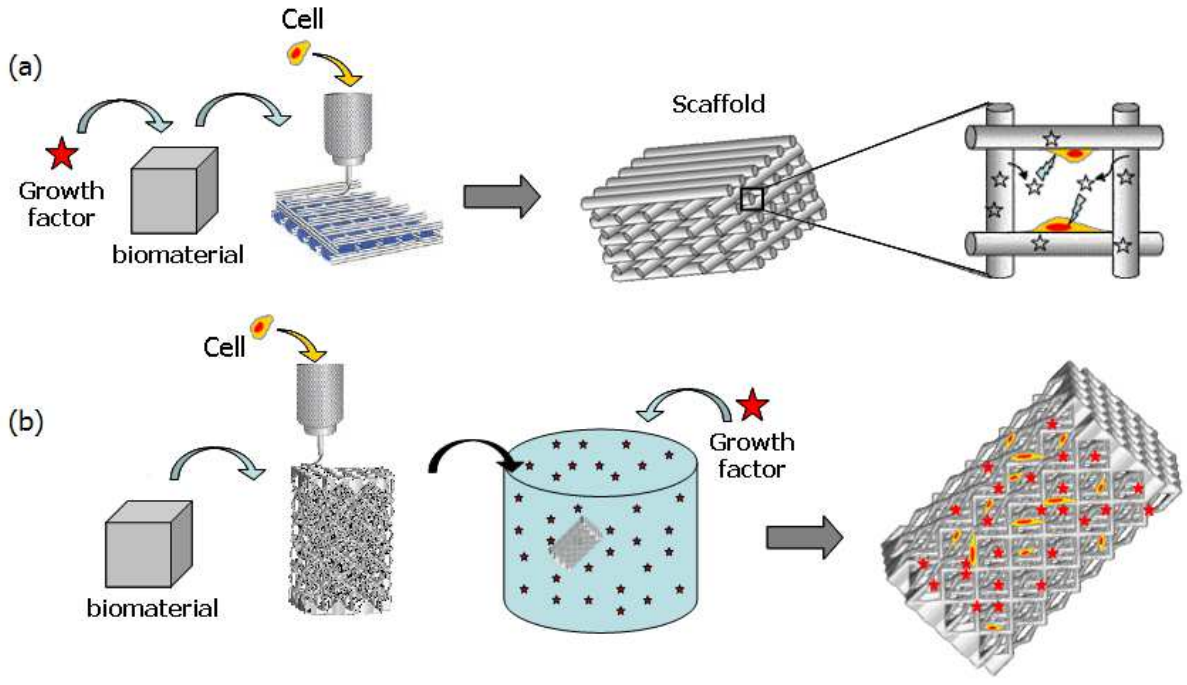

Figure 2.1. Schematic diagram of direct GF incorporation into fabricating scaffolds (a) and pre-formed scaffold (b).

order to bind GFs to the scaffold matrix [55, 56]. Small oligopeptides (e.g. arginine–glycine–aspartic acid (RGD)) exhibiting adhesion properties have been used for linking GFs to the scaffold matrix for prolonged delivery of GFs [57-59]. Covalent binding of GFs with the scaffold matrix can provide more prolonged release compared to the non-covalent incorporation. GFs are conjugated with the scaffold via functional groups [60]; however, there are some limitations including the specificity of functional sites that can be difficult to assign selectively and possible loss of bioactivity of GFs due to potential damage to functional groups during immobilization. Furthermore, although some GFs can be active in the bound state, some need to be cleaved to become active [39] such that enzymatic and hydrolytic reactions, which can potentially affect the conformation and biological activity of GFs, will be necessary. Since GFs are immobilized into the scaffold matrix, the GF delivery will be localized so that the delivery system will be unable to provide GF spatial concentration gradient as a cue to stimulate cell migration and proliferation.

Contrary to the chemical immobilization approach, physical entrapment of GFs in the scaffold biomaterials is simple with more flexibility to control the release rate based on the biopolymer molecular weight (MW), hydrophobicity and porosity. The GF presentation pattern is regulated by the scaffold matrix degradation rate, diffusivity of GFs and the composition and structure of the scaffold. One of the simplest ways to physically incorporate GFs into or onto the scaffold biomaterials is the immersion of pre-formed scaffolds in a GF solution allowing for diffusion and entrapment of GFs into the scaffold matrix (Fig. 2.1b). With the aid of 3D micro-patterning technologies, the efficacy of GF delivery have been significantly enhanced by precisely controlling the spatial distribution of GF-containing biomaterials within a 3D scaffold. In addition, since GFs can diffuse through the scaffold pores, GF concentration gradients as

stimulating cues to guide cellular migration can be provided. The drawback of this method is associated with low loading capacity, long loading time, burst release, and tightly composition-dependent release properties of GFs from the scaffold the property of which need to have been optimized mechanically, chemically and biologically. Since GFs are exposed to the scaffold microenvironment in this delivery approach, the loss of GF bioactivity due to oxidation, proteolysis, hydrolysis and enzymatic reactions occurring in the scaffold microenvironment remains one of the major issues. One of very prominent approaches to bypass the above limitations and also to improve the biofunctionality of the scaffolds is to employ nano-particulate delivery systems to modulate GF release profiles and to protect the bioactivity of GFs during the release process.

Generally nanoparticles can be structurally divided into several classes of micelles, dendrimers, liposomes, solid-lipid nanoparticles, and polymeric nanoparticles (Fig. 2.2). Depending on applications, the size of the nanoparticles varies between 20 and 1000 nm. Among these particulate delivery vehicles, polymeric particles provide a wide range of particle size ranging from 40-1000 nm (nanoparticles) to 1-100 μm (microparticles). Polymeric nanoparticles offer several advantages over other types of nanoparticles including high stability, biodegradability, high flexibility in modulating the release rate of GFs, protection properties that significantly prevent bioactivity loss of GFs, high loading capacity, feasibility of incorporation of both hydrophilic and hydrophobic substances. These distinct characteristics make the polymeric nanoparticles very suitable delivery vehicles for controlling the release profile of GFs within the scaffolds. GF-loaded polymeric nanoparticles and cells are incorporated into biomaterials which are used to fabricate three dimensional tissue engineered scaffolds using bioplotter (Fig. 2.3).

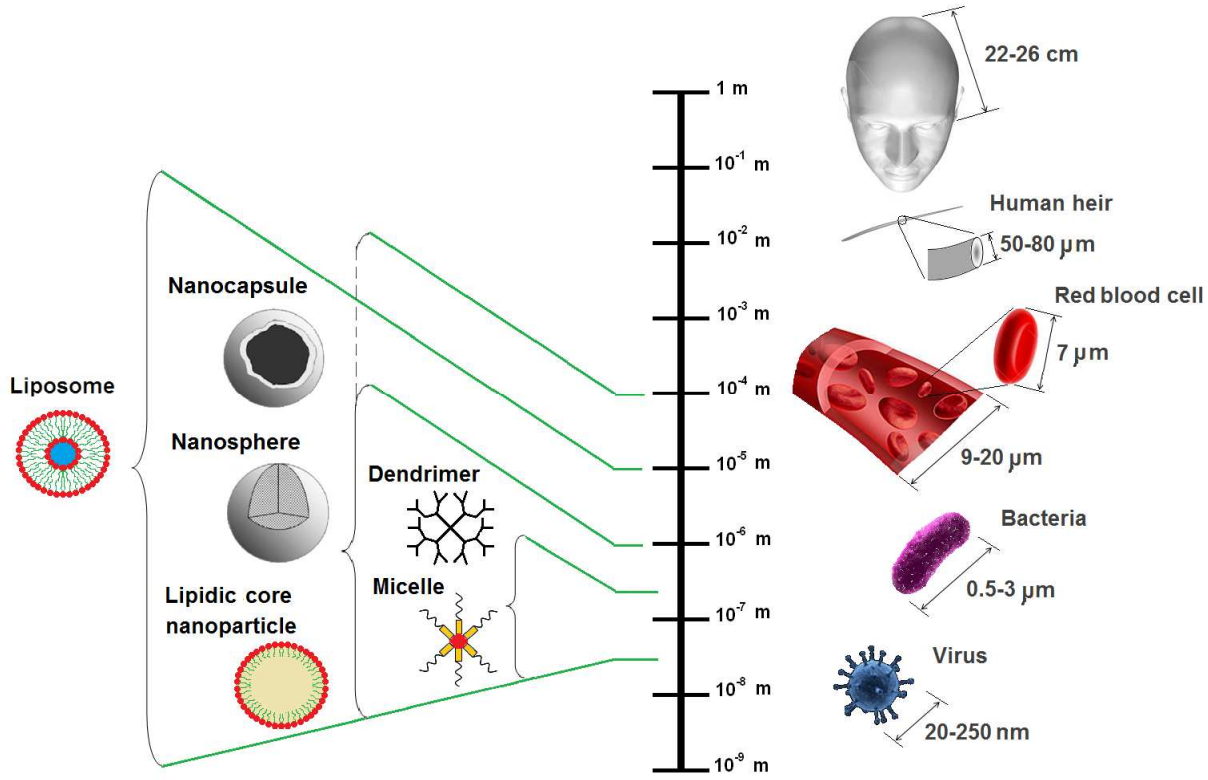

Figure 2.2. Typical nanoparticles compared to biological elements.

The release rate of GFs can be manipulated based on different release limiting factors attributed to the composition, structure, and architecture of the nanoparticles as well as the mechanisms governing the GF release from nanoparticles. Recent studies have successfully used polymeric nanoparticles for dual and multiple GF delivery for guiding tissue regeneration [61-63]. The advantages offered by polymeric nanoparticles suggest that nano-particulate delivery systems have high potentials for controlling GF presentation patterns within bioactive scaffolds.

2.5. Rate-programming of nanoparticles to control GF release

One of the most important characteristics of smart scaffolds is their ability to regulating the dose, timing and sequence of GF release in the ECM mimicking microenvironment. As mentioned earlier, polymeric nano-particulate delivery systems play an important role in protecting GF

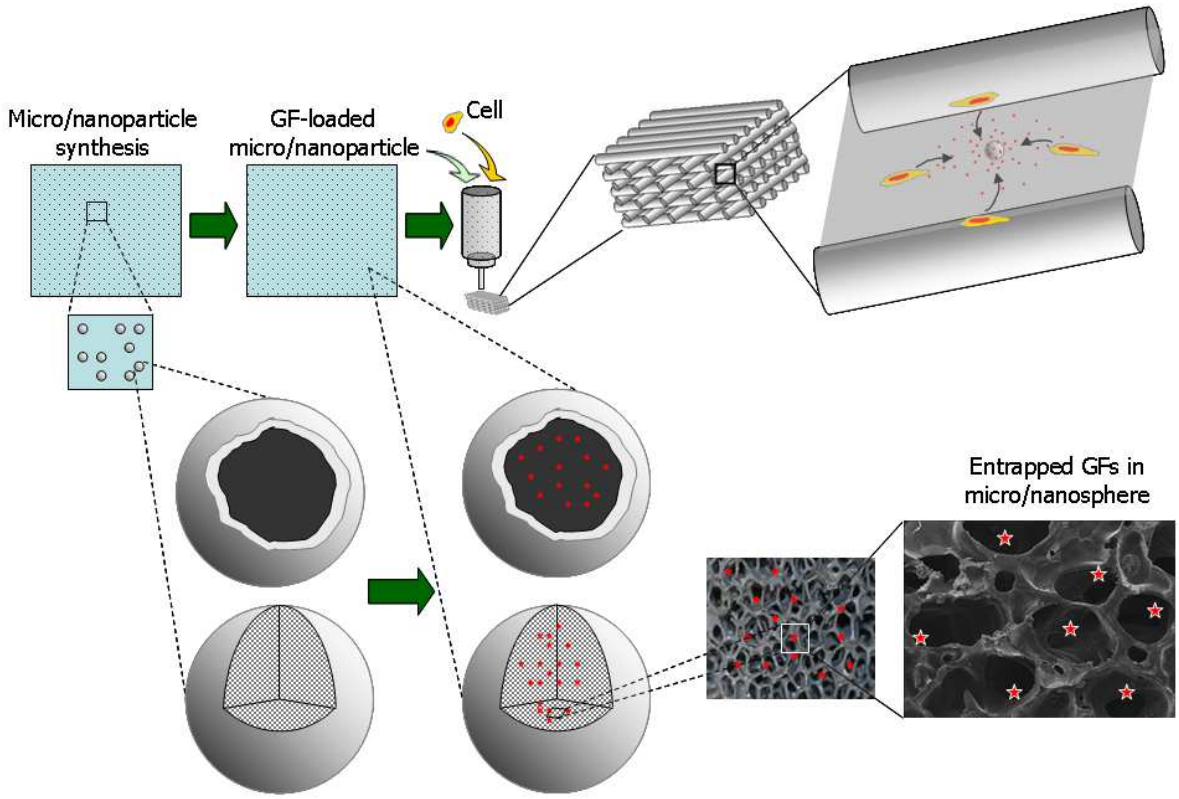

Figure 2.3. Schematic diagram of incorporation of GF-loaded micro/nanoparticles into tissue engineered scaffolds for controlled delivery of GFs to cells.

biological functionality and controlling GF release profiles within the scaffolds during tissue regeneration. The release profile of GFs from nano-particulate delivery vehicles can be either pre-programmed by manipulating physicochemical and structural characteristics of polymeric nanoparticles, or actively controlled by triggering the nanoparticles in-situ using external or internal stimuli.

2.5.1. Critical factors in pre-programming of polymeric nanoparticles

Physicochemical properties, architectural and structural characteristics and release mechanisms are the most important factors affecting the design of nano-particulate delivery systems to provide pre-determined GF release profiles.

Chemical properties including polymer hydrophobicity, MW and inherent viscosity, cross-linking and crystallinity as well as number of functional groups are critical factors affecting release kinetics of GFs from polymeric nanoparticles. Besides, pore size, porosity, tortuosity and packing density of the polymer matrix constituting the polymeric nanoparticle influence GF release profiles from the nanoparticles. Structural characteristics and architectural features such as average size, polydispersity, size distribution, zeta potential, number of shells and the type of polymer of the shell can significantly affect GF loading capacity and efficiency as well as release characteristics of GFs from polymeric nano-particulate delivery systems. These physical properties of polymeric nanoparticles are affected by fabrication conditions during the preparation of the nanoparticles. A recent study by the authors has revealed that the size, polydispersity, zeta potential and protein loading capacity of high MW PLGA nanoparticles are significantly (p-value<0.05) affected by the concentration of poly vinyl alcohol (PVA), polymer concentration, PVA:organic phase ratio, the interaction between the polymer and PVA concentrations, and the interaction between PVA concentration and PVA:organic phase ratio. The authors have developed a model to be used for designing PLGA nanoparticle structural and physical characteristics, protein loading capacity and efficiency, zeta potential, and optimizing the fabrication conditions of the nanoparticles. The number of shells, the thickness and the polymer of each shell can significantly contribute to the control of the rate of GF release from multi-shelled nanoparticles in which the core contains the GF and the shell(s) acts as a rate-limiting barrier to delay the GF release. In addition, double-shelled nanoparticles encapsulating two GFs in the core and shell allow for sequential release of GFs in various stages to achieve synergistic effects of the GFs. Such delivery systems would be useful for the simultaneous or sequential release of multiple GFs for expediting GF driven tissue regeneration in tissue

engineering [64]. Recently, several triple-walled particulate delivery systems have been developed to control release profiles of multiple factors [65-70].

Another critical factor affecting the design of nano-particulate delivery systems is associated with the mechanism(s) governing GF release from polymeric nanoparticles. In order to design a nano-particulate delivery system to provide a pre-determined GF release profile, having a good understanding of release mechanisms and their relationship with physicochemical properties of polymeric structure of nanoparticles are essential. In general, major release mechanisms in polymeric nano-particulate delivery systems include diffusion-dissolution [71-73], erosion [73, 74], osmotic pump [75], swelling [76], polymer relaxation [77], pore closure [78], and heterogeneous degradation, crack formation and collapse of polymer matrix [79-81]. In most scenarios, combinations of above mechanisms control the release rate of GFs from the polymeric nanoparticles. Diffusion-dissolution mechanism, which is involved in most of release mechanisms, is governed by GF solubility and diffusivity in water, porosity, pore size and interconnectivity, packing density, and tortuosity of the polymer matrix of nanoparticles. In addition, the nanoparticle structure including the thickness and number of shells of nanoparticles are the limiting factors influencing mass transfer rate and release rate of GFs in nanoparticles. Bulk and surface erosions due to enzymatic reaction, hydrolysis or disentanglement of the polymer chains [82, 83], are important mechanisms governing GF release processes in polymeric nanoparticles. Bulk erosion is the major release mechanism in PLA, poly(glycolic acid) (PGA), and PLGA nanoparticles, which are characterized by ester linkages in the backbone of the polymers [84]. Rate of water infusion into the polymer matrix, which is affected by crystallinity of the polymeric nanoparticle, porosity and interconnected pores of the polymer matrix, and the polymer degradability are the most critical factors controlling bulk erosion mechanism. Bulk

erosion is characterised by an initially small increase in GF release from nanoparticles attributed to the solubility of GFs at the particle surface followed by a S-shape release kinetics (Fig. 2.4). In this mechanism of release, water penetrates into the amorphous regions of the polymer while GF release remains low due to low porosity and low pore interconnectivity of the polymer matrix (Fig. 2.4b). Over time, polymer hydrolysis causes acidic conditions in water-filled pores catalyzing the degradation reactions leading to exponentially increasing pore size within the particle. The growth and coalescence of the pores increase the pore interconnectivity [85], which boosts GF release rate [86]. When most of the amorphous regions of polymer are degraded, the hydrolysis rate gradually decreases due to the remaining crystalline parts [85]. Beside bulk erosion, surface erosion is another main mechanism of release in polymeric nanoparticles that are made of polyanhydrides because of their low glass transition temperature that causes the polymer to rapidly respond to the water erosion [82, 83]. Contrary to bulk erosion, surface erosion provides zero order release kinetics.

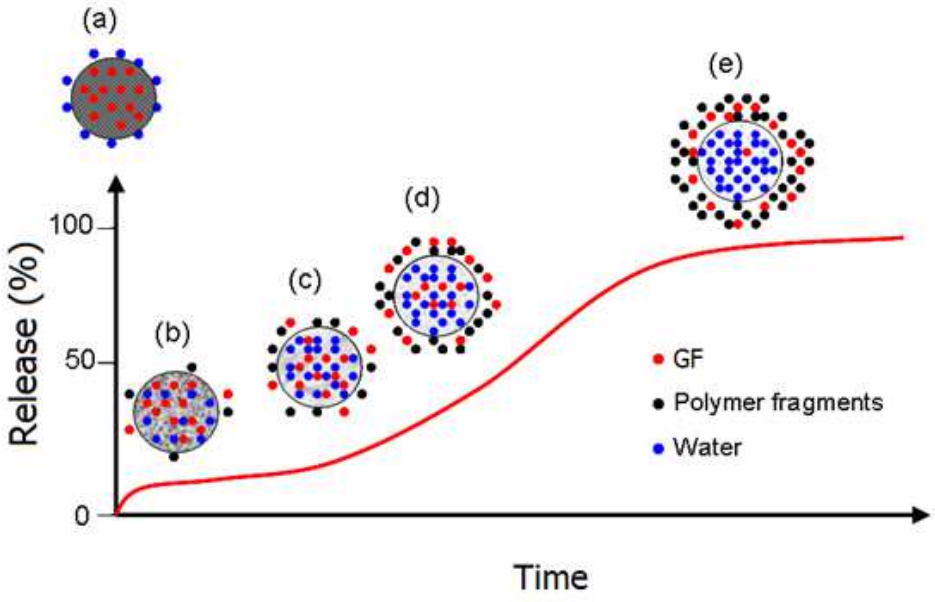

Figure 2.4. Schematic diagram of GF release during bulk erosion (a-e).

Swelling that refers to an increase in the volume of a polymeric matrix due to hydration is an important release mechanism in which a phase transition in the polymer matrix takes place from swells, and performs as a moving front that separates the interior glassy region from the exterior glassy state to the rubbery state. In the glassy state, polymer resists water uptake and GFs remain immobile in the matrix; however, the superficial layer of the matrix gradually absorbs water, swollen part of the matrix. As the water penetrates to the matrix interior, GFs are dissolved in the water in the swollen layer enhancing GF release due to an enhanced GF diffusivity [87, 88]. If GF diffusivity in water is high, swelling rate will be the rate-limiting factor; however, dissolution-diffusion mechanism will control the release process if the GF diffusivity is low [89, 90].

A critical issue in designing and optimization of nano-particulate delivery systems is associated with burst release which is defined as the initial large bolus of GF release before the release rate reaches a stable profile. Burst release presents a high initial GF dose to the microenvironment and can effectively reduce the life-time of the delivery system [91] with potentially inverse therapeutic effects (e.g. massive vessel formation due to a large dose of VEGF [92, 93]. Burst release can be caused by minor damages to the shell of nanocapsules leading to serious leaks during nanoparticle degradation [94]. Burst release can occur in nanogels where high loading conditions increases the chance of trapping more GFs on the surface of nanospheres [95-97]. Low polymer MW [96, 98, 99], low polymer concentration [100], high solvent removal rate and high drying rate during freeze drying [101-103] contribute to burst release from polymeric nanoparticles. Double-shelled particulate delivery systems have exhibited significant reduction in burst release due to the rate-limiting role of the exterior shell of the particles [104, 105].

2.5.2. The relationship between critical factors and release patterns

Table 2.3 provides typical release profiles associated with critical factors and release mechanisms involved in GF release process. While surface erosion and swelling can provide zero order release kinetics of GFs, other mechanisms provide nonlinear release profiles. Table 2.3 also indicates that GF effective diffusivity and polymer characteristics including polymer MW, glassy state, and hydrophilic properties as well as GF effective diffusivity are the most influential factors affecting release profiles. A good understanding of the relationship between these factors and the GF release profiles (Table 2.3) contribute to the design and rate-programming of polymeric nanoparticles to provide desired GF release profiles.

Physicochemical properties and structural characteristics of the polymeric nanoparticles can be manipulated so that combined effects of different factors lead to the desired GF release profile from the nanoparticles. In fact, rate-programming and optimizing polymeric nanoparticles rely on our ability to mechanistically describe the release process based on the critical factors that are involved. In this context, mathematical models play very important role in designing nanoparticles, analyzing the sensitivity of release kinetics with respect to the physicochemical properties of nanoparticles, and rate-programming of GF release.

The first mathematical models of controlled release systems were developed by Noyes and Whitney (1897) and Nernst and Brunner (1904); however, due to oversimplifications associated with neglected mass transfer in porous polymer, the models were unable to well describe the release process mechanistically. Higuchi (1961) presented a model based on a pseudo-steady state mass transfer in a porous matrix but the model was confined to slab shape delivery systems [119]. Koizumi and Panomsuk (1995) improved Higuchi model and described the release process for non-erodible spherical particles [120]. Recently, Wang et al. (2010) developed an

Table 2.3. Critical factors and typical release profiles associated with major release mechanisms.

Release mechanism	Critical factors	Typical release profile	Ref.
Dissolution-diffusion	Polymer and GF MW↓⇒release rate↑ Particle size↓⇒release rate↑ Porosity↑⇒release rate↑ Tortusity↓⇒release rate↑ Polymer/solvent ratio↓⇒release rate↑	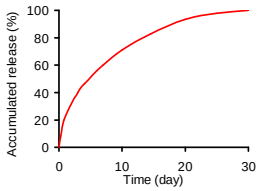	[106- 109]
Surface erosion	Glassy point↓⇒release rate↑ Polymer MW↓⇒release rate↑ Fatty acid dimmer-sebacic acid fraction↑⇒release rate↑	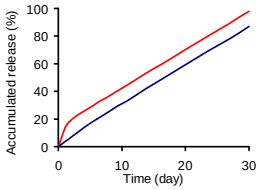	[109, 110, 111]
Surface erosion & dissolution-diffusion	Hydration rate↑⇒release rate↑ Porosity↑⇒release rate↑ Interconnected pores↑⇒release rate↑ Tortusity↓⇒release rate↑ Glassy point↓⇒release rate↑	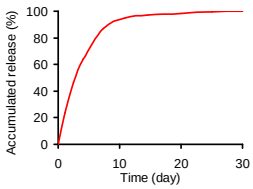	[109, 110, 112, 113]
Bulk erosion	Crystalline/amorphous↓⇒release rate↑ Hydration rate↑⇒release rate↑ Polymer MW↓⇒release rate↑	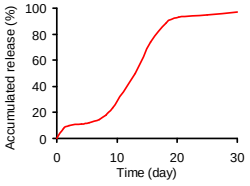	[114, 115-117, 109]

	Lactic:Glycolic↓⇒release rate↑		
	Particle size↓⇒release rate↑		
Bulk erosion & dissolution-diffusion	Effective diffusivity↑⇒release rate↑	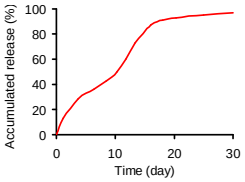	[114, 118, 109]
	Polymer and GF MW↓⇒release rate↑		
	Lactic:Glycolic↓⇒release rate↑		
	Crystalline/amorphous↓⇒release rate↑		
	Particle size↓⇒release rate↑		
	Hydration rate↑⇒release rate↑		
Swelling	Glassy point↓⇒release rate↑	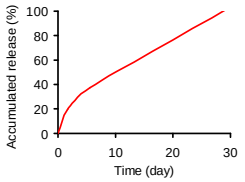	[118]
	Hydrophilic polymer↑⇒release rate↑		

analytical model of dissolution-diffusion with burst release for polymeric particulate delivery systems [121]. Sophisticated models include dissolution, diffusion, and erosion governing equations which are solved simultaneously to describe bulk and surface erosion mechanisms of release for different physicochemical characteristics of polymeric particles [118]. Rothstein et al. (2008) recently developed a system of partial differential equations taking into account pore formation, diffusion-reaction, hydration, polymer MW change, dissolution, and crystallinity of the polymer to describe erosion controlled release process [122]. Table 2.4 summarizes well-known mathematical models of release process form polymeric particulate delivery systems.

2.5.3. The role of mathematical modeling of controlled release for designing smart scaffolds

One of the challenges that smart bioactive scaffolds are facing to is spatiotemporal control of GF release to facilitate cellular fate regulation *in-situ*. GF-loaded polymeric nanoparticles with flexible release characteristics play a crucial role in designing smart scaffolds with spatiotemporal GF control capability. Development of such scaffolds requires precise design and optimization of structural, architectural and physicochemical characteristics of the GF-loaded nanoparticles for pre-programmed GF release profiles within the scaffolds. Mathematical models of controlled release of GFs are efficient and effective tools for designing and optimizing GF-

Table 2.4. Well-known mechanistic models and limitations for controlled release from particulate delivery systems.

Model name	Model	Limitation	Ref.
Noyes-Whitney/ Nernst-Brunner	$\frac{dM}{dt} = \frac{D_{AB}S}{h}(C_s - C_b)$	No structural characteristics of the matrix involved Perfect sink condition required Inapplicable to spherical particles Constant concentration gradient during mass transfer process Unable to describe the transient period of GF transportation	[123, 124]

Higuchi	$M(t)=\left[(2C_0-\varepsilon C_a)C_a\left(\frac{\varepsilon D_{AB}}{\tau}\right)t\right]^{1/2}$	Invalid for polymeric particles with heterogeneous structure Constant GF diffusivity Unable to describe the transient period of GF transportation Constant concentration gradient during the release Initial GF concentration should be much larger than the GF solubility in the matrix to avoid significant errors Perfect sink condition needs to be satisfied	[119]
Korsmeyer-Peppas	$M(t)=4\pi r^2\left[\begin{array}{l}\sqrt{2(C_0-C_s)C_sD_{eff}t}+\\ \frac{4C_sD_{eff}t}{9r}\left(\frac{C_s}{2C_0-C_s}-3\right)\end{array}\right]$	Invalid for polymeric particles with heterogeneous structure	[120]

		High initial excess GF Constant GF diffusivity Unable to predict the transient period of GF transportation	
Baker-Lonsdale (for spherical geometries)	$\frac{3}{2}\left[1-\left(1-\frac{M(t)}{M_\infty}\right)^{2/3}\right]-\frac{M(t)}{M_\infty}=\frac{3D_{AB}C_s\varepsilon}{r_0C_0\tau}$	Invalid for heterogeneous polymeric Constant GF diffusivity Unable to predict the transient period of GF transportation	[125]
Diffusion model (considering the initial burst effect with spherical Bessel functions)	$\frac{M(t)}{M_\infty}=1-\frac{6\sigma}{(1-\sigma^3)}\left(\sum_{n=1}^{\infty}\frac{j_1^2(\sigma\alpha_n)}{\sin^2\alpha_n}\exp\left(\left(-\alpha_n^2\left(D_1\left(t-t_c\right)+D_0\right)t_c\right)/r_2^2\right)\right)$ For $t>t_c$ t_c : threshold time, $\alpha_n=r_2\sqrt{\lambda}$, λ: eigenvalue of the problem, j_1: the first order spherical Bessel function, D_0: a constant, r_2: the radius of the particle.	Perfect sink condition needs to be satisfied Invalid for polymeric particles with heterogeneous structure	[121]

Hopfenberg	$\frac{M(t)}{M_\infty}=1-\left(1-\frac{k_0 t}{C_0 R}\right)^n$ M(t): Cumulative amount of released GF at time t M_∞: Cumulative amount of released GF at infinite time k_0: erosion rate constant C_0: Initial GF concentration within the polymeric matrix r: The radius of sphere, cylinder, or half thickness of the slab polymer n: Shape factor (n=3, 2 and 1 for spherical, cylindrical and slab geometries, respectively)	Surface eroding polymers Zero-order surface detachment of the GF Spherical, cylindrical, slab particles	[126]
Katzhendler et. al	$\frac{M(t)}{M_\infty}=1-\left(1-\frac{k_a t}{C_0 a_0}\right)^2\left(1-\frac{2k_b t}{C_0 b_0}\right)$ k_a: Radial erosion rate constant k_b: Axial erosion rate constant a_0, b_0: Initial radius and thickness of the cylindrical geometry, respectively	A general model for bulk erosion-controlled release Takes into account radial and axial erosion Release rate can be well described when ka≅ ka	[127]
Linear Erosion model	$\begin{cases}\frac{\partial C_L}{\partial t}=\frac{1}{r^2}\frac{\partial}{\partial r}\left(Dr^2\frac{\partial C_L}{\partial r}\right)+C_{Se}K_{Lero}-\frac{\partial C_{Se}}{\partial t}\left(1-K_{Lero}t\right)\ (Liquid\ phase)\\ \frac{\partial C_S}{\partial t}=\frac{\partial C_{Se}}{\partial t}\left(1-K_{Lero}t\right)-C_{Se}K_{Lero}\ (Virtual\ solid\ phase)\\ \frac{\partial C_{Se}}{\partial t}=-k_{dis}\left(\varepsilon C_{sat}-C_L\right)\ (Effective\ solid\ phase)\end{cases}$ C_L: Agent concentration in liquid phase C_s:Agent concentration in solid phase C_{se}: Agent concentration in the effective solid phase	Amorphous to crystalline polymer ratio and free to rigid chains are comparable.	[128]

Csat:Saturation concentration

D: Effective diffusivity

K_{Lero}:Linear erosion rate constant for bulk erosion

K_{dis}:Dissolution rate constant

r: Distance from the surface of particle

"S" Erosion model	$\begin{cases} \frac{\partial C_L}{\partial t} = \frac{1}{r^2}\frac{\partial}{\partial r}\left(Dr^2\frac{\partial C_L}{\partial r}\right) - \frac{\partial C_{Se}}{\partial t}\left(1 - \frac{1}{1+b\exp(-K_{Sero}t)}\right) + \frac{C_{Se}bK_{Sero}\exp(-K_{Sero}t)}{[1+b\exp(-K_{Sero}t)]^2} \\ \frac{\partial C_S}{\partial t} = -\frac{C_{Se}bK_{Sero}\exp(-K_{Sero}t)}{[1+b\exp(-K_{Sero}t)]^2} + \frac{\partial C_{Se}}{\partial t}\left(1 - \frac{1}{1+b\exp(-K_{Sero}t)}\right) \\ \frac{\partial C_{Se}}{\partial t} = -k_{dis}(\varepsilon C_{sat} - C_L) \end{cases}$	Amorphous part blocked by crystalline region -Degradation is initially very slow causing a release lag time	[128]

K_{Sero}: "S" erosion rate constant for bulk erosion

Rothstein et al.	$\begin{cases} \frac{\partial C_w}{\partial t} = \nabla(D_w \nabla C_w) - kC_w M_w \\ \frac{\partial M_w}{\partial t} = -kC_w M_w \\ \frac{\partial C_s}{\partial t} = -k_{dis} C_{sn} C_{wn} C_{an} \\ \frac{\partial C_A}{\partial t} = \nabla(D_{eff} \nabla C_A) + k_{dis} C_{sn} C_{wn} C_{an} \end{cases}$	Unified model for both surface and bulk erosion-controlled GF release	[122]

C_w: time-dependent water concentration

D_w: diffusivity of water in the matrix

k: degradation rate constant

M_w: polymer MW

C_s: saturation concentration

k_{dis}: intrinsic dissolution rate constant

C_{sn}: normalized solid GF in the polymer matrix

C_{an}: difference between aqueous agent concentration and its maximum solubility

C_{wn}: normalized concentration of water

t: time

C_A: GF concentration

loaded particulate delivery systems to be used in smart bioactive scaffolds. Since the mechanistic models take into account GF release critical factors (see section 2.4.1), computational simulation of GF release can significantly contribute to the design and optimization of physicochemical and structural properties of nanoparticles leading to desired GF release profiles. Furthermore, the models can be coupled with governing equations of nutrient transports and cell growth/proliferation/migration [129, 130] in order to not only predict spatiotemporal distribution of GFs and cell population within scaffolds but also to assess the efficacy of the smart scaffold characteristics for tissue regeneration.

One of the most important applications of modeling of smart scaffolds can be defined in the context of vascularization of implanted scaffolds, which is recognized as a major challenge in tissue engineering in general, and in myocardial infarction repair in particular [131]. Vascularization of implanted scaffolds includes the formation of new blood capillaries from pre-existing capillaries of the surrounding tissue and the ingrowth of the vessels into the implanted scaffolds. Briefly, endothelial cells of existing capillaries remain undifferentiated unless they detect VEGF and/or FGF gradient in the microenvironment where tip cells are formed. The tip cells lead the new vessel sprouting while a lumen is created by stalk cells trailing behind the tip cells [132]. A steep and directional VEGF gradient leads to a rapid and directional migration of tip cells while non-directional VEGF concentration gradient causes very slow tip cell migration and dilated blood vessels [133]. To induce blood vessel sprouting into an implanted scaffold surrounded by a vascularized tissue, the smart scaffold should not only exhibit ECM characteristics but also control VEGF concentration gradient spatiotemporally within the scaffold such that the steep and directional VEGF gradient is maintained across the scaffold. Stage-wise release strategy can provide a VEGF concentration gradient that gradually travels from the

scaffold-tissue interface (scaffold outer boundary) to the scaffold center in order to guide capillary growth in the scaffold. Figure 2.5 schematically illustrates an implanted scaffold composed of a stage-wise VEGF release system (a three-stage release) to guide tip cells from the surrounding tissue into the scaffold. As shown, the symmetric scaffold is composed of three zones that include three physicochemically and structurally different VEGF-loaded nanoparticles (i.e. low MW, high MW, double-shelled nanoparticles) (Figs. 2.5a-c). The release of VEGF in each zone occurs in a timely manner to provide a dynamic VEGF concentration gradient that gradually travels from the outer to the inner zone of the scaffold (Fig. 2.5d-f). As seen in Fig. 2.5a, during the first stage of release, the capillary sprouting takes place from the tissue into the first zone of the scaffold due to the VEGF concentration gradient induced by the low MW polymeric nanoparticles loaded with VEGF (Fig. 2.5d). As the release rate of VEGF in the first zone decreases, high MW polymeric nanoparticles in the second zone start releasing VEGF where the induced VEGF concentration gradient directs the capillaries from zone I towards zone II of the scaffold (Figs. 2.5b, e). In the third stage of release, a delayed VEGF delivery provided by double-shelled nanoparticles occurs in the zone III where the induced VEGF concentration gradient guide the blood capillaries from zone II to zone III (Figs. 2.5c, f). Such a spatiotemporal release pattern relies on precise design and optimization of VEGF-loaded nanoparticle characteristics (e.g. MW, size, structure) that can be achieved using computational simulation of the stage-wise release of VEGF.

Knowing that the average velocity of capillary growth is a function of VEGF concentration gradient [131], mathematical modeling of the stage-wise release can be used to predict the VEGF release process at different conditions. In general, the mechanistic model consists of a system of differential equations as:

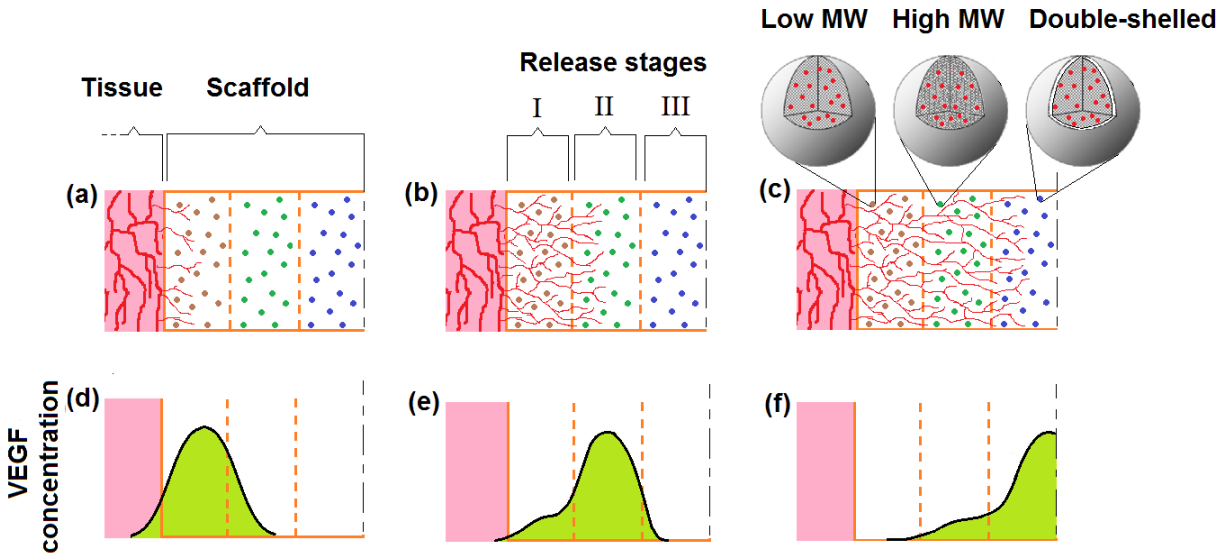

Figure 2.5. Schematic illustration of stage-wise VEGF release to induce vascularization in an implanted smart bioactive scaffold.

$$\begin{cases} \overline{R}(x,t) = f\left(C_{VEGF}(x,t), \overline{d}_p, PDI, \Gamma\right) \\ \dfrac{\partial C_{VEGF}(x,t)}{\partial t} = f\left(\vec{\nabla} C_{VEGF}, k_{VEGF\_d}, \varepsilon_f, \psi\right) \\ \varepsilon_f = f\left(M_w, k_{\deg}, C_w(x,t)\right) \\ \dfrac{\partial C_w(x,t)}{\partial t} = f\left(D_{eff}, k_{\deg}\right) \\ k_{\deg} = f\left(M_w, C_{polymer}, \beta, \vartheta\right) \\ \dfrac{\partial M_w(x,t)}{\partial t} = f\left(k_{\deg}, C_w\right) \end{cases} \tag{2.1}$$

where $\overline{R}$ is the release rate, C_{VEGF} is VEGF concentration in the nanoparticle matrix, $\overline{d}_p$ is the average nanoparticle size, *PDI* is the polydispersity index, Γ is the shell numbers, $\vec{\nabla} C_{VEGF}$ is VEGF concentration gradient, k_{VEGF_d} is the VEGF decomposition rate constant, ε_f is the porosity of the nanoparticle matrix, ψ is VEGF loading capacity, $k_{\deg}$ is the degradation rate constant of the nanoparticle polymer, C_w is the water concentration in the nanoparticle, D_{eff} is

the effective diffusivity of water, $C_{polymer}$ is the polymer concentration of the nanoparticle, β is the crystallinity index, and ϑ is the hydrophilicity index of the polymeric nanoparticles. The rate-programming procedure of the VEGF-loaded nanoparticles includes the determination of design parameters of the nanoparticles leading to the desired stage-wise release (see Fig. 2.5) of VEGF in the scaffold. Figure 2.6 illustrates the procedure for predicting the design parameters of the nanoparticles. The design parameters of the nanoparticles including $\bar{d}_p$, PDI, Γ, k_{VEGF_d}, ψ, $C_{polymer}$, β, and ϑ are defined and assigned as the inputs to the mechanistic model (Eq. (2.1)). The governing equations are solved numerically to simulate the VEGF release process and predict spatiotemporal VEGF concentration variations within the scaffold (Fig. 2.6). The results

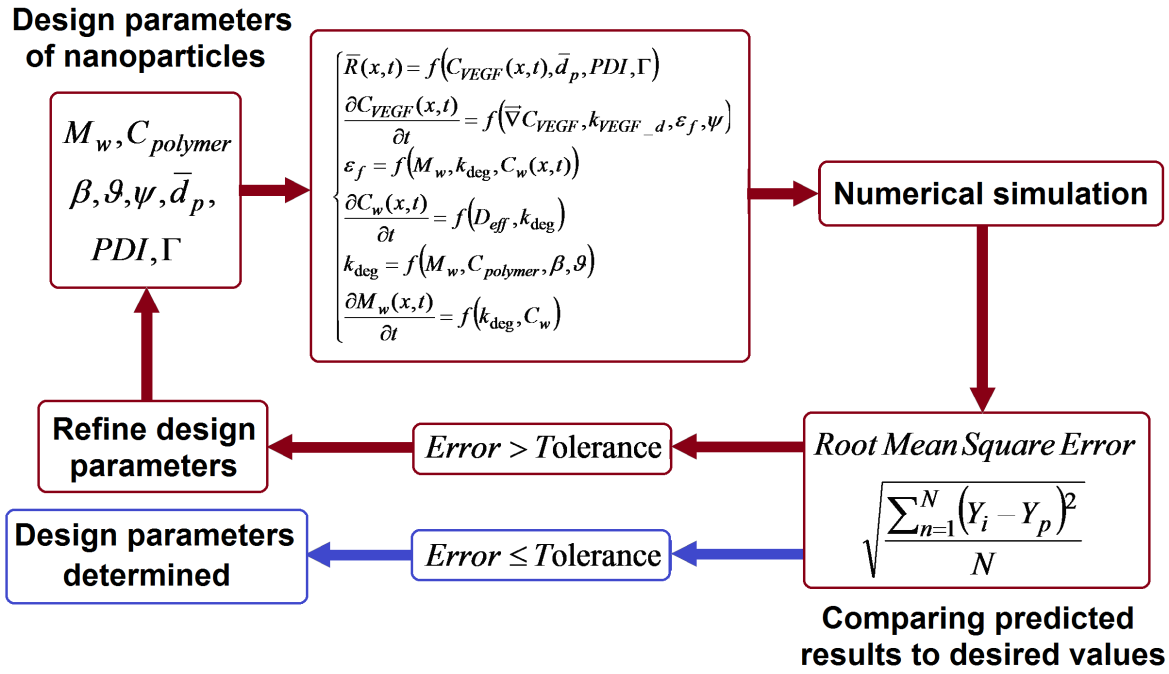

Figure 2.6. Computational procedure to predict optimum design parameters of nanoparticles for a smart bioactive scaffold using a mechanistic model of controlled release

from the simulation are then compared to those of the desired VEGF release profile(s), which can be determined from experimental studies (see Table 2.2) or estimated based on the average rate of vascularization in response to VEGF concentration gradient [131]. If the discrepancy between the predicted and desired values is greater than a tolerance, the design parameters will be refined based on an optimization algorithm, and the numerical simulation and prediction assessment will be performed again. This computational process will continue until the simulation results converge to the desired spatiotemporal variation of VEGF release profile where the optimum design parameters of the VEGF-loaded nanoparticles are obtained (Fig. 2.6).

2.6. Actively controlled GF release from nanoparticles

The concept of actively controllable nanoparticles owes to the behaviour of responsive polymers that can undergo large conformational changes in response to environmental stimuli such as temperature, pH, particular chemicals, and enzymes. The environmentally induced changes in nanoparticle polymeric structure and physicochemical properties affect the mechanisms of release involved in GF release process. Thus, external and internal stimuli can be used to manipulate GF release characteristics of polymeric nanoparticles performing as actively controlled particulate delivery systems in smart tissue engineered scaffolds. Most important triggering systems that can be used for modulating the release rate of GFs from triggerable nanoparticles are magnetic field resonance, radio frequency and microwave, ultrasound, radiation, enzyme-substrate interaction, ion-substrate interaction, and cellular metabolites. The externally controlled GF release systems are provided in this section.

2.6.1. pH-responsive delivery systems

Acidic and basic conditions caused by cellular activities or enzymatic reactions in biological microenvironment can be used for triggering the release of bioactive compounds in tissue

engineering. When the microenvironmental pH reaches a certain level, pH responsive polymers of delivery systems undergo conformational changes leading to the release of GFs that are entrapped or encapsulated by the polymeric particles. These polymeric delivery vehicles are stable in physiological pH but their stability declines due to protonation or deprotonation of polymer functional groups in acidic and basic microenvironments, respectively. Also, the sensitivity of swelling and de-swelling characteristics of these polymers is an important factor contributing to actively controlling the release rate of bioactive compounds in response to the local pH [134]. Matsusaki and Akashi (2005) successfully used a pH-sensitive biopolymer composing of poly(gamma-glutamic acid) and sulfonated gamma-poly(glutamic acid) with variable de-swelling properties at a pH ranging between 2.0 and 6.0 to regulate the release rate of bFGF [135]. Kim et al. (2009) developed a thermo/pH sensitive sulfamethazine oligomer-poly(epsilon-caprolactone-co-lactide)-poly(ethylene glycol)-poly(epsilon-caprolactone-co-lactide) (SMO-PCLA-PEG-PCLA) that could respond to basic microenvironment (pH=8.0) by transforming from gel to sol at 37°C [136]. Poly(acrylic acid), poly(methacrylic acid), poly(2-ethyl acrylic acid), and poly(2-propyl acrylic acid) are the most investigated pH-responsive polyacids [137, 138], and poly(N,N-dimethyl aminoethyl methacrylate), poly(N,N-diethyl aminoethyl methacrylate), poly(4-vinylpyridine), and poly(vinyl imidazole) are the most studied pH-responsive polybases [139].

2.6.2. Temperature-triggered delivery systems

Temperature has been one of the most important triggering stimuli in triggerable controlled release systems. The triggering mechanism is based on characteristics of thermo-responsive polymers that undergo a significant phase separation at a critical temperature called lower critical solution temperature (LCST) and an upper critical solution temperature (UCST), below and

above which, respectively, the thermosensitive polymers are completely miscible in the hydrophilic microenvironment [122]. Table 2.5 presents well-known thermo-responsive polymers with their LCST and biocompatibility, biodegradability and toxicity characteristics

Table 2.5. Biocompatibility, biodegradability, cytotoxicity, and LCST characteristics of well-known thermo-responsive polymers [144].

	Biocompatibility	Biodegradability	Biotoxicity	LCST(°C)
PNIPAAm	Lack	High	Unknown	32-37
PEG-PPO-PEO[1]	Unknown	High	Low	5-30
PEG-PLGA-PEG[2]	High	High	Unknown	30-35
PMPA[3]	Unknown	Unknown	Unknown	50.6
PNVCL[4]	High	High	Low	32-34
EPG[5]	High	Unknown	Low	32-42
PLGA-PEG-PLGA[6]	High	High	Unknown	37

[1]Poly(ethylene oxide-b-propylene oxide-b-ethylene oxide), [2]poly(ethylene glycol-b-(lactic acid-co-glycolic acid)-b-ethylene glycol), [3]poly(methyl 2-propionamidocrylate), [4]poly(N-vinylcaprolactam), [5]Eudragit RS and polyethylene glycol blend, [6]poly(lactic acid-co-glycolic acid-b-ethylen glycol-b-lactic acid-co-glycolic acid)

[140]. Among these polymers, poly(N-isopropylacrylamide) (PNIPAAm) is a highly popular thermo-responsive polymer which can be modulated for different LCST close to body temperature (32-39°C); however, low biocompatibility and potential cytotoxicity of the monomers has been drawbacks for using this polymer in tissue engineering. Figure 2.7 schematically illustrates the conformational changes in a thermo-responsive polymeric particle loaded with a bioactive compound. Upon increasing the temperature above LCST, the particle shrinks due to the polymer precipitation leading to a positive internal pressure in pores pumping the entrapped GFs to the surrounding environment (Fig. 2.7).

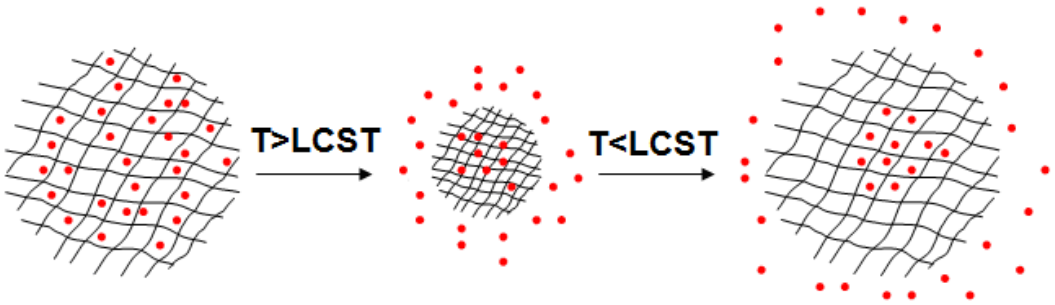

Figure 2.7. Schematic diagram of temperature-triggered release of GFs from a thermo-responsive polymeric particle.

Magnetic resonance (MR), radio frequency (RF) wave, microwave (MW), and ultrasound are typically external triggering systems to induce temperature rise in thermo-responsive particulate delivery vehicles to trigger GF release within implanted tissue scaffolds (Fig. 2.8a-c). In brief, the energy associated with MR, RF (500 kHz, 500 MHz), MW (>3 GHz), and ultrasound (20-100 kHz) energy is partially absorbed by the polymeric particles while propagating in the tissue. Energy absorption agents such as superparamagnetic materials (10-20 nm) (e.g Fe_3O_4 (ferrite) and γ -Fe_2O_3 (maghemite)) for MR heating and 1.4 nm gold nanocrystals for RF/MW heating are incorporated in the core of the thermo-sensitive particulate delivery systems to promote the efficiency of the energy absorption by the particulate delivery vehicles (Fig. 2.8d). The energy absorption in the core induces temperature rise in the thermo-sensitive polymeric particles that undergo conformational changes and release GFs when the temperature exceeds LCST (Fig. 2.8d).

Such triggering systems can be used for coordinating multiple GF release from particulate delivery systems that include thermo-responsive polymers with different LCST. As shown in Fig. 2.8e, three types of thermo-sensitive polymeric particles loaded with GFs can release three

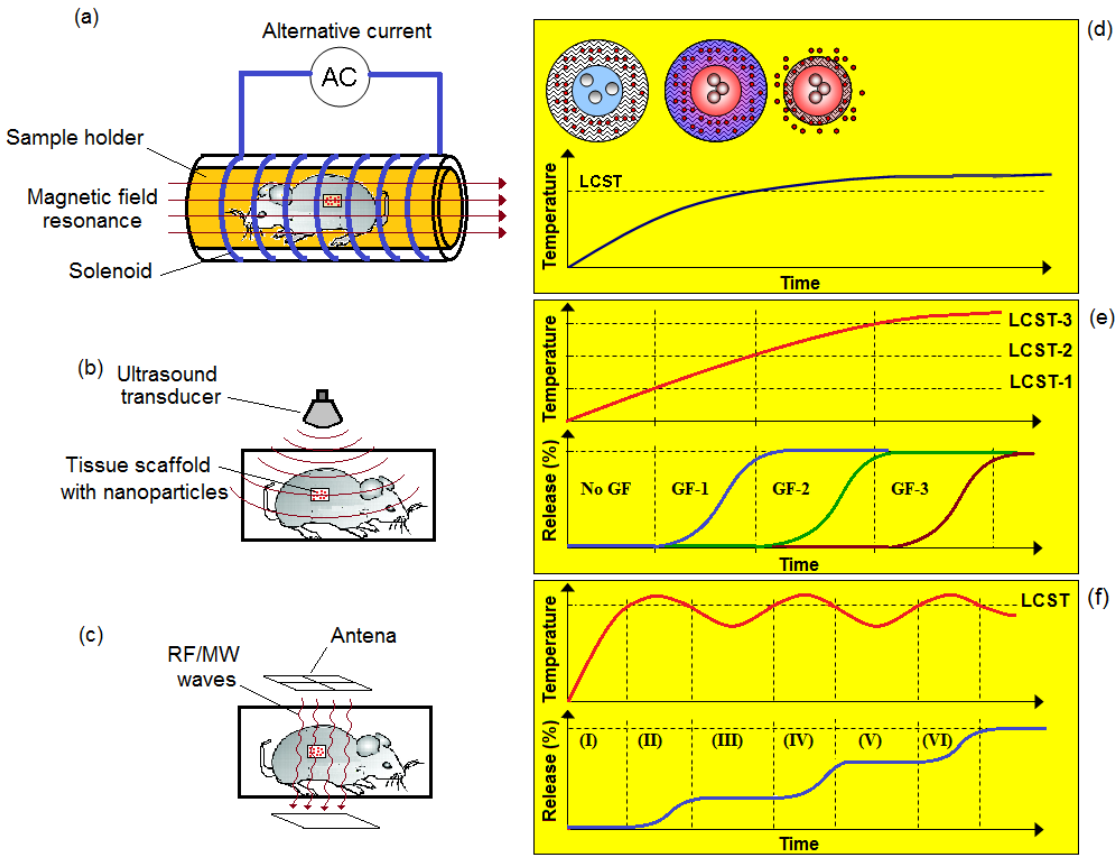

Figure 2.8. Ultrasound (a), RF/MW (b) and MR (c) triggering strategies, and schematic diagrams for thermo-responsive delivery vehicle behaviour (d), stage-wise GF release (e), and temporal control of GF release (f).

different types of GFs in a stage-wise fashion when the temperature of particles reaches their associated LCST with time. Furthermore, in a scaffold with a thermo-responsive polymeric particulate delivery system, the release of a GF can be temporally controlled by oscillating the external stimuli (MR, RF/MW, ultrasound) leading to fractional release of GF during tissue regeneration within the scaffold (Fig. 2.8f). Experimental and computational studies on RF-induced heating of chitosan scaffolds for controlling spatiotemporal temperature distribution within implanted scaffolds have been recently done by Izadifar and Chen (2012) [141]. The heat transfer simulation results from their study suggest that periodic RF heating of chitosan scaffolds

can be potentially used to temporally trigger GF release from thermo-responsive polymeric particulate delivery system in the scaffolds. For some particular tissue engineering applications where the release of a large dose of GF (e.g. VEGF) must be prevented, the temporally controlled release fashion allows for regulating the dose of GFs *in-situ*.

2.6.3. Light-triggerable delivery systems

Ultraviolet (UV) and visible lights can be used for externally controlling GF release from nanogels within tissue scaffolds. UV radiation can induce phase transition in the gels accompanied by reversible volume changes that can be used for releasing GFs entrapped within the nanogels [142]. Also, embedding light-absorbing chromophores in the core of nanogels makes the polymeric nanoparticles visible-light responsive. Depending on the intensity of the light, chromophores generate heat and increase the gel temperature altering nanogel swelling rate based on which GF release rate from the nanogels are controlled. The major drawbacks of light-triggering are associated with low penetration depth of UV and visible light that are largely absorbed by the skin. In contrast, near-infrared (NIR) radiation has proven to be a promising tool for triggering nano-particulate delivery vehicles within 650-900 nm wavelength [143]. Gold nanorodes [144], gold nanoshells [145], and gold nanocages [146] are NIR-energy absorption agents that can be used for tuning NIR-induced heating of polymeric particulate delivery systems to release GFs within the implanted scaffolds. GF-loaded gold nanocages coated with a thermo-sensitive polymer (i.e. PNIPAAm) can entrap GFs inside the cage as the polymer closes the pores of the nanocage. After implantation of a tissue scaffold that includes the gold nanocages, the site of implantation is exposed to a predetermined dose and exposure time of NIR (Fig. 2.9) where gold nanocages absorb NIR radiation that generates heat and causes polymer precipitation

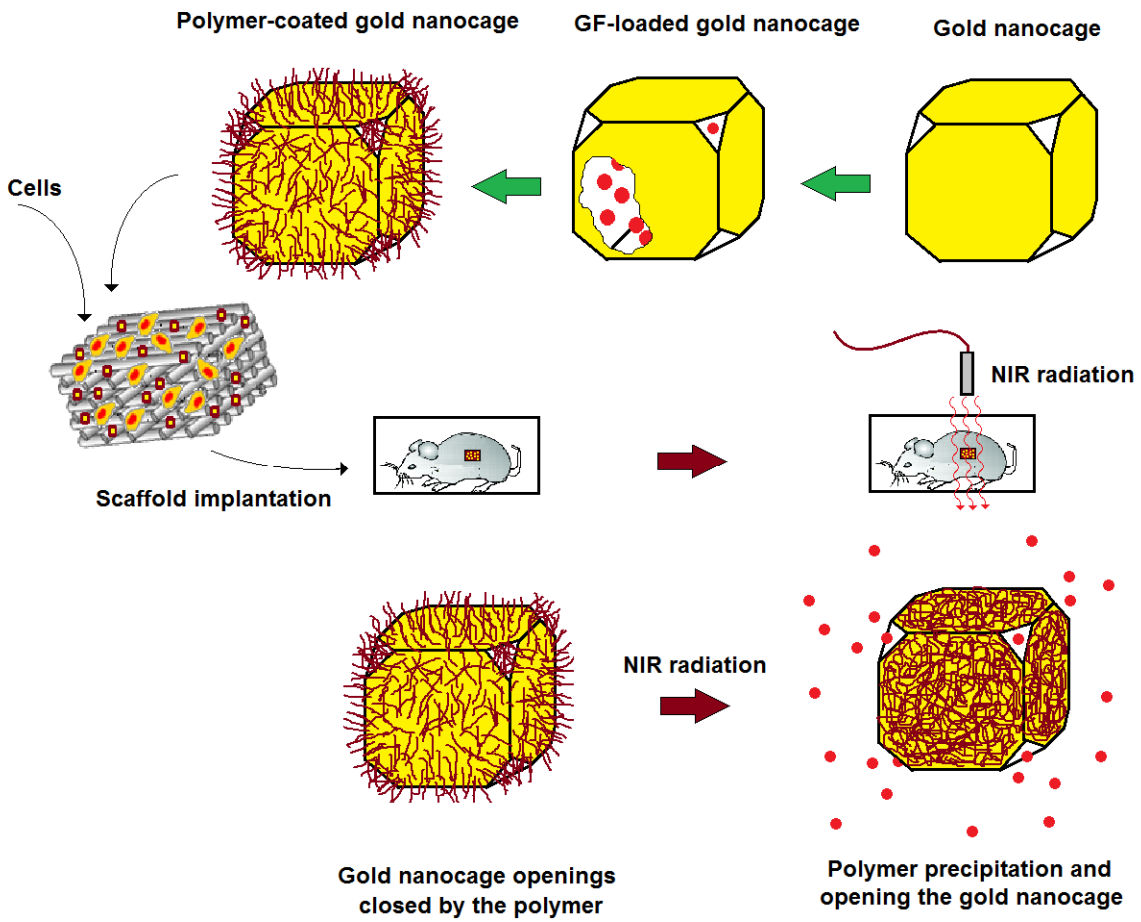

Figure 2.9. Light-triggering of GF release using NIR radiation and polymer coated gold nanocage.

opening the nanocage pores leading to GF release into the scaffold microenvironment (Fig. 2.9). The applied power of radiation must be adjusted to avoid tissue damage.

2.7. Spatiotemporal control of GF release in smart scaffolds

The complex processes of cell migration, differentiation and proliferation typically rely on both the presence of particular GFs, and their time-dependent and spatial distributions. For example, the first step of angiogenesis demands VEGF, FGF and Ang-2 to destabilize pre-existing blood vessels, and to promote the proliferation and migration of endothelial cells to form new immature vessels. Next, Ang-1 and PDGF-BB stabilize these newly formed tubes to become

mature blood vessels [147, 148]. Sequential and simultaneous delivery of these GFs has been shown to enhance vascularization [149, 150]. Despite the significance of such GF delivery systems, designing and optimization of spatiotemporal delivery strategies in regenerative medicine remain a challenge that requires an interdisciplinary cooperation among cell biologists, biomaterial scientists, tissue engineers and clinicians. In this context, rate-programming of nanoparticles including pre-programmed polymeric nanoparticles or actively controlled delivery systems play a critical role in developing spatiotemporal control of GF release in the cellular micro-environments.

A number of local delivery and spatial gradient systems have been developed for spatial control delivery of GFs; however, few studies met the challenge to construct tissue-engineered scaffolds to deliver spatial GF concentration gradient. A recently successful approach has been reported by Chen et al. (2007) who prepared several scaffolds composed of layered biomaterials incorporating different amounts of GFs to provide spatially localized and temporally controlled release of GFs [150, 151]. An important issue related to the scaffold-based GF release is associated with the release of GFs to the outside of defects that might induce unpredictable outcomes; thus spatial control of GF delivery should prevent or reduce the GF release into the surrounding healthy tissues [152].

Several approaches including direct adsorption of GFs to biomaterials, blending GF-loaded microspheres into the scaffolds, and covalently conjugating GFs to the scaffold polymers have been studied for controlling spatial distribution of GFs within tissue engineered scaffolds [153]. Burst release and low loading efficiency are the major disadvantages of direct adsorption while incorporation of GF-loaded particulate delivery system into the scaffold biomaterials provides more control over GF release because the release pattern can be controlled not only by the

scaffold degradation but also by rate-programming of nanoparticulate delivery system. Yilgor et al. (2009) incorporated BMPs-loaded nanoparticles into/on 3D fiber tissue engineered scaffolds made of chitosan and chitosan-poly(ethyleneoxide) (PEO), and found that BMPs retained their bioactivities and exhibited different release profiles by releasing the GF from the scaffold to fiber first, and then to media [154]. Kim et al. (2006) rate-programmed PLGA nanoparticles by conjugating heparin to PLGA nanospheres to achieve long-term, zero-order delivery of bFGF. The release of bFGF from the heparin conjugated nanospheres could be sustained for more than 1 month when the nanospheres were suspended in fibrin gel; and the bFGF release from the fibrin gel was controllable by the fibrinogen concentration [155]. Recently, White et al. (2013) developed a novel particulate delivery system made of a hydrophilic PLGA-PEG-PLGA triblock copolymer with 50:50 and 85:15 PLGA to provide customisable, localised and controlled delivery with adjustable release profiles of BMP-2, PDGF and VEGF [156]. Rate-programming of the proposed delivery system was performed by mixing two different formulations in order to modulate the release kinetics of the GFs [156]. Li et al. al (2011) also developed a double-layered collagen delivery system for spatiotemporal control over GF delivery [157]. A dense layer and a loose layer which incorporated bFGF-loaded chitosan-heparin nanoparticles enabled spatiotemporal control of release process such that the release of protein in undesired direction was lessened [157]. Furthermore, different release amounts of bFGF from the different layers of the membrane resulted in significant difference in cell proliferation when the cells were seeded on the different layers of the membrane *in-vitro*[157]. Rate-programming this type of double-layered collagen membrane can be potentially used for controlling time-dependent and spatial distribution of GFs in regenerative medicine. Several fabrication methods for preparation of double and multi-layered particulate delivery systems have been reported [158-164].

Furthermore, collagen structure, which can be influenced by preparation conditions such as freezing, drying and/ or cross-linking conditions [165, 166], can affect the release of loaded GFs. De Paoli Lacerda et al. (2005) studied the release characteristics of fluorescent substances which bonded covalently with collagen, and found a clear correlation between the release profile and the structure of the collagen gels [167]. Therefore, the structure of collagen matrix can also be used as a factor for rate-programming the particulate delivery systems to provide a spatiotemporal control of GF during tissue regeneration.

Recently, Ishizuka et al. (2014) developed a spatiotemporal method to control molecular function by using silica-based photodegradable nanoparticles [168]. They used a short-term light irradiation (20 s) to trigger the release of encapsulated molecules from the network of the nanoparticle gel [168]. The nanoparticles prepared under mild conditions can be useful to control the spatiotemporal release of GFs in tissue-engineered scaffolds containing the nanoparticles by adjusting the time and location of the light exposure to the scaffold. Furthermore, stimuli responsive nanoparticles that have been increasingly gaining more attentions in the field of smart scaffolds can also be used to engineer signalling networks and spatial self-organization inside a cell environment. Recently, Hoffmann et al. (2014) conjugated magnetic nanoparticles to key regulatory proteins in order to spatiotemporally control the Ran/RCC1 signalling pathway that regulates the cell cytoskeleton [169]. RanGTP proteins conjugated to superparamagnetic nanoparticles were able to provide microtubules to assemble into asymmetric arrays of polarized fibres in the presence of a magnetic field [169].

Rapid developments in 3D printing techniques for scaffold fabrication are opening a new window towards precisely controlled release of GFs within tissue engineered scaffolds. Different GFs can be pre-loaded into micro/nanospheres which are entrapped in dispensable hydrogels

(e.g. alginate) to be used in a 3D bioplotter for fabrication of scaffolds. Micro/nanoparticles, made of appropriately selected biopolymers and loaded with different amounts of multiple GFs, are entrapped into a hydrogel that will be precisely printed into a 3D scaffold layer-by-layer leading to spatially customized GF release profiles in each layer of the scaffold. The release characteristics can be modified by rate-programming of particulate delivery system according to physicochemical properties of the micro/nanoparticles. Also, when the GF-loaded particles are stimuli responsive, time-dependent and spatial GF release can be controlled using external stimuli (e.g. MR, light). Thus, if the size of nanoparticles is large enough to avoid diffusing away from one location to another, spatial and temporal presentation patterns of multiple GFs may be theoretically achieved [170].

2.8. Challenges and future directions

The ultimate goal of smart GF delivery systems is to mimic the biological release patterns of GFs to effectively orchestrate tissue regeneration in a tissue scaffold. However, the development of such delivery systems is facing significant challenges. The optimum dose and release profile of different GFs that are involved in various types of tissue regeneration have not been well characterized yet. Despite immense studies on GF-based tissue engineering, the number of systematic investigations focusing on characterization of optimum GF presentation patterns for various tissue regeneration therapies is very limited. Such information is essential to the rate-programming of GF release profiles in tissue engineered scaffolds. Furthermore, due to the various types of GFs that require different release patterns in different issue regenerative applications, particulate delivery systems need to provide sufficient flexibilities in modulating the spatial and temporal release characteristics of GFs.

Spatially micro-patterning of 3D tissue engineered scaffolds incorporated with rate-programmed nanoparticles demands further investigation to promote the scaffold bio-functionality to closely mimic native ECM.

A comprehensive characterization of physicochemical, architectural and structural characteristics of particulate delivery systems, and a good understanding of the relationship between release kinetics of GFs and the critical characteristics of polymeric nanoparticles are essential for optimization and development of smart GF delivery systems. In this context, development of sophisticated mathematical models, which are powerful and efficient tools for prediction and optimization of GF release patterns from nanoparticles, is of critical importance. Moreover, comprehensive experimental and computational studies need to be conducted for optimization of nanoparticle fabrication variables that influence physicochemical characteristcs of the nanoparticles. Furthermore, it is crucially important to develop biologically active nanoparticles that enable time-delayed release of GFs, which is essential for sequential release of multiple GFs for cardiac tissue regeneration and vascularization. Besides, along with the experimental studies, novel computational models are needed for pre-programming of GF release rates of nanoparticulate delivery systems incorporated with 3D-printable hydrogels for bioactive hydrogel-based cardiac constructs in myocardium tissue engineering.

Also, further studies on the development of novel stimuli responsive biopolymers that possess high biocompatibility, no cytotoxicity and slow conformational changes upon stimulation are required.

References

[1] Dhandayuthapani, B, Yoshida Y, Maekawa T and Kumar S D 2011 Polymeric Scaffolds in Tissue Engineering Application: A Review Int. J. Polym. Sci. **2011** 1-19.

[2] Atala A 2012 Regenerative medicine strategies J. Pediatr. Surge. **47** 17.

[3] Le-Huu A, Paul A, Xu L, Prakash S and Shum-Tim D 2013 Recent advancements in tissue engineering for stem cell-based cardiac therapies Ther Deliv. **4** 503.

[4] Cross M and Dexter T M 1991 Growth factors in development, transformation, and tumorigenesis Cell **64** 271.

[5] Schulte V A, Hahn K, Dhanasingh A, Heffels K H and Groll J 2014 Hydrogel–fibre composites with independent control over cell adhesion to gel and fibres as an integral approach towards a biomimetic artificial ECM Biofabrication **6** 4106.

[6] Shevach M, Soffer-Tsur N, Fleischer S, Shapir A and Dvir T 2014 Fabrication of omentum-based matrix for engineering vascularized cardiac tissues. Biofabrication **6** 4101.

[7] Lee J S, Hong J M, Jung J W, Shim J H, Oh J H and Cho D W 2014. 3D printing of composite tissue with complex shape applied to ear regeneration. Biofabrication **6** 024103.

[8] Kim P, Yuan A, Nam K H, Jiao A and Kim D H. Fabrication of poly(ethylene glycol): gelatin methacrylate composite nanostructures with tunable stiffness and degradation for vascular tissue engineering. Biofabrication **6** 024112.

[9] Galler K M, Hartgerink J D, Cavender A C, Schmalz G and D'Souza R N 2012 A Customized Self-Assembling Peptide Hydrogel for Dental Pulp Tissue engineering.Tissue Eng Part A. **18** 176–84.

[10] Hussain A, Collins G, Yip D and Cho CH 2013 Functional 3-D cardiac co-culture model using bioactive chitosan nanofiber scaffolds. Biotechnol Bioeng **110** 637-47

[11] Jiang T, Kumbar S G, Nair L S, Laurencin CT 2008 Biologically active chitosan systems for tissue engineering and regenerative medicine. Curr Top Med Chem. **8** 354-64.

[12] Hayashi Y, Yamada S, Yanagi Guchi K, Koyama and Ikeda T 2012 Chitosan and fish collagen as biomaterials for regenerative medicine. Adv. Food Nutr. Res. **65** 107-20

[13] Bryant S J and Anseth K S 2002 Hydrogel properties influence ECM production by chondrocytes photoencapsulated in poly(ethylene glycol) hydrogels. J. Biomed. Mater. Res., **59** 63–72.

[14] Woodfield T B, Van Blitterswijk C A, De Wijn J, Sims T J, Hollander A P and Riesle J 2005 Polymer scaffolds fabricated with pore-size gradients as a model for studying the zonal organization within tissue-engineered cartilage constructs. Tissue Eng. **11** 1297–1311.

[15] Li W J, Jiang Y J and Tuan R S 2006 Chondrocyte phenotype in engineered fibrous matrix is regulated by fiber size. Tissue Eng. **12** 1775–85.

[16] Seeherman H and Wozney J M 2005 Delivery of bone morphogenetic proteins for orthopedic tissue regeneration. Cytokine Growth Factor Rev. **16** 329–45.

[17] Hynes R O 2002 Integrins: bidirectional, allosteric signaling machines. Cell. **110** 673–87.

[18] Giancotti F G 2000 Complexity and specificity of integrin signalling. Nat. Cell Biol. **2** E13–14.

[19] Lee K, Silva E A and Mooney D J 2011 Growth factor delivery-based tissue engineering: general approaches and a review of recent developments. J. R. Soc. Interface. **8** 153-70.

[20] Nimni M E 1997 Polypeptide growth factors: targeted delivery systems. Biomaterials **18** 1201-25.

[21] Mark Saltzman W, Baldwin S P 1998 Materials for protein delivery in tissue engineering. Adv. Drug Deliv. Rev. **33** 71-86.

[22] Cleland J L, Duenas E T, Park A, Daugherty A, Kahn J, Kowalski J and Cuthbertson A 2001 Development of poly-(D,Llactide-coglycolide) microsphere formulations containing recombinant human vascular endothelial growth factor to promote local angiogenesis. J. Control. Release **72** 13–24.

[23] Chiu L L, Radisic M 2010 Scaffolds with covalently immobilized VEGF and Angiopoietin-1 for vascularization of engineered tissues. Biomaterials **31** 226-41.

[24] Karal-Yilmaz O, Serhatli M, Baysal K, Baysal BM 2011 Preparation and in vitro characterization of vascular endothelial growth factor (VEGF)-loaded poly(D,L-lactic-co-glycolic acid) microspheres using a double emulsion/solvent evaporation technique. J Microencapsul. **28** 46-54.

[25] Singh S, Wu B M and Dunn J C 2011 The enhancement of VEGF-mediated angio-genesis by polycaprolactone scaffolds with surface cross-linked heparin. Biomaterials **32** 2059-69.

[26] Golub J S, Kim Y T, Duvall C L, Bellamkonda R V, Gupta D, Lin A S, Weiss D, Robert Taylor W and Guldberg R E 2010 Sustained VEGF delivery via PLGA nanoparticles promotes vascular growth. Am. J. Physiol. Heart. Circ. Physiol. **298** H1959-65.

[27] Zieris A, Prokoph S, Levental K R and Welzel P B, Grimmer M, Freudenberg U and Werner C 2010 FGF-2 and VEGF functionalization of starPEG-heparin hydro-gels to modulate biomolecular and physical cues of angiogenesis. Biomaterials **31** 7985-94.

[28] Silva E A and Mooney D J 2010 Effects of VEGF temporal and spatial presentation on angiogenesis. Biomaterials **31** 1235-41.

[29] Nagai N, Kumasaka N, Kawashima T, Kaji H, Nishizawa M and Abe T 2010 Preparation and characterization of collagen microspheres for sustained release of VEGF. J Mater Sci Mater Med. **21** 1891-98.

[30] Parajo Y, D'Angelo I, Welle A, Garcia-Fuentes M and Alonso M J 2002 Hyaluronic acid/Chitosan nanoparticles as delivery vehicles for VEGF and PDGF-BB. Drug Deliv.**17** 596-604.

[31] Raschke M, Wildemann B, Inden P, Bail H, Flyvbjerg A, Hoffmann J, Haas N P, and Schmidmaier G 2002 Insulin-like growth factor-1 and transforming growth factor-beta1 accelerates osteotomy healing using polylactide-coated implants as a delivery system: a biomechanical and histological study in minipigs. Bone. **30** 144-51.

[32] Lee J Y, Nam S H, Im S Y, Park Y J, Lee Y M, Seol Y J, Chung C P, and Lee S J 2002 Enhanced bone formation by controlled growth factor delivery from chitosan-based biomaterials. J. Control. Release **78** 187–197.

[33] Wang X, Wenk E, Zhang X, Meinel L, Vunjak-Novakovic G and Kaplan D L 2009. Growth Factor Gradients via Microsphere Delivery in Biopolymer Scaffolds for Osteochondral Tissue Engineering. J. Control Release. **134** 81-90.

[34] Phipps M C, Xu Y, Bellis S L 2012 Delivery of Platelet-Derived Growth Factor as a Chemotactic Factor for Mesenchymal Stem Cells by Bone-Mimetic Electrospun Scaffolds. PLoS ONE **7** e40831.

[35] Mierisch C M, Cohen S B, Jordan L C, Robertson P G, Balian G and Diduch D R 2002 Transforming growth factor-beta in calcium alginate beads for the treatment of articular cartilage defects in the rabbit. Arthroscopy **18** 892–900.

[36] Chuang W Y, Young T H and Yao C H 1999 Properties of the poly (vinyl alcohol) / chitosan blend and its effect on the culture of fibroblast in vitro. Biomaterials **20** 1479-87.

[37] Graeme I H, Dettmar P W, Goddard P A, Hampsor F C, Michael D, Edward J W 2001 The effect of chitin and chitosan on the proliferation of human fibroblasts and keratinocytes in vitro. Biomaterials **22** 2959-66.

[38] Gokce A, Yilmaz I, Bircan R, Tonbul M, Gokay N S and Gokce C 2012 Synergistic Effect of TGF-β1 And BMP–7 on Chondrogenesis and Extracellular Matrix Synthesis: An In Vitro Study. The Open Orthop. J. **6** 406-13.

[39] Ulubayram K, Nur Cakar A, Korkusuz P, Ertan C, and Hasirci N 2001 EGF containing gelatin-based wound dressings. Biomaterials **22** 1345–56.

[40] Mizuno K, Yamamura K, Yano K, Osada T, Saeki S, Takimoto N, Sakurai T and Nimura Y 2003 Effect of chitosan film containing basic fibroblast growth factor on wound healing in genetically diabetic mice. J. Biomed. Mater. Res. **64** 177–181.

[41] Niu X, Feng Q, Wang M, Guo X and Zheng Q 2009 Porous nano-HA/collagen/PLLA scaffold containing chitosan microspheres for controlled delivery of synthetic peptide derived from BMP-2. J. Control Release. **134** 111-7.

[42] Hildebrand K A, Woo S L., Smith D W, Allen C R, Deie M, Taylor B J and Schmidt C C 1998 The effects of platelet-derived growth factor-BB on healing of the rabbit medial collateral ligament: an in vivo study. Am. J. Sports Med. **26** 549–54.

[43] Blattert T R, Delling G, Dalal P S, Toth C A, Balling H and Weckbach A 2002 Successful transpedicular lumbar interbody fusionby means of a composite of osteogenic protein-1 (rhBMP-7) and hydroxyapatite carrier: a comparison with autograft and hydroxyapatite in the sheep spine. Spine **27** 2697–05.

[44] Hunziker E B, Driesang I M and Morris E A 2001 Chondrogenesis in cartilage repair is induced by members of the transforming growth factor-beta superfamily. Clin. Orthop. Relat. Res., **391** S171–181.

[45] Holland T A, Tabata Y, Mikos A G 2005 Dual growth factor delivery from degradable oligo(poly(ethylene glycol) fumarate) hydrogel scaffolds for cartilage tissue engineering. J. Control. Release. **101** 111–125.

[46] Lee J and Lee K Y 2009 Local and sustained vascular endothelial growth factor delivery for angiogenesis using an injectable system. Pharm. Res.**26** 1739–44.

[47] Silva E A and Mooney D J 2010 Effects of VEGF temporal and spatial presentation on angiogenesis. Biomaterials **31** 1235.

[48] Tengood J E, Kovach K M, Vescovi P E, Russell A and Little S R 2010 Sequential Delivery of Vascular Endothelial Growth Factor and Sphingosine 1-Phosphate for Angiogenesis. Biomaterials **31** 7805–12.

[49] Bai Y, Li P, Yin G, Huang Z, Liao X, Chen X, Yao Y 2013 BMP-2, VEGF and bFGF synergistically promote the osteogenic differentiation of rat bone marrow-derived mesenchymal stem cells. Biotechnol Lett. **35** 301-8.

[50] Ikeuchi M, Dohi Y, Horiuchi K, Ohgushi H, Noshi T, Yoshikawa T, Yamamoto K and Sugimura M 2002 Recombinant human bone morphogenetic protein-2 promotes osteogenesis within atelopeptide type I collagen solution by combination with rat cultured marrow cells. J. Biomed. Mater. Res. **60** 61–69.

[51] Silva A K, Richard C, Bessodes M, Scherman D and Merten O W 2009 Growth factor delivery approaches in hydrogels. Biomacromolecules **10** 9–18.

[52] Schense J C and Hubbell J A 1999 Cross-linking exogenous bifunctional peptides into fibrin gels with factor XIIIa. Bioconjug. Chem. **10** 75–81.

[53] Sakiyama-Elbert S E, Panitch A and Hubbell J A 2001 Development of growth factor fusion proteins for cell-triggered drug delivery. FASEB J. **15** 1300–02

[54] Schmoekel H G, Weber F E, Schense J C, Gratz K W, Schawalder P and Hubbell J A 2005 Bone repair with a form of BMP-2 engineered for incorporation into fibrin cell ingrowth matrices. Biotechnol. Bioeng. **89** 253–62.

[55] Nillesen S T, Geutjes P J, Wismans R, Schalkwijk J, Daamen W F and Van Kuppevelt T H 2007 Increased angiogenesis and blood vessel maturation in acellular collagen-heparin scaffolds containing both FGF2 and VEGF. Biomaterials **28** 1123–31

[56] Yoon J J, Chung H J and Park T G 2007 Photocrosslinkable and biodegradable Pluronic/heparin hydrogels for local and sustained delivery of angiogenic growth factor. J. Biomed. Mater. Res. A **83** 597–605.

[57] Lin C C and Anseth K S 2009 Controlling affinity binding with peptide-functionalized poly(ethylene glycol) hydrogels. Adv. Funct. Mater. **19** 2325.

[58] Lin C C, Boyer P D, Aimetti A A and Anseth K S 2010 Regulating MCP-1 diffusion in affinity hydrogels for enhancing immuno-isolation. J. Control. Release b 384–91

[59] Soontornworajit B, Zhou J, Shaw M T, Fan T H and Wang Y 2010 Hydrogel functionalization with DNA aptamers for sustained PDGF-BB release. Chem. Commun. **46** 1857–59.

[60] Ito Y 2008 Covalently immobilized biosignal molecule materials for tissue engineering. Soft Matter. **4** 46–56.

[61] Zhang L, Zhou Y, Li G, Zhao Y, Gu X and Yang Y 2014 Nanoparticle mediated controlled delivery of dual growth factors. Sci. China Life Sci. **57** 256-62.

[62] Wang H, Zou Q, Boerman O C, Nijhuis A W, Jansen J A, Li Y, Leeuwenburgh S C 2013 Combined delivery of BMP-2 and bFGF from nanostructured colloidal gelatin gels and its effect on bone regeneration in vivo. J. Control Release. **166** 172-81.

[63] Dyondi D, Webster T J and Banerjee R 2013 A nanoparticulate injectable hydrogel as a tissue engineering scaffold for multiple growth factor delivery for bone regeneration. Int. J. Nanomedicine. **8** 47-59.

[64] Choi D H, Park C H, Kim I H, Chun H J, Park K and Han D K 2010 Fabrication of core-shell microcapsules using PLGA and alginate for dual growth factor delivery system. J. Control Release. **147** 193e201.

[65] Ahmad Z, Zhang H B, Farook U, Edirisinghe M, Stride E and Colombo P 2008 Generation of multilayered structures for biomedical applications using a novel tri-needle coaxial device and electrohydrodynamic flow. J. R. Soc. Interface. **5** 1255e61

[66] Lee Y H, Bai M Y and Chen D R 2011 Multidrug encapsulation by coaxial tri-capillary electrospray. Colloids Surf. B Biointerfaces **82** 104e10.

[67] Kim W and Kim S S 2011 Synthesis of biodegradable triple-layered capsules using a triaxial electrospray method. Polymer **52** 3325e36.

[68] Lee W L, Hong M, Widjaja E and Loo S C 2010 Formation and degradation of biodegradable triple-layered microparticles. Macromol. Rapid Commun. **31** 1193e200.

[69] Lee W L, Widjaja E Loo S C 2012 Designing drug-loaded multi-layered polymeric microparticles. J. Mater. Sci. Mater. Med. **23** 81e8.

[70] Lee W L, Yu P O, Hong M, Widjaja E and Loo S C 2012 Designing multilayered particulate systems for tunable drug release profiles. Acta Biomater. **8** 2271e8.

[71] Wong H M, Wang J J and Wang C H 2001 In vitro sustained release of human immunoglobulin G from biodegradable microspheres. Ind. Eng. Chem. Res. **40** 933.

[72] Kim, H.K., Chung, H.J., Park, T.G 2006 Biodegradable polymeric microspheres with "open/closed" pores for sustained release of human growth hormone. J. Control. Release **112** 167.

[73] Sun Y, Wang J C, Zhang X, Zhang Z, Zheng Y, Chen D W 2008 Zhang Q Synchronic release of two hormonal contraceptives for about one month from the PLGA microspheres: in vitro and in vivo studies. J. Control. Release. **129** 192.

[74] Shah S S, Cha Y and Pitt C G 1992 Poly(glycolic acid-co-dl-lactic acid): diffusion or degradation controlled drug delivery. J. Control. Release **18** 261.

[75] Jonnalagadda S and Robinson D H 2000 A biodegradable, polylactide reservoir for diffusional and osmotically controlled drug delivery. AAPS PharmSciTech. **1** 26.

[76] Mochizuki A, Niikawa T, Omura I and Yamashita S 2008 Controlled Release of argatroban from PLA film-effect of hydroxylesters as additives on enhancement of drug release. J. Appl. Polym. Sci. b 3353.

[77] Gagliardi M, Silvestri D, Cristallini C, Guadagni M, Crifaci G and Giusti P 2010 Combined drug release from biodegradable bilayer coating for endovascular stents. J. Biomed. Mater. Res. Part B: Appl. Biomater. **93** 375-85.

[78] Kang J and Schwendeman S P 2007 Pore closing and opening in biodegradable polymers and their effect on the controlled release of proteins. Mol. Pharm. **4** 104.

[79] Park T G 1995 Degradation of poly(lactic-co-glycolic acid) microspheres: effect of copolymer composition. Biomaterials **16** 1123.

[80] Matsumoto A, Matsukawa Y, Horikiri Y and Suzuki T 2006 Rupture and drug release characteristics of multi-reservoir type microspheres with poly(dl-lactide-co-glycolide) and poly(dl-lactide). Int. J. Pharm. **327** 110.

[81] Friess, W and Schlapp M 2002 Release mechanisms from gentamicin loaded poly(lactic-co-glycolic acid) (PLGA) microparticles. J. Pharm. Sci. **91** 845.

[82] Zhang M, Yang Z, Chow L and Wang C H 2003 Simulation of Drug Release from Biodegradable Polymeric Microspheres with Bulk and Surface Erosions. J. Pharm. Sc. **92** 2040.

[83] Fu Y and Kao W J 2010 Drug Release Kinetics and Transport Mechanisms of Nondegradable and Degradable Polymeric Delivery Systems. Expert Opin. Drug Deliv. **7** 429.

[84] Singh L, Kumar V and Ratner B D 2004 Generation of porous microcellular 85/15 poly (DL-lactide-coglycolide) foams for biomedical applications. Biomaterials **25** 2611.

[85] Zhao A and Rodgers V G J 2006 Using TEM to couple transient protein distribution and release for PLGA microparticles for potential use as vaccine delivery vehicles. J. Control. Release **113** 15.

[86] Smith M B and March J. In march's advanced organic chemistry. 5th ed. Wiley Interscience, NewYork, NY, 2001.

[87] Zarzycki R, Modrzejewska Z and Nawrotek K 2010 Drug release from hydrogel matrices. Ecol. Chem. Eng. S. **17** 117.

[88] Siepmann J and Siepmann F 2008 Mathematical mdeling of drug delivery. Int. J. Pharm. **364** 328.

[89] Lin C C and Metters A T 2006 Hydrogels in controlled release formulations: Network design and mathematical modeling. Adv. Drug Deliv. Rev. **58** 1379.

[90] Grassi M and Grassi G 2005 Mathematical modelling and controlled drug delivery: Matrix systems. Curr. Drug Deliv. **2** 97.

[91] Huang X and Brazel C S 2001 On the importance and mechanisms of burst release in matrix-controlled drug delivery systems. J. Control. Release **73** 121.

[92] Andrae J, Gallini R and Betsholtz C 2008 Role of platelet-derived growth factors in physiology and medicine. Genes Dev. **22** 1276.

[93] Perets A, Baruch Y, Weisbuch F, Shoshany G, Neufeld G and Cohen S 2003 Enhancing the vascularization of three-dimensional porous alginate scaffolds by incorporating controlled release basic fibroblast growth factor microspheres. J. Biomed. Mater. Res. A. **65** 489.

[94] Baker, R. Controlled Release of Biologically Active Agents. Wiley, NewYork, NY, 1987.

[95] Batycky R P, Hanes J, Langer R and Edwards D A 1997 A theoretical model of erosion and macromolecular drug release from biodegrading microspheres. J. Pharm. Sci. **86** 1464.

[96] Brazel C S and Peppas N A 1999 Recent studies and molecular analysis of drug release from swelling-controlled devices. STP Pharma. Sci. **9** 473.

[97] Tzafriri A R 2000 Mathematical modeling of diffusion-mediated release from bulk degrading matrices. J. Control. Release **63** 69.

[98] Kishida A Murakami K, Goto H, Akashi M, Kubita H and Endo T 1998 Polymer drugs and polymeric drugs X: slow release of 5-fluorouracil from biodegradable poly(g-glutamic acid) and its benzyl ester matrices. J. Bioact. Compat. Polym. **13** 270.

[99] Mallapragada S K, Peppas N A and Colombo P 1997 Crystal dis solution-controlled release systems. II. Metronidazole release from semicrystalline poly(vinyl alcohol) systems. J. Biomed. Mater. Res. **36** 125.

[100] Sah H K, Toddywala R and Chien Y W 1994 The influence of biodegradable microcapsule formulations on the controlled release of a protein. J. Control. Release **30** 201.

[101] Park T G, Cohen S, Langer R 1992 Controlled protein release from polyethyleneimine-coated poly(L-lactic acid) / pluronic blend matrices. Pharm. Res. **9** 37.

[102] Park T G, Cohen S and Langer R 1992 Poly(L-lactic acid) / pluronic blends: characterization of phase separation behavior, degradation, and morphology and use as protein-releasing matrices. Macromolecules **25** 116.

[103] Jalil R and Nixon J R 1990 Biodegradable poly(lactic acid) and poly(lactide-co-glycolide) microcapsules: problems associated with preparative techniques and release properties. J. Microencapsulation **7** 297.

[104] Tan E C, Lin R and Wang C H 2005 Fabrication of double-walled microspheres for the sustained release of doxorubicin. J. Colloid Interface Sci. **291** 135e43.

[105] Zheng W 2009 A water-in-oil-in-oil-in-water (W/O/O/W) method for producing drug-releasing, double-walled microspheres. Int. J. Pharm. **374** 90e5.

[106] Perugini P, Genta I, Conti B, Modena T and Pavanetto F 2001 Long-term release of clodronate from biodegradable microspheres. AAPS Pharm. Sci. Tech. **2** 6.

[107] Rothstein S N, Federspiel W J and Little S R 2009 A unified mathematical model for the prediction of controlled release from surface and bulk eroding polymer matrices. Biomaterials **30** 1657.

[108] Park E S, Maniar M and Shah J C 1998 Biodegradable polyanhydride devices of cefazolin sodium, bupivacaine, and taxol for local drug delivery: preparation, and kinetics and mechanism of in vitro release. J. Control Release **52** 179.

[109] Berchane N S, Carson K H, Rice-Ficht A C and Andrews M J 2007 Effect of mean diameter and polydispersity of PLG microspheres on drug release: experiment and theory. Int. J. Pharm. **337** 118.

[110] Gopferich A and Langer R 1993 Modeling of polymer erosion. Macromolecules **26** 4105.

[111] Gopferich A and Langer R 1993 Influence of microstructure and monomer properties on the erosion mechanism of a class of polyanhydrides. J. Polym. Sci. Part. A Polym. Chem. **31** 2445.

[112] Katzhendler I Mäder K, Friedman M 2000 Structure and hydration properties of hydroxypropyl methylcellulose matrices containing naproxen and naproxen sodium. Int. J. Pharm. **200** 161-79.

[113] Stephens D, Li L, Robinson D, Chen S, Chang H C and Liu R M 2000 Investigation of the in vitro release of gentamicin from a polyanhydride matrix. J. Control Release **63** 305.

[114] Zilberman M and Grinber O 2008 HRP-loaded biodegradable microspheres: effect of copolymer composition and molecular weight on microstructure and release profile. J. Biomater. Appl. **22** 391.

[115] Alexis F, Venkatraman S, Rath S K, Gan L H 2006 Some insight into hydrolytic scission mechanisms in bioerodible polyesters. J. Appl. Polym. Sci. **102** 3111.

[116] Makadia H K and Siegel S J 2011 Poly Lactic-co-Glycolic Acid (PLGA) as biodegradable controlled drug delivery carrier, Polymers (Basel) **3** 1377-97.

[117] Zhang M, Yang Z, Chow L L and Wang C H 2003 Simulation of drug release from biodegradable polymeric microspheres with bulk and surface erosions. J. Pharm. Sci. **92** 2040.

[118] Colombo P, Bettini R, Santi P, De Ascentiis A and Peppas N A 1996 Analysis of the swelling and release mechanisms from drug delivery systems with emphasis on drug solubility and water transport. J. Control Release. **39** 231.

[119] Higuchi T 1963 Mechanisms of sustained action mediation: theoretical analysis of rate of release of solid drugs dispersed in solid matrices. J. Pharm. Sci. **52** 1145.

[120] Koizumi T and Panomsuk S P 1995 Release of medicaments from spherical matrices containing drug in suspension: Theoretical aspects. Int. J. Pharm. **116** 45.

[121] Wang S, Mahali S M, McGuiness A and Lou X 2010 Mathematical models for estimating effective diffusion parameters of spherical drug delivery devices. Theor. Chem. Acc. **125** 659.

[122] Rothstein S N, Federspiel W J and Little S R 2008 A simple model framework for the prediction of controlled release from bulk eroding polymer matrices. J. Mater. Chem. **18** 1873.

[123] Noyes A A and Whitney W R 1897 The rate of solution of solid substances in their own solutions. J. Am. Chem. Soc. **19** 930.

[124] Nernst W 1904 Theorie der Reaktionsgeschwindigkeit in heterogenen Systemen. Z. Phys. Chem. **47** 52.

[125] Baker R W, Lonsdale, H.S. Controlled release: mechanisms and rates. Plenum press, NewYork, NY, 1974.

[126] Gohel M 2009 Osmotic Drug Delivery: An Update. Pharmainfo. Net. **4** 15.

[127] Karasulu H Y, Ertan G and Kose T 2000 Modeling of theophylline release from different geometrical erodible tablets. Eur. J. Pharm. Biopharm. **49** 177.

[128] von-Burkersroda F, Schedl L and Göpferich A 2002 Why degradable polymers undergo surface erosion or bulk erosion. Biomaterials **23** 4221.

[129] Izadifar M 2013 Biomanufacturing versus superficial cell seeding: simulation of chondrocyte proliferation in a cylindrical cartilage scaffold. Int. J. Tissue Eng. **2013** 407047.

[130] Izadifar M A porous media approach for physiological modeling. LAP LAMBERT Academic Publishing, Germany, 2013.

[131] Izadifar M, Kelly E M and Chen X B 2014 Engineering angiogenesis for myocardial infarction repair: recent developments, challenges, and future directions. Cardiovasc. Eng. Technol. Cardiovasc. Eng. Technol. **5** 281-307.

[132] Van-Hinsbergh V W and Koolwijk P 2008 Endothelial sprouting and angiogenesis: matrix metalloproteinases in the lead. Cardiovasc. Res. **78** 203-12.

[133] Gerhardt H 2008 VEGF and endothelial guidance in angiogenic sprouting. Organogenesis **4** 241-46.

[134] Lee K, Silva E A and Mooney D J 2011 Growth factor delivery-based tissue engineering: general approaches and a review of recent developments. J. R. Soc. Interface. **8** 153-70.

[135] Matsusaki M and Akashi M 2005 Novel functional biodegradable polymer IV: pH-sensitive controlled release of fibroblast growth factor-2 from a poly(gamma-glutamic acid)-sulfonate matrix for tissue engineering. Biomacromolecules **6** 3351.

[136] Kim H K, Shim W S, Kim S E, Lee K H, Kang E, Kim J H, Kim K, Kwon I C and Lee D S 2009 Injectable in situ-forming pH/thermo-sensitive hydrogel for bone tissue engineering. Tissue Eng. Part A **15** 923.

[137] Connal L A, Li Q, Quinn J F, Tjipto E, Caruso F and Qiao G G 2008 pH-responsive poly(acrylic acid) core cross-linked star polymers: morphology transitions in solution and multilayer thin films. Macromolecules **41** 2620.

[138] He E, Yue C Y and Tam K C 2005 Binding and Release Studies of a Cationic Drug from a Star-Shaped Four-arm Poly(ethylene oxide)-b-poly(methacrylic acid) in Aqueous Medium. Langmuir **25** 4892.

[139] Gil E S and Hudson S M 2004 Stimuli-reponsive polymers and their bioconjugates. Prog. Polym. Sci. **29** 1173 .

[140] Jun L, Bochu W and Yazhou W 2006 Thermo-sensitive polymers for controlled release drug delivery systems. Int. J. Pharmacology **2** 513.

[141] Izadifar M and Chen X B 2013 Radio frequency heating of implanted tissue engineered scaffolds: simulation and experimental studies. Frontiers in Heat and Mass Transfer **3** 043004 .

[142] Mamada A, Tanaka T, Kungwatchakun D and Irie M 1990 Photoinduced phase transition of gels. Macromolecules **23** 1517.

[143] Ntziachristos V, Ripoll J, Wang L H V and Weissleder R 2005 Shedding light onto live molecular targets. Nat. Biotechnol. **23** 313.

[144] Huang X H, El-Sayed I H, Qian W and El-Sayed M A 2006 Cancer cell imaging and photothermal therapy in the near-infrared region by using gold nanorods. J. Am. Chem. Soc. **128** 2115.

[145] Day E S, Morton J G and West J L 2009 Nanoparticles for thermal cancer theray. J. Biomech. Eng. **131** 074001.

[146] Yavuz M S, Cheng Y Y, Chen J Y, Cobley C M, Zhang Q, Rycenga M, Xie J W, Kim C, Song K H, Schwartz A G, Wang L H V and Xia Y N 2009 Gold nanocages covered by smart polymers for controlled release with near-infrared light. Nat. Mater. **8** 935-9.

[147] Carmeliet P 2003 Angiogenesis in health and disease. Nat. Med. 9 653–60

[148] Carmeliet P 2005 Angiogenesis in life, disease and medicine. Nature **438** 932–36.

[149] Chapanian R and Amsden B G 2010 Combined and sequential delivery of bioactive VEGF(165) and HGF from poly(trimethylene carbonate) based photo-cross-linked elastomers. J. Control. Release **143** 53–63.

[150] Chen R R, Silva E A, Yuen W W, Brock A A, Fischbach C, Lin A S, Guldberg R E and Mooney D J 2007 Integrated approach to designing growth factor delivery systems. FASEB J. **21** 3896–3903.

[151] Chen R R, Silva E A, Yuen W W and Mooney D J. 2007 Spatio-temporal VEGF and PDGF delivery patterns blood vessel formation and maturation. Pharm. Res. **24** 258–64.

[152] Cao L and Mooney D J 2007 Spatiotemporal control over growth factor signaling for therapeutic neovascularization. Adv. Drug Deliv. Rev. **59** 1340–50.

[153] Tayalia P and Mooney D J 2009 Controlled growth factor delivery for tissue engineering. Adv. Mater. **21** 3269–85.

[154] Yilgor P, Tuzlakoglu K, Reis R L, Hasirci N and Hasirci V 2009 Incorporation of a sequential BMP-2 BMP-7 delivery system into chitosan-based scaffolds for bone tissue engineering. Biomaterials **30** 3551–59.

[155] Jeon O, Kang SW, Lim H W, Hyung-Chung J, Kim B S 2006 Long-term and zero-order release of basic fibroblast growth factor from heparin-conjugated poly(L-lactide-co-glycolide) nanospheres and fibrin gel. Biomaterials **27** 1598–1607.

[156] White L J, Kirby G T, Cox H C, Qodratnama R, Qutachi O, Rose F R and Shakesheff K M 2013 Accelerating protein release from microparticles for regenerative medicine applications. Mater Sci Eng C Mater Biol Appl. **33** 2578-83.

[157] Li X, Wang J, Su G, Zhou Z, Shi J, Liu L, Guan M and Zhang Q 2011 Spatiotemporal control over growth factor delivery from collagen-based membrane. J. Biomed. Mater. Res. A. **2011** 33282.

[158] Choi D H, Park C H, Kim I H, Chun H J, Park K and Han D K 2010 Fabrication of core-shell microcapsules using PLGA and alginate for dual growth factor delivery system. J. Control. Release **147** 193e201.

[159] Ahmad Z, Zhang H B, Farook U, Edirisinghe M, Stride E and Colombo P 2008 Generation of multilayered structures for biomedical applications using a novel tri-needle coaxial device and electrohydrodynamic flow. J. R. Soc. Interface **5** 1255e61.

[160] Lee Y H, Bai M Y and Chen D R 2011 Multidrug encapsulation by coaxial tri-capillary electrospray. Colloids Surf. B Biointerfaces **82** 104e10.

[161] Kim W and Kim S S 2011 Synthesis of biodegradable triple-layered capsules using a triaxial electrospray method. Polymer **52** 3325e36.

[162] Lee W L, Hong M, Widjaja E and Loo S C 2010 Formation and degradation of biodegradable triple-layered microparticles. Macromol. Rapid Commun. **31** 1193e200.

[163] Lee W L, Widjaja E and Loo S C 2012 Designing drug-loaded multi-layered polymeric microparticles. J. Mater. Sci. Mater. Med. **23** 81e8.

[164] Lee W L, Yu P O, Hong M, Widjaja E and Loo S C 2012 Designing multilayered particulate systems for tunable drug release profiles. Acta Biomater. **8** 2271e8.

[165] Abraham L C, Zuena E, Perez-Ramirez B and Kaplan D L 2008 Guide to collagen characterization for biomaterial studies. J. Biomed. Mater. Res. B Appl. Biomater. **87** 264–85.

[166] Ramshaw J A, Peng Y Y, Glattauer V, Werkmeister J A 2009 Collagens as biomaterials. J. Mater. Sci. Mater. Med. **20** S3–8.

[167] De Paoli Lacerda S H, Ingber B and Rosenzweig N 2005 Structure-release rate correlation in collagen gels containing fluorescent drug analog. Biomaterials **26** 7164–72.

[168] Ishizuka F, Liu X, Murayama S, Santa T, Kato M 2014 Development of a spatiotemporal method to control molecular function by using silica-based photodegradable nanoparticles. J. Mater. Chem. B. **2** 4153-58.

[169] Hoffmann C, Mazari E, Lallet S, Le-Borgne R, Marchi V, Gosse C and Gueroui Z 2013 Spatiotemporal control of microtubule nucleation and assembly using magnetic nanoparticles. Nat. Nanotech. **8** 199–205.

[170] Chena F M, Zhangb M and Wua Z 2010 Toward delivery of multiple growth factors in tissue engineering. Biomaterials **31** 6279–6308.

CHAPTER 3

OPTIMIZATION OF NANOPARTICLES FOR CARDIOVASCULAR TISSUE ENGINEERING

“This chapter has been published as “M. Izadifar, M. Kelly, A. Haddadi and X. B. Chen, 2015, Optimization of Nanoparticles for Cardiovascular Tissue Engineering, *Nanotechnology*, 26(1), 235301” According to the Copyright Agreement, "the authors retain the right to include the journal article, in full or in part, in a thesis or dissertation".

3.1. Abstract

Nano-particulate delivery systems have increasingly been playing important roles in cardiovascular tissue engineering. Properties of nanoparticles (e.g. size, polydispersity, loading capacity, zeta potential, morphology) are essential to system functions. Notably, these characteristics are regulated by fabrication variables, but in a complicated manner. This raises a great need to optimize fabrication process variables to ensure the desired nanoparticle characteristics. This paper presents a comprehensive experimental study on this matter, along with a novel method, the so-called Geno-Neural approach, to analyze, predict and optimize fabrication variables for desired nanoparticle characteristics. Specifically, ovalbumin was used as a protein model of growth factors used in cardiovascular tissue regeneration, and six fabrication variables were examined with regard to their influence on the characteristics of nanoparticles made from high molecular weight poly(lactide-co-glycolide). The six-factor five-level central composite rotatable design was applied to the conduction of experiments, and based on the experimental results, a geno-neural model was developed to determine the optimum fabrication conditions. For desired particle sizes of 150, 200, 250 and 300 nm, respectively, the optimum conditions to achieve the low polydispersity index, higher negative zeta potential and higher

loading capacity were identified based on the developed geno-neural model and then evaluated experimentally. The experimental results revealed that the polymer and the external aqueous phase concentrations and their interactions with other fabrication variables were the most significant variables to affect the size, polydispersity index, zeta potential, loading capacity and initial burst release of the nanoparticles, while the electron microscopy images of the nanoparticles showed their spherical geometries with no sign of large pores or cracks on their surfaces. The release study revealed that the onset of the third phase of release can be affected by the polymer concentration. Circular dichroism spectroscopy indicated that ovalbumin structural integrity is preserved during the encapsulation process. Findings from this study would greatly contribute to the design of high molecular weight poly(lactide-co-glycolide) nanoparticles for prolonged release patterns in cardiovascular engineering.

3.2. Introduction

Cardiovascular diseases remain a critical health issue accounting for ~40% fatalities worldwide. Among them, myocardial infarction or heart attack stands out because the cardiac tissue is terminally developed and may fail to repair itself. Despite significant achievements in cardiovascular therapy, current therapeutic methods have failed to provide a definitive therapy for myocardial infarction repair. As such there has been a great interest in cardiovascular tissue engineering, which integrates cell biology, engineering, material science and medicine to provide a suitable environment for cardiac tissue regeneration and vascularization. One of critical issues in cardiac tissue engineering strategies is to carefully regulate the microenvironment by controlling the biological conditions *in-situ* in micro and nanoscale [1]. With recent advances in nanotechnology, it has been increasingly possible to rate-program nanoparticles to control the delivery of biologically signaling molecules instructing cellular fates for cardiac tissue

regeneration and stimulating neovascularization in the myocardial infarction area [2]. In this context, growth-factor (GF)-loaded polymeric nanoparticles have received considerable attentions [3].

Among synthetic biopolymers, poly(D,L-lactide-co-glycolide) (PLGA) micro/nan-particles have significantly attracted attentions due to its attractive properties, which include (i) biodegradability and biocompatibility, (ii) Food and Drug Administration and European Medicine Agency approval, (iii) well described formulations and methods of production, (iv) protection of loaded substances from degradation, (v) possibility to modify surface properties to provide better interaction with biological materials, (vi) possibility to target nanoparticles to specific organs or cells, and (vii) commercially available with different physicochemical properties [4]. Recent studies have employed PLGA particulate delivery systems to tailor release profiles of GFs in the context of cardiovascular tissue engineering and brain regeneration, including the sequential delivery of vascular endothelial GF (VEGF) and TAT-HSP27 for angiogenesis therapy [5], sustained release of VEGF for neovascularization [6-8], co-delivery of VEGF and CoQ10 to improve angiogenesis in myocardial ischemia [9], and sequential delivery of GFs to stimulate brain tissue regeneration [10]. The GF release profiles are affected by the size, polydispersity index (PDI) and loading capacity of the nanoparticles, while the surface charge of the nanoparticles influences the interaction between the nanoparticles and the extra cellular matrix components as well as the tissue scaffold components *in-situ*. Since these nanoparticle characteristics are mainly affected by the fabrication conditions, it is very crucial to identify the significant fabrication variables and optimize them for desired nanoparticle characteristics.

Lamprecht et al. [11, 12] studied the effects of bovine serum albumin (BSA) concentrations, PLGA concentration, amount of surfactant, volume of the external aqueous phase, and duration of homogenization on encapsulation efficiency and the size of PLGA nanoparticles. However, in their studies the coupling effects of variables were not investigated [11, 12]. Berchane et al. [13] characterized the effect of mean diameter and PDI of PLGA microspheres on release profiles, but did not investigate the effects of fabrication conditions on microparticle size and size distribution. Jimenez et al. (2010) used a 3-factor 2-level full factorial design to analyze the effect of lactic acid ratio and other conditions on the size, zeta potential and encapsulation efficiency of methyl trypsin-loaded PLGA particles [14]. While Igartua et al. (1998) reported that harsh conditions induced by dichloromethane and ultrasound energy had no significant effects on BSA encapsulation in the first emulsification step [15], the observations by Kang and Singh (2003) [16] and Bilati et al. (2005) showed that sonication time is a crucially important variable affecting the protein loading efficiency and stability [17]. Feczkó et al. (2011) studied the influence of fabrication process parameters on the efficiency of BSA encapsulation and particle size in 50:50 PLGA nanoparticles based on a 5-factorial 3-level Box–Behnken type experimental design; however, they did not analyze the effects of preparation conditions on PDI, zeta potential and yield [18]. They observed that the effect of surfactant concentration on protein encapsulation efficiency was insignificant and PLGA concentrations above 4% (w/v) decreased the protein loading efficiency. Using 3-factor central composite design, Zhou et al. (2013) studied the effects of PLGA concentration, surfactant concentration and solvent removal rate on encapsulation efficiency and particle size of L-DOPA loaded PLGA nanoparticles [19]. Taken together, the aforementioned studies illustrate that nanoparticle characteristics such as their size, PDI, surface charge, and loading capacity can be related to the fabrication variables in

complicated manners. This raises a great need of multi-objective weighted variable optimization approaches in order to determine the optimum fabrication conditions based on desired nanoparticle characteristics for cardiovascular engineering applications. Typically, the desired nanoparticle size varies from ~100 nm for intravascular applications to ~500-1000 nm for scaffold-based cardiac tissue regeneration; while the PDI of the nanoparticles is desired to be less than 0.3 for uniform size distribution in all applications. Higher negative surface charge of the nanoparticles is more desirable due to the cytotoxicity associated with cationic nanoparticles. Also, higher negative zeta potential can enhance the dispersion of the nanoparticles in water and physiological systems (e.g. PBS, blood). Higher loading capacity directly increases the loading efficiency can provide higher dose. Furthermore, since prolonged release of growth factors is generally desired for myocardial regeneration and neovascularisation, the molecular weight (MW) of PLGA is an important factor as well.

The main objectives of this study was to (1) analyze the effects of six fabrication variables on the nanoparticle characteristics based on 6-factor 5-level central composite rotatable design (CCRD), (2) develop a generalized Geno-Neural hybrid model to predict the nanoparticle fabrication outcomes, (3) identify and experimentally validate optimal fabrication conditions to provide desired nanoparticle characteristics with preserved structural integrity of the encapsulated protein, (4) assess the effects of the fabrication variables on the burst release of the protein from the PLGA nanoparticles. High MW PLGA with L:G ratio of 75:25 that contributes to prolonged release patterns was used in this study. Ovalbumin (OVA) that has a similar MW as VEGF, insulin-like GF (IGF), and transforming GF (TGF) was used as a protein model for characterization of loading properties of the nanoparticles. Response surface equations were derived and an artificial neural network (ANN) was developed to predict the nanoparticle

characteristics of size, PDI, zeta potential and OVA loading capacity with respect to fabrication variables. The generalization of the ANN was tested, and then a Geno-Neural hybrid model was developed by coupling the ANN with genetic algorithm to search for optimum fabrication conditions leading to desired nanoparticle size (150, 200, 250, 300 nm), low PDI (<0.3), high negative zeta potential (<-20 mV) and high loading capacity. The predicted optimum conditions were experimentally evaluated and the morphology of the nanoparticles was characterized using scanning electron microscopy (SEM).

3.3. Materials and methods

3.3.1. Materials

High MW (66,000-107,000 Daltons) ester-terminated PLGA (75:25) with an average inherent viscosity of 0.67 dL/g (in chloroform at 30°C) was received from DURECT (DURECT Co., Cupertino, CA), and lyophilized OVA (MW: 44,287 Daltons), PVA (MW: 31,000-50,000 Daltons), phosphate-buffered saline (PBS), and HPLC grade chloroform were the product of Sigma (Sigma-Aldrich, MO).

3.3.2. Fabrication of OVA-loaded PLGA nanoparticle

PLGA nanoparticles were prepared by a double emulsion-solvent evaporation technique at room temperature [20]. Briefly, 125 µl of OVA solution (1.1-9.4% w/v) in PBS (pH 7.4) as the inner aqueous phase was added to 1 ml chloroform containing PLGA at variable concentrations between 1.6-6.4% (w/v). OVA solution was emulsified in the organic phase for 50 s at 20% of total input power (~40 W, 40 kHz) using a probe sonicator (Branson Ultrasonics Co., Ltd., Shanghai, China) in an ice bath to obtain the first water-in-oil (W_1/O) emulsion system. The W_1/O emulsion was then added into aqueous PVA solutions (0.25-7% w/v) varying between 1 and 7 ml as the external aqueous phase followed by sonication for 19-91 s at 40% of total input

power (~80 W) to obtain water-in-oil-in-water ($W_1/O/W_2$) double emulsion. Then the chloroform was allowed to evaporate under magnetic stirring at different stirring rates between 93 and 804 rpm for 4 hours. Nanoparticles were then separated by ultracentrifugation (Optima L-Series, Becman Coulter Inc., Palo Alto, CA) for 20 min at 15,000 rpm. Particles were re-suspended in double distilled water, washed twice and dried by freeze-drier (LABCONCO, MO) at -80°C for 48 h before being used for physical, morphological and loading capacity characterization. 1% sucrose solution was used as cryoprotectant to reduce the coalescence of nanoparticles during freeze drying.

3.3.3. Characterization of physical, morphological and encapsulation properties

The size, PDI, size distribution and zeta potential of nanoparticles were measured by a Dynamic Light Scattering technique (Zetasizer, Nano ZS3000; Malvern Instruments, Malvern, UK) based on backscattering detection at a scattering angle of 173° at 25°C. Morphology of the nanoparticles were characterized by scanning electron microscopy (SEM) where the nanoparticles were mounted on stubs, coated with a thin layer of gold with Sputter Coater (S150B, Edwards, Crawley, UK) and then were examined under a field-emission scanning electron microscope (JSM-6010 LV, JEOL, Ltd., Tokyo, Japan) at 15 kV.

Loading capacity of the PLGA nanoparticles was measured by extracting and quantifying OVA from the nanoparticles. Briefly, nanoparticles were dispersed in 0.1 M sodium hydroxide containing 5% of sodium dodecyl sulphate which was incubated at room temperature overnight in an orbital shaker. The supernatant was collected by centrifugation at 15’000 rpm for 10 min. BCA assay kit (Sigma-Aldrich, MO) was used and OVA concentration was quantified by reading the absorbance of the samples at 562 nm using a UV spectrophotometer (Synergy HT,

BioTek Instruments, Inc., Winooski, VT). Loading capacity and loading efficiency were calculated as follows, respectively:

$$\psi = \frac{C_{a,OVA}}{C_{NP}} \tag{3.1}$$

$$\eta = \frac{C_{a,OVA}}{C_{i,OVA}} \times 100 \tag{3.2}$$

where ψ is the loading capacity (mg OVA/mg nanoparticles), $C_{a,OVA}$ is the actual OVA concentration from direct extraction of the nanoparticles (mg OVA/ml), C_{NP} is the concentration of nanoparticles used for the OVA extraction (mg nanoparticles/ml), $C_{i,OVA}$ is the initial OVA concentration used for loading of OVA into nanoparticles (mg OVA/ml), and η is the loading efficiency.

3.3.4. Experimental design

The main experiments were designed based on six-factor five-level CCRD using statistical analysis software (SAS Institute Inc., Cary, NC). The CCRD is ideal for sequential experimentation, well suited for fitting quadratic surface for optimization, and can provide reasonable amount of information for testing the lack of fit while reducing unusually large number of design points [21-25]. A CCRD consists of two-level factorial design points, axial points, and center points such that the effects of independent variables are studied at five levels of factors coded as $-\alpha$, -1, 0, 1, $+\alpha$, where the value of α is calculated to fulfill the rotatability and orthogonality in the experimental design. Table 3.1 presents the coded and the corresponding actual experimental levels designed using SAS. The CCRD design matrix includes a total number of 58 experiments consisting of 32 factorial points, 12 axial points, and 14 replicates at the center point for estimation of pure error of sum of squares. This experimental design allows

for deriving multiple regression equations including linear, quadratic and two-factor interaction terms. The coded variables in CCRD are converted to actual values as:

Table 3.1. Coded and actual values of nanoparticle fabrication conditions used in CCRD.

Independent variables	Symbol	Coded and actual experimental levels				
		-α (-2.37841)	-1	0	1	α (+2.37841)
PVA concentration (% w/v)	C_{PVA}	0.61	2.40	3.70	5.00	6.80
PLGA concentration (% w/v)	C_{PLGA}	1.62	3.00	4.00	5.00	6.40
OVA concentration (% w/v)	C_{OVA}	1.1	3.50	5.30	7.00	9.40
PVA volumetric phase ratio	R_{PVA}	1.97	3.00	3.75	4.50	5.53
Sonication time (s)	t	19	40	55	70	91
Stirring rate (rpm)	S	93	300	450	600	807

$$x_i^a = x_{(-1)}^a + \frac{\left(x_i^{coded} + 1\right)\left(x_{(+1)}^a - x_{(-1)}^a\right)}{2} \tag{3.3}$$

where $x_{(-1)}^a$ and $x_{(+1)}^a$ are the actual low and high values corresponding to coded values of -1 and +1, respectively, x_i^{coded} is the coded values of the design points in CCRD, and x_i^a is the actual value corresponding to x_i^{coded} .

3.3.5. Statistical analyses

Analysis of variance (ANOVA) study was carried out using SAS in order to identify the variables having significant effect (p-value<0.05) on size, PDI, zeta potential, yield, and encapsulation capacity and efficiency of the nanoparticles. Multiple regression analyses was also

performed by SAS to evaluate two-factor interaction influences as well as the linear and quadratic effects of fabrication variables on the dependent variables at a probability of significance of <0.05. The predictability of the multiple regression equations was assessed based on coefficient of determination, mean prediction error, and distribution of residual prediction errors.

3.3.6. Artificial neural network development

Simulating human brain analytical function, ANNs have an inherent ability to learn and recognize nonlinear and complex relationships by experience. In an ANN, basically a neuron sums weighted inputs from input connections and then applies a transfer function from which the result propagates to the succeeding neurons through outgoing connections. Three distinct layers of neurons are input, intermediate and output neurons (Fig. 3.1) that receive signals from the real world, process the signals, and return the results, respectively [26, 27]. ANN training is based on adjusting synaptic weight and bias values using training and validating datasets in order to learn complex relationships between inputs and outputs. In this study, the experimental data collected from the CCRD were randomly divided into three datasets, training, validating and testing datasets containing 30, 8 and 7 samples, respectively.

Based on the number of independent and dependent variables, 6 and 4 neurons were devoted to the input and output layers. Backpropagation training algorithm based on Bayesian Regularization (BR) algorithm combined with Levenberg–Marquardt was used for training the ANN model in MATLAB 7.4. The magnitudes of variables in the datasets were normalized between -1 and +1 to improve the training process. Since the number of intermediate layers and neurons depends on the complexity of the problem, sensitivity analyses were performed to determine number of intermediate neurons. The training and validating processes were allowed

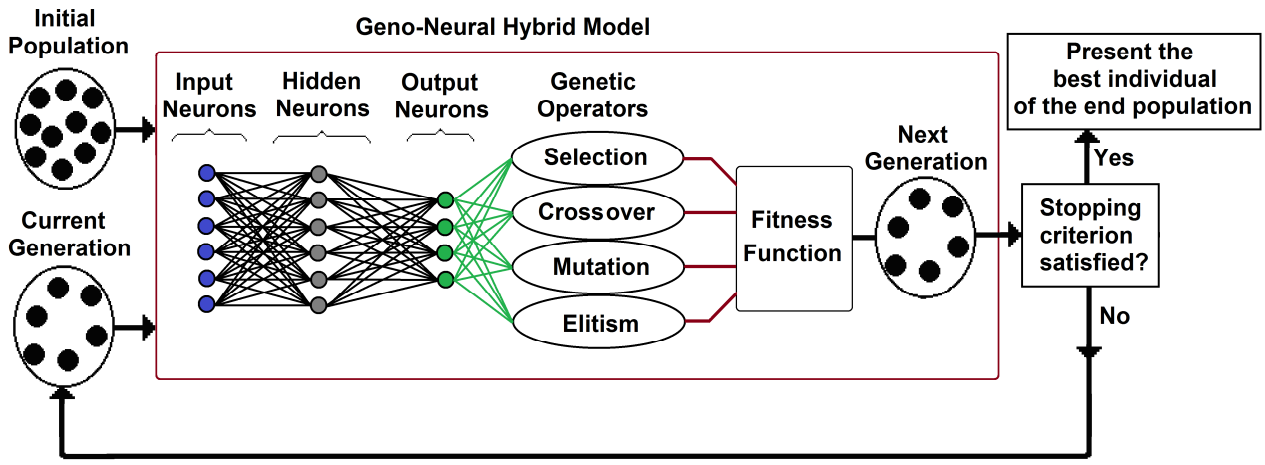

Figure 3.1. Schematic diagram of the Geno-Neural model and the procedure for optimization of fabrication conditions of the nanoparticles.

to execute until sum of squared error (SSE) and sum of squared weights (SSW) remained relatively unchanged and network parameters truly converged and SSE reached its global minimum value over iterations. The validating dataset was used to prevent overtraining the ANN model. Based on the sensitivity analyses a single hidden layer containing 6 intermediate neurons possessing tangent hyperbolic transfer function was used in the ANN. The generalization of the ANN model was assessed using a testing dataset, which was not involved in the training process. A mathematical representation of the developed ANN model was proposed to facilitate the use of the model through simple matrix arithmetic in any spreadsheet by general users as:

$$\overline{\mathbf{O}} = \overline{\mathbf{N}} \times \begin{bmatrix} \dfrac{e^{(\overline{\mathbf{M}}_1 \times \overline{\mathbf{P}} + q_1)} - e^{-(\overline{\mathbf{M}}_1 \times \overline{\mathbf{P}} + q_1)}}{e^{(\overline{\mathbf{M}}_1 \times \overline{\mathbf{P}} + q_1)} + e^{-(\overline{\mathbf{M}}_1 \times \overline{\mathbf{P}} + q_1)}} \\ \vdots \\ \dfrac{e^{(\overline{\mathbf{M}}_6 \times \overline{\mathbf{P}} + q_6)} - e^{-(\overline{\mathbf{M}}_6 \times \overline{\mathbf{P}} + q_6)}}{e^{(\overline{\mathbf{M}}_6 \times \overline{\mathbf{P}} + q_6)} + e^{-(\overline{\mathbf{M}}_6 \times \overline{\mathbf{P}} + q_6)}} \end{bmatrix} + \overline{\mathbf{r}} \qquad (3.4)$$

where $\overline{\mathbf{M}}_i$ and q_i are the i^{th} rows of the weight matrix of $\overline{\mathbf{M}}$ and bias vector of $\overline{\mathbf{q}}$, respectively, associated with hidden neurons, $\overline{\mathbf{N}}$ and $\overline{\mathbf{r}}$ are weight matrix and bias vector of the output layer,

$\overline{\mathbf{O}}$ is the output vector normalized between -1 and +1, and $\overline{\mathbf{P}}$ is the input vector containing normalized values of the nanoparticle fabrication conditions as:

$$\overline{\mathbf{P}} = \begin{bmatrix} C_{PVA} \\ C_{PLGA} \\ C_{OVA} \\ R_{pva} \\ t \\ S \end{bmatrix} \tag{3.5}$$

The predicted values ranging between -1 and +1 are converted to the real values of the nanoparticle characteristics as:

$$\begin{bmatrix} D_p \\ PDI \\ \xi \\ \psi \end{bmatrix} = \frac{\left(\overline{\mathbf{O}}+1\right)\left(\overline{\mathbf{O}}_{\max}-\overline{\mathbf{O}}_{\min}\right)}{2} + \overline{\mathbf{O}}_{\min} \tag{3.6}$$

where $\overline{\mathbf{O}}_{\max}$ and $\overline{\mathbf{O}}_{\min}$ are vectors containing the upper and lower limits, respectively, of the measured values of size, PDI, zeta potential and loading capacity.

3.3.7. The Geno-Neural hybrid model for optimization of fabrication conditions

Based on principles of biological concepts of evolution and genetics, genetic algorithm is essentially an iterative, population based and parallel global search algorithm. In this study, the ANN model was coupled with genetic algorithm to establish a Geno-Neuro model to search for optimum fabrication conditions of OVA-loaded PLGA nanoparticles. Figure 3.1 illustrates the Geno-Neuro system in which the ANN model predicts the outcomes of the genes (fabrication variables) in the current generation which undergo crossover, mutation, selection and elitism (genetic operators) and then evaluated by a fitness function in order to generate the next generation. The genes of the new generation undergo the same evolving process until a stopping criterion (e.g. termination generation) is met. In the present study, Genetic Algorithm for Optimization Toolbox (GAOT) in MATLAB was used for developing the Geno-Neuro system.

Initial population was randomly generated and a pre-specified number of generations were assigned as the evolution stopping criterion. The ANN model preformed as a predictor of particle size, PDI, zeta potential, and loading capacity corresponding to PVA, PLGA and OVA concentrations, PVA volumetric ratio, sonication time, and solvent removal rate representing the genes of the individuals in the current generation. The fitness of the genes of the individuals were then evaluated based on a weighted multi-objective fitness function as:

$$f = \begin{cases} -w_1\left(D_p^T - D_p\right) + w_2\left(1 - PDI^T\right) - w_3\xi + w_4(\psi - 1) & if\ D_p \langle D_p^T \\ +w_1\left(D_p^T - D_p\right) + w_2\left(1 - PDI^T\right) - w_3\xi + w_4(\psi - 1) & if\ D_p \rangle D_p^T \end{cases} \quad (3.7)$$
$$w_1 + w_2 + w_3 + w_4 = 1\ \&\ \left(w_1, w_2, w_3, w_4\right) > 0$$

where f is the fitness function, D_p^T is the desired size (nm), PDI^T is the desired PDI, and w_1, w_2, w_3 and w_4 represent the weights associated with the importance of each term in the fitness function for optimization. The variables were normalized between 0 and +1 in order to scale the terms in the fitness function into the same range of magnitude. The weights of 0.35, 0.35, 0.1, and 0.2 were assigned to w_1, w_2, w_3 and w_4 associated with the terms of size, PDI, loading capacity and zeta potential, respectively, in Eq. (3.7). The initial population of 5000, number of generations of 100, selection rate of 0.08, mutation rate of 0.05, and crossover rate of 0.6 were determined by performing sensitivity analyses, and then applied to the Geno-Neural model to search for optimum fabrication conditions by maximizing the fitness function (Eq. (3.7)).

3.3.8. Release kinetics

The release kinetics of OVA from the high MW PLGA (75:25) nanoparticles was characterized *in-vitro* based on a fractional factorial design corresponding to the CCRD axial points (-α and +α) (Table 3.1) including PVA, OVA and PLGA concentrations, and sonication time at an external aqueous phase ratio of 4 and stirring rate of 450 rpm. Pre-weighed OVA-loaded

nanoparticles were added to PBS solutions in vials for release measurements at 9 time points (0, 1, 3, 5, 9, 14, 17, 20 and 24 days) under standard tissue culture conditions (37°C, 5% CO_2). BCA protein assay (Sigma-Aldrich, MO) was used to determine OVA concentrations at each time point based on the absorbance of the solution at 562 and 572 nm using UV spectrophotometer. Time-dependent changes in OVA cumulative concentration were used to analyze the OVA release profiles from the nanoparticles prepared at different fabrication conditions. Minimizing sum of squared residuals, the modified Weibull function [28] was fitted into the experimental release data in order to estimate the initial burst release of OVA corresponding to the fabrication conditions:

$$X(t) = X_{burst} + \left(1 - \exp(-\vartheta t^{\beta})\right) \tag{3.8}$$

where $X(t)$ is the fraction of OVA released at time *t*, X_{burst} is the fraction of OVA released due to the initial burst effect, ϑ is a scale factor corresponding to the apparent rate constant, *t* is time, and β is a shape factor. After the values of initial burst release associated with the fabrication variables were determined, ANOVA study was carried out to identify the fabrication variables having significant effects (p-value<0.05) on OVA burst release.

3.3.9. Circular dichroism (CD) spectroscopy

CD spectra were recorded using Chirascan Plus CD Spectrometer (Applied Photophysics Ltd, Surrey, UK) to assess the structural integrity of OVA during the loading and release processes at the nanoparticle fabrication conditions proposed by the Geno-Neural model. CD data were collected from 205 to 260 nm at a scan time of 0.5 s per point with a step size of 1 nm at 20°C using a quartz cell with 0.1 cm path length. Data were averaged over 5 scans and expressed as millidegrees. OVA solution (9% w/v) in PBS was used as the reference for CD spectroscopy.

Since the burst release is attributed to the dissolution of non-encapsulated protein molecules on the surface or from the cracks of the nanoparticles [29], the OVA released by the burst effect is less likely affected by PLGA bulk degradation, and its secondary structure during the fabrication process can remain in the same state during the burst release. As such, if the OVA collected from the burst release is denatured; its secondary structure has been affected by the nanoparticle fabrication conditions rather than PLGA bulk degradation. Therefore, OVA samples from the burst release (within the first 18 hours according to the release profile) were used for CD spectroscopy to evaluate the effect of nanoparticle fabrication conditions on the structural integrity of OVA. Furthermore, OVA samples were collected after 15 days to be assessed for the structural integrity during the release process based on an optimum fabrication condition proposed by the Geno-Neural model. Samples were concentrated at room temperature using a vacuum concentrator (LABCONCO., MO), filtered using filter syringe (0.45 μm), and degassed at 560 mmHg and 25°C for an hour before they were used for CD spectroscopy. CD Spectra Deconvolution software Ver. 2.1 (Gerald Böhm, Germany) was used for deconvolution of the CD spectra in order to estimate the percentage of alpha-helix, anti-parallel and parallel beta sheet, beta-turn and random coil of the secondary structure of ovalbumin of the samples. The recorded CD spectra and the deconvolution results of the samples were compared to those of the standard to evaluate changes in the secondary structure of OVA samples.

3.4. Results and discussion

Preliminary experiments were performed with chloroform and dichloromethane at the same fabrication conditions and the results showed that chloroform could result in smaller particle size. In the second screening experiment with chloroform, three solvent evaporation times (2, 4, 6 hours) were applied to the solvent extraction/evaporation process performed in 30 mL and 100

mL of water as the solvent extraction/evaporation medium at 400 rpm and room temperature. The two-hour evaporation time with water volume of 30 mL led to a relatively high PDI and low loading capacity, which could be attributed to insufficient polymer hardening time that can increase the chance of coalescence and collapse of the particles during ultracentrifugation. In contrast, a relatively low PDI with spherical geometries of nanoparticles and enhanced loading capacity were observed when the evaporation times of 4 hours and 6 hours at 100 mL stirring water (data not shown) were applied. As such, based on the preliminary screening observations, chloroform was used as the organic solvent, and a solvent evaporation time and water volume of 4 hours and 100 mL, respectively, were applied to the double-emulsion solvent evaporation method for the entire study.

3.4.1. CCRD-based measurements and significant fabrication variables

Table 3.2 shows the measured values of size, PDI, zeta potential, yield and loading capacity of OVA-loaded nanoparticles corresponding to the fabrication conditions defined by the 6-factor CCRD. As for the pure error calculation, standard deviations of the response variables at the central point were 14.6 nm, 0.02, 0.06, 0.98 mV and 3 µg OVA/mg nanoparticle for size, PDI, yield and zeta potential, respectively, which are reasonably acceptable.

For the statistical analyses, linear and quadratic effects of the fabrication variables as well as the linear interactions were taken into account to identify the factors having significant effects (p-value<0.05) on the size, PDI, zeta potential, loading capacity, and loading efficiency. Results from ANOVA, as presented in Table 3.3, revealed that PVA concentration not only had linear and quadratic effects on nanoparticle size but also its linear interaction with PLGA concentration was significant. The linear interaction between sonication time and external aqueous phase volume ratio also significantly affected the size of particles. While the external aqueous phase

volume ratio had both quadratic and linear effect on PDI, OVA concentration only exhibited a quadratic effect. Interactions between sonication time and PVA concentration, OVA and PLGA concentrations, and PLGA and PVA concentrations significantly affected the variation of nanoparticle size during the fabrication process. Zeta potential was affected by PLGA concentration and its interactions with PVA concentration and PVA volume ratio. PVA concentration and its volumetric ratio as well as OVA concentration and its interaction with PLGA concentration significantly affected loading efficiency. The loading capacity is affected by PLGA concentration, and linear interactions between OVA concentration and PVA concentration as well as PVA volumetric ratio. ANOVA results (Table 3.3) indicate that unlike solvent removal rate that has no significant effect, PLGA and PVA concentrations are very important variables that either their linear/quadratic effects or their interactions with other variables significantly affect the size, PDI, zeta potential, loading capacity and encapsulation efficiency. The linear interaction between PVA volume ratio and PVA concentration had a significant effect on the nanoparticle fabrication yield.

Table 3.2. Measured values of size, PDI, zeta potential, yield and loading capacity of nanoparticles corresponding to the fabrication conditions defined in the 6-factor CCRD.

C_{PVA} (%)	C_{PLGA} (%)	C_{OVA} (%)	R_{PVA}	t (s)	S (rpm)	D_p (nm)	PDI	ξ (mV)	Y (%)	ψ (µg OVA/mg PLGA)
2.4	3.0	3.5	3.0	40	300	340±20	0.45±0.05	-24.1±0.5	0.66	89±5
2.4	3.0	3.5	3.0	70	600	341±11	0.41±0.04	-23.1±0.7	0.66	105±5
2.4	3.0	3.5	4.5	40	600	304±12	0.45±0.06	-19.9±0.9	0.67	107±2
2.4	3.0	3.5	4.5	70	300	292±27	0.41±0.04	-21.3±0.8	0.64	94±2
2.4	3.0	7.0	3.0	40	600	315±22	0.35±0.07	-22.7±0.9	0.73	97±1

2.4	3.0	7.0	3.0	70	300	267±7	0.29±0.04	-23.5±0.4	0.66	87±5
2.4	3.0	7.0	4.5	40	300	290±10	0.31±0.03	-19.8±2.8	0.64	144±5
2.4	3.0	7.0	4.5	70	600	304±8	0.31±0.04	-20.2±1.1	0.60	133±13
2.4	5.0	3.5	3.0	40	600	535±20	0.59±0.11	-27.0±1.8	0.67	42±1
2.4	5.0	3.5	3.0	70	300	355±16	0.48±0.03	-28.9±0.3	0.79	55±1
2.4	5.0	3.5	4.5	40	300	402±18	0.53±0.08	-22.4±0.8	0.75	65±2
2.4	5.0	3.5	4.5	70	600	387±14	0.48±0.06	-23.3±0.7	0.52	49±2
2.4	5.0	7.0	3.0	40	300	541±34	0.51±0.01	-25.9±1.2	0.79	67±1
2.4	5.0	7.0	3.0	70	600	445±20	0.46±0.04	-26.6±0.5	0.63	65±2
2.4	5.0	7.0	4.5	40	600	430±6	0.39±0.02	-23.6±0.5	0.44	76±2
2.4	5.0	7.0	4.5	70	300	332±15	0.42±0.03	-23.2±0.5	0.67	80±2
5.0	3.0	3.5	3.0	40	600	275±34	0.40±0.12	-16.4±1.1	0.70	90±3
5.0	3.0	3.5	3.0	70	300	208±33	0.35±0.07	-16.1±1.5	0.61	117±7
5.0	3.0	3.5	4.5	40	300	225±5	0.29±0.02	-14.8±1.0	0.56	102±2
5.0	3.0	3.5	4.5	70	600	248±8	0.35±0.02	-13.4±0.4	0.60	101±4
5.0	3.0	7.0	3.0	40	300	233±2	0.29±0.03	-17.4±0.1	0.61	138±7
5.0	3.0	7.0	3.0	70	600	220±6	0.31±0.04	-16.3±1.0	0.67	145±13
5.0	3.0	7.0	4.5	40	600	230±6	0.28±0.04	-14.5±0.4	0.70	130±8
5.0	3.0	7.0	4.5	70	300	199±4	0.23±0.03	-13.5±0.4	0.56	168±7
5.0	5.0	3.5	3.0	40	300	331±11	0.52±0.03	-18.8±1.2	0.65	65±1
5.0	5.0	3.5	3.0	70	600	307±7	0.46±0.02	-19.2±0.8	0.46	64±2
5.0	5.0	3.5	4.5	40	600	313±36	0.44±0.12	-15.7±1.0	0.52	61±1
5.0	5.0	3.5	4.5	70	300	257±5	0.34±0.03	-17.3±0.5	0.63	63±2
5.0	5.0	7.0	3.0	40	600	330±3	0.38±0.03	-19.1±1.1	0.50	87±3
5.0	5.0	7.0	3.0	70	300	242±7	0.28±0.03	-20.4±0.5	0.65	86±1

5.0	5.0	7.0	4.5	40	300	241±3	0.23±0.02	-15.8±0.6	0.59	84±2
5.0	5.0	7.0	4.5	70	600	224±4	0.28±0.04	-17.0±1.0	0.40	99±4
0.6	4.0	5.3	3.8	55	450	700±99	0.59±0.03	-22.4±1.1	0.64	103±3
6.8	4.0	5.3	3.8	55	450	255±15	0.38±0.06	-18.3±0.7	0.57	107±1
3.7	1.6	5.3	3.8	55	450	243±15	0.41±0.08	-19.5±1.1	0.56	147±2
3.7	6.4	5.3	3.8	55	450	456±29	0.56±0.07	-20.3±0.7	0.70	53±1
3.7	4.0	1.1	3.8	55	450	292±15	0.41±0.08	-21.4±0.5	0.52	40±1
3.7	4.0	9.4	3.8	55	450	278±6	0.30±0.03	-22.1±0.3	0.59	137±1
3.7	4.0	5.3	2.0	55	450	365±16	0.34±0.01	-19.8±0.4	0.77	93±2
3.7	4.0	5.3	5.5	55	450	231±7	0.23±0.02	-21.3±0.4	0.54	133±3
3.7	4.0	5.3	3.8	19	450	420±1	0.52±0.09	-19.8±1.3	0.64	119±6
3.7	4.0	5.3	3.8	91	450	268±10	0.43±0.01	-20.4±1.2	0.50	124±5
3.7	4.0	5.3	3.8	55	93	299±15	0.47±0.05	-21.3±0.9	0.15	88±5
3.7	4.0	5.3	3.8	55	807	280±42	0.45±0.08	-17.3±0.7	0.60	80±4
3.7	4.0	5.3	3.8	55	450	297±20	0.45±0.03	-17.6±0.9	0.62	105±5
3.7	4.0	5.3	3.8	55	450	328±11	0.44±0.02	-17.1±1.0	0.65	108±2
3.7	4.0	5.3	3.8	55	450	304±8	0.48±0.02	-16.5±0.8	0.67	103±1
3.7	4.0	5.3	3.8	55	450	315±26	0.45±0.01	-17.9±0.6	0.72	97±2
3.7	4.0	5.3	3.8	55	450	311±15	0.48±0.05	-18.4±1.5	0.67	97±2
3.7	4.0	5.3	3.8	55	450	325±16	0.48±0.03	-17.0±0.9	0.72	100±7
3.7	4.0	5.3	3.8	55	450	320±21	0.47±0.04	-17.6±1.4	0.52	111±2
3.7	4.0	5.3	3.8	55	450	353±10	0.46±0.05	-18.5±1.3	0.57	95±3
3.7	4.0	5.3	3.8	55	450	311±25	0.50±0.14	-17.2±1.8	0.70	106±3
3.7	4.0	5.3	3.8	55	450	319±28	0.48±0.09	-16.9±1.5	0.74	101±3
3.7	4.0	5.3	3.8	55	450	299±20	0.45±0.05	-18.9±1.1	0.70	98±3

3.7	4.0	5.3	3.8	55	450	299±22	0.47±0.10	-18.5±1.0	0.72	104±3
3.7	4.0	5.3	3.8	55	450	304±11	0.44±0.12	-20.4±1.5	0.77	99±2
3.7	4.0	5.3	3.8	55	450	327±3	0.40±0.04	-18.3±1.7	0.62	110±3

3.4.2. Multiple regression analysis and response surface equations

Multivariable regression analysis to fit regression surface to the experimental results provided response surface equations, as given in Table 3.4, applicable for predicting the response variables with respect to the fabrication conditions. The mean deviations of ~8% and coefficient of determination of >0.80 associated with the predicted values could be considered reasonable for estimating the size, PDI, and loading capacity of nanoparticles with respect to fabrication conditions. Although the coefficient of determination (0.78) associated with the zeta potential surface response equation is smaller than that of the other equations, the equation can be useful for sensitivity analysis of zeta potential of nanoparticles with respect to fabrication variables.

3.4.3. Validation of response surface equations

Figure 3.2 shows the relationship between the experimental results (Table 3.2) versus predicted values from the multiple regression equations (Table 3.4), and illustrates the distribution of prediction errors for nanoparticle size, PDI and encapsulation capacity. In Figs. 3.2a, c and d the upper and lower dash lines, which correspond to a deviation of ±5%, and the coefficients of determination of >0.80 show a reasonable agreement between the calculated values and experimental data for size, PDI and encapsulation capacity of the nanoparticles. Furthermore, as shown in Figs. 3.2b, d, and f, the residuals exhibit a random distribution indicating unbiased predictability associated with the response surface equations of size, PDI and loading efficiency of the nanoparticles.

Table 3.3. Summary of the fabrication conditions having significant effects on the response variables.

Response variable	Statistical significance (p-value)				
	D_p (nm)	PDI	ξ (mV)	ψ (µg OVA/mg NP)	η (%)
C_{PVA}	<0.0001*	0.601	0.834	0.832	0.777
C_{PLGA}	<0.0001*	0.088	<0.0001*	<0.0001*	0.246
C_{OVA}	0.102	0.09	0.814	0.335	<0.0001*
R_{PVA}	0.991	<0.0001*	<0.0001*	0.989	0.378
C_{PVA}^2	<0.0001*	0.618	0.638	0.795	0.804
R_{PVA}^2	0.378	<0.0001*	0.907	0.912	0.329
C_{OVA}^2	0.081	<0.0001*	0.578	0.286	0.008*
C_{PLGA}^2	0.204	0.183	0.089	0.093	0.005*
$C_{PLGA} \times t$	0.001*	0.820	0.508	0.456	0.471
$C_{PVA} \times t$	0.068	0.005*	0.763	0.346	0.505
$C_{PVA} \times R_{PVA}$	0.508	0.079	0.619	0.735	0.007*
$C_{PLGA} \times C_{OVA}$	0.215	<0.0001*	0.957	0.537	0.039*
$C_{PLGA} \times R_{PVA}$	<0.0001*	0.403	<0.0001*	0.750	0.324
$C_{OVA} \times R_{PVA}$	0.105	0.521	0.091	<0.0001*	0.996
$t \times R_{PVA}$	0.027*	0.837	0.624	0.346	0.350
$C_{PLGA} \times C_{PVA}$	0.006*	0.018*	<0.0001*	0.750	0.927
$C_{OVA} \times C_{PVA}$	0.095	0.141	0.084	0.001*	0.996

*significant effect ($p<0.05$)

Table 3.4. Multiple regression equations applicable for prediction of size, PDI, zeta potential and loading capacity of the PLGA nanoparticles.

Surface response equation	Mean deviation	R^2
$D_p = 172.26 + 213.309C_{PLGA} - 1.048C_{PLGA}\,t - 13.582C_{PLGA}C_{PVA} + 14.655C_{PVA}^2 - 104.818C_{PVA} - 16.535C_{PLGA}\,R_{PVA} + 0.684R_{PVA}\,t$	7.8%	0.86
$PDI = -0.2383 - 0.0061C_{OVA}^2 - 0.0003C_{PVA}\,t + 0.01C_{PLGA}C_{OVA} - 0.064R_{PVA}^2 + 0.448R_{PVA} - 0.00416C_{PLGA}C_{PVA}$	8.5%	0.81
[a] $\xi = -1.362 - 7.613C_{PLGA} + 0.513C_{PLGA}\,C_{PVA} - 3.532R_{PVA} + 1.194C_{PLGA}\,R_{PVA}$	8.1%	0.78
$\psi = 0.1386 - 0.02216C_{PLGA} + 0.00147C_{OVA}R_{PVA} + 0.000884C_{PVA}C_{OVA}$	8.9%	0.81

[a]An additional zeta potential measurement for a water system (C_{PVA}= C_{PLGA}= C_{OVA} = R_{PVA} = t=S=*0*) was performed and included in the multiple regression analysis.

3.4.4. Effect of fabrication conditions on the size and PDI of nanoparticles

Figure 3.3 depicts the variation of nanoparticle size with respect to different fabrication variables. As seen in Fig. 3.3a, the size of nanoparticles decreases with an increase in PVA concentration for all levels of PLGA concentration. PVA, which performs as the external aqueous phase in the second nano-emulsion system, is an amphiphilic compound undergoing self-assembly in water when PVA concentration exceeds a critical micelle concentration (CMC). By decreasing the PVA concentration (particularly below CMC), the emulsion nano-droplets become increasingly unstable so that the chance of coalescence of the nano-droplets increases; therefore larger nanoparticles are resulted (Fig. 3.3a). In contrast, for larger PVA concentrations,

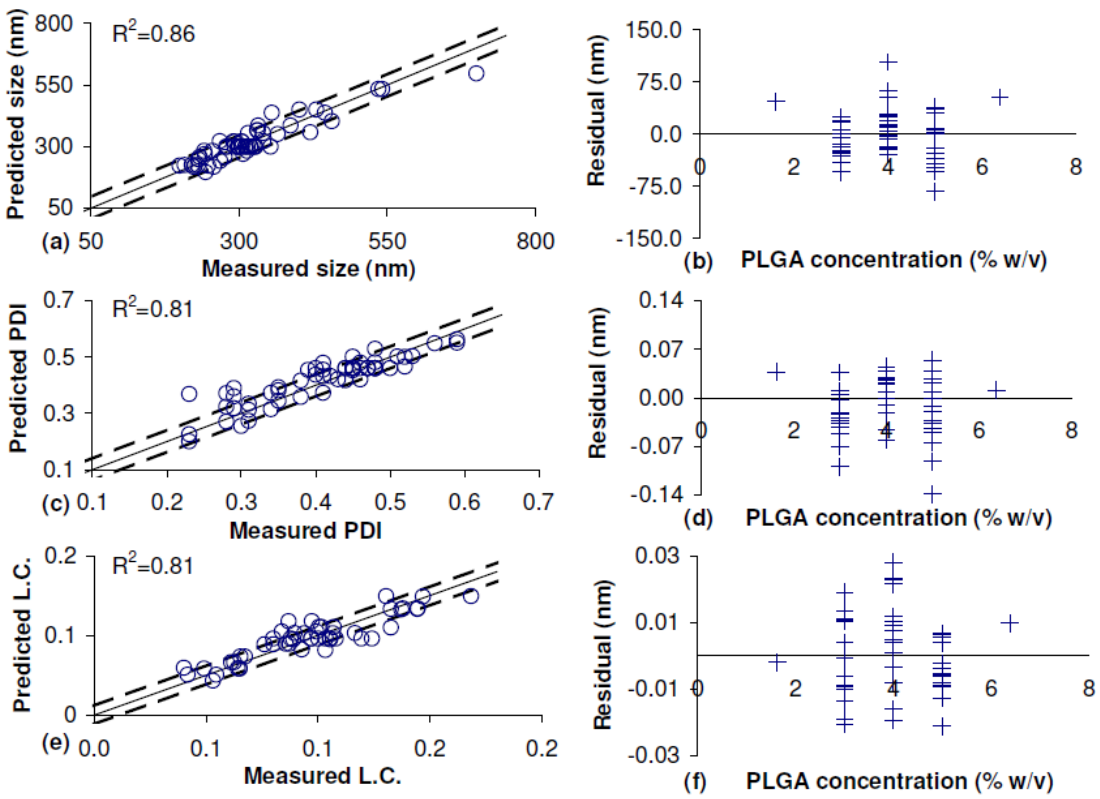

Figure 3.2. Predicted values from response surface equations *vs.* measurements (a, c, d), and distribution of residual prediction errors (b, d, f) for size, PDI and OVA-loading capacity (L.C.) of the nanoparticles.

PVA molecules align themselves at the interface between the water and organic phase and stabilize the produced nano-droplets leading to smaller nanoparticles. However, as shown in Fig. 3.3a, as PVA concentration increases beyond 4%, the size of the produced nanoparticles does not further decrease significantly. This could be attributed to the reduced net shear stress [30] caused by the increase in the external aqueous phase viscosity due to high PVA concentration. The external ultrasound energy provides shear stress to the organic phase. The shear stress-induced turbulence is the predominant mechanism of the organic phase break-up into nanodroplets. The size of the nanodroplets is inversely correlated to the magnitude of the shear rate. Increasing the external ultrasound energy directly increases the shear stress in the organic phase resulting in

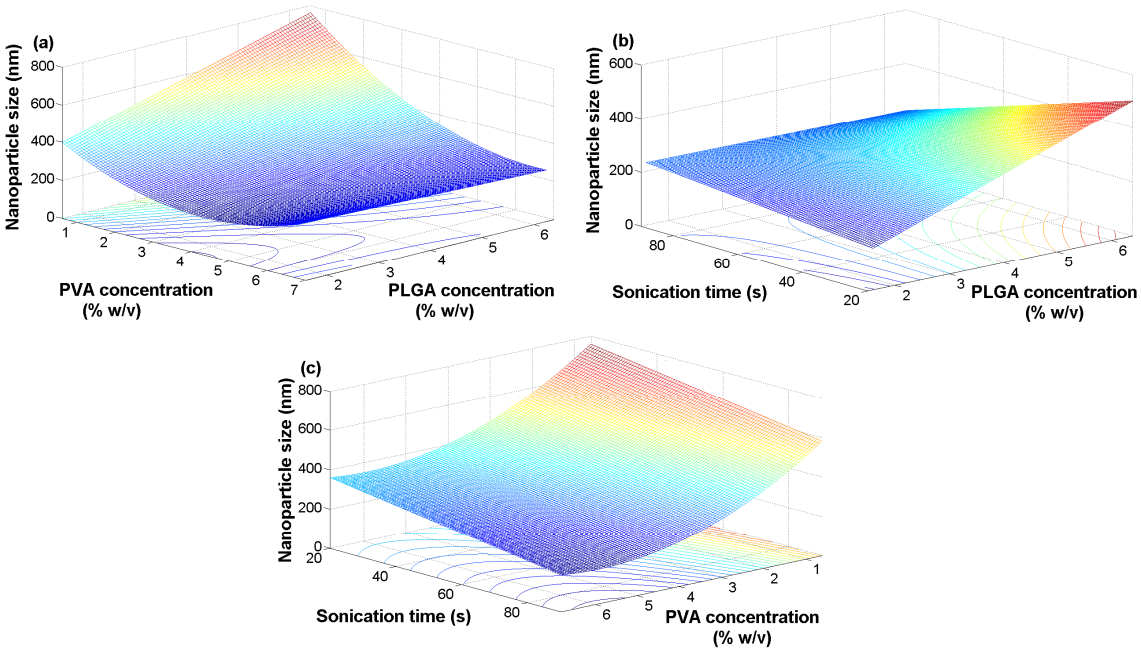

Figure 3.3. Variation of nanoparticle size with respect to fabrication conditions based on the nanoparticle size response surface equation at t=60 s, R_{PVA}=4 (a); C_{PVA}=4%, R_{PVA}=4 (b); C_{PLGA}=5%, R_{PVA}=4 (c).

more efficient droplet breadown and reduction in nanodroplet size. At a constant external energy per unit total volume, an increase in the viscosity of the organic phase and/or aqueous phase opposes the shear rate and leads to nanodroplets. Reducing the viscosity, the viscouse force decreases, and the resultant higher net shear stress in the organic phase leads to smaller size of nanodroplets. Also, the size of nanoparticles increases with PLGA concentration (Fig. 3.3a) due to the increase in the viscosity of the organic phase. Higher PLGA concentration causes higher organic phase viscosity that resists for droplets to be broken down by sonication and leads to larger nanoparticles. However, at higher levels of PVA concentration (Fig. 3.3a), the effect of PLGA concentration becomes less significant at higher levels of PVA concentration at which the organic phase viscosity associated with the mass fraction of high MW PLGA in the system is reduced and the amount of PVA in the system becomes sufficient to stabilize the sonication-

induced droplets. Figure 3.3b illustrates the variation of nanoparticle size with sonication time and PLGA concentration where the effect of sonication time becomes clearly more significant with an increase in PLGA concentration. At lower PLGA concentrations, sonication can more easily break down the droplets due to the lower organic phase viscosity that is caused by the high MW PLGA concentration; however, as the PLGA concentration increases, longer sonication time will be required to break down the droplets. As seen in Fig. 3.3b, the significance of sonication effect on nanoparticle size considerably increases at higher PLGA concentrations where the size of nanoparticles can drop from ~500 nm to ~230 nm by increasing the sonication time from 20 to 90 s. In contrast, the effect of low PVA concentration cannot be compensated by sonication time due to highly significant effect of PVA concentration on sonication-induced nano-droplet formation. As seen in Fig. 3.3c, the size of nanoparticles increases for all levels of sonication time when PVA concentration decreases below a certain level (~4.5%) such that even at a sonication time of 90 s, the size of nanoparticles can reach 700 nm at PVA concentration of 1%. It should be noted that the relative motion between the nanodroplets results in their collision leasing to the droplet coalescence. With an increase in the sonication time, the chance for the droplet coalescence also increases; however, the higher PVA concentrations (>4%) improve the nanodroplet stability, which contribute to less chance of the coalescence.

PDI that represents the relative variation of the particle size distribution is affected by fabrication variables as shown in Fig. 3.4. Generally, PDI<0.3 is considered a desired value for an acceptable narrow range of nanoparticle size. Figure 3.4a shows that PDI of the nanoparticles first increases with OVA concentration and PVA volume ratio followed by a decreasing trend such that PVA volume ratios greater than 5.3 results in PDI<0.3 at any OVA concentration. The lowest PDI value (0.08) is resulted at OVA concentration and PVA volume ratio of 9% and 5.5,

respectively (Fig. 3.4a). At higher PVA volume ratios, the availability of the external aqueous phase to the sonication-induced droplets will be sufficient enough to contribute to individualization and stabilization of the droplets by reducing the chance of random coalescence of the droplets. Furthermore, as shown in Fig. 3.4b, lower PLGA concentration at higher PVA volume ratio reduces PDI value such that PVA volume ratios greater than 5.3 will be sufficient enough for all levels of concentration of high MW PLGA (75:25) to reduce the random coalescence of droplets and result in PDI<0.3 at a sonication time, PVA concentration and sonication power of 60 s, 4% and ~80 W. Similar trend can be seen in Fig. 3.4c where PDI

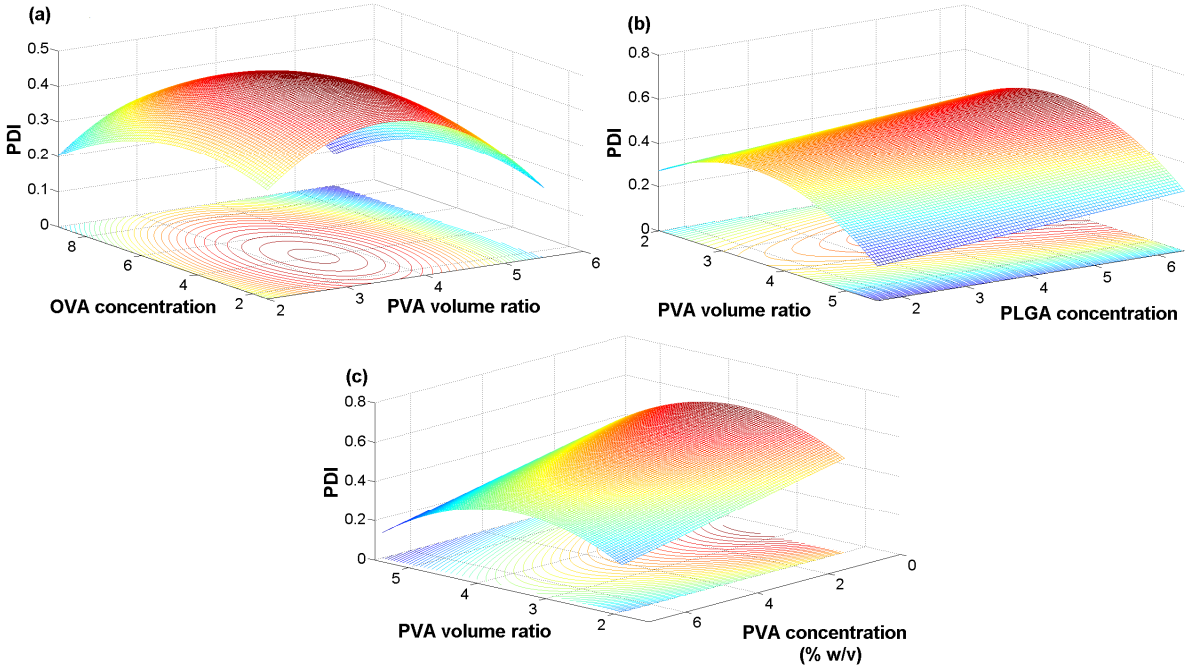

Figure 3.4. PDI variation with fabrication conditions based on PDI response surface equation at t=60 s, C_{PVA}=4%, C_{PLGA}=5% (a); t=60 s, C_{PVA} =4%, C_{OVA} =4% (b); t=60 s, C_{OVA} =4%, C_{PLGA}=5% (d).

decreases with PVA concentration such that a PVA volume ratio greater than 5.1 will be sufficient enough to reduce PDI below 0.3 at any PVA concentrations larger than 4%.

3.4.5. Nanoparticle zeta potential variations with fabrication conditions

Figure 3.5a illustrates the variation of zeta potential with respect to PVA and PLGA concentrations. While the negative zeta potential of the nanoparticles clearly increases with PLGA concentration, the effect of PLGA concentration becomes less significant as the PVA concentration increases. As shown in Fig. 3.5b, both PVA concentration and volumetric ratio directly cause the negative zeta potential to decrease. The effect of PVA concentration and volumetric ratio can be attributed to the coating PVA layer that shield the surface charge of PLGA. Redhead et al. (2001) have also reported similar reduction in the zeta potential of PLGA nanoparticles after coating with amphiphilic polymers [31]. Furthermore, when lower PVA volume ratio is used for nanoparticle fabrication, the amount of residual PVA is relatively decreased so that less shielding and subsequently higher negative zeta potential of the nanoparticles are resulted (Figs. 3.5b). The zeta potential of PLGA nanoparticles is determined by the surface charge that is influenced by the fraction of uncapped end carboxyl groups of PLGA nanoparticles. Stolnik et al. (1995) reported that zeta potential of PLGA nanoparticles without any PVA in a neutral buffer is about -45 mV [32]. Since the high negative zeta potential is mostly associated with carboxyl-terminated (uncapped end) PLGA of the nanoparticles; thus the lower negative zeta potential values measured in this study (-13 mV$<\xi<$-29 mV) is attributed to the ester-terminated PLGA used for nanoparticle fabrication.

3.4.6. Effect of fabrication variables on the loading capacity

Since PVA performs as the external aqueous phase in the second emulsification, it plays no role in the first emulsification where the loading process takes place; however, the interaction

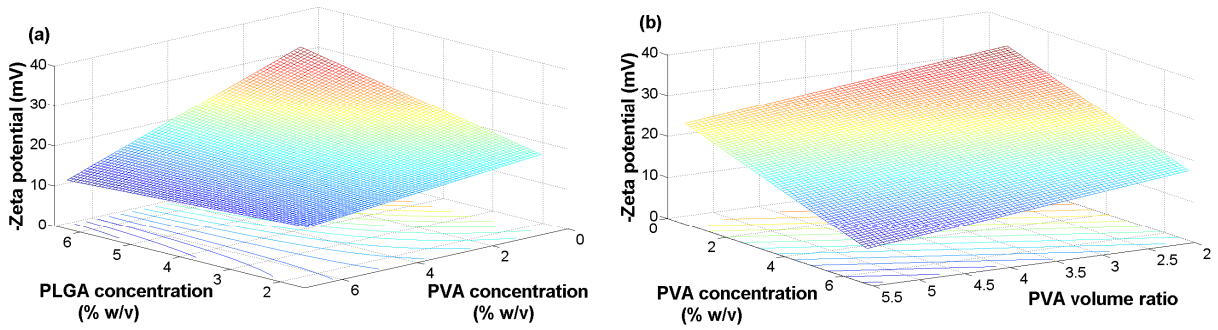

Figure 3.5. Zeta potential versus PLGA and PVA concentrations (a) and PVA concentration and external aqueous phase volume ratio (b) based on zeta potential surface equation.

between OVA and PVA concentrations can affect the loading capacity. Figure 3.6a shows a clear trend where the loading capacity increases with PVA concentration particularly for OVA concentrations above 4%. The influence of PVA on the loading capacity can be likely associated with the increased viscosity of the external aqueous phase at higher PVA concentrations that increases the difficulty of OVA to partition across the interface from the internal water phase to the external aqueous phase enhancing the retention of OVA in the particle. Figure 3.6b illustrates the variation of loading efficiency with PLGA and OVA concentrations. A clear trend where the loading efficiency decreases with increasing OVA concentration for all levels of PLGA concentration can be seen. The decreasing trend of the loading efficiency is attributed to the low entrapment capacity of the nanoparticles particularly at high PLGA concentrations which increase packing density of PLGA nanoparticles. The multiple regression equation of loading capacity (Table 3.4) confirms this effect where PLGA concentration has a negative relationship with loading capacity. The lower PLGA concentration decreases packing density of the PLGA nanoparticles providing sufficient entrapment capacity for OVA. The decreasing trend of OVA concentration leads to a higher fraction of entrapped OVA out of the present OVA in the

aqueous system, as so the loading efficiency increases (Fig. 3.6b). Figure 3.6c illustrates the variation of loading efficiency with PLGA concentration and PVA volumetric ratio. The highest loading efficiency is attained at PLGA concentration of 2.6 % (w/v) while higher packing density of the high MW PLGA nanoparticles at higher PLGA concentrations leads to lower loading efficiency for all levels of PVA volumetric ratio. As seen in Fig. 3.6c, the loading efficiency is enhanced with PVA volumetric ratio. During the secondary sonication of the double emulsion, higher PVA volumetric ratio contributes to the reduction of ultrasound power density per unit volume of the medium resulting in lower breakdown of the inner aqueous phase of the

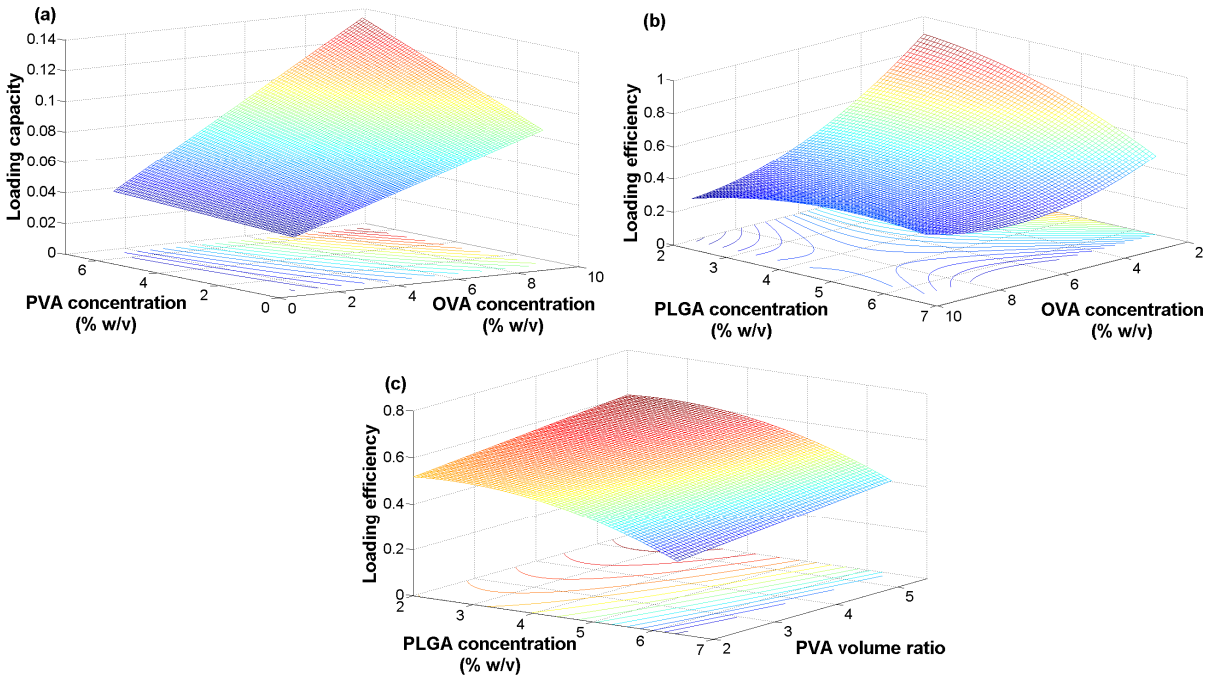

Figure 3.6. Loading capacity *versus* PVA concentration and OVA concentration at C_{PLGA}=5%, R_{PVA}=4 (a), loading efficiency *versus* PLGA concentration and OVA concentration at C_{PVA}=4%, R_{PVA}=4 (b), and loading efficiency *versus* PLGA concentration and PVA concentration at C_{OVA}=5%, C_{PVA}=5% (c).

PLGA droplets containing OVA. As such the retention of OVA in the droplets is enhanced as PVA volumetric ratio increases. The influence of PVA volumetric ratio on OVA loading efficiency becomes less significant at higher PLGA concentrations that reduce nanoparticle loading capacity due to higher packing density of PLGA in the nanoparticle structure (Fig. 3.6c).

3.4.7. Validation of the Geno-Neural model and optimal fabrication conditions

Based on training and validating datasets, an ANN model constituting of 6, 6 and 4 input, hidden and output neurons, respectively, was trained and validated, and the generalization of the model was assessed using a testing dataset. Figures 3.7a-d illustrate the correlation between measured values and predicted results from the ANN model for the testing dataset within a 5% deviation

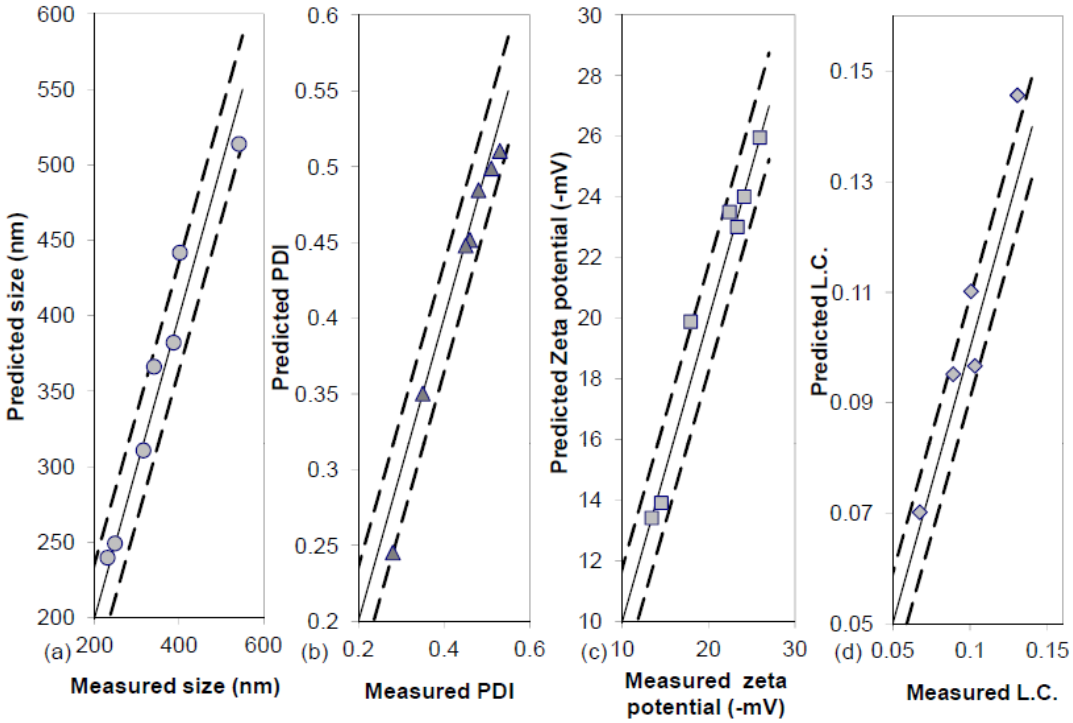

Figure 3.7. Measured values versus predicted results by the ANN model for the size (a), PDI (b), -zeta potential (c) and loading capacity (L.C.) (d) of the nanoparticles within 5% confidence limit.

limit. A mean prediction error of 4.9% and coefficients of determination of 0.96, 0.98, 0.97 and 0.93 associated with size, PDI, zeta potential, and loading capacity values predicted by the ANN model for the testing dataset suggest that the ANN model possesses a very good predictability. A comparison between the ANN model and the multiple regression equations (see Table 3.4) in terms of the mean error of predictions and coefficients of determination indicates that the ANN model has a better predictability (R^2>0.92, prediction error<5%) compared to the multiple regression equations (R^2<0.86, prediction error>7.5%). Thus, the ANN model can be used for optimization of the fabrication process of the nanoparticles. The neural network synaptic matrices ($\overline{\mathbf{M}}, \overline{\mathbf{N}}$) and vectors ($\bar{\mathbf{q}}, \bar{\mathbf{r}}$) to be used for evaluating Eq. (3.4) to predict nanoparticle characteristics are provided in appendix A. The Geno-Neural model, based on the ANN model and genetic algorithm (see Fig. 3.1), was used to search for optimum conditions within 100 generations. Figure 3.8a illustrates the variation of the best fitness values of generations during the optimization process. The best fitness value increases with evolution of generations until it becomes relatively constant after 40 generations leading to optimum fabrication conditions that result in the desired particle size (250 nm) (Fig. 3.8b), PDI<0.3 (Fig. 3.8c), lower zeta potential (<-20 mV) (Fig. 3.8d) and loading capacity>0.15 mg OVA/mg PLGA (Fig. 3.8e). Table 3.5 shows the optimum fabrication conditions corresponding to desired particle sizes of 150, 200, 250 and 300 nm. Applying the optimum conditions proposed by the Geno-Neural model to the actual experiments, the nanoparticles were prepared, characterized and compared with the Geno-Neural model predictions. Comparing the experimental results to the predicted values, except for the desired size of 150 nm, a good agreement between the measurements and predictions can be observed (Table 3.5).

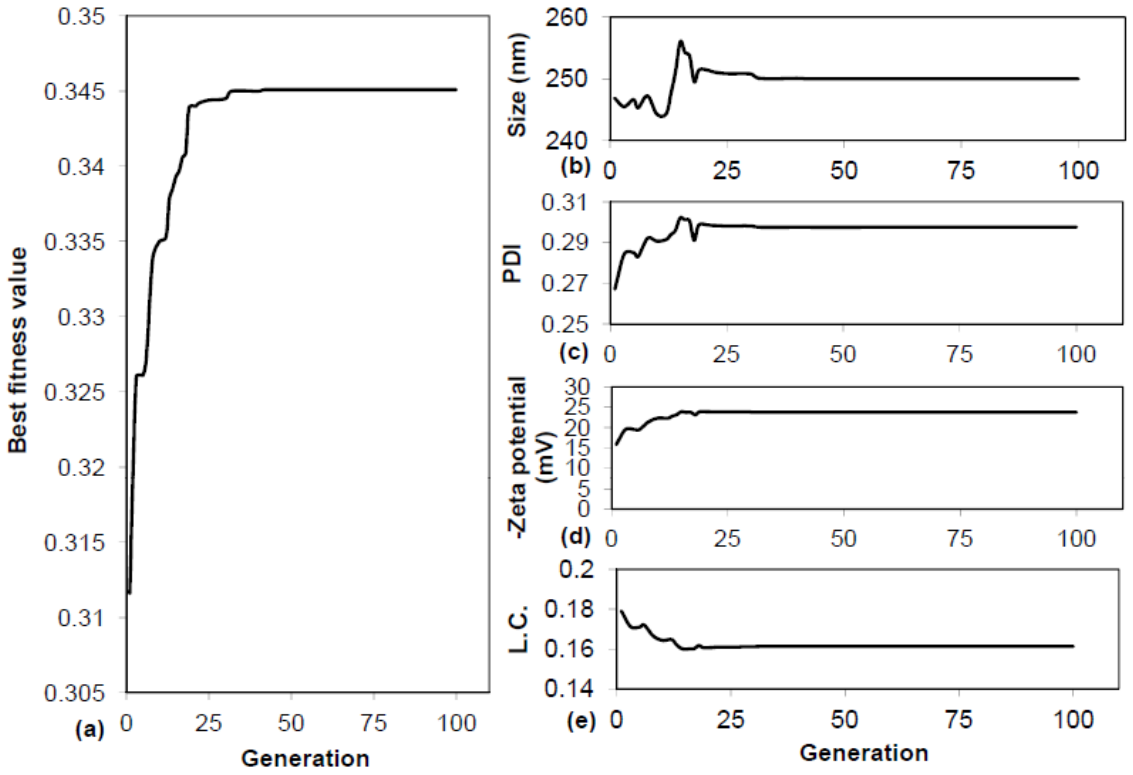

Figure 3.8. Variation of the best fitness values (a), and evolving values of nanoparticle size (b), PDI (c), -zeta potential (d), and loading capacity (e) with generations for a desired particle size of 250 nm.

3.4.8. Surface morphology of the nanoparticles

Surface morphology of the nanoparticles was assessed based on SEM images. As shown in Figs. 3.9a-c, the nanoparticles are spherical although adhered to each other after being re-suspended in water following freeze drying. A comparison between Figs. 3.9a and b shows that the presence of 1% sucrose solution during freeze drying can slightly improve the re-suspension of the nanoparticles in water. As seen in Fig. 3.9c, it seems that there are no large pores on the surface of the nanoparticles. The lack of cracks on the surface of the nanoparticles contributes to slower release properties benefiting prolonged release of growth factors (e.g. VEGF) in cardiovascular

Table. 3.5. Optimum conditions proposed by the Geno-Neural model and corresponding experimental results and predicted values of nanoparticle characteristics.

Optimum conditions						Geno-Neural model predictions				Experimental results			
C_{PVA} (%)	C_{PLGA} (%)	C_{OVA} (%)	R_{PVA}	t (s)	S (rpm)	D_p (nm)	PDI	ξ (mV)	ψ	D_p (nm)	PDI	ξ (mV)	ψ
2.9	1.6	9	3.92	90	400	150	0.21	-24	0.15	192	0.18	-19	0.15
2.6	1.6	9	4.1	57	400	200	0.26	-23	0.16	214	0.20	-20	0.15
2.3	1.6	9.4	4.1	40	400	250	0.28	-24	0.16	247	0.27	-21	0.14
2.2	2.1	9.0	3.9	42	401	300	0.29	-23	0.16	315	0.23	-25	0.16

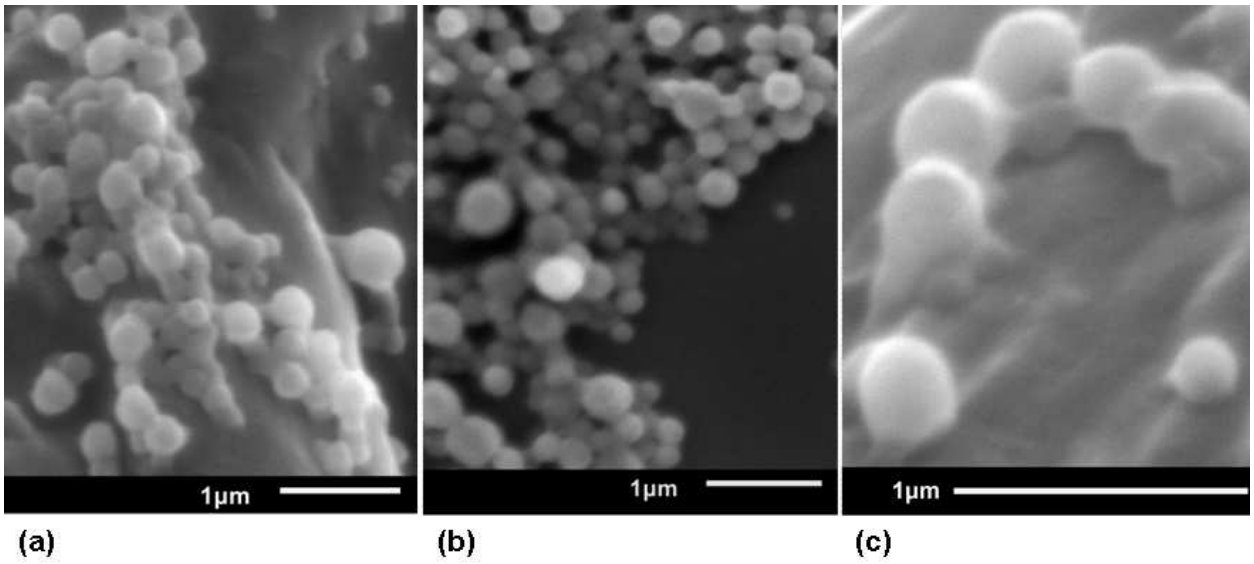

Figure 3.9. SEM images of high MW PLGA nanoparticles at PLGA concentration of 4%, PVA concentration of 3.7%, PVA ratio of 3.8, sonication time of 55 s, and stirring rate of 450 rpm in the absence (a, c) and presence of 1% sucrose (b) during freeze drying.

tissue engineering. Figure 3.9c also well depicts the spherical shape of the nanoparticles and shows that the predicted particle size is well comparable with that observed by SEM.

3.4.9. OVA release

Figure 3.10 illustrates *in-vitro* release profiles of OVA from the nanoparticles fabricated at different fabrication conditions. An initial rapid OVA release lasting for 24-36 hours of incubation can be observed for all the OVA-loaded nanoparticles prepared at different fabrication conditions; however, as seen in Fig. 3.10, depending on the fabrication conditions, the extent of the burst effect can vary from ~9% to ~38%. Following the initial burst release, OVA release rate decreases to a stable and low level. The release rate lasts about 14 days followed by an increase in release rate for the nanoparticles fabricated at a PLGA concentration of 1.6%. In contrast, the level of OVA release rate remains relatively low within 24 days for the OVA-loaded nanoparticles prepared at a PLGA concentration of 6.4% (Fig. 3.10). Comparing the OVA release pattern from the nanoparticles prepared at 1.6% PLGA to that reported by Zhao and Rodgers (2006) [33], who also visualized time-dependent bulk degradation/erosion of PLGA (75:25) microparticles, the enhanced release rate of OVA after 14 days can be attributed to the onset of the bulk degradation/erosion of PLGA matrix of the nanoparticles. Since the release of OVA in the second phase of release is mainly affected by hydration rate and PLGA degradation of the nanoparticles, a lower PLGA concentration (1.6%), which causes a lower packing density (higher porosity) of the PLGA matrix, contributes to a higher water absorption and PLGA degradation. The onset of PLGA bulk degradation/erosion improves OVA effective diffusivity [2, 33] that enhances OVA diffusion rate through the eroding nanoparticle matrix and leads to an increased OVA release rate after 14 days (Fig. 3.10). On the other hand, the higher polymer concentration of 6.8% causes a lower porosity with higher tortusity in the PLGA matrix of the

nanoparticles reducing the hydration rate with slow PLGA degradation that causes a relatively low OVA release rate within 24 days (Fig. 3.10).

3.4.10. The effects of fabrication variables on OVA burst release

Table 3.6 presents the percentage of OVA burst release (X_{burst}) estimated by fitting the modified Weibull function (Eq. (3.8)) into the experimental OVA release data using the least squares method. The sum of squared residual of ≤0.001 (with a coefficient of determination of >0.97) between experimental release data and predicted values indicate a reliable curve fitting for estimation of burst release corresponding to the fabrication variables. As shown, the burst release varies from 8.9% to 37.8% depending on the nanoparticle fabrication conditions. ANOVA analysis at a significance level of 0.05 revealed that concentrations of PVA and PLGA had

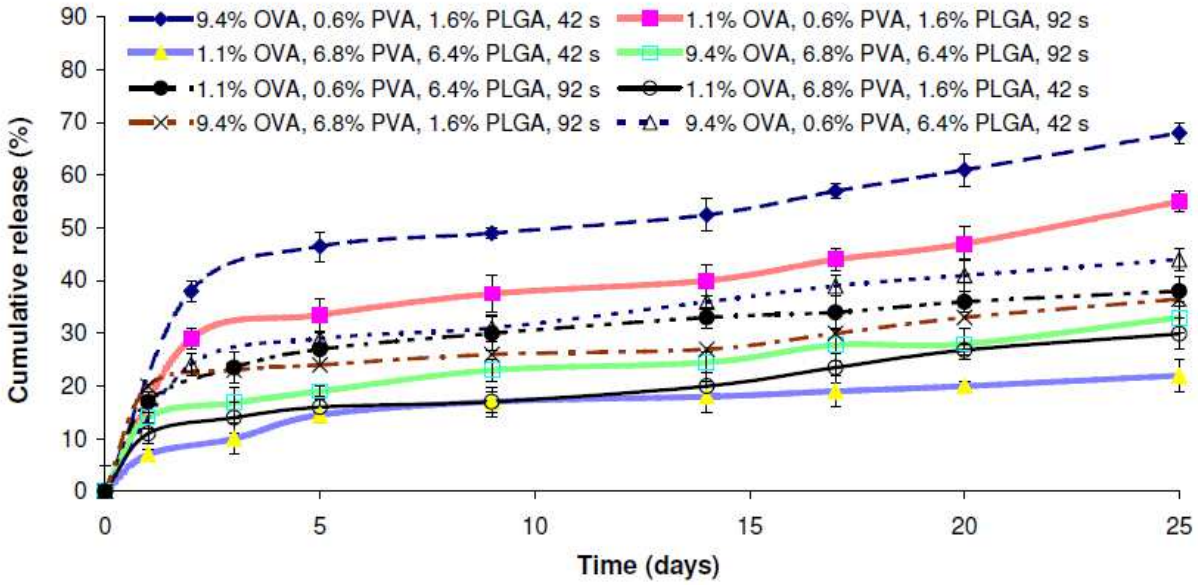

Figure 3.10. Release profiles of OVA from high MW PLGA (75:25) nanoparticles corresponding to eight different fabrication conditions.

Table 3.6. Burst release of OVA associated with different nanoparticle fabrication conditions at a stirring rate of 450 rpm and external aqueous phase ratio of 4.

Fabrication variables					
C_{OVA} (%)	C_{PVA} (%)	C_{PLGA} (%)	t (s)	Burst release (%)	SSR*
9.4	0.6	1.6	42	37.8	0.001
9.4	0.6	6.4	42	23.2	<0.001
9.4	6.8	1.6	92	21.1	<0.001
9.4	6.8	6.4	92	12.3	0.003
1.1	6.8	1.6	42	11.7	<0.001
1.1	6.8	6.4	42	8.9	0.001
1.1	0.6	1.6	92	30.1	0.001
1.1	0.6	6.4	92	15.0	<0.001

*Sum of squared residual for estimation of burst release using Eq. (3.8).

significant effects (p-value<0.05) on the burst release while OVA concentration (p-value=0.08) and sonication time (p-value=0.2) had no significant effects on the burst release. Figure 3.11 illustrates the effects of concentrations of OVA, PVA and PLGA on the burst release. As shown, OVA burst effect can be significantly decreased if higher concentrations of PVA and PLGA are used for fabrication of the OVA-loaded nanoparticles (Fig. 3.11). The effect of higher PVA concentration on reducing the burst release can be attributed to the higher viscosity of the external aqueous phase hindering the diffusivity of the encapsulated OVA in the external aqueous phase during the second emulsion. As such, the increased difficulty for OVA to diffuse to the surface of the nanoparticles contributes to more entrapped OVA within the interior of the

nanoparticles. In contrast, a low PVA concentration can result in less stable nano-emulsion with higher diffusivity of OVA in the external aqueous phase facilitating OVA mass transfer outward, causing more loosely associated OVA at the nanoparticle exterior that leads to a higher burst effect during the release process.

The higher burst effect at lower PLGA concentration can be attributed to the higher porosity (lower packing density) and lower tortusity caused by lower polymer concentration within the PLGA matrix, particularly at the nanoparticle exterior. The higher porosity coupled with lower tortusity results in a higher mass transfer surface area and enhanced effective OVA diffusion at the surface of the OVA-loaded nanoparticles contributing to an initially rapid release rate during

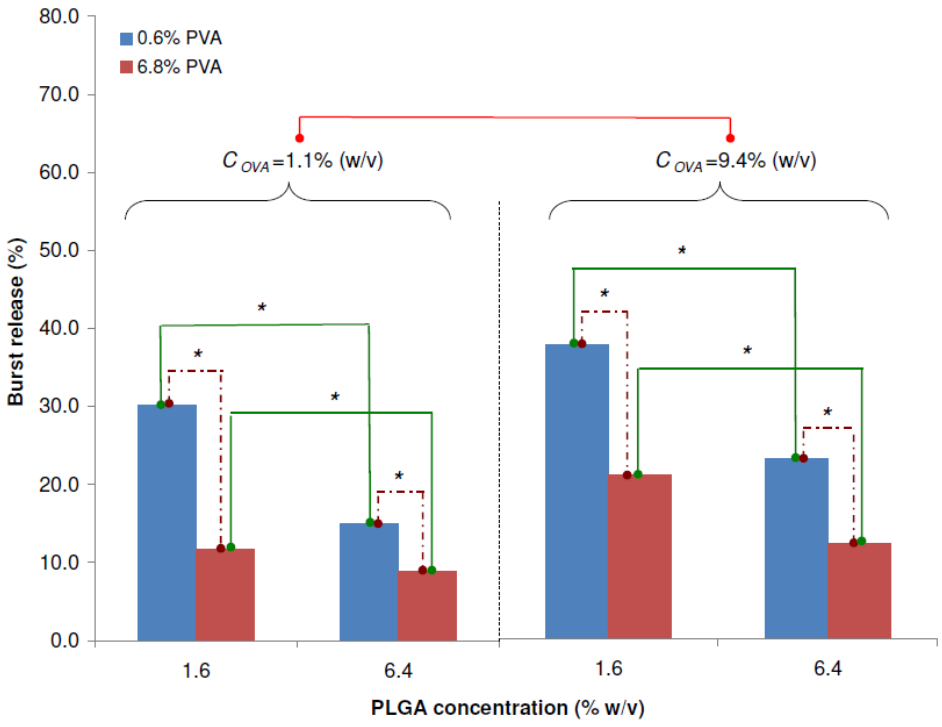

Figure 3.11. Effects of OVA, PLGA and PVA concentrations on the burst release of OVA from high MW PLGA (75:25) nanoparticles at a significance level of 0.05 (* indicates significant effect).

the release process. In contrast, a higher PLGA concentration can improve the entrapment of OVA at the nanoparticle matrix exterior due to a higher packing density leading to a lower burst effect. As shown in Fig. 3.11, although a lower OVA concentration (1.1%) can reduce the burst release, the effect of OVA concentration on the burst release is statistically insignificant (p-value=0.08). Apparently, with an increase in the amount of OVA loading, a larger protein concentration gradient from the nanoparticle interior toward the release medium is expected to form to enhance OVA diffusion rate; however, the concentration gradient associated with the OVA concentration of 9.4% (compared to that of 1.1%) may have been insufficiently high to cause a significant effect on OVA burst release in this study.

3.4.11. CD spectroscopy analyses of OVA structural integrity

Figure 3.12 illustrates CD spectra and the relative proportion of α-helix, β-sheets and random coil of the secondary structure of OVA for the standard OVA solution in PBS (150 μg/ml), the released OVA after 20 days, and the OVA encapsulated under four optimum fabrication conditions that were suggested by the Geno-Neural hybrid model (see Table 3.5). The CD spectra and the percentage of α-helix and β-sheets were consistent with the measurements (~36% α-helix and ~38% β-sheets) reported by Perkins et al. (1992) [34, 35]. As seen in Fig. 3.12a, the CD spectra of the OVA released after 20 days and the OVA encapsulated under the four optimum fabrication conditions have similar patterns as the CD spectrum of the standard OVA sample. The differences in the height of the valleys of the spectra can be attributed to the different OVA concentrations of the OVA samples. Furthermore, α-helix, β-sheets and random coil of the secondary structure of OVA of the samples have similar proportions (Fig. 3.12b). To evaluate any statistically significant difference between the secondary structure of OVA of the

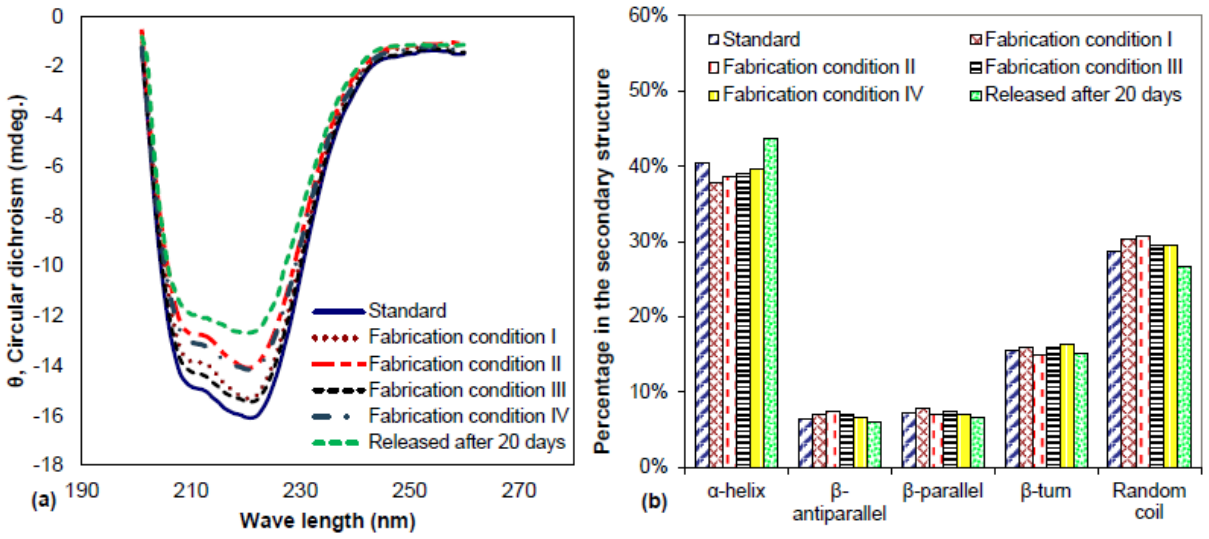

Figure 3.12. CD spectra (a) and the percentage of α-helix, β-sheets and random coil of the secondary structure of OVA standard, encapsulated OVA at four optimum nanoparticle fabrication conditions, and released OVA after 20 days.

samples and that of the standard OVA solution, an independent sample t-test was performed in SPSS at a significance level of 0.05 and the relative proportions of α-helix, β-sheets and random coil of the OVA samples were compared to those of the standard. The results from the t-test revealed that the optimum fabrication conditions (Table 3.5) and the release process within 20 days had no significant effect (p-value>0.05) on the structural integrity of OVA.

3.5. Conclusions

In this study, OVA was used as a protein model for VEGF, IGF and TGF, which are considered as the main regulating GFs in cardiovascular tissue engineering. Fabrication conditions need to be determined and optimized in order to achieve desired nanoparticle characteristics, as required in cardiovascular tissue engineering. Investigation was carried out to assess the effects of six major fabrication variables on size, PDI, zeta potential, loading capacity, loading efficiency and yield of high MW PLGA nanoparticles.

Statistical analyses revealed that PLGA and PVA concentrations were influential variables and that their interactions with other variables could significantly affect the nanoparticle properties of size, PDI, zeta potential, loading capacity and encapsulation efficiency. Multiple regression equations with reasonable standard prediction errors were derived and used for sensitivity analyses of response variables. Higher and lower PVA and PLGA concentrations, respectively, were generally beneficial to improve loading efficiency and achieve lower size and PDI of the high MW PLGA nanoparticles. Both PVA concentration and volumetric ratio directly caused the negative zeta potential to decrease. The effect of PVA concentration and volumetric ratio can be attributed to the coating PVA layer that shield the surface charge of PLGA. Attributed to the ester-terminated PLGA used for nanoparticle fabrication in this study, the highest negative zeta potential of -29 mV, was smaller than that of -45 mV reported by Stolnik et al. (1995). Most likely, due to the increased viscosity of the external aqueous phase at higher PVA concentrations, the OVA loading capacity increased with PVA concentration. Since lower concentrations of high MW PLGA can decrease the packing density of the polymer matrix of the nanoparticles, higher OVA loading capacity was resulted from lower PLGA concentrations. During the secondary sonication of the double emulsion, higher PVA volumetric ratio that contributes to the reduction of ultrasound power density per unit volume of the medium, results in enhanced loading efficiency due to lower breakdowns of the inner aqueous phase of the PLGA droplets.

An ANN model was developed and its generalization was assessed using a testing dataset. The mean prediction error of <5% and coefficients of determination of 0.96, 0.98, 0.97 and 0.93 corresponding to the size, PDI, zeta potential, and loading capacity indicated that the model had a good predictability. The ANN model parameters (see Appendix A) were compiled into Eq. (3.4) to be used in spreadsheets for general users. A Geno-Neural hybrid model was successfully

developed by coupling the ANN model with Genetic Algorithm to be used as an optimization tool to search for optimum fabrication conditions. The optimum conditions leading to PDI<0.3, higher negative zeta potentials and loading capacity for four desired sizes of 150, 200, 250, and 300 nm were obtained and experimentally validated. Except for the size of 150 nm, the Geno-Neural model could successfully predict the optimal fabrication conditions. Surface morphology assessment from SEM images showed spherical shapes of the fabricated nanoparticles that seemed to have no large pores or cracks on the surface and had sizes comparable with predicted values. Also SEM images revealed that for high MW PLGA nanoparticles, the use of 1% sucrose solution as a cryoprotectant can improve the re-suspension of the nanoparticles in water after freeze drying. While OVA release rate remained relatively low and constant within 24 days for OVA-loaded nanoparticles, which were prepared at 6.4% PLGA concentration, the release rate was enhanced at the PLGA concentration of 1.6% after 14 days. PVA and PLGA concentrations significantly affected OVA burst release while the effects of OVA concentration and sonication time on the burst release were insignificant in this study. CD spectroscopical analyses revealed that the optimum nanoparticle fabrication conditions (Table 3.5) predicted by the Geno-Neural model had no significant effect (p-value>0.05) on OVA structural integrity.

References

[1] Izadifar M, Kelly EM, Chen XB 2014 Engineering Angiogenesis for Myocardial Infarction Repair: Recent Developments, Challenges, and Future Directions. Cardiovasc. Eng. Tech. **5** 281-307.

[2] Izadifar M, Haddadi A, Chen XB, Kelly ME 2014 Rate-programming of nano-particulate delivery systems for smart scaffolds in tissue engineering. Nanotechnology 26 012001.

[3] Zhang SF, Uludag H 2009 Nanoparticulate systems for growth factor delivery. Pharm. Res. **26** 1561–1580.

[4] Danhier F, Ansorena E, Silva JM, Coco R, Le-Breton A, Préat V 2012 PLGA-based nanoparticles: An overview of biomedical applications. J Control. Release **161** 505–522.

[5] Shin S H, Lee J, Lim K S, Rhim T, Lee S K, Kim Y H and Lee K Y 2013 Sequential delivery of TAT-HSP27 and VEGF using microsphere/hydrogel hybrid systems for therapeutic angiogenesis. J Control. Release **166** 38-45.

[6] Formiga FR, Pelacho B, Garbayo E, Abizanda G, Gavira JJ, Simon-Yarza T, Mazo M, Tamayo E, Jauquicoa C, Ortiz-de-Solorzano C, Prósper F, Blanco-Prieto MJ 2010 Sustained release of VEGF through PLGA microparticles improves vasculogenesis and tissue remodeling in an acute myocardial ischemia-reperfusion model. J. Control. Release **147** 30-37.

[7] Golub JS, Kim YT, Duvall CL, Bellamkonda RV, Gupta D, Lin AS, Weiss D, Robert Taylor W, Guldberg R E 2010 Sustained VEGF delivery via PLGA nanoparticles promotes vascular growth. Am. J. Physiol. Heart Circ. Physiol. **298** H1959-65.

[8] Geng H, Song H, Qi J, Cui D 2011 Sustained release of VEGF from PLGA nanoparticles embedded thermo-sensitive hydrogel in full-thickness porcine bladder acellular matrix. Nanoscale Res. Lett. **6** 312.

[9] Simón-Yarza T, Tamayo E, Benavides C, Lana H, Formiga F R, Grama C N, Ortiz-de-Solorzano C, Kumar M N, Prosper F, Blanco-Prieto M J 2013 Functional benefits of PLGA particulates carrying VEGF and CoQ10 in an animal of myocardial ischemia. Int. J. Pharm. **454** 784-790.

[10] Wang Y, Cooke M J, Sachewsky N, Morshead C M, Shoichet M S 2013 Bioengineered sequential growth factor delivery stimulates brain tissue regeneration after stroke. J. Control. Release **172** 1-11.

[11] Lamprecht A, Ubrich N, Hombreiro Pérez M, Lehr C M, Hoffman M, Maincent P 1999 Biodegradable monodispersed nanoparticles prepared by pressure homogenization-mulsification. Int. J. Pharm. **184** 97–105.

[12] Lamprecht A, Ubrich N, Hombreiro Pérez M, Lehr C M, Hoffman M, Maincent P 2000 Influences of process parameters on nanoparticle preparation performed by a double emulsion pressure homogenization technique. Int. J. Pharm. **196** 177–182.

[13] Berchane N S, Carson K H, Rice-Ficht A C, Andrews M J 2007 Effect of mean diameter and polydispersity of PLG microspheres on drug release: Experiment and theory. Int. J. Pharm. **337** 118–126.

[14] Jimenez N, Galan J, Vallet A, Egea M A, Garcia M L 2010 Methyl trypsin loaded poly(d,l-lactide-coglycolide) nanoparticies for contact lens care. J. Pharm. Sci. **99** 1414–1426.

[15] Igartua M, Hernández R M, Esquisabel A, Gascón A R, Calvo M B, Pedraz J L 1998 Stability of BSA encapsulated into PLGA microspheres using PAGE and capillary electrophoresis. Int. J. Pharm., **169** 45–54.

[16] Kang F, Singh J 2003 Conformational stability of a model protein (bovine serum albumin) during primary emulsification process of PLGA microspheres synthesis. Int. J. Pharm. **260** 149–156.

[17] Bilati U, Allemann E, Doelker E 2005 Strategic approaches for overcoming peptide and protein instability within biodegradable nano- and microparticles. Eur. J. Pharm. Biopharm. **59** 375–388.

[18] Feczkó T, Tótha J, Dósac G, Gyenis J 2011 Optimization of protein encapsulation in PLGA nanoparticles. Chem. Eng. Process. **50** 757–765.

[19] Zhou Y Z, Alany R G, Chuang V, Wen J 2013 Optimization of PLGA nanoparticles formulation containing L-DOPA by applying the central composite design. Drug Dev. Ind. Pharm. **39** 321-330.

[20] Panyam J, Dali M M, Sahoo S K W M, Chakravarthi S S, Amidon G L, Levy R J, Labhasetwar V 2003 Polymer degradation and in vitro release of a model protein from poly(d,l-lactide-co-glycolide) nano- and microparticles. J. Control. Release **92** 173–187.

[21] Montgomery D C 1996 Design and analysis of experiments Wiley, New York.

[22] Sahu JN, Acharya J, Meikap B C 2009 Response surface modeling and optimization of chromium (VI) removal from aqueous solution using tamarind wood activated carbon in batch process. J. Hazard. Mater. **172** 818–825.

[23] Özer A, Gürbüz G, Çalımlı A, Körbahti BK 2009 Biosorption of copper(II) ions on Enteromorpha prolifera: application of response surface methodology (RSM). Chem. Eng. J. **146** 377–387.

[24] Moghaddam SS, Alavi Moghaddam MR,Arami M 2010 Coagulation/flocculation process for dye removal using sludge from water treatment plant: optimization through response surface methodology. J. Hazard. Mater. **175** 651–657.

[25] Myers R H, Montgomery DC 2002 Response surface methodology: process and product optimization using designed experiments Wiley, New York.

[26] Izadifar M 2005 Neural network modeling of trans isomer formation and unsaturated fatty acid changes during oil hydrogenation. J Food Eng **66** 227–232.

[27] Izadifar M, Abdolahi F 2006 Comparison between neural network and mathematical modeling of supercritical CO2 extraction of black pepper essential oil. J. Supercrit. Fluids **38** 37–43.

[28] D'Souza S S, Faraj J A, DeLuca P P 2005 A model-dependent approach to correlate accelerated with real-time release from biodegradable microspheres. AAPS Pharm Sci Tech **6** E553–564.

[29] Wang J, Wang B M, Schwendeman SP 2002 Characterization of the initial burst release of a model peptide from poly(d,l-lactide-co-glycolide) microspheres. J. Control. Release **82** 289–307.

[30] Budhian A, Siegel SJ, Winey KI 2007 Haloperiodol-loaded PLGA nanoparticles: systemic study of particle size and drug content. Int. J. Pharm. **336** 367-375.

[31] Redhead HM, Davis SS, Illum L 2001 Drug delivery in poly (lactide-co-glycolide) nanoparticles surface modified with copoloxamer 407 and poloxamine 908: in vitro characterization and in vivo evaluation. J. Control. Release **70** 353–363.

[32] Stolnik S, Garnett MC, Davies MC et al. 1995 The colloidal properties of surfactant-free biodegradable nanospheres from poly (b-malic acid-co-benzyl malate)s and poly (lactic acid- co-glycolide) Coll. Surf. 97 235-245.

[33] Zhao A, Rodgers VG J 2006 Using TEM to couple transient protein distribution and release for PLGA microparticles for potential use as vaccine delivery vehicles. J. Control. Release **113** 15-22.

[34] Perkins SJ, Smith KF, Nealis AS, Haris PI, Chapman D, Bauer CJ, Harrison RA 1992 Secondary structure changes stabilize the reactive-centre cleaved form of SERPINs. A study by H nuclear magnetic resonance and Fourier transform infrared spectroscopy. J. Mol. Biol. **228** 1235–1254.

[35] Koseki T, Kitabatake N, Doi E 1988 Conformational Changes in Ovalbumin at Acid pH. J. Biochem. **103** 425-430.

CHAPTER 4

REQULATION OF SEQUENTIAL RELEASE OF GROWTH FACTORS USING BI-LAYER POLYMERIC NANOPARTICLES FOR CARDIAC TISSUE ENGINEERING

“This chapter has been submitted as “M. Izadifar, M. Kelly, and X. B. Chen, 2016, Regulation of Sequential Release of Growth Factors using Bi-layer Polymeric Nanoparticles for Cardiac Tissue Engineering, *Nanomedicine* (Under Review)” According to the Copyright Agreement, "the authors retain the right to include the journal article, in full or in part, in a thesis or dissertation".

4.1 Abstract

Cardiac tissue engineering aims to develop engineered constructs for myocardial infarction repair, where a challenge is the control of sequential release of growth factors (GFs). Bi-layer polymeric nanoparticles composed of a GF-encapsulating core surrounded by an adjustable shell thickness have been developed for sequential GF release. The bi-layer nanoparticles featured low burst effect, structural integrity of the encapsulated protein and time-delayed release patterns. Allowing for adjusting the timing of release, preconditioned nanoparticles demonstrated bioactive in the context of angiogenesis. The bi-layer nanoparticles successfully regulated sequential release of platelet-derived GF following co-release of vascular endothelial GF and basic fibroblast GF, and significantly promoted angiogenesis in fibrin matrix. Moreover, a novel Geno-Neural model was developed and validated for rate-programming of the nanoparticles.

4.2. Introduction

Myocardial infarction (MI) is the most common cause of heart failure. Current therapies can only slow down the progression of heart failure, but not tackle the progressive loss of cardiomyocytes

after heart attack [1-3]. Cardiac tissue engineering aims to develop implantable constructs (e.g., cardiac patches) that provide physical and biochemical cues allowing for myocardium regeneration [4, 5]. To this end, spatiotemporal control of growth factor (GF) release is of critical importance and yet remains unachievable [6]. GF immobilization and non-covalent encapsulation, which have been used in previous studies [7-14], suffer from limited control over the release rate and the possible loss of GF bioactivities due to covalent bonding and cleaving reactions for immobilization and release, respectively [14, 15]. Recent advances in polymeric particulate delivery systems enable improvements over the control of GF release [14]. Among various polymers, the use of poly(lactide-co-glycolide) (PLGA) and poly(L-lactide) (PLLA) stands out due to their biocompatibility, biodegradability, and approval for use by the Food and Drug Administration and European Medicine Agency [16]. Recent studies have employed PLGA microparticles to control GFs for improving angiogenesis in myocardial ischemia [17-21]. The commonality in these studies is the use of single polymer microparticles, which are severely undermined by several limitations including the initial burst effect, difficulty in achieving zero-order release kinetics, and lack of time-delayed release pattern.

To overcome the above limitations, we present a polymeric nano-particulate delivery system including bioactive bi-layer nanoparticles for simultaneous and/or sequential release of multiple GFs, such as vascular endothelial GF (VEGF), basic fibroblast GF (bFGF), and platelet derived GF (PDGF). The core-shell composition, structure, surface morphology, protein localization, release kinetics and physical properties of the nanoparticles are characterised, and the structural integrity of the encapsulated protein are assessed over 70 days of release. The bioactivity of the nanoparticles is assessed using rat aortic ring bioassay. A combination of PLGA and bi-layer nanoparticles are employed to regulate three release scenarios of VEGF release only, co-release

of VEGF and bFGF, and sequential release of PDGF following VEGF and bFGF, which are statistically compared in the context of angiogenesis in fibrin matrix of a cardiac patch. Furthermore, a predictive Geno-Neural model is developed, validated and applied for pre-programming of release rates of the polymeric nanoparticles to provide pre-determined release patterns of interest. The predictability of the model is statistically assessed using the experimental data from release kinetics study and the measured values of physical and polymeric characteristics of the nanoparticles.

4.3. Materials and methods

Capped and uncapped PLGA with an average inherent viscosity of 0.2 and 0.65 dL/g (in chloroform), respectively, and capped PLLA with an average inherent viscosity of 0.9 dL/g (in chloroform) were purchased from DURECT (DURECT Co., Cupertino, CA). Ovalbumin (OVA), polyvinyl alcohol (PVA) (MW=31,000-50,000), phosphate-buffered saline (PBS), bovine serum albumin (BSA), sodium bicarbonate, HPLC grade dichloromethane (DCM), MEM-10x, and Bicinchoninic acid ***(BCA)*** protein ***assay kits were received from*** Sigma (Sigma-Aldrich, MO). OVA Texas Red® Conjugate, human recombinant VEGF, bFGF, PDGF, and gentamicin were purchased from Life Technologies Thermo Fisher Scientific Inc. (Life Technologies, Grand Island, NY). Fibrinogen and thrombin were received from Baxter Healthcare Corporation (Westlake Village, CA) and essential basal medium (EBM) was purchased from Lonza (Lonza, Allendale, NJ). Sodium hydroxide and sodium dodecyl sulphate (SDS) were the products of Life Technologies Thermo Fisher Scientific Inc. (Life Technologies, Grand Island, NY).

4.3.1. Fabrication of bi-layer and single polymer nanoparticles

A water-in-oil-in-oil-in-water (W/O/O/W) double emulsion solvent extraction technique was modified to fabricate the bi-layer nanoparticles. PLLA and PLGA polymers were separately dissolved in DCM at concentrations of 16.6, 20, and 23.5% (w/v). The internal aqueous phase (IAP), consisting of OVA (20 μg/mL), sucrose (10%), and sodium bicarbonate (6.7%) in PBS, was added to the PLGA organic phase followed by sonication for 50 s at 40 W. The emulsion was gently mixed with PLLA solution on a vortex mixer to obtain a uniform cloudy solution. The mixture was then sonicated at 40 W for 120 s. PVA was added to the emulsion, which was subsequently sonicated at 70 W for 120 s. The emulsion was added drop-wise to a DCM-saturated PVA solution (0.5%) stirring at 450 rpm. After 24 h, the nanoparticles were collected by ultracentrifugation (Optima L-Series, Becman Coulter Inc., Palo Alto, CA) at 15,000 rpm for 30 min, and washed three times with de-ionized water. Nanoparticles were re-suspended in de-ionized water containing sucrose (1%) as the cryoprotectant and then stored at -20 °C. The above procedure was applied to the preparation of angiogenic factor-loaded bi-layer nanoparticles where human recombinant VEGF, bFGF, and PDGF in sterile 0.2% BSA solution were used instead of OVA with sodium bicarbonate and sucrose as buffering and stabilizing agents in the IAP.

To be able to cross section the core-shell structures and assess the internal structure and morphology, bi-layer microspheres were also prepared by adding the IAP to a PLGA solution that was subsequently homogenized at 3000 rpm for 1 min. The emulsion was added to the PLLA solution and homogenized at 5000 rpm for 3 min followed by adding the emulsion to the stirring PVA solution. The microparticles were collected after 24 h by centrifugation at 8000 rpm for 10 min. The collected microparticles were washed with de-ionized water, freeze-dried, and

then stored at -20 °C. For protein localization assessment using fluorescence microscopy, OVA Texas Red® Conjugate was used as the encapsulated protein.

Single polymer (PLGA) nanoparticles were prepared using a water-in-oil-in-water (W/O/W) double emulsion method. Polymers with different lactide to glycolide (L:G) ratios were dissolved in DCM at total concentrations of 3, 7, and 9% (w/v). The IAP was added to the organic phase followed by sonication at 20 W for 50 s. The external aqueous phase was then added to the W/O emulsion and sonicated for 120 s at 40 W followed by adding the emulsion to a PVA solution (0.5%) that was allowed to stir for 24 h at 450 rpm at room temperature. Six experimental conditions featuring different polymer characteristics were used to prepare the single polymer and bi-layer nanoparticle groups compared in this study (Table 4.1).

Table 4.1. Polymer characteristics of the experimental groups.

Characteristics	Experimental Group					
	A	B	C	D	E	F
PLGA concentration (%)	4.0	7.0	9.0	16.6	16.6	16.6
PLLA viscosity (dL/g)	n/a	n/a	n/a	0.9	0.9	0.9
PLGA viscosity (dL/g)	0.20	0.65	0.20	0.65	0.65	0.65
Terminal group	Acid	Ester	Ester	Ester	Ester	Ester
L:G ratio	50:50	50:50	75:25	50:50	50:50	50:50
PLLA/PLGA mass ratio	0	0	0	1	2	3

4.3.2. Preparation of nanoparticle-incorporated fibrin matrix

Nanoparticle-incorporated fibrin gel was prepared at fibrinogen concentrations of 1 and 4 mg/mL. Three hundred μg of nanoparticles were re-suspended in 800 μL of PBS on the vortex

mixer. Then, 50 and 200 µL of a fibrinogen solution (40 mg/mL) in calcium chloride were mixed with the PBS solution containing the nanoparticles, resulting in 2 and 8 mg/mL fibrinogen solutions, respectively. Addition of thrombin (2 U/mL) to the fibrinogen solutions initiated polymerization, resulting in fibrin gels at final fibrinogen concentrations of 1 and 4 mg/mL. Immediately after mixing with thrombin, the fibrinogen solutions were transferred into a disk-shaped mold and incubated at 37 °C to allow for complete polymerization. The nanoparticle-incorporated fibrin matrices were used for surface morphology assessment.

4.3.3. Structural characterization and morphological analyses

The size, polydispersity index (PDI), and zeta potential of the nanoparticles were measured using Dynamic Light Scattering (Zetasizer, Nano ZS3000; Malvern Instruments, Malvern, UK) based on backscattering detection at a scattering angle of 173° at 25 °C. Scanning electron microscopy (SEM) was used to examine the surface morphology of the nanoparticles. Freeze-dried nanoparticles were re-suspended in distilled water followed by placing one droplet of the suspension on a carbon tape attached to SEM stubs, which were subsequently allowed to dry for 24 h at room temperature. The samples were coated with a thin layer of gold with a Sputter Coater (S150B, Edwards, Crawley, UK) and then examined using a field-emission scanning electron microscope (JSM-6010 LV, JEOL, Ltd., Tokyo, Japan) at 5-15 kV.

To visualize and characterize the internal core-shell structures, bi-layer microspheres were suspended in a solution of gelatine (20%) and glycerine (5%) for 8 h at room temperature. The suspension was then transferred into a cryostat mold and frozen at -80 °C for 1 h. The mold was placed over liquid nitrogen and then the gelled suspension removed and sectioned at a thickness of 8-14 µm using a cryostat at -30 °C. The sections were mounted on carbon tape attached to SEM metal stubs, dehydrated for 24 h, coated with gold, and then imaged using SEM.

Morphological analyses of the nanoparticle-incorporated fibrin matrix were performed at two final fibrinogen concentrations of 1 and 4 mg/mL and a thrombin concentration of 1 U/mL. After preparation of the nanoparticle-incorporated fibrin, an appropriate size of the gel was cut using a scalpel blade, placed on a carbon tape attached to a stub, and then freeze dried at -80 °C for 24 h. The freeze-dried sample was gold-coated and imaged using SEM (JSM-6010 LV, JEOL, Ltd., Tokyo, Japan) at 5 kV.

4.3.4. Identification of core and shell polymeric compositions

Under an inverted phase contrast microscope, cross-sectioned bi-layer microparticles were viewed to visualize core-shell structures. An ethyl acetate assay [22] based on the different solubilities of PLLA and PLGA in ethyl acetate was applied to determine the core and shell polymeric composition. The microscope slides holding the microparticle cross sections were immersed in ethyl acetate for 12 h, and then the remnants of the core-shell structure were visually characterized under the microscope. Because the solubility of PLGA (580 mg/mL) in ethyl acetate is much higher than PLLA (0.1 mg/mL) [23], a hollow structure (ring shape) or solid core of the remnant would indicate that PLLA mainly constituted the shell or core, respectively. The experiment was performed at different PLLA and PLGA mass ratios to evaluate the effect of polymer mass ratio on the core-shell polymer orientation. The surface morphology of ethyl acetate-treated cross sections of PLLA shells was assessed at three solvent removal conditions that may affect PLLA-PLGA phase separation during particle preparation. SEM imaging and quantitative image analysis of PLLA shells using ImageJ software (National Institutes of Health, Bethesda, Maryland, USA) was employed to examine the uniformity of the shell texture. Pixel intensity standard deviation across an area of 0.01 mm^2 was used as a

criterion to evaluate shell texture uniformity, on which the best solvent removal rate was determined and applied to the nanoparticle preparation procedure.

4.3.5. Encapsulation capacity and release kinetics

Measurement of the loading capacity of the bi-layer and single polymer (PLGA) nanoparticles was based on extracting and quantifying OVA from the nanoparticles. Nanoparticles were dispersed in 0.1 M sodium hydroxide containing 5% SDS, and incubated at room temperature overnight in an orbital shaker. The supernatant was collected by centrifugation at 15000 rpm for 10 min. A BCA assay kit (Sigma-Aldrich, MO) was used and OVA concentration was quantified by reading the absorbance of the samples at 562 nm with a UV spectrophotometer (Synergy HT, BioTek Instruments, Inc., Winooski, VT). Loading capacity was then calculated as

$$\psi = \frac{C_{OVA}}{C_{NP}} \tag{4.1}$$

where ψ is the loading capacity (mg OVA/mg nanoparticles), C_{OVA} is OVA concentration from the direct extraction (mg OVA/mL), and C_{NP} is the OVA-loaded nanoparticle concentration (mg/mL). An *in-vitro* release study was conducted based on direct measurement of OVA released from the nanoparticles in the release medium. A given amount of nanoparticles was transferred into glass vials containing PBS. Vials were placed in a swinging sample holder mounted on an orbital shaker to provide rotational and axial shaking (200 rpm) at 37 °C. At predetermined time intervals over 70 days, 800 µL of the nanoparticle suspension were withdrawn from each vial and centrifuged at 10,000 rpm. Then 450 µL of the supernatant, subsequently replaced by 450 µL fresh PBS, were removed and the OVA concentration quantified. The nanoparticle pellet in the centrifugation tube was re-suspended in the fresh PBS on a vortex mixer and then the contents (800 µL) transferred into the corresponding vial on an

orbital shaker. The experiment was carried out in triplicate for all polymeric mass ratios. The concentration of OVA was measured based on the absorbance of the solution at 562 and 572 nm using a UV spectrophotometer (Synergy HT, BioTek Instruments, Inc., Winooski, VT).

4.3.6. Localization of the loading protein in the double-layered structures

To evaluate the protein distribution across core-shell structures, PLGA and bi-layer microspheres were loaded with fluorescent OVA (OVA Texas Red® Conjugate), cross sectioned, and observed using fluorescence microscopy. The microspheres, which were prepared at PLLA/PLGA mass ratios of 0, 1, 2, and 3, were embedded in resin, cross sectioned at 10 µm, and then observed using fluorescence and bright field phase contrast microscopy. Superimposed bright field and fluorescence microscopy images were used for protein distribution mapping across the core and shell. For each selected microparticle, the cross section with the largest diameter, which most likely represented the cross section at the center of the microparticle, was used for quantitative assessment of the protein distribution across the core and shell. Average fluorescence intensity profiles and the area under the curve associated with the composite images of the cross sections were determined in ImageJ software and used as measures for comparing protein distribution and encapsulation across the microparticles at different PLLA/PLGA mass ratios.

4.3.7. Circular dichroism (CD) spectroscopy

A Chirascan Plus CD Spectrometer (Applied Photophysics, Surrey, UK) was used to record CD spectra to assess the structural integrity of OVA during the release process from the bi-layer nanoparticles. CD spectra were collected at a scan time of 0.5 s per point with a step size of 1 nm from 205 to 260 nm at 20 °C using a quartz cell with a 0.1 cm path length. The recorded data were averaged over five scans and expressed as millidegrees. An OVA solution in PBS was used

as the control sample while the buffer (sucrose and bicarbonate in PBS) was used to compensate for noise in the spectroscopic analysis. OVA samples, which were collected within the first 18 h, were used to assess the effect of the fabrication conditions on the structural integrity of the encapsulated protein based on CD spectra analyses. OVA samples were also collected after 7, 25, and 50 days to assess the protein structural integrity during the release process from the single and bi-layer nanoparticles. Samples were filtered using a 0.45 μm filter syringe, and degassed at 560 mmHg at 25 °C for 1 h before being subjected to CD spectroscopic analysis. Deconvolution of the CD spectra was conducted using CD Spectra Deconvolution software Ver. 2.1 (Gerald Böhm, Germany) to estimate the percentage of proteins in the samples featuring alphahelix, anti-parallel and parallel beta sheet, beta-turn, and random coil structures. The recorded CD spectra and the deconvolution results were statistically compared to those of the controlled OVA sample to assess the structural integrity of the proteins.

4.3.8. *Ex vivo* angiogenesis study for angiogenic factor-loaded nanoparticle bioactivity

The rat aortic ring assay, which is considered a physiologically relevant angiogenesis model similar to that observed *in vivo* [24], was used to assess the bioactivity of angiogenic factor-encapsulating nanoparticles and evaluate the performance of the nano-particulate delivery system with respect to providing simultaneous and sequential release of multiple angiogenic factors. Two-month old rats were euthanized by carbon dioxide and their thoracic/abdominal skin shaved and then disinfected using 70% ethanol. Each rat was pinned down in supine position on a dissection board covered with a sterile impermeable pad. From the shoulders downward medially to the lower abdomen, a Y-shape incision was made, the ribs cut to expose the thoracic cavity, and then the sternal plate displaced to the upper side of the animal with a haemostat (Fig. 4.1a). After cutting the diaphragm and displacing the abdominal organs, the thoracic aorta (yellow

arrow in (Fig. 4.1b) was exposed and a knot tied just below the diaphragm at the distal end of the aorta using a 2-0 silk suture (blue arrow in Fig. 4.1b) with a reverse cutting needle (green arrow in Fig. 4.1b). While holding the suture, the aorta was dissected and excised at the aortic arch as close as possible to the heart (white arrow in Fig. 4.1b) using sterile micro-dissection scissors and forceps. The aorta was immediately transferred into EBM on ice. Attention was given to perform the procedure in less than 15 min, excluding the euthanasia time, and to hold the aorta only by the suture at all times to avoid damaging the endothelium. Submerged in EBM containing gentamicin, the isolated aorta was carefully cleaned of fibroadipose tissue, fat, and blood using sterile micro-dissection scissors and curved forceps under a dissection microscope (Fig. 4.1c).

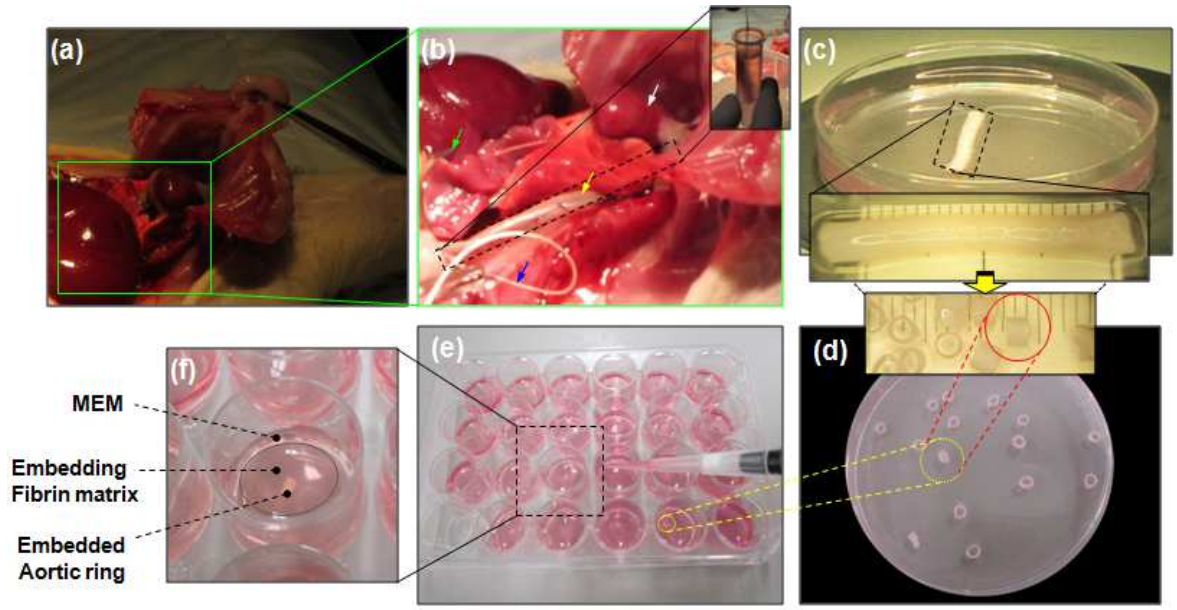

Figure 4.1. The procedure for (a) dissection and (b) excision of the rat aorta, (c) cleaning and (d) cutting the aorta into ~1.5 mm rings in EBM, and (e) transferring the rings into a 24-well culture plate and (f) embedding the aortic rings in nanoparticle-incorporated fibrin matrix in MEM.

During the 60-min cleaning procedure, the aorta was transferred into a new petridish containing fresh EBM every 10 min. The aorta was cut into 1-1.5 mm rings using a scalpel blade (Fig. 4.1c). Excluding the rings from either end, the aortic rings were washed five times in EBM before being transferred into a 24-well tissue culture plate (Fig. 4.1d). VEGF, bFGF, and PDGF- loaded nanoparticles were added to 200 μL of MEM (10x) followed by shaking on a vortex mixer to re-suspend the nanoparticles in the solution. The amount of nanoparticles was calculated based on the loading capacity and the desired release rate over the angiogenesis study as:

$$M_{np} = \sum_{i=1}^{n=15} \frac{\dot{m_d}\, t_i}{\Delta X(t_i)\psi} \tag{4.2}$$

where M_{np} is the estimated average amount of protein-loaded nanoparticles (mg), $\Delta X(t_i)$ is the time-dependent cumulative (fractional) release, t is time (day), $\dot{m_d}$ is the desired release rate (mg/day), and ψ is the loading capacity (mg/mg). The numerator represents the total delivered dose over the release time of 15 days. Based on Eq. (4.2), the mass of required nanoparticles was calculated to obtain total doses of ~30, ~60, and ~10 ng/day for VEGF, bFGF, and PDGF, respectively.

Fibrinogen (200 μL) at 40 mg/mL in calcium chloride that contained 10 μg/mL of aprotinin was mixed with the nanoparticle-containing MEM solution. PBS was added to the mixture to obtain a total volume of 1 mL with a fibrinogen concentration of 8 mg/mL. Then, 60-μL aliquots of the fibrinogen solution were prepared and kept on ice. Aortic rings (three rings at a time) were transferred into the center of wells of a 24-well culture plate (Fig. 4.1e). Sixty μL of thrombin (2 U/mL) were mixed with each 60-μL aliquot. The fibrin solution at a concentration of 4 mg fibrinogen/mL was then applied to embed each aortic ring in the culture plate wells, which were

then incubated at 37 °C for 30 min. After incubation, MEM-containing gentamicin with or without angiogenic factor-loaded nanoparticles was added to the wells (Fig. 4.1f).

Because the release lag phase of the bi-layer nanoparticles was beyond the duration of the entire experiment, the time-delayed release was adjusted by pre-conditioning the angiogenic factor-loaded bi-layer nanoparticles in MEM/PBS for 25 days before being used in the fibrin matrix and MEM. Single polymer (PLGA) and bi-layer nanoparticles, which were loaded with VEGF and/or bFGF and/or PDGF, were employed to provide simultaneous and sequential GF release compared to VEGF release alone. Saline-loaded nanoparticles were used as control samples in all experiments.

The aortic rings were viewed and monitored under a phase-contrast inverted microscope each day. Sprouting microvessels were quantitatively (e.g., number of vessels, maximum sprout length, and sprouting rate of new microvessels) and qualitatively (colocalization of endothelial cells and pericytes, microvessel regression phase) assessed on a daily basis and statistically compared to the control sample at a significance level of 0.05. ImageJ software (National Institutes of Health, Bethesda, Maryland, USA) was used for image analyses. Experiments were conducted in six replications.

4.3.9. Development of a Geno-Neural model for rate-programming of the nanoparticles

A Geno-Neural model consisting of a trained artificial neural network (ANN) coupled with genetic algorithm (GA) was developed to predict optimum combinations of multiple physical and polymeric variables of the nanoparticles in order to achieve a pre-determined release pattern(s). GA is based on the principal of ‘survival of the fittest’ and biological concepts of genetics and evolution. In this study, the DNA of each individual consists of 7 genes which are defined as the nanoparticle physical and polymeric characteristics of PLGA concentration,

viscosity, G:L ratio, ester/carboxyl terminal group, and PLLA/PLGA mass ratio, nanoparticle size and PDI (Fig. 4.2). The ANN that simulate human brain analytical function consists of input, intermediate and output neurons which sum weighted inputs and apply a transfer function from which the results propagate to the succeeding neurons. The ANN is trained by adjusting the synaptic weights using training and validating datasets to learn the relationships between inputs and outputs. In this study, 80, 10, and 20% of the experimental data pool from the release study as well as the measurements of loading capacity, were randomly divided to training, validating, and testing datasets. Release information associated with bi-layer nanoparticles of group E was entirely transferred to the testing dataset to assess the predictability and generalization of the ANN. Eight variables including release time and nanoparticle characteristics were assigned to the input neurons, and cumulative release and loading capacity were considered as the outputs of the ANN.

Inputs and outputs were normalized between -1 and +1 to improve the training process, and the ANN was trained using a Backpropagation training algorithm based on Bayesian Regularization combined with the Levenberg–Marquardt method in MATLAB 7.4 [25, 26]. Tangent hyperbolic and linear transfer functions were assigned to the hidden and output neurons, respectively (Fig. 4.2). Synaptic weights (Appendix B) of the tested neural network architecture were compiled into a mathematical model expressing a relationship between nanoparticle physicochemical design parameters and the release characteristics:

$$\begin{bmatrix} \vartheta_n \\ \psi_n \end{bmatrix} = \overline{\mathbf{N}} \times \begin{bmatrix} \dfrac{e^{(\overline{\mathbf{M}}_1 \times \overline{\mathbf{P}} + q_1)} - e^{-(\overline{\mathbf{M}}_1 \times \overline{\mathbf{P}} + q_1)}}{e^{(\overline{\mathbf{M}}_1 \times \overline{\mathbf{P}} + q_1)} + e^{-(\overline{\mathbf{M}}_1 \times \overline{\mathbf{P}} + q_1)}} \\ \vdots \\ \dfrac{e^{(\overline{\mathbf{M}}_4 \times \overline{\mathbf{P}} + q_4)} - e^{-(\overline{\mathbf{M}}_4 \times \overline{\mathbf{P}} + q_4)}}{e^{(\overline{\mathbf{M}}_4 \times \overline{\mathbf{P}} + q_4)} + e^{-(\overline{\mathbf{M}}_4 \times \overline{\mathbf{P}} + q_4)}} \end{bmatrix} + \overline{\mathbf{r}} \tag{4.3}$$

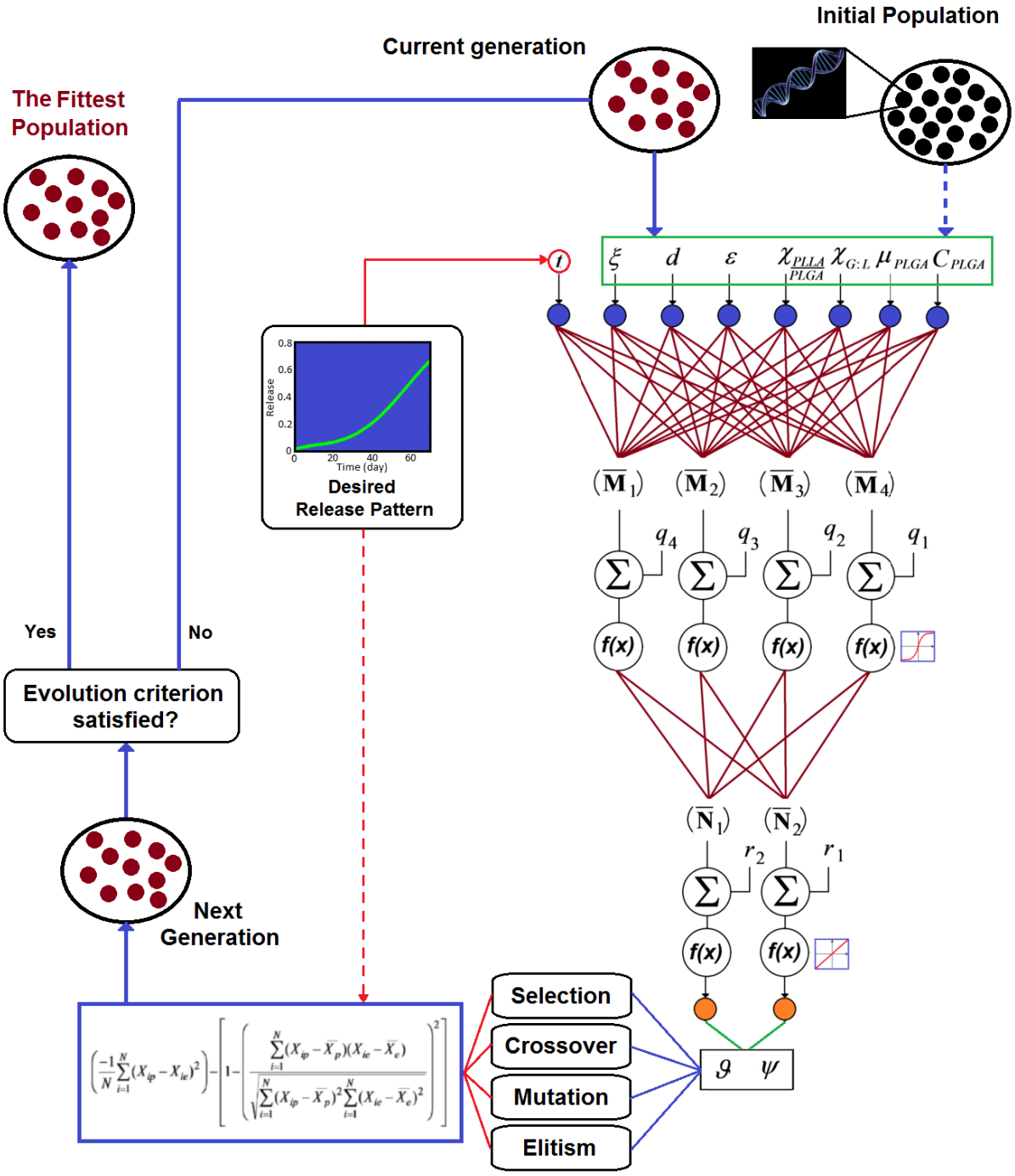

Figure 4.2. Schematic diagram of the Geno-Neural approach for rate-programming of nanoparticles.

where ϑ_n and ψ_n are normalized values of predicted cumulative release and loading capacity (μg/mg), respectively; $\overline{\mathbf{M}}_{1-4}$ and q_{1-4} are the synaptic weights and bias vector, respectively, corresponding to the 1st to 4th neurons of the hidden layer; $\overline{\mathbf{N}}$ and $\bar{\mathbf{r}}$ are the synaptic weights and bias vectors corresponding to the neurons of the output layer, respectively; and $\overline{\mathbf{P}}$ is the input vector normalized between -1 and +1 and defined by eight physicochemical parameters of the nanoparticles as:

$$\overline{\mathbf{P}} = \begin{bmatrix} C_{PLGA} \\ \mu_{PLGA} \\ \chi_{G:L} \\ \chi_{PLLA:PLGA} \\ \varepsilon \\ d \\ \xi \\ t \end{bmatrix} \tag{4.4}$$

where C_{PLGA}, μ_{PLGA}, and $\chi_{G:L}$ are PLGA concentration (%), inherent viscosity in chloroform (dg/L), and G:L ratio, respectively; $\chi_{PLLA:PLGA}$ is PLLA to PLGA mass ratio; ε is the PLGA terminal group (0 for carboxyl and 1 for ester); d is the average size of the nanoparticles (nm); ξ is PDI; and t is the release time (day). The normalized values of ϑ_n and ψ_n are converted to the actual values of cumulative release and loading capacity using:

$$\begin{bmatrix} \vartheta \\ \psi \end{bmatrix} = \frac{\left(\begin{bmatrix} \vartheta_n \\ \psi_n \end{bmatrix} + 1\right)\left(\begin{bmatrix} \vartheta \\ \psi \end{bmatrix}_{\max} - \begin{bmatrix} \vartheta \\ \psi \end{bmatrix}_{\min}\right) + 2\begin{bmatrix} \vartheta \\ \psi \end{bmatrix}_{\min}}{2} \tag{4.5}$$

where $\begin{bmatrix} \vartheta \\ \psi \end{bmatrix}_{\max}$ and $\begin{bmatrix} \vartheta \\ \psi \end{bmatrix}_{\min}$ are the vectors of the upper and lower boundaries, respectively, of cumulative release and loading capacity corresponding to the training dataset.

GA is coupled with the trained ANN in such a way the genes of the initial population, which are randomly generated, are assigned to the ANN, while the time variable is defined by the release

pattern of interest (desired release pattern) (Fig. 4.2). The ANN predicts the release profiles and loading capacity corresponding to the genes of the initial population, which are subsequently compared to the desired release profile to compute fitness values of the genes (Fig. 4.2). Through the genetic operators, genes are evolved to produce the next generation. The evolutions continue until the fitness function is maximized to return the fittest genes (nanoparticle characteristics) that satisfy the pre-determined release pattern of interest (desired release profile). An initial population of 1000, number of evolution of 500, selection rate of 0.08, mutation rate of 0.05, and crossover rate of 0.6 were assigned to the GA based on a preliminary sensitivity analysis.

To assess the precision of the Geno-Neural approach, two arbitrary release patterns similar to release profiles of the experimental groups C and D were assigned to the Geno-Neural model and the predicted fittest genes were compared to the corresponding measured values.

4.4. Results

4.4.1. Structural and morphological assessments and localization of encapsulated protein

The SEM image of a cross-sectioned bi-layer microsphere that was prepared at PLLA/PLGA mass ratio of 1 and polymer concentration of 16.6% clearly shows core-shell architecture (Fig. 4.3a). Both core and shell exhibit porous structures but pores in the shell are relatively smaller than those in the core. Notably, no large pores or cracks can be identified on the surface of the bi-layer microsphere (Fig. 4.3a). Figure 4.3b depicts the bright field microscopy images of the cross-sections of bi-layer microspheres that were prepared at PLLA/PLGA mass ratios of 1, 3 and 0.5. Applying ethyl acetate assay to the cross-sections resulted in hollow ring configurations and solid core remnant corresponding to PLLA/PLGA mass ratios ≥1 and <1, respectively (Fig. 4.3c). Moreover, the ethyl acetate assay unveiled some pores on the shell that may be associated with the dissolution of scattered PLGA residues in the shell (Fig. 4.3c). Figure 4.3d depicts SEM

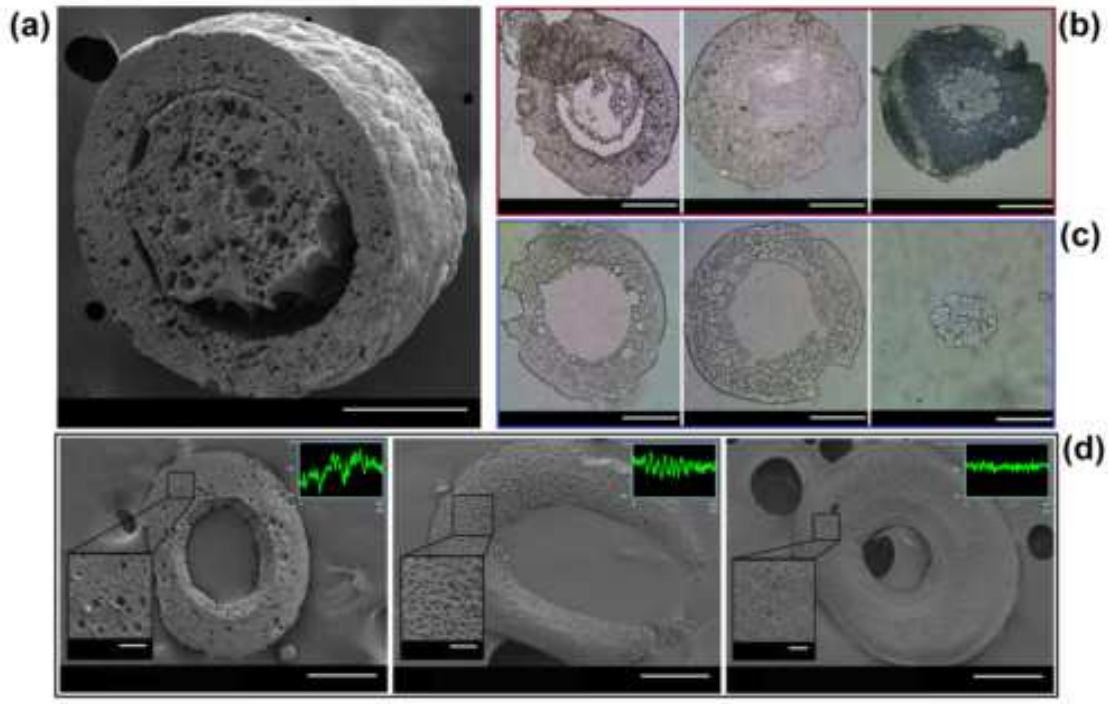

Figure 4.3. (a) SEM image of a bi-layer microsphere cross section (scale bar=100 μm). (b) Bright field microscopy images of cross sections of bi-layer microparticles at PLLA/PLGA mass ratios of 1 (left), 3 (middle), and 0.5 (right) before applying the ethyl acetate assay (scale bars=100 μm). (c) The hollow ring configurations and solid core remnant resulted from ethyl acetate assay for PLLA/PLGA mass ratios of 1 (left), 3 (middle), and 0.5 (right) (scale bars=100 μm). (d) Surface morphology of the ethyl acetate-treated cross sections of bi-layer microspheres prepared at three polymer concentrations and EAP of 23.5% in 100 mL water (left), 20% in 50 ml of 0.5% PVA solution (middle), and 16.6% in 30 ml of DCM-saturated 0.5% PVA (right) (scale bar=100 μm) (scale bar of magnified images=20 μm).

images of the ethyl acetate-treated cross sections of the bi-layer microspheres that were prepared at different polymer concentrations and external aqueous phase (EAP) compositions. The SEM images revealed that the surface morphology of the ethyl acetate-treated shell may be improved when the polymer concentration and EAP are adjusted from 23.5% at 100 ml EAP of water (Fig.

4.3d, left image) to 20% at 50 ml EAP of 0.5% PVA (Fig. 4.3d, middle image), and 16.6% at 30 ml EAP of DCM-saturated 0.5% PVA. The pixel intensity variation associated with the shell SEM images represents a quantitative measure of the shell texture uniformity that improves at the lower polymer concentration (16.6%) and the adjusted EAP (Fig. 4.3d).

Figure 4.4a shows the surface morphology, geometry and agglomeration level of PLGA (top-left image) and bi-layer nanoparticles that were prepared at PLLA/PLGA mass ratios of 1 (top-right image), 2 (bottom-left image) and 3 (bottom-right image). Spherical geometry and low particle agglomeration of the nanoparticles that are featured with no large superficial pores or cracks can be noted from the SEM images (Fig. 4.4a). The surface morphology of the nanoparticle-incorporated fibrin matrix at two levels of thrombin to fibrinogen ratio of 0.25 (left image) and 1 U/mg (right image). Coarser fibers with higher apparent nanoparticle density per fiber at thrombin to fibrinogen ratio of 0.25 U/mg can be distinguished from fine fibers with small number of nanoparticles per fiber at thrombin to fibrinogen ratio of 1 U/mg (Fig. 4.4b). Figures 4.4c-e illustrate the fluorescence microscopy images of cross-sections of bi-layer microparticles encapsulating labelled ovalbumin at different PLLA/PLGA mass ratios. The protein can be identified largely in the core at PLLA/PLGA mass ratios of 1 (Fig. 4.4c) and 2 (Fig. 4.4d); however, the fraction of protein in the shell relatively increases at PLLA/PLGA ratio of 3 (Fig. 4.4e). By overlaying bright field and fluorescence microscopy images, the protein distribution over the shell and core was visualized at four PLLA/PLGA mass ratios of 1(Fig. 4.4f), 2 (Fig. 4.4g) and 3 (Fig. 4.4h) and 0 (Fig. 4.4i). The composite images and the fluorescence intensity profiles revealed that the encapsulated protein was largely confined in the core of the bi-layer structures (Figs. 4.4f-h) but distributed across the entire PLGA microparticles (Fig. 4.4i). Figures 4.4f-h indicate that the shell thickness of the bi-layer microparticles increases with PLLA/PLGA

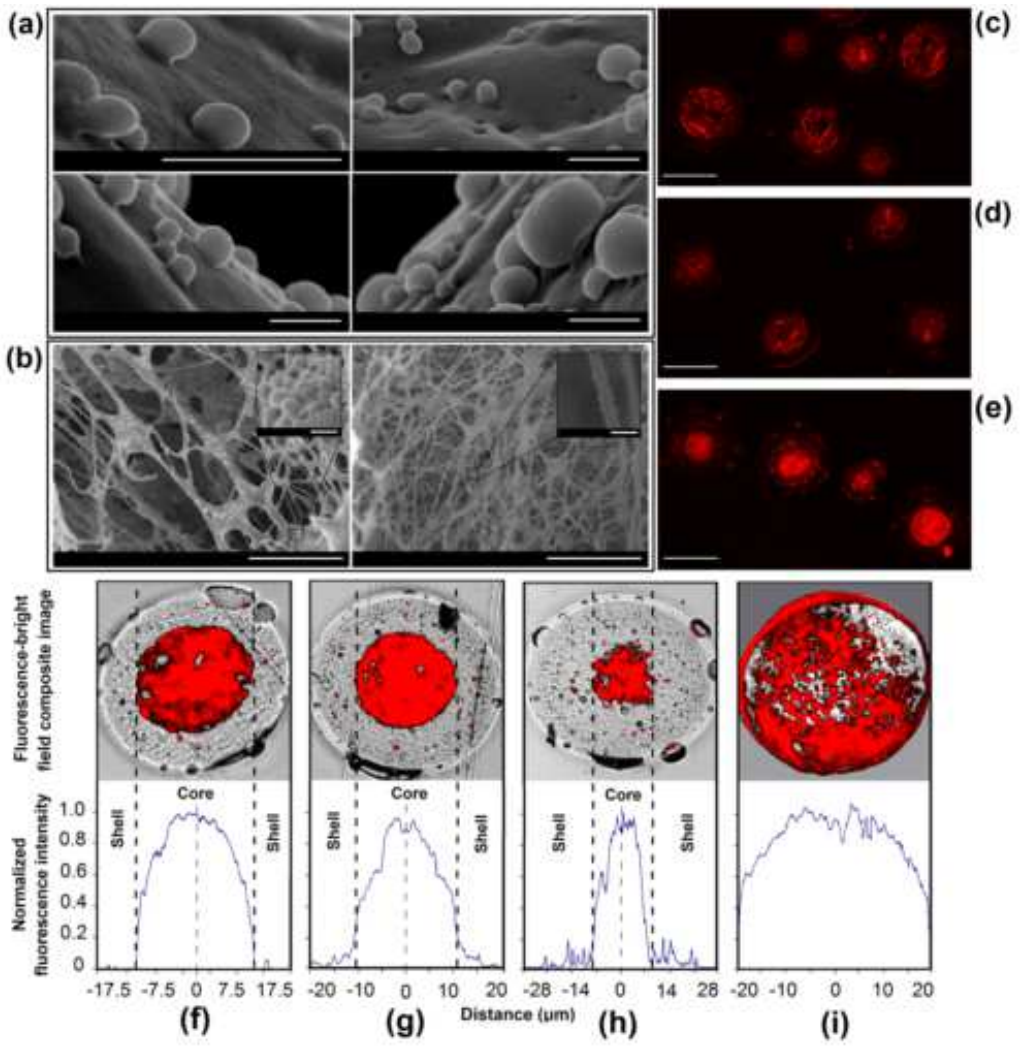

Figure 4.4. (a) Nanoparticle surface morphology at PLGA/PLLA ratios of 0 (top left), 1 (top right), 2 (bottom left), and 3 (bottom right) (scale bar=500 nm). (b) Surface morphology of nanoparticle-incorporated fibrin matrix at thrombin to fibrinogen ratios of 0.25 (left) and 1 U/mg (right) (scale bar=10 μm) (scale bar of the magnified images=500 nm). (c-e) Fluorescence microscopy images for protein localization assessment at PLLA/PLGA ratios of 1, 2, and 3, respectively (scale bar=50 μm). (f-i) Superimposed images of fluorescence and bright field microscopy with the fluorescence intensity profiles of cross-sections of microparticles at polymeric mass ratios of 1 (f), 2 (g), 3 (h), and 0 (i).

mass ratio while the area under the curve of the fluorescence intensity profiles, which represent apparent protein encapsulation capacity, decreases with PLLA/PLGA mass ratio (Figs. 4.4f-i). Unlike the core-shell structures, a significant amount of surficial protein can be identified on the surface of PLGA microparticles (Fig. 4.4i).

Table 4.2 presents the size range, loading capacity and PDI of the nanoparticles corresponding to polymer characteristics given in Table 4.1. PLGA nanoparticles offer significantly larger loading capacity than bi-layer nanoparticles with relatively more uniform size distribution represented by PDI. The measured values imply that the loading capacity of bi-layer nanoparticles decrease with PLLA/PLGA mass ratio (Table 4.2).

4.4.2. Protein loading capacity, release kinetics and structural integrity assessment

Figure 4.5a illustrates the kinetics of release of the nanoparticles corresponding to the polymeric characteristics given in Table 4.1. The nanoparticles with carboxyl terminal groups, which offered the highest loading capacity (Table 4.2), provided the most rapid protein release among the nanoparticles (Fig. 4.5a). The release rate decreased with an increase in the polymer concentration and L:G ratio. Notably, PLGA nanoparticles at polymer concentration of 9% and L:G ratio of 75:25 resulted in a sustained zero order release kinetics (Fig. 4.5a). Bi-layer nanoparticles provided a distinct time-delayed release pattern that can be clearly distinguished from the release kinetics of PLGA nanoparticles (Fig. 4.5a). The lag phase of protein release slightly increased with PLLA to PLGA mass ratio of bi-layer nanoparticles (Fig. 4.5a).

Figures 4.5b-d illustrate CD spectra of the released protein after 1, 25 and 50 days of release, compared to the standard protein sample. Deconvolution of the CD spectra led to the percentage of α-helix, β-sheets and random coil of the secondary structure of the released protein and the control sample after 1, 25 and 50 days of the release, respectively (Fig. 4.5e-g).

Table 4.2. Physical properties of nanoparticles corresponding to the experimental groups.

Characteristics	Experimental Groups					
	A	B	C	D	E	F
Size (nm)	220±7	211±33	258±12	340±29	490±16	685±43
PDI	0.21±0.02	0.18±0.04	0.30±0.03	0.32±0.08	0.38±0.05	0.46±0.04
Loading capacity (μg/mg)	1.3	0.9	0.2	0.05	0.02	0.01

The CD spectra and the relative proportion of α-helix, β-sheets and random coil were consistent with the measurements reported in literature [27, 28]. It should be noted that the CD spectra of the protein that is released over the 1st day is mostly associated with the surficial protein dissolution, which is less likely affected by PLGA degradation. As such, any changes in the secondary structure of the protein within the first day of release can be attributed to the fabrication process. In contrast, changes in the secondary structure of the protein during a prolonged release (e.g. after 25 and 50 days) can be associated with the acidic microenvironment resulted from PLGA and PLLA degradation.

4.4.4. Angiogenic bioactivity of the GF-loaded nanoparticles

Figures 4.6a-d depict angiogenic response of aortic rings to saline-loaded (Fig. 4.6a) and angiogenic factor-loaded nanoparticles (Figs. 4.6b-d) in the fibrin matrix (0.25 U/mg). Angiogenic factor-loaded nanoparticles that were prepared at PLLA/PLGA mass ratios of 0, 1 and 2 corresponding to the experimental groups of A (Fig. 4.6b), D (Fig. 4.6c) and E (Fig. 4.6d) significantly stimulated sprouting angiogenesis compared to a very limited angiogenic response of saline-loaded nanoparticles (Fig. 4.6a). Figure 4.6e depicts the time course of the sprouting

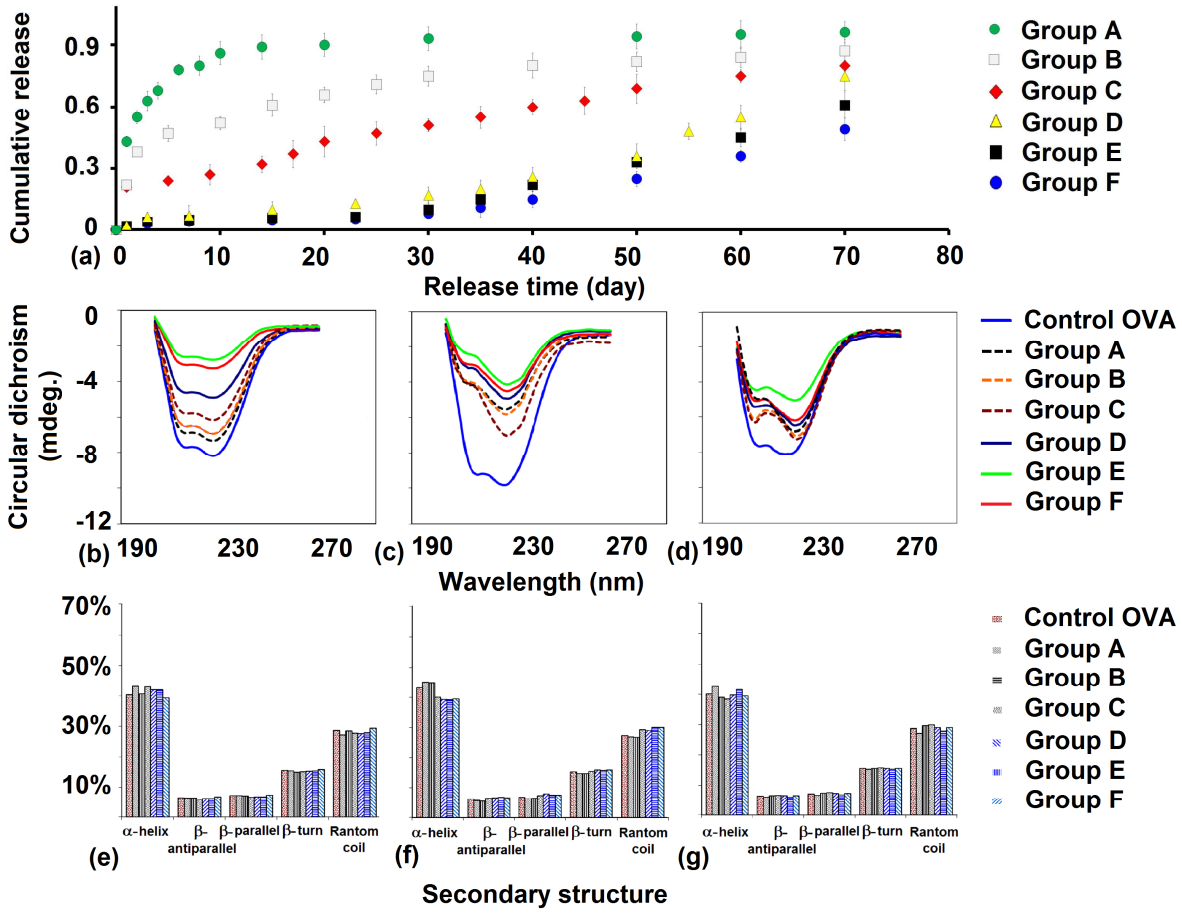

Figure 4.5. (a) Release kinetics of the nanoparticles corresponding to the polymeric characteristics of the experimental groups. (b-d) CD spectra and (e-g) secondary structure percentage of the releasing protein after 1 day (b, e), 25 days (c, f) and 50 days (d, g) of release compared to those of the control sample.

angiogenesis at three different release scenarios over 8 days for VEGF release alone, simultaneous release of VEGF, bFGF and PDGF, and sequential release of PDGF after 5 days following co-delivery of VEGF and bFGF. Co-delivery and sequential release of the angiogenic factors apparently resulted in a higher microvessel sprout density after 8 days (Fig. 4.6e). Figures 4.7a, b illustrate the number of sprouts and the maximum length of sprouts at different angiogenic factor release conditions compared to those of the control sample. Figure 4.6c illustrates the rate of new sprout formation over 9 days associated with the three release patterns

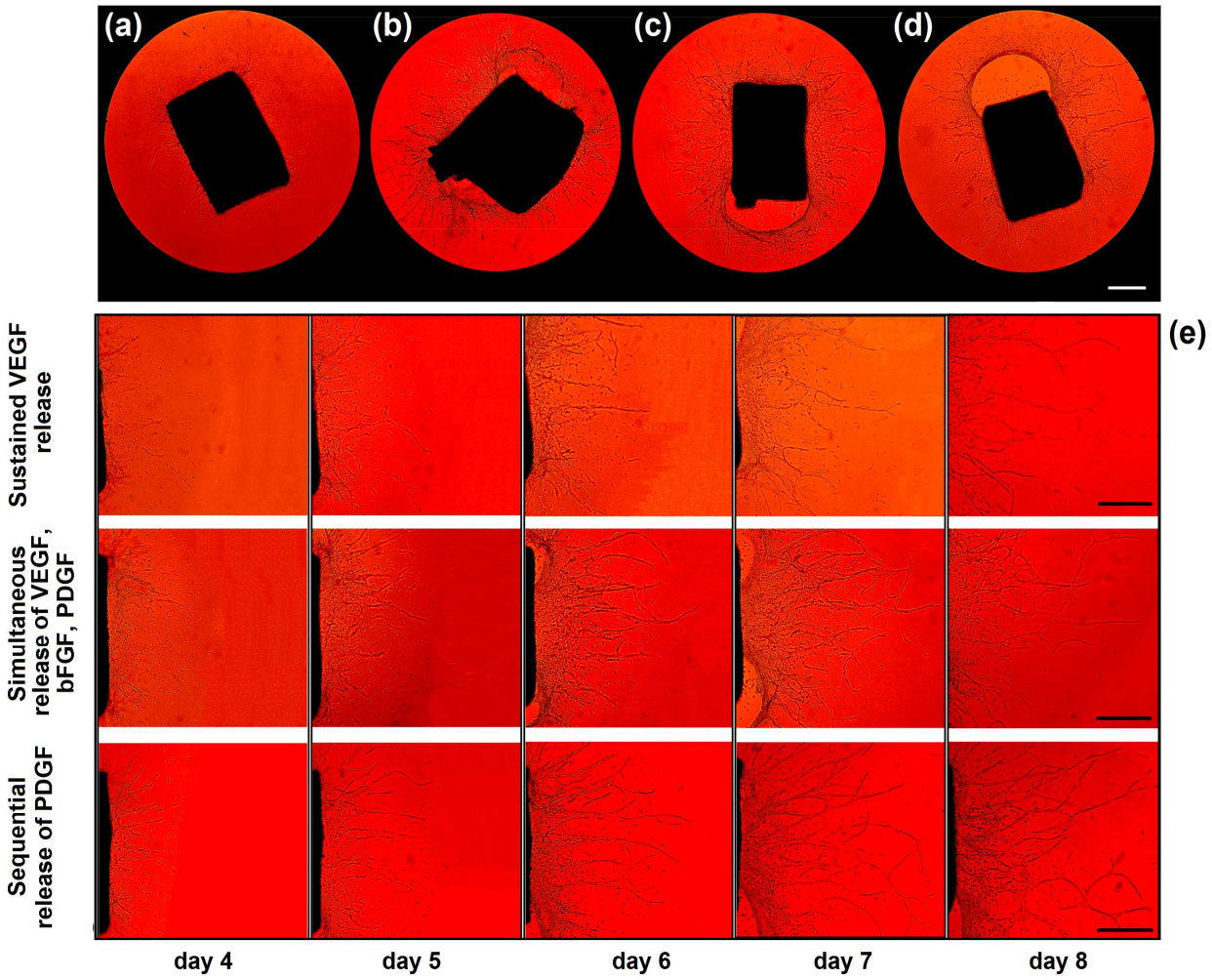

Figure 4.6. Angiogenic response of aortic rings to (a) saline-loaded nanoparticles, (b) VEGF-and bFGF-loaded PLGA nanoparticles, (c, d) bi-layer nanoparticles after 6 days (scale bar=500 μm). (e) Time course of sprouting angiogenesis for VEGF release alone, and simultaneous and sequential release of VEGF, bFGF, and PDGF over 8 days (scale bars=1000 μm).

shown in Fig. 4.6e. In terms of average sprout diameter of microvessels which were measured over 3-mm distance from the aortic ring, a comparison between VEGF release alone, co-release of the angiogenic factors and PDGF sequential release indicated that simultaneous and sequential release of multiple angiogenic factors significantly (p-value<0.05) improved the average

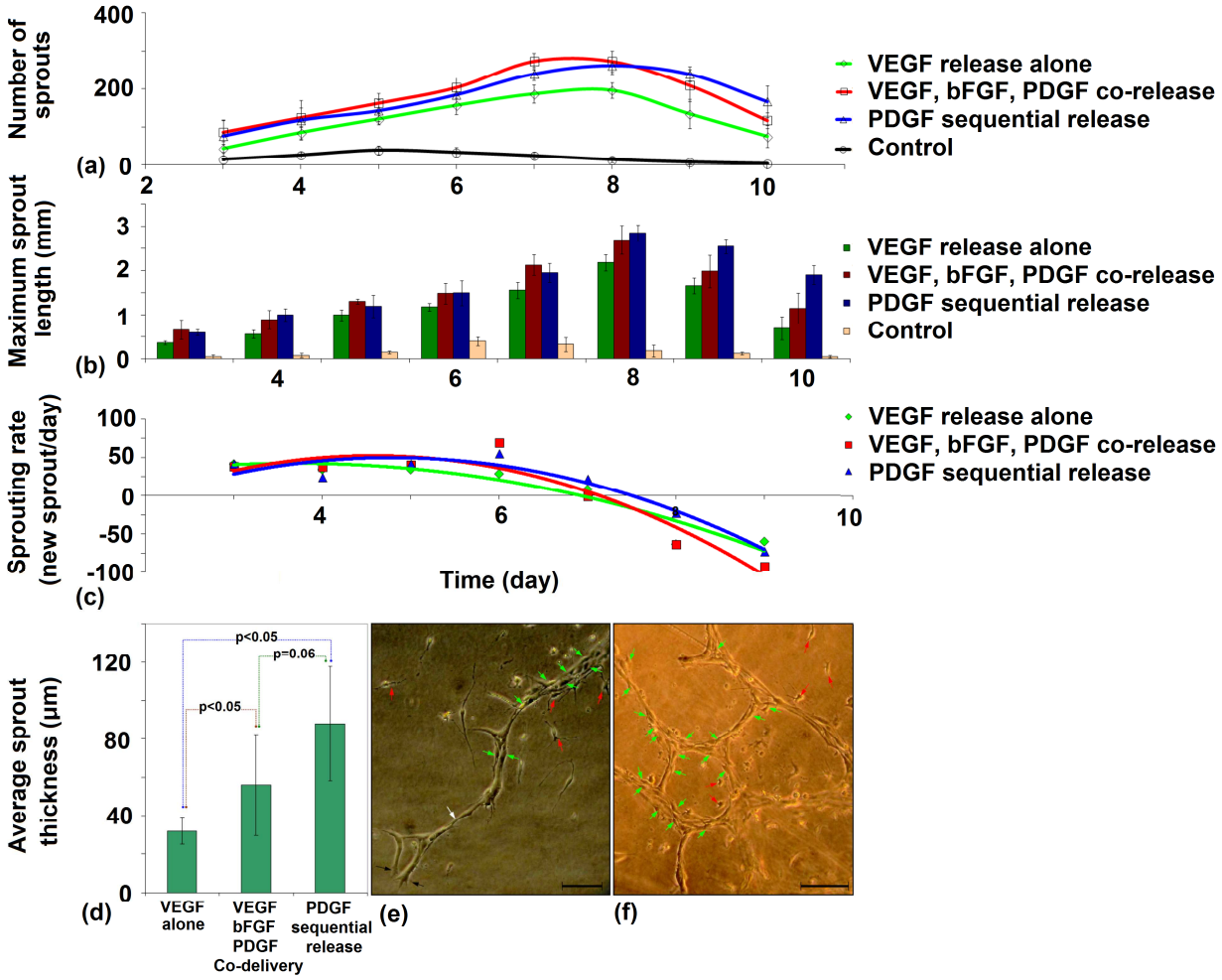

Figure 4.7. Quantitative evaluation of sprouting angiogenesis stimulated by the angiogenic factor-loaded nanoparticles in fibrin matrix: variation of number of sprouts (a), maximum sprout length (b), sprouting regression phase (c) and the average sprout thickness (d) at three angiogenic factor release scenarios, and the maturing lumens composed of endothelial cell (white arrow), pericytes (green arrow), fibroblasts (red arrow), and tip cells (black arrow) after 5 days (scale bar=50 μm) (e) and 9 days (scale bar=100 μm) (f) for sequential PDGF release following co-release of bFGF and VEGF.

microvessel diameter (Fig. 4.7d). With sequential release of PDGF, the microvessels began to recruit pericytes surrounding endothelial cells as an indication of maturing lumen after 5 days (Fig. 4.7e) leading to anastomosis after 9 days (Fig. 4.7f).

4.4.3. Predictability and sensitivity analyses of the ANN model

Figures 4.8a illustrates the correlation between predicted and experimental data within 95% confidence level. The high coefficient of determination and low mean prediction error represent a good agreement between experimental release data and the predicted values from Eqs. (4.3)-(4.5) associated with the testing data set. Moreover, the random distribution of the residual error represents unbiased predictability of the model (Fig. 4.8b). Figure 4.8c illustrates the experimental and predicted release kinetics associated with bi-layer nanoparticles of Group E, which was not involved in the training process of the model. The predicted release profile of bi-layer nanoparticle demonstrated a very good agreement with the corresponding experimental data (Fig. 4.8c). Based on the predictability of the validated and tested model, the sensitivity of release profiles and loading capacity were analyzed with respect to different nanoparticle design parameters. The sensitivity analysis illustrates the variation of release profile with respect to PLGA concentration (Fig. 4.8d), PLGA viscosity (Fig. 4.8e), and glycolide to lactide ratio (Fig. 4.8f) at the given nanoparticle design parameters. Besides, the model predicted that the fractional dose of the released protein over a certain period of time of interest (e.g. 15 days) can be regulated by adjusting PLLA/PLGA and G:L ratios of bi-layer nanoparticles (Fig. 4.8g), while the loading capacity is changed accordingly (Figs. 4.8h, i).

4.4.4. The Geno-Neural model potential for rate-programming of the nanoparticles

Figure 4.9a illustrates the variation of the best fitness value of populations over 500 generations in order to identify the fittest genes (nanoparticle characteristics) that provide the desired release

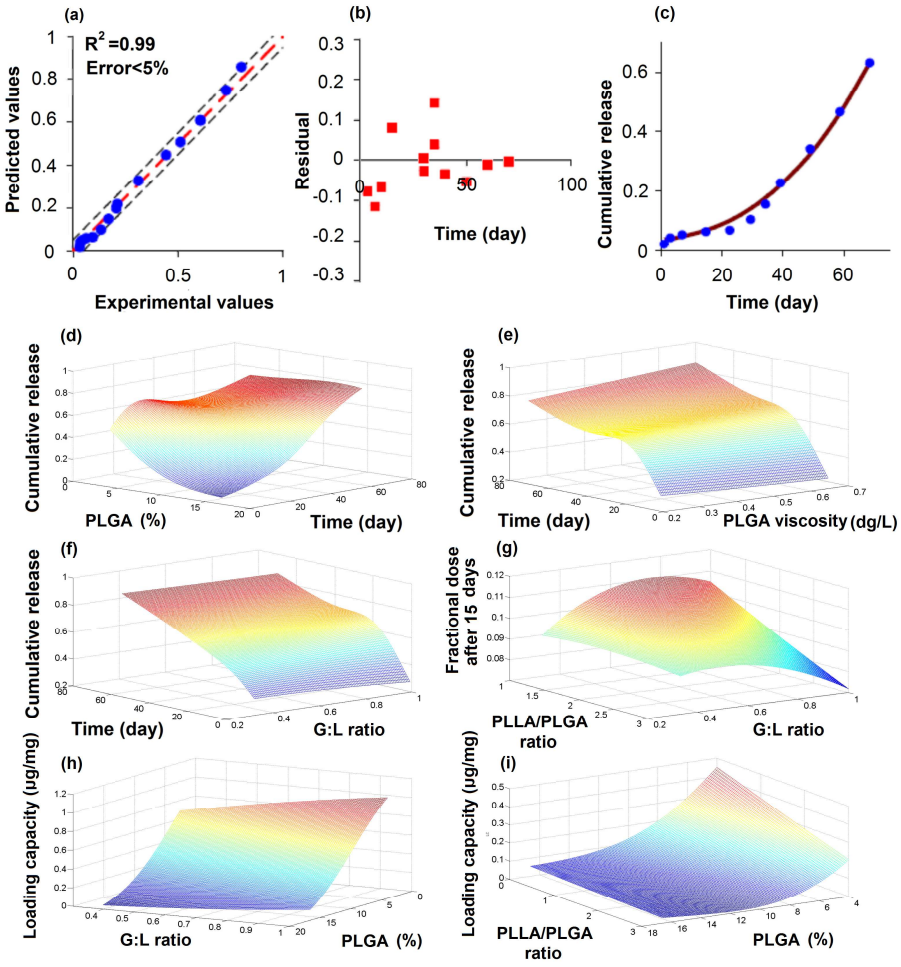

Figure 4.8. (a) The correlation between predicted and experimental values within 95% confidence limit, (b) Random distribution of the residual of prediction errors. (c) Agreement between predicted release profile and experimental data for bi-layer nanoparticles at PLLA/PLGA mass ratio of 2 (group E). (d-i) Sensitivity analyses of release and loading capacity with respect to the nanoparticle design parameters at (d) μ_{PLGA}=0.2 dg/L, $\chi_{G:L}$=1, $\chi_{PLLA:PLGA}$=0, ε=1, d=220 nm, and PDI=0.21, (e) C_{PLGA}=7%, $\chi_{G:L}$ =1, $\chi_{PLLA:PLGA}$=0, ε=1, d=220 nm, and PDI=0.21, μ_{PLGA}, (f) C_{PLGA}=7%, μ_{PLGA}=0.5 dg/L, $\chi_{PLLA:PLGA}$=0, ε=1, d=250 nm, and PDI=0.21, (g) C_{PLGA}=16.6%, ε=1, d=550 nm, and PDI=0.21, (h, i) μ_{PLGA}=0.2 dg/L, $\chi_{PLLA:PLGA}$=0, ε=1, d=220 nm, and PDI=0.21.

patterns of interest (Fig. 4.9b). The fitness value significantly improves over 50 evolutions and then converges to the fittest value after 285 generations (Fig. 4.9a). Figure 4.9b illustrates the release patterns associated with the fittest nanoparticle characteristics proposed by the Geno-Neural model (Fig. 4.9b). Notably, there is a very good agreement between the desired and predicted release profiles.

Since the desired release profiles were very similar to those associated with experimental groups C and D, the nanoparticle characteristics of groups C and D were used as a reference to evaluate the predictability of the Geno-Neural model. Table 4.3 presents the nanoparticle characteristics proposed by the Geno-Neural model and those of experimental groups C and D. A comparison

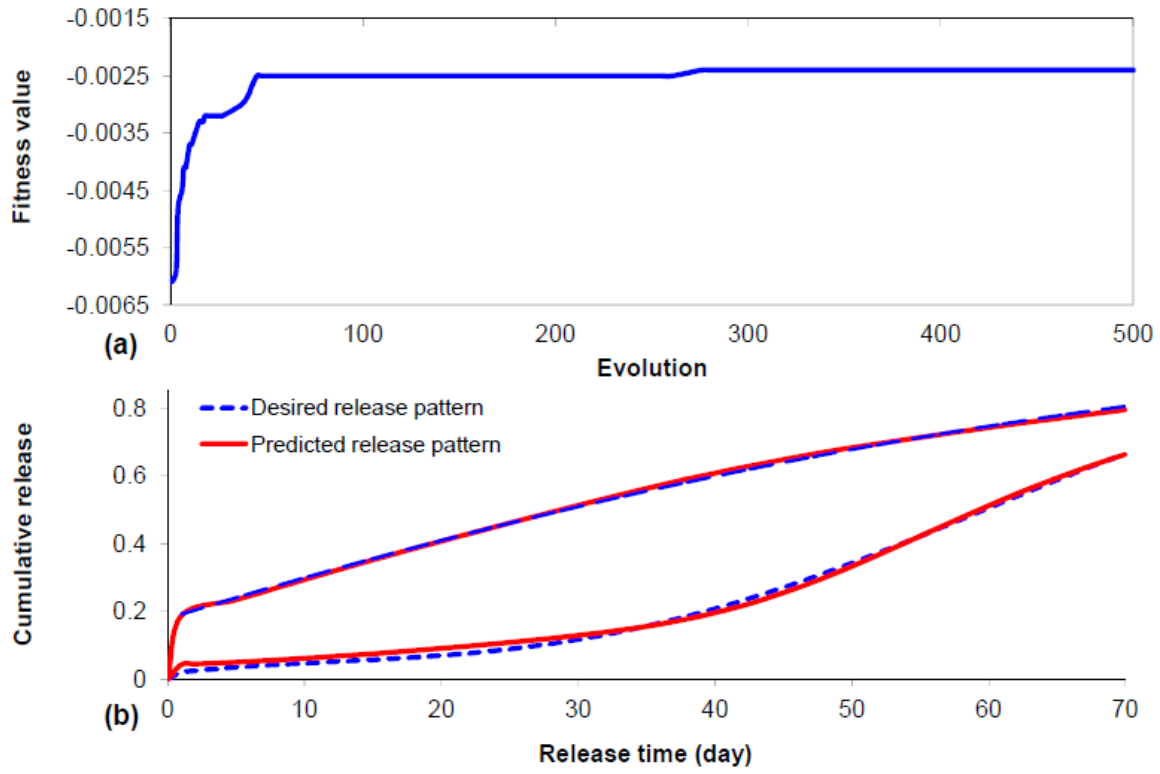

Figure 4.9. The evolution of the fittest individuals over 500 generations (a), and the release patterns associated with the fittest nanoparticle characteristics and the pre-determined release profiles (b).

Table 4.3. The nanoparticle characteristics associated with the fittest values proposed by the Geno-Neural model and the experimental groups C and D corresponding to the desired release patterns of zero-kinetics and time-delayed release.

	Release patterns of interest			
Nanoparticle characteristics	Zero-order kinetics release		Time-delayed release	
	Experimental group C	Geno-Neural model	Experimental group D	Geno-Neural model
C_{PLGA} (%)	9	8.7	16.6	15.8
μ_{PLGA} (dL/g)	0.2	0.2	0.2	0.2
$\chi_{G:L}$	0.33	0.33	1	0.87
$\chi_{PLLA:PLGA}$	0	0.18	1	1.1
d (nm)	258	216	340	211
PDI	0.3	0.31	0.32	039

between the experimental and predicted characteristics of the nanoparticles indicates a very low discrepancy, suggesting that the Geno-Neural model is a reliable tool for pre-programming of the nanoparticles to achieve release rates of interest.

4.5. Discussion

The modified double emulsion solvent removal technique was successfully used to fabricate bi-layer nanoparticles and microspheres with different structural and architectural characteristics. SEM images of the internal structures of bi-layer microparticles revealed porous core and shell where the pores represent the IAP that is entrapped in the polymeric network and sublimated during freeze-drying. Compared to small pores in the shell, the core featured larger pores,

indicating that a larger fraction of IAP was entrapped in the core rather than the shell (Fig. 4.3a). Since PLGA is the polymer that was primarily loaded with IAP during the first sonication, a larger fraction of entrapped IAP was expected to appear in PLGA, which mainly constituted the core. The scattered pores in the shell can be attributed to the second sonication (homogenization) during which the entrapped IAP in PLGA could be fractionally dispersed in PLLA.

Although various PLLA/PLGA mass ratios resulted in bi-layer microparticles (Fig. 4.3b), the core and shell polymer composition was dependent on the polymer ratio. Based on the fact that PLGA has much higher solubility in ethyl acetate than PLLA [22], the hollow ring and solid core configurations from the ethyl acetate assay indicated that PLLA largely constituted the shell and core at PLLA/PLGA ratios of ≥1 and <1, respectively (Fig. 4.3c). A comparison between the cross-sections of the bi-layer microparticles before (Fig. 4.3b) and after (Fig. 4.3c) applying ethyl acetate assay suggests that some pores are appeared on the shell as a result of ethyl acetate dissolution. These pores could be attributed to PLGA residues in the shell due to incomplete polymer phase separation. Based on the fact that the polymer phase separation is a dynamic process occurred during solvent removal process at a critical polymer concentration, the solvent removal conditions may affect PLLA-PLGA phase separation. In case of incomplete phase separation, PLGA may appear in PLLA shell in a scattered pattern (Fig. 4.3c) that can consequently affect the rate-controlling characteristics of the shell. Since PLGA has a higher hydrolytic degradation rate than PLLA [14], the faster degradation of PLGA residues in the shell during the release process leads to the formation of scattered pores in the shell that increases the shell permeability and potentially causes impaired release of a bi-layer nanoparticle.

Surface morphology assessment of ethyl acetate-treated shells revealed that the shell uniformity texture can be improved by adjusting the solvent removal rate and total polymer concentration

(Fig. 4.3d). Attempts were made to control the solvent removal rate by varying the EAP volume and composition, and polymer concentration in order to evaluate relatively high and low solvent removal rates at 100 ml of water and 30 ml of DCM-saturated 0.5% PVA solution, respectively. Examination of the cross-sectional surface morphology of ethyl acetate-treated shells confirmed that the size and distribution of PLGA-associated pores in the shell were reduced when the total polymer concentration decreased from 23.5 to 16.6% and the volume and composition of the EAP were changed from water (100 mL) to DCM-saturated 0.5% PVA (30 mL) (Fig. 4.3d). Pixel intensity standard deviation across an area of 0.01 mm^2 was used to statistically evaluate the uniformity of the ethyl acetate-treated shell textures (Fig. 4.3d). The texture uniformity significantly ($p<0.05$) improved at a polymer concentration of 16.6% and EAP of DCM-saturated 0.5% PVA (Fig. 4.3d, right image), which was applied to the preparation of bi-layer nanoparticles.

Surface morphology assessment of single and bi-layer nanoparticles revealed spherical nanoparticles with no superficial cracks or large pores (Fig. 4.4a) but rather a smooth nanoparticle surface that would reduce the initial burst effect, which is often recognized as a significant defect of nano-particulate delivery systems. Notably, the nanoparticles exhibited a low agglomeration (Fig. 4.4a) which can be attributed to the use of 1% sucrose as the cryoprotectant for prevention of nanoparticle coalescence during freeze-drying. The presence of sucrose at the interface between freeze-dried nanoparticles also contributed to re-suspension of the nanoparticles in the fibrinogen solution due to high sucrose solubility in aqueous phase. SEM images also show that the size of the nanoparticles increased from ~200 to ~550 nm with PLLA/PLGA ratio (Fig. 4.4a), which is consistent with the measurements from dynamic light scattering (Table 4.2).

The nano-scale size, spherical geometry, smooth surface, reasonably low PDI (Table 4.2), and low agglomeration of the nanoparticles are the features that enhance surface area, bio-reactivity, and uniform distribution of the nanoparticles in the context of a fibrin matrix. With specific emphasis on the surface morphology of the nanoparticles on the fibers, SEM images showed that the fibers were coarser and less interconnected at the lower thrombin to fibrinogen ratio of 0.25 U/mg compared to that at 1 U/mg (Fig. 4.4b); however, the nanoparticles exhibited a better distribution and coating over the fibers at the lower thrombin to fibrinogen ratio (Fig. 4.4b, left image). The effect of the fibrinogen-thrombin ratio on the fiber diameter may be explained by the higher rate of fibrin monomer formation at the higher thrombin per unit mass of the substrate. Although a thrombin to fibrinogen ratio of 1 U/mg could provide a larger surface area (Fig. 4.4b, right image), the fibrin matrix benefits an enhanced bio-reactive surface area at the lower ratio of 0.25 U/mg due to better nanoparticle distribution over the fibers (Fig. 4.4b, left image). Localization of encapsulated protein in the core of the bi-layer nanoparticles is essential for achieving time-delayed release patterns with low initial burst effect. Fluorescence microscopy imaging revealed that the encapsulated proteins were largely confined in the core of the bi-layer microparticles at PLLA/PLGA ratios of 1 and 2 (Figs. 4.4c, d), while the encapsulated protein was identified in a scattered pattern in the shell at a PLLA/PLGA ratio of 3 (Fig. 4.4e). Given that the proteins exhibit greater affinity for the PLGA core, the scattered proteins in the shell may be attributed to incomplete PLGA core separation from PLLA shel at the higher PLLA/PLGA ratio of 3. The fluorescence intensity profile across the core and shell (Figs. 4.4f-h) indicated that the area under the curve declined with PLLA/PLGA mass ratio, indicating lower apparent encapsulation capacity of bi-layer nanoparticles at higher polymer mass ratios. In contrast, PLGA microspheres offered the highest protein encapsulation capacity but

demonstrated the highest amount of surficial protein which contributes to a higher initial burst effect. The observations from the composite images and fluorescence intensity profiles of the microspheres (Figs.4.4f-i) are consistent with measured values of protein loading capacity of the nanoparticles (Table 4.2). The fact that the loading capacity decreased with the PLLA/PLGA ratio of bi-layer nanoparticles (Table 4.2) suggests that, at higher PLLA/PLGA ratios, larger amounts of bi-layer GF-encapsulating nanoparticles would be required for a certain GF dose.

In terms of release kinetics, bi-layer nanoparticles provided very low initial burst release (<7%) with a distinct time-delayed release pattern (~18-35 days) that was followed by zero order release kinetics (Fig. 4.5a). Ester-terminated PLGA nanoparticles (group C in Table 4.1) provided zero order kinetics following an initial release of ~20% whereas carboxyl-terminated nanoparticles (group A in Table 4.1) released nearly the entire payload within 10 days (Fig. 4.5a). Due to the fact that the carboxyl terminal group and lower L:G ratio at the reducced polymer concentrations increase hydrophilicity of the matrix, which subsequently enhance polymer degradability in an aqueous system, uncapped PLGA nanoparticles (4 and 7% w/v) at L:G ratio of 50:50 are more susceptible to bulk degradation than capped nanoparticles (9% w/v) at L:G ratio of 75:25. As such, uncapped PLGA nanoparticles at the lowest polymer concentration (4% w/v) lead to a rapid release profile with a high initial burst effect (Fig. 4.5a) that is attributed to the surficial protein attached to the surface (Fig. 4.4i). In contrast, bi-layer nanoparticles provide a very low initial burst effect of <7% (Fig. 4.5a), which is associated with the protein localization in the core and low surficial protein (Figs. 4.4f-h). The distinct lag phase that is provided by the bi-layer nanoparticles suggests that the shell can effectively control the protein release from the core (Fig. 4.5a). The zero order release kinetics following the lag phase indicates a progressive

bulk degradation of the shell that allows for steady diffusion of the protein from core to the surface.

Given that PLGA and PLLA degradation leads to the generation of acidic products, the encapsulated protein is potentially susceptible to be denatured during the release process. Moreover, the fabrication process can also cause protein denaturation due to the large interface between aqueous and organic phases. These issues become more critical for bi-layer nanoparticles due to the fact that PLGA degradation acidic products can be accumulated in the core surrounded by PLLA shell. As such, it is crucially important to protect the protein during the release process and nanoparticle fabrication. Although the CD spectra of the releasing protein seem to slightly change after 25 and 50 days of release, compared to those of the control sample (Figs. 4.5c, d), an independent sample t-test at a significance level of 0.05 indicates no significant difference between the percentage of α-helix, β-sheets and random coil of the released protein and those of the standard sample (p-value>0.05) (Figs. 4.5e-g). Results from CD spectroscopy suggest that in the presence of sodium bicarbonate and sucrose, which were used as the buffering and stabilizing agents in IAP, the structural integrity of the encapsulated protein was preserved during nanoparticle preparation (Figs. 4.5b, e) and protein release (Figs. 4.5c, d, f, g).

The rat aortic ring bioassay [24] revealed that the angiogenic factor-loaded nanoparticles were biologically active and significantly stimulated endothelial sprouting angiogenesis in the nanoparticle-incorporated fibrin matrix (Figs. 4.6a-d). Moreover, PLGA nanoparticles (group C) provided VEGF release only and co-release of VEGF, bFGF and PDGF (Fig. 4.6e). Particularly, a combination of bi-layer (group D) and PLGA nanoparticles (group C), which were loaded with PDGF and VEGF&bFGF, respectively, were successfully employed to provide sequential release

of PDGF after 5 days following co-release of VEGF&bFGF (Fig. 4.6e). While all of the pre-designed release patterns improved angiogenesis compared to the control, the co-release and sequential release patterns provided significantly ($p<0.05$) larger number of sprouts and maximum sprout length than VEGF release alone (Figs. 4.7a, b). Moreover, the assessment of the rate of new sprout formation indicated that the sequential release of PDGF that followed simultaneous release of VEGF and bFGF may postpone the sprout regression phase that is represented by the negative sprouting formation rate (Fig. 4.7c). Furthermore, the sequential release of PDGF may improve the average sprout thickness, which appeared to be significantly larger than that of VEGF release alone (Fig. 4.7d). PDGF sequential release also resulted in morphologically maturing sprouts, which were characterized by the recruitment of pericytes surrounding endothelial sprouts and microvessel anastomosis after 5 and 9 days, respectively (Figs. 4.7e, f). The qualitative and quantitative assessments of the angiogenesis associated with different release scenarios suggest that the designed nanoparticles can be successfully used for regulation of simultaneous and sequential release of multiple GFs. In particular, pre-conditioning of the bi-layer nanoparticles in PBS for 30 days demonstrated effective in order to achieve an adjusted lag-phase for sequential release of PDGF after 5 days. As such, the bi-layer nanoparticles offer a great potential for temporal control of GF release.

The fact that the release patterns rely on polymeric nanoparticle characteristics including polymer concentration, MW, terminal group, L:G ratio and PLLA/PLGA mass ratio (Fig. 4.5a) suggests that the release kinetics may be pre-designed by modulating these properties. The sensitivity analysis shows that the lag phase of release can be nonlinearly adjusted by tuning PLGA concentration from 10% to 16% w/v (Fig. 4.8d), the initial burst release can be reduced by increasing PLGA viscosity (Fig. 4.8e), and nearly zero order release profiles may be achieved

by adjusting G:L ratio between 0.33 and 0.65 (Fig. 4.8f). When a certain protein dose is required to be released within a pre-determined period of time, the right combination of PLLA/PLGA mass ratio and G:L ratio of the nanoparticles can satisfy the release conditions. For instance, the nanoparticles prepared at PLLA/PLGA ratio of 1 and G:L ratio of 0.67 can lead to a fractional dose of 11.6% after 15 days of release, while nanoparticles with G:L ratio of 0.4 would provide a fractional dose of 9.1% (Fig. 4.8g). Excellent predictability (Figs. 4.8a, 4.9b), unbiased prediction residual error (Fig. 4.8b), and good agreement between predicted results and experimental dataset (Fig. 4.8c) (Table 4.3) suggest that the developed Geno-Neural model (Fig. 4.2) can be a reliable tool to identify the optimum nanoparticle characteristics (Table 4.3) that result in desired release profiles; a process so call 'rate-programming of the nanoparticles'. Moreover, the model can predict the nanoparticle loading capacity corresponding to the determined polymeric design parameters in order to estimate (Eq. 4.2) the total amount of the GF-loaded nanoparticles which will be required for a particular release pattern. The proposed Geno-Neural model offers a great potential for designing a nano-particulate delivery system that may require different designs of the nanoparticles to provide simultaneous and sequential release of multiple GFs.

4.6. Conclusion

We have developed bioactive bi-layer nanoparticles which are composed of protein-encapsulating PLGA core that is surrounded by PLLA shell and featured low initial burst effect, time-delayed release and structural integrity of the encapsulated protein during a prolonged release. To the best of our knowledge, no other bioactive bi-layer nanoparticles have been reported for sequential GF release. The nanoparticle-incorporated fibrin matrix demonstrated bioactive to stimulate angiogenesis from embedded rat aortic rings (Figs. 4.6q-d). The bi-layer

nanoparticles provided time-delayed release patterns with very low initial burst effect, essential for sequential release of GFs. A combination of GF-loaded PLGA and bi-layer nanoparticles were successfully employed to provide different GF release scenarios as VEGF release only, VEGF, bFGF and PDGF co-release, and sequential release of PDGF following co-release of VEGF and bFGF (Fig. 4.6e). Quantitative analyses of the sprouting angiogenesis indicated a significant difference in angiogenic response between the three GF release scenarios (Fig. 4.7), suggesting that the nano-particulate delivery systems were able to regulate the pre-designed GF release patterns to promote angiogenesis in fibrin matrix of a cardiac patch.

Based on the fact that the physical and polymeric characteristics of the nano-particulate delivery system can be adjusted to provide various release patterns, a predictive Geno-Neural model was developed, tested, and successfully employed to rate-program nanoparticles for achieving desired zero-order kinetics and time-delayed release of interest. There was an excellent agreement between the predicted and experimental values of the nanoparticle physical and polymeric characteristics resulting in the desired release patterns of interest. The proposed Geno-Neural approach offer a great potential for designing and optimization of PLLA/PLGA-based nanoparticles to facilitate pre-programming of various release profiles for different tissue engineering applications.

Finally, the potential of the developed nanoparticles is not limited to temporal control of GFs. Using the proposed Geno-Neural model, the nanoparticles are rate-programmed and fabricated, a and then incorporated into a hydrogel (e.g. fibrin) which can be precisely micro-patterned into a 3D cardiac patch with 3D-bioprinting technique to achieve spatiotemporal control over the release of GFs in the patch.

References

[1] Izadifar M, Kelly ME, Chen XB 2014 Engineering Angiogenesis for Myocardial Infarction Repair: Recent Developments, Challenges, and Future Directions. Cardiovasc. Eng. Technol.**5** 281-307.

[2] Morice MC, Serruys PW, Kappetein AP, et al 2010 Outcomes in patients with de novo left main disease treated with either percutaneous coronary intervention using paclitaxel-eluting stents or coronary artery bypass graft treatment in the Synergy Between Percutaneous Coronary Intervention with TAXUS and Cardiac Surgery (SYNTAX) trial. Circulation **121** 2645-2653.

[3] Parolari A, Pesce LL, Trezzi M, et al 2009 Performance of EuroSCORE in CABG and off-pump coronary artery bypass grafting: single institution experience and meta-analysis. Eur. Heart J. **30** 297-304.

[4] Jacques P, Charest JM, Mills RW, et al 2016 Bioengineering human myocardium on native extracellular matrix. Circ. Res. **118** 56-72.

[5] Feng X, Tonnesen MG, Mousa SA, Clark RAF 2013 Fibrin and collagen differentially but synergistically regulate sprout angiogenesis of human dermal microvascular endothelial cells in 3-dimensional matrix. Int. J. Cell Biol. **2013** 231279.

[6] Joshua I, Shields DJ, Barillas SG, et al 2008 A role for VEGF as a negative regulator of pericyte function and vessel maturation. Nature **456** 809-813.

[7] Tengood JE, Kovach KM, Vescovi PE, Russell A, Little SR 2010 Sequential delivery of vascular endothelial growth factor amd sphingosine 1-phosphate for angiogenesis. Biomaterials **31** 7805-7812.

[8] Nillesen ST, Geutjes PJ, Wismans R, Schalkwijk J, Daamen WF, van Kuppevelt TH 2007 Increased angiogenesis and blood vessel maturation in acellular collagen-heparin scaffolds containing both FGF2 and VEGF. Biomaterials **28** 1123–1131.

[9] Riley CM, Fuegy PW, Firpo MA, Shu XZ, Prestwich GD, Peattie RA 2006 Stimulation of in vivo angiogenesis using dual growth factor-loaded crosslinked glycosaminoglycans hydrogels. Biomaterials **27** 5935–5943.

[10] Richardson TP, Peters MC, Ennett AB, Mooney DJ 2001 Polymeric system for dual growth factor delivery. Nat. Biotechnol. **19** 1029–1034.

[11] Chen RR, Silva EA, Yuen WW, Mooney DJ 2007 Spatio-temporal VEGF and PDGF delivery patterns blood vessel formation and maturation. Pharm. Res. **24** 258–264.

[12] Davies NH, Schmidt C, Bezuidenhout D, Zilla P 2012 Sustaining neovascularization of a scaffold through staged release of vascular endothelial growth factor-A and platelet-derived growth factor-BB. Tissue Eng. Part A, **18** 26-34.

[13] Zhang H, Jia X, Han F, Zhao J, Zhao Y, Fan Y, Yuan X 2013 Dual-delivery of VEGF and PDGF by double-layered electrospun membranes for blood vessel regeneration. Biomaterials **34** 2202-2212.

[14] Izadifar M, Haddadi A, Chen XB, Kelly ME 2015 Rate-programming of nano-particulate delivery systems for smart bioactive scaffolds in tissue engineering. Nanotechnology **26** 012001.

[15] Lee K, Silva EA, Mooney DJ 2011 Growth factor delivery-based tissue engineering: general approaches and a review of recent developments. J. R. Soc. Interface **8** 153-170.

[16] Danhier F, Ansorena E, Silva JM, Coco R, Le-Breton A, Préat V 2012 PLGA-based nanoparticles: An overview of biomedical applications. J. Control. Release **161** 505–522.

[17] Shin SH, Lee J, Lim KS, Rhim T, Lee SK, Kim YH, Lee KY 2013 Sequential delivery of TAT-HSP27 and VEGF using microsphere/hydrogel hybrid systems for therapeutic Angiogenesis. J. Control. Release **166** 38-45.

[18] Formiga F.R., Pelacho B., Garbayo E., et al 2010 Sustained release of VEGF through PLGA microparticles improves vasculogenesis and tissue remodelling in an acute myocardial ischemia-reperfusion model. J. Control. Release **147** 30-37.

[19]. Golub JS, Kim YT, Duvall CL, et al 2010 Sustained VEGF delivery via PLGA nanoparticles promotes vascular growth. Am. J. Physiol. Heart Circ. Physiol. **298** H1959-65

[20] Geng H, Song H, Qi J, Cui D 2011 Sustained release of VEGF from PLGA nanoparticles embedded thermo-sensitive hydrogel in full-thickness porcine bladder acellular matrix. Nanoscale Res. Lett. **6** 312.

[21] Simón-Yarza T, Tamayo E, Benavides C 2013 Functional benefits of PLGA particulates carrying VEGF and CoQ10 in an animal of myocardial ischemia. Int. J. Pharm. **454** 784-790.

[22] Lee TH, Wang J, Wang CH 2002 Double-walled microspheres for the sustained release of a highly water soluble drug: characterization and irradiation studies. J. Control. Release **83** 437-452.

[23] Tan EC, Lin R, Wang CH 2005 Fabrication of double-walled microspheres for the sustained release of doxorubicin. J. Colloid Interface Sci. **291** 135-143.

[24] Baker M, Robinson SD, Lechertier T, et al 2011 Use of the mouse aortic ring assay to study angiogenesis. Nat. Protoc. **7** 89-104.

[25] Izadifar M 2005 Neural network modeling of trans isomer formation and unsaturated fatty acid changes during oil hydrogenation. J. Food Eng. **66** 227–232.

[26] Izadifar M, Abdolahi F 2006 Comparison between neural network and mathematical modeling of supercritical CO_2 extraction of black pepper essential oil. J. Supercrit. Fluids **38** 37–43.

[27] Perkins SJ, Smith KF, Nealis AS, et al 1992 Secondary structure changes stabilize the reactive-centre cleaved form of SERPINs. A study by 1H nuclear magnetic resonance and Fourier transform infrared spectroscopy. J. Mol. Biol. **228** 1235–1254.

[28] Koseki T, Kitabatake N, Doi E 1988 Conformational changes in ovalbumin at acid pH. J. Biochem. **103** 425–430.

CHAPTER 5

MODELING OF CONTROLLED RELEASE OF BIOACTIVE AGENTS FROM BI-LAYER NANOPARTICLES FOR TISSUE ENGINEERING

"This chapter has been submitted as "M. Izadifar, M. Kelly, and X. B. Chen, 2016, Development of Bi-layer Nanoparticles for Temporal Control of Release of Bioactive Agents for Tissue Engineering: an Experimental and Computational Study, *Journal of Biomechanical Engineering*, (Under Review)" According to the Copyright Agreement, "the authors retain the right to include the journal article, in full or in part, in a thesis or dissertation".

5.1. Abstract

Spatiotemporal control of release of bioactive agents from nanoparticles is essential to many tissue engineering applications, yet remains a challenge due to its complicated behaviour. Notably, the release behaviour relies on the physical and chemical properties of the nanoparticles, which may be regulated and optimized for achieving desired release profiles. To this end, this paper presents two novel modeling approaches based on local volume averaging (LVA) and Geno-Mechanistic modeling to represent the controlled-release of bioactive agents from bi-layer nanoparticles. Differential mass transfer governing equations based on LVA method were derived and numerically solved to provide the insight on the transport and degradation properties of the nanoparticles. Also, a system of analytical governing equations of release of pseudo bi-layer nanoparticles was coupled with genetic algorithm to provide a hybrid model, so called 'Geno-Mechanistic' model, to predict volume-averaged release properties of the nanoparticles at various conditions. Single polymer and bi-layer nanoparticles were fabricated from poly(lactide-co-glycolide) and poly(L-lactide) with varying fabrication conditions where ovalbumin was used as a protein model for the release study, loading capacity examination, and

protein structural integrity assessment over 70 days. The experimental data were used to assess the model predictability. The models presented in this study will be powerful, effective and efficient tools to predict and optimize the controlled release of bioactive agents from polymeric nanoparticles for many tissue engineering applications.

5.2. Introduction

Tissue engineering aims to develop functionally bioactive and viable constructs (e.g. cell-incorporated cardiac patch) for damaged tissue/organ repair. Development of bio-functional constructs is quite challenging due to the fact that the biological events involved in tissue regeneration are really complex. Increasing level of complexity and functionality in the design of the constructs demands incorporation of sophisticated delivery systems allowing for temporal control over the sequential release of multiple growth factors (GFs) in constructs [1]. Biodegradable polymeric nano-particulate delivery systems are increasingly gaining interest in the field of GF controlled release in tissue engineering. Specifically, bi-layer polymeric nanoparticles offer fundamental advantages over their conventional monolithic counterparts to provide sequential release of multiple GFs [2] and avoid antagonism effects of GFs, such as vascular endothelial GF (VEGF) and platelet-derived GF (PDGF) [3], by physically separating them in core-shell constructs and/or suppressing the initial burst effect [2]. Moreover, the nano-scale GF-encapsulating polymeric devices enhance bio-reactive surface area of cardiac constructs, thereby improving cell-construct interactions.

Physical, chemical, structural and architectural characteristics of the polymeric nanoparticles have profound effects on release behaviour. Mathematical models are powerful and efficient tools that facilitate the development and optimization of the GF delivery systems. Furthermore, mechanistic modeling combined with precise experimental evaluation of the nano-particulate

delivery systems improves the understanding of the mechanisms of GF release, and thus help to determine crucial parameters that regulate the release rate. Also, predictive models can reduce and even eliminate the need for experiments, thus saving time and the associated costs. Comprehensive reviews of release kinetics from biodegradable matrices including particulate delivery systems have been reported in the previous studies [1-5]. Some models consider initial burst release and bulk degradation of nanoparticles [6], while more complex models involve diffusion-dissolution mechanism combined with bulk/surface degradation to describe the release [7-9]. Another release modeling approach is based on the summation of three sequential mechanisms of burst release, relaxation-induced payload dissolution and diffusion [10, 11]. Monte Carlo-based simulation have been also employed to describe random chain scission process during polymer degradation in order to predict the corresponding drug release from polymeric delivery systems [12]. Despite numerous models for controlled release, there is no report on mechanistic models to elucidate governing mechanism and provide predictive means on release behaviour and parameters for bi-layer polymeric nanoparticles. Considering the great potential of GF-encapsulating bi-layer nanoparticles for sequential release of GFs in cardiovascular tissue engineering, it is crucial to develop mechanistic models of release for bi-layer nanoparticles which are specifically composed of poly(lactide-co-glycolide) (PLGA) and poly(L-lactide) (PLLA) due to their biocompatibility and biodegradability, as well as the approval for use from the Food and Drug Administration and European Medicine Agency [13]. In this study, a mathematical model based on local volume averaging (LVA) approach and local equilibrium was developed and numerically solved for simulation of controlled release and identification of transport and degradation properties of the core and shell of a bi-layer nanoparticle. Also, a Geno-Mechanistic model consisting of a system of governing equations of

release coupled with genetic algorithm (GA) was developed to provide a predictive tool for estimation of crucial transport properties and release parameters from PLLA-PLGA bi-layer nanoparticles and their conventional monolithic counterparts. The nanoparticles were fabricated and their physical, chemical and structural parameters were characterized and applied to the models to predict release behaviours at various conditions for the verification of the developed models. The predictability of the models and estimation of release parameters were assessed based on experimental data collected from release study of the protein -encapsulating nanoparticles.

5.3. Theory and experiments

5.3.1. Development of the mechanistic model using LVA

A polymeric nanoparticle is a matrix that can be described as a porous medium consisting of a solid phase (polymer) and the spaces which are filled with fluid phase (e.g. aqueous phase during the release) (Fig. 5.1a). Depending on the polymer packing density, the range of pore size may vary from molecular size (Å) to several nanometres. When the polymeric matrix structure cannot be fully described within the pore size, a representative elementary volume (REV) (Fig. 5.1a) is typically used to describe the porous medium [14]. A differential volume as small as the size of a pore may not be a representative element to describe a porous medium property (e.g. porosity) but as the size of the differential volume increases the volume-averaged properties of the porous medium converges to a certain value (Figs. 5.1b, c). As such, the REV is defined as the smallest differential volume with a characteristic length (ℓ) (Fig. 5.1a) and volume (V_{REV}) (Figs. 5.1b, c) that results in statistically meaningful average properties of the porous medium as [15]:

$$\langle \phi \rangle = \frac{1}{V_{REV}} \int_{V_{REV}} \phi dV \tag{5.1}$$

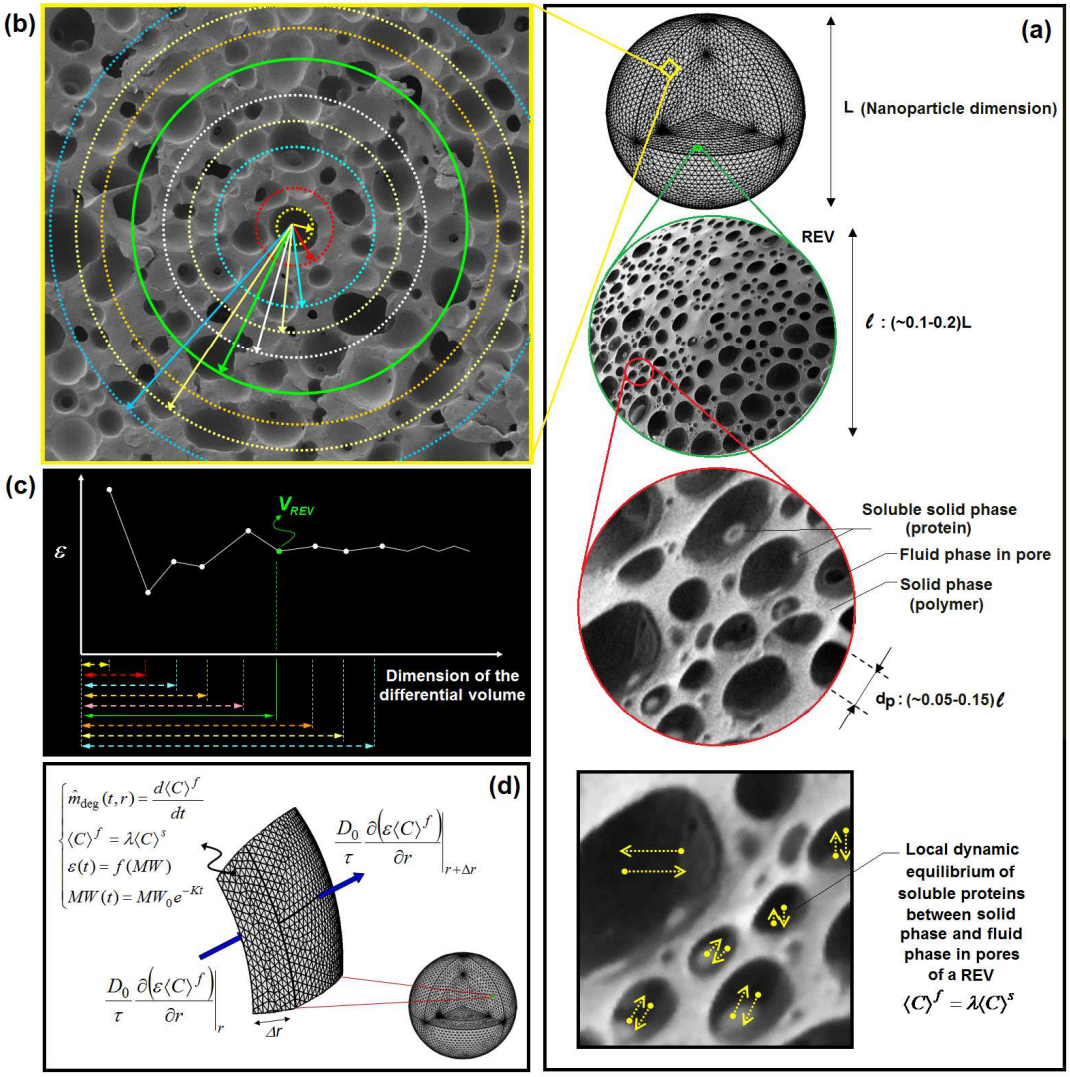

Figure 5.1. A polymeric nanoparticle from a porous media point of view: (a) the linear dimension of a nanoparticle, the characteristic length of the REV, the pore size with respect to REV length, and the local volume averaged equilibrium at pores between the fluid phase and the solid phase; (b) the smallest differential volume with meaningful properties of the porous medium; (c) the effect of REV size on a matrix property such as porosity for determination of the characteristic length of REV; and (d) the local volume averaged mass flux and properties to set a differential mass balance over a REV of a polymeric nanoparticle.

where ϕ is a property of interest of the fluid or solid phase of the medium, and $\langle\phi\rangle$ represents the local volume averaged property. Development of transport governing equations based on conservation of mass, heat and momentum over the REV and local volume averaged properties is considered as the local volume averaging (LVA) approach. In general, LVA can be applied to a porous medium when the pore size (d_p) of a polymeric matrix is smaller than REV, and the characteristic length of REV (ℓ) is much smaller than the linear dimension (L) of the porous medium (Fig. 5.1a). Extending the concept of LVA to nano-scale (Fig. 5.1a), mass transport equations can be integrated over the REV based on LVA approach in a spherical nanoparticle where the dynamic equilibrium of a soluble species (e.g. protein) between the solid phase (polymeric matrix) and fluid phase (aqueous phase) in the REV can be also averaged over the REV. When a nanoparticle is exposed to an aqueous medium (e.g. water, hydrogel, physiological fluid), the protein molecules attached to the polymeric matrix reach a dynamic equilibrium with the aqueous phase filling the pores, which is defined by a partition coefficient of λ that relates the local volume averaged concentration of the protein in the solid phase ($\langle C\rangle^s$) to that in the fluid phase ($\langle C\rangle^f$) (Fig. 5.1a). However, the protein diffusion toward the nanoparticle surface is suppressed because of low porosity, high tortusity and non-interconnected pores of the matrix, while hydrolytic reactions begin to degrade the polymer and reduce the polymer molecular weight (MW). Depending on the degree of crystallinity, initial MW, terminal group (ester or carboxyl) of the polymer and nanoparticle structure, the polymer degradation rate varies, and subsequently the time for bulk degradation onset changes. As such, a lag phase (T_d) between the hydration and the diffusional mass transfer-based release of the protein may be occurred. When the amorphous regions of the polymer matrix, which are degraded faster than the crystalline regions, are eroded, the pores begin to grow and enhance the protein diffusion across

the matrix where the dynamic local equilibrium is maintained. Figure 5.1d illustrates the schematic diagram of the polymeric nanoparticle differential volume with a thickness of Δr and the corresponding input and output diffusional mass flows. Since the local volume averaged properties such as porosity, protein concentration and polymer molecular weight (MW) changes with time (Fig. 5.1d), the flux of the mass flow varies with both space and time. Applying local equilibrium and LVA method to the differential mass balance over the different REV results in the mass transport governing equation as:

$$\frac{\partial \langle C \rangle^f (r,t)}{\partial t} = D_{eff} \frac{\partial^2 \langle C \rangle^f (r,t)}{\partial r^2} + \frac{\partial D_{eff}}{\partial r} . \frac{\partial \langle C \rangle^f (r,t)}{\partial r} + \frac{2}{r} D_{eff} \frac{\partial \langle C \rangle^f (r,t)}{\partial r} - \hat{m}_{\deg} \tag{5.2}$$

where t is time (s), r is radius (m), $\hat{m}_{\deg}$ is the local volume averaged protein degradation rate ($mgm^{-3}s^{-1}$) due to protein denaturation associated with the acidic PLGA and PLLA degradation products, and D_{eff} is the effective diffusion coefficient (m^2s^{-1}) which can be defined by [10]:

$$D_{eff}(t) = D_i + \frac{K}{MW(t)} \tag{5.3}$$

where D_i is the initial effective diffusivity (m^2s^{-1}), MW is the polymer molecular weight (kDa) associated with the core and shell, and K is constant ($m^2s^{-1}kDa$). The effective diffusivity is related to the time-dependent porosity of the matrix as [14, 15]:

$$D_{eff}(t) = \frac{D_0 \varepsilon(t)}{\vartheta} \tag{5.4}$$

where D_0 is the protein diffusivity in the aqueous phase (m^2s^{-1}) (e.g. 7.76×10^{-11} m^2s^{-1} for ovalbumin in water at 25°C [17]), ϑ is the tortusity, and ε is the porosity. Assuming that PLGA and PLLA follow a pseudo-first order degradation rate [16], the average time-dependent polymer MW can be estimated by:

$$MW(t) = MW_0 \exp(-K_d t) \tag{5.5}$$

where K_d is the polymer degradation rate constant (s^{-1}).

Under the assumptions that the protein is homogenously distributed within the matrix and that the mass transfer resistance at the surface of the nanoparticle is negligible, the boundary conditions (Fig. 5.2a) of Eq. (5.2) can be defined by:

$$\begin{cases} \left.\dfrac{\partial \langle C \rangle^{f}}{\partial r}\right|_{r=0,t} = 0 \\ \left.\langle C \rangle^{f}\right|_{r=R,\,t} = \gamma C \\ -D_{eff}^{core}\left.\dfrac{\partial \langle C \rangle_{core}^{f}}{\partial r}\right|_{r=R_{core},t} = -D_{eff}^{shell}\left.\dfrac{\partial \langle C \rangle_{shell}^{f}}{\partial r}\right|_{r=R_{core},t} \end{cases} \tag{5.6}$$

where C is the total protein concentration in the release medium, R is the radius of the nanoparticle, γ is the partition coefficient that relates the interfacial protein concentrations at the interface between the nanoparticle surface and the release medium, $\langle C \rangle_{core}^{f}$ and $\langle C \rangle_{shell}^{f}$ are the interfacial local volume averaged protein concentrations at the interface between core and shell matrices with corresponding effective diffusivities of D_{eff}^{core} and D_{eff}^{shell} and core and shell thicknesses of R_{core} and R_{shell}, respectively. The initial condition is given by:

$$\left.\langle C \rangle^{f}\right|_{R_{core}\langle r\langle 0,\, t=0} = \psi\left(\varepsilon\rho_w + (1-\varepsilon)\bar{\rho}_{pol}\right) \tag{5.7}$$

where ψ is the loading capacity in terms of mass of protein per unit mass of encapsulating nanoparticle, ρ_w is the density of the fluid phase (aqueous phase) (kgm^{-3}) and $\bar{\rho}_{pol}$ is the average polymer density (kgm^{-3}).

5.3.2. Numerical simulation and estimation of the release mechanistic parameters

Assuming that i) the protein denaturation in the nanoparticle is negligible due to the presence of buffering excipients that neutralize acidic degradation products; ii) the mass transfer resistance at

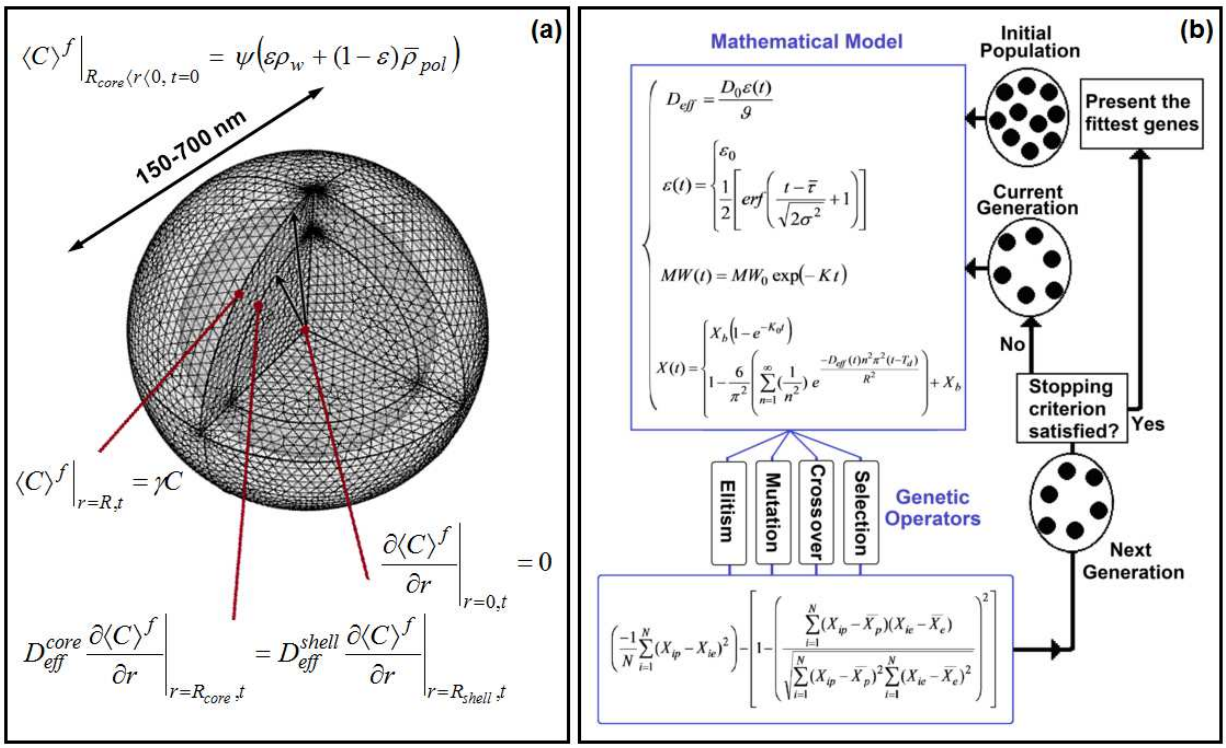

Figure 5.2. (a) the boundary and initial conditions associated with the LVA-based mechanistic model to describe controlled release from a bi-layer nanoparticles and (b) schematic diagram of the developed Geno-Mechanistic model.

the particle-release medium interface is negligible due to sufficiently high mixing, iii) nanoparticles are spherical with relatively uniform size distribution associated with reasonably low PDI, iv) at each differential time step, time-dependent polymer MW, porosity and effective diffusivity can be averaged over PLGA core and PLLA shell independently, and v) the solubility of ovalbumin in water is sufficiently high to allow for rapid dissolution in the water-filled pores, Eqs. (5.2)-(5.6) were numerically solved using the finite element method in COMSOL (4.4) for core-shell bi-layer nanospheres at three PLLA/PLGA mass ratios. The protein concentration across the nanosphere that was computed at each temporal and spatial step of the numerical solution was normalized with respect to the initial condition, and the time-dependent cumulative protein release ($X(t)$) corresponding to each time step was calculated from:

$$X(t) = 1 - S(t) \tag{5.8}$$

where *S(t)* is the cumulative fraction of protein retained in the core and shell at each time step. Simulation parameters, including the nanoparticle size and the shell to core thickness, were identified based on the measurement from dynamic light scattering and the measurements of PLLA shell to PLGA core thickness ratios from extrapolated results corresponding to bi-layer microspheres (Fig. 5.3k). The initial polymer MW was adopted from polymer information supplied by the supplier. Starting from initial values of the parameters suggested by GA, the model was numerically solved in an iterative fashion to search for optimal core and shell transport and degradation properties such that sum of squared of prediction error and coefficient of determination between experimental data and the predicted values of cumulative release were minimized and maximized, respectively. Then, the estimated degradation and diffusivity values were compared to those reported by Wu and Wang (2001) [22]. Also, the estimated values of core and shell transport and degradation properties were then compared to the volume-averaged values predicted by the Geno-Mechanistic model presented in the following.

5.3.3. Development of the Geno-Mechanistic model

5.3.3.1. Governing equations

It is reasonable to develop the governing equations of release based on a pseudo bi-layer nanoparticle that exhibits similar release kinetics as a core-shell bi-layer nanoparticle. The pseudo bi-layer nanoparticle is assumed to be a PLLA-PLGA composite nanosphere that possesses volumetrically averaged properties of release. Unlike the LVA approach in which the local volume averaged transport and degradation properties and equations are used to predict spatial and temporal release behaviour of core and shell, the pseudo bi-layer nanoparticle-based

properties and governing equations approximate the temporal release and property changes that are volumetrically averaged over the entire nanoparticle.

When the nanoparticles are placed in a release medium, the hydration is occurred quickly for bulk eroding polymers such as PLGA [18] where the protein molecules attached to the nanoparticle surface or entrapped within the superficial pores are quickly dissolved and released into the medium, a process called 'initial burst release'. Although often happening within a short period of time, the burst release is a non-linear process, depending on the protein concentration and solubility. The time-dependent cumulative protein release, *X(t)*, due to the burst effect [20] can be defined by:

$$X(t) = \frac{M^b}{M_\infty}\left(1 - \exp(-K_0 t\right) \tag{5.9}$$

where M^b is the volume-averaged amount of surficial protein (mg), M_∞ is the total amount of the protein which can be eventually released over an infinite time from the entire nanoparticles, K_0 is the burst release rate constant (day^{-1}).

With the assumption of the quick polymer matrix hydration [18], polymer bonds begin to break down because of hydrolysis where the kinetics of the polymer degradation can be described by Eq. (5.5). While polymer degradation begins after hydration, it is assumed that the diffusion of the degradation products of the polymer matrix considerably takes place after the onset of bulk erosion of the matrix. As such, depending on the induction time and bulk erosion period, the polymer degradation rate (K_{deg}) in Eq. (5.5) may take different values accordingly.

Assuming that the polymer degradation and pore formation take place heterogeneously with spatially equal probability of pore formation within a polymeric matrix, porosity simply exhibits time-dependent with a random fashion of pore formation that is normally distributed within the

polymeric matrix during bulk degradation. Taking into account the coalescence of pores that makes the pore formation cumulative, the time-dependent porosity is defined by:

$$\varepsilon(t) = \frac{1}{2}\left[erf\left(\frac{t-\bar{\tau}}{\sqrt{2\sigma^2}} \right) + 1 \right] \tag{5.10}$$

where σ^2 is the variance in the time for pore formation that represents the degree of crystallinity of the polymeric matrix, and $\bar{\tau}$ is the mean time of pore formation for PLGA and PLLA that follows the first order degradation rate given by:

$$\bar{\tau} = \frac{-\ln\left|\frac{MW(t)}{MW_0}\right|}{K_{\deg}} \tag{5.11}$$

where K_{deg} is the average pseudo-first order degradation rate, *MW(t)* is the time-dependent polymer MW.

After the induction time when the polymer MW and pores are sufficiently decreased and formed, respectively, diffusional mass transfer takes control over the protein release across the matrix and can be expressed by the modified dimensionless Fickian diffusion model:

$$\frac{\langle C \rangle^f(t)}{\langle C_0 \rangle} = \frac{6}{\pi^2}\left(\sum_{n=1}^{\infty} \left(\frac{1}{n^2}\right) e^{\frac{-D_{eff}(t) n^2 \pi^2 (t-T_d)}{R^2}} \right) \tag{5.12}$$

Combining Eqs. (5.9) and (5.12), the total cumulative mass fraction of the released protein from nanoparticles is:

$$X(t) = \begin{cases} X_b\left(1-e^{-K_0 t}\right) & 0 \le t \le T_d \\ 1 - \frac{6}{\pi^2}\left(\sum_{n=1}^{\infty} \left(\frac{1}{n^2}\right) e^{\frac{-D_{eff}(t) n^2 \pi^2 (t-T_d)}{R^2}} \right) + X_b & t > T_d \end{cases} \tag{5.13}$$

where X_b is the cumulative mass fraction of the protein (M^b/M_∞) released during the initial burst, R is the radius of the nanosphere, and D_{eff} is the time-dependent effective diffusivity that relies on the average polymer MW, which changes with time as a function of degradation rate constant (K_{deg}) associated with the induction time and bulk erosion period. Based on the average pseudo-first order degradation rate constant (K_{deg}), the distribution of mean time of pore formation ($\bar{\tau}$) is obtained from Eq. (5.11) for the given initial MW, the associated standard deviation is calculated and adjusted by crystallinity-based factors of 5, 4, and 4.5 corresponding to PLGA lactide to glycolide ratios of 50:50, 75:25 [20], and composite PLGA and PLLA. The variance (σ^2) is calculated using the adjusted standard deviation of the mean time of pore formation, and then used for estimation of time-dependent porosity in Eq. (5.10).

5.3.3.2. Geno-Mechanistic modeling approach

GA, which is based on biological concepts of evolution and genetics, is an iterative and population-based search algorithm for optimization problems [21]. Coupled with the governing equations of controlled release, GA-mathematical model, or so called "hybrid model" afterwards, allows for identification of multi objective inverse simulation of the release process where the fittest values of the release parameters can be estimated. Figure 5.2b illustrates the schematic diagram of the modeling approach in which a system of governing equations involving Eqs. (5.3), (5.5), (5.9)-(5.13) are solved simultaneously in order to map the fittest genes that are defined as the critical mechanistic release parameters in an evolutionary fashion. Gens undergo genetic operators (crossover, mutation, selection and elitism), and then are applied to the mathematical model to predict the outcome of each individual in the generation. The outcome is evaluated by a fitness function to generate the next generation. The evolving process continues until the fitness of the genes is maximized (Fig. 5.2b). Based on a preliminary sensitivity

analysis, an initial population of 500, number of generations of 200, selection rate of 0.08, mutation rate of 0.05, and crossover rate of 0.6 were chosen for the hybrid model to search for the fittest genes (release parameters corresponding to the range of nanoparticle size measured by dynamic light scattering method. The release profiles predicted based on the estimated release parameters (the fittest genes) was statistically compared to the experimental data to verify the performance of the inverse simulation approach.

5.3.4. Fabrication of PLGA and bi-layered nanoparticles

Bi-layered nanoparticles were fabricated using a modified double emulsion solvent extraction technique as described in our previous study [2]. Briefly, polymers were dissolved in HPLC grade dichloromethane (DCM) (Sigma-Aldrich, MO) and ovalbumin (OVA) (Sigma-Aldrich, MO) solution was used as the protein model in the internal aqueous phase (IAP). The IAP was added to PLGA (DURECT Co., Cupertino, CA) organic phase followed by sonication and the emulsion was subsequently mixed with PLLA (DURECT Co., Cupertino, CA) solution. The mixture was sonicated in polyvinyl alcohol (PVA) (Sigma-Aldrich) solution and then added to the external aqueous phase (EAP) that stirred for 24 h. The nanoparticles were collected by ultracentrifugation (Optima L-Series, Becman Coulter Inc., Palo Alto, CA) and washed three times with de-ionized water followed by freeze drying at at -80°C for 3 days. The modified double emulsion solvent removal technique was applied to the preparation of single polymer (PLGA) nanoparticles [19]. Table 5.1 summarizes the conditions used to prepare the nanoparticles and their groups for the subsequent experiments.

5.3.5. Physical, structural and morphological assessments

Dynamic Light Scattering technique (Zetasizer, Nano ZS3000; Malvern Instruments, Malvern, UK) was used to measure the size, polydispersity index (PDI) and zeta potential of nanoparticles.

Table 5.1. Groups of the protein-loaded bi-layered and single polymer nanoparticles and their fabrication conditions.

Polymer characteristic	Experimental Group			
	I	II	III	IV
Concentration (% w/v)	9	16.6	16.6	16.6
PLGA viscosity (dLg^{-1})	0.2	0.65	0.65	0.65
PLLA viscosity (dLg^{-1})	n/a	0.9	0.9	0.9
PLGA L:G ratio	75:25	50:50	50:50	50:50
PLGA to PLLA mass ratio	0	1	2	3

Surface morphology of the nanoparticles was assessed under a field-emission scanning electron microscope (JSM-6010 LV, JEOL, Ltd., Tokyo, Japan) at 15 kV.

To view the internal bi-layered structure and to identify the composition of the core and shell, microspheres were suspended in a mixture of gelatine (20%) and glycerine (5%) for 8 h at room temperature in a cryostat mould and frozen at -80°C for an hour before the mould was placed over liquid nitrogen. The solidified gel was removed from the mould and sectioned at 10 µm using a cryostat at -30°C. The cross sectioned particles were viewed under a phase contrast microscope to view the core and shell structure. The microscope slides holding the particle cross-sections were immersed in ethyl acetate for 12 hours allowing PLGA to be dissolved while leaving PLLA in place due to higher PLGA solubility (580 $mgml^{-1}$) than PLLA solubility (0.1 $mgml^{-1}$) [4] in ethyl acetate. Ring shape or a solid core configuration of the remnant of the cross sections in ethyl acetate was viewed under a phase contrast to identify the composition of the shell and core of the bi-layered structures.

To gauge the protein distribution across the bi-layered structures, the microspheres loaded with labelled protein (OVA Texas Red® Conjugate, Life Technologies, Grand Island, NY) were cross-sectioned and viewed under a fluorescence microscope. To assess the effect of particle size and PLLA to PLGA mass ratio on the protein distribution and shell thickness of the bi-layered configurations, two dimensionless indices of shell-to-core thickness ratio and shell-to-core fluorescence intensity ratio defined as the average shell thickness divided by the core radius and the average fluorescence intensity of the shell divided by that of the core were defined, respectively, and evaluated for 100 microparticles at the largest diameter of the cross-sections (x-y plane at the particle center) and statistically compared for three polymer mass ratios of 1:1, 2:1 and 3:1.

5.3.5. Release study and protein encapsulation capacity assessment

To determine the protein encapsulation capacity, protein-loaded nanoparticles were re-suspended in 0.1 M sodium hydroxide containing 5% of sodium dodecyl sulphate followed by incubation at room temperature overnight in an orbital shaker. Centrifuging at 15000 rpm for 10 min, the supernatant was collected and used for quantifying OVA concentration based on Bicinchoninic acid (BCA) protein assay (Sigma-Aldrich, MO). Reading the absorbance of the samples including the standards at 562 nm using a UV spectrophotometer (Synergy HT, BioTek Instruments, Inc., Winooski, VT), OVA concentration was determined and the loading capacity was then calculated as:

$$\psi = \frac{C_{OVA}}{C_{NP}} \tag{5.14}$$

where ψ is the loading capacity (mg OVA mg^{-1} nanoparticles), C_{OVA} is OVA concentration from

the direct extraction (mg OVA ml^{-1}), and C_{NP} is the concentration ($mgml^{-1}$) of OVA-loaded nanoparticles used for OVA extraction.

Based on direct measurement of OVA in the release medium, the release study was conducted *in-vitro* for the protein-loaded nanoparticles. Certain amounts of nanoparticles were re-suspended in phosphate-buffered saline (PBS) (Sigma-Aldrich, MO) in glass vials which were placed on an orbital shaker with a swinging sample holder to provide rotational and axial mixing at 37°C. At predetermined time intervals over 70 days, 800 µl of each sample was centrifuged at 10000 rpm at 4°C. 450 µl of the supernatant was used for quantifying OVA concentration and then was replaced by 450 µl fresh PBS. The nanoparticles pallet in each vial was then re-suspended in PBS on a vortex and transferred into its corresponding vial on the orbital shaker. The protein concentration was quantified by reading the absorbance of the samples at 562 and 572 nm using UV spectrophotometer (Synergy HT, BioTek Instruments, Inc., Winooski, VT). The experiments were carried out in triplicates.

5.4. Results and discussion

5.4.1. Physical, structural and release characteristics of bi-layer nanoparticles

Figure 5.3a illustrates SEM image of the cross-section of a bi-layer microsphere at a PLLA/PLGA mass ratio of 1. A porous core can be distinguished from the less porous shell. The pores in the core represent the freeze-dried IAP that is largely entrapped in the core matrix. Figures 5.3b, c illustrate the bright field and fluorescence microscope images, respectively, of a cross-sectioned bi-layer microsphere at PLLA/PLGA mass ratio of 3. The encapsulated protein can be largely identified in the core (Fig. 5.3c), while a scattered pattern of the protein can be noted in the shell. Figure 5.3d depicts ethyl-acetate treated cross-section of the bi-layer microsphere. The hollow ring configuration indicates that PLGA largely constitutes the core

because of much larger PLGA solubility in ethyl acetate than PLLA [2]. Considering that PLGA is the main constituting polymer of the core (Fig. 5.3d), the localization of the protein in the core (Fig. 5.3c) indicates that the encapsulating protein has higher affinity to PLGA than PLLA. Also, the first sonication in which IAP is encapsulated in PLGA contributes to localization of the IAP that contains protein in the core (Fig. 5.3a). The presence of the scattered pattern of protein in the shell may be attributed to the presence of PLGA in the shell [2]. Figure 5.3e depicts pores associated with PLGA dissolution in ethyl acetate. Depending on the degree of polymer phase separation during the preparation process, the fraction of PLGA residue in the shell increases if the phase separation is incomplete. As such, due to the higher PLGA affinity of the protein (Fig. 5.3c), the presence of the protein in the shell is elevated if polymer phase separation is incomplete.

Figures 5.3f-i illustrate the surface morphology, geometry and level of agglomeration of the nanoparticles prepared at different PLLA/PLGA mass ratios. Spherical geometry and low nanoparticle agglomeration can be noted from the SEM images. The size of the nanoparticles increases with PLLA/PLGA mass ratio from ~180 nm (Fig. 5.3f) at PLLA/PLGA mass ratio of 0 to ~670 nm (Fig. 5.3i) at PLLA/PLGA mass ratio of 3. This observation is consistent with the average nanoparticle size measurements resulted from dynamic light scattering (Table 5.2). Surface morphology of the nanoparticles reveals no superficial pores or cracks, which can significantly contribute to the reduction of initial burst effect. Measurements from dynamic light scattering indicated reasonably low polydispersity index (PDI) at PLLA/PLGA mass ratios of 0-2 (Table 5.2) indicating a relatively uniform size distribution of the nanoparticles. However, PDI of bi-layer nanoparticles increased (>0.4) at PLLA/PLGA mass ratio of 3, reflecting less uniform size distribution that can also be seen in the corresponding SEM image (Fig. 5.3i).

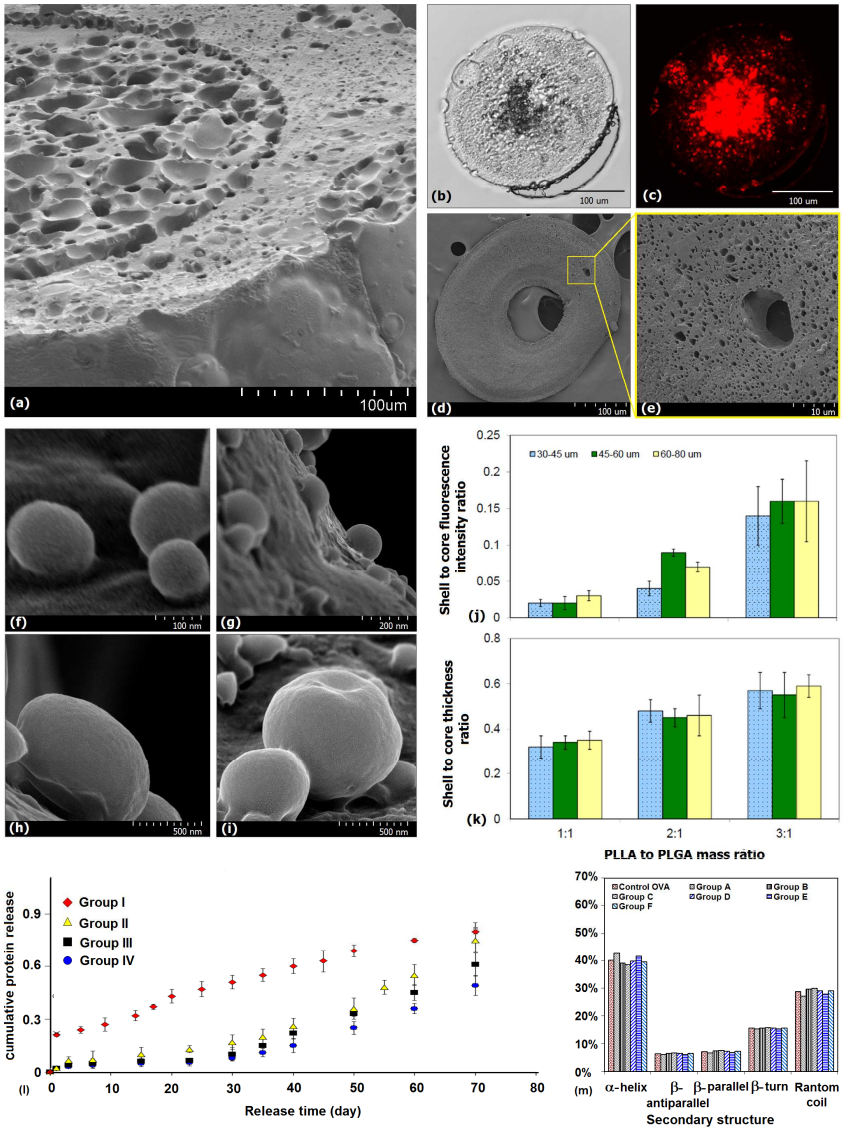

Figure 5.3. (a) SEM image, (b) bright field and (c) fluorescence microscopy images of the core-shell structures, (d) SEM image of the ethyl acetate-treated cross-section of a bi-layer structure, (e) the emerging pores on the shell after applying ethyl acetate assay, (f-i) surface morphology of the nanoparticles at PLLA/PLGA mass ratios of 0, 1, 2 and 3, respectively, (j, k) the effects of particle size and PLLA/PLGA mass ratios on the shell-to-core protein distribution ratio and shell-to-core thickness ratio; (l) the protein release profiles of the nanoparticles, and (m) deconvolution of the protein CD spectra compared to control.

Figures 5.3j, k illustrate the average values of shell/core fluorescence intensity and thickness ratios, respectively, corresponding to three average particle size ranging from 30 to 80 μm at polymer mass ratios of 1, 2 and 3. The shell/core fluorescence intensity ratio (Fig. 5.3j) and the shell/core thickness ratio (Fig. 5.3k) increase with the polymer mass ratio (p-value<0.05), while the effect of average particle size is insignificant (p-value>0.05). Statistically being independent of particle size, the indices may be extrapolated to explain the shell/core protein distribution and thickness ratios for bi-layer nanoparticles.

Figure 5.3l illustrates the release profile of the nanoparticles that were prepared at different conditions (Table 5.1) over 70 days. A very distinct time-delayed release and low initial burst release of bi-layer nanoparticles, which were prepared at PLLA/PLGA mass ratios of 1-3 (Figs. 5.3g-i), can be distinguished from the nanoparticles that were prepared with PLGA only (Fig. 5.3f). The release lag phase of the bi-layer nanoparticles is followed by a zero order kinetics (Groups II-IV), while PLGA nanoparticles exhibit a zero order kinetics from the beginning (Fig. 5.3l). Figure 5.3m illustrates the secondary structure in terms of relative proportion of α-helix, β-sheets and random coil of the protein released over 70 days compared to those of the control sample. An independent sample t-test at a significance level of 0.05 indicate no significant difference between the percentage of α-helix, β-sheets and random coil of the released protein and those of the standard sample (p-value>0.05), suggesting that the structural integrity of the encapsulated protein has been preserved during the release process (Fig. 5.3m).

Table 5.2 summarizes measured values of size, PDI and loading capacity of the nanoparticles corresponding to the experimental groups.

Table 5.2. Measured physical characteristics of the nanoparticles corresponding to the experimental groups.

Physical characteristic	Experimental Group			
	I	II	III	IV
Size (nm)	258±12	340±29	490±16	685±43
PDI	0.30±0.03	0.32±0.08	0.38±0.05	0.46±0.04
Loading capacity (μg/mg)	0.2	0.05	0.02	0.01

5.4.2. Evolutionary-based parameter estimation and predictability of the Geno-Mechanistic model

Figures 5.4a-e illustrate the evolution of the fitness of the best individual and major release mechanistic parameters, so called genes, of each generation over 500 generations. The best fitness value of each generation is significantly improved after 50 evolutions and is further enhanced and reaches its best and constant value after 300 generations (Fig. 5.4a). Consistent with the improving fitness value, the gens that represent the mechanistic release parameters such as initial effective diffusivity of the matrix (D_0), degradation rate constant (k_{deg}) and the release lag phase evolve and converge to their fittest values over 500 generations (Figs. 5.4b-e). Applying the fittest values of the release parameters to the system of governing equations (Eqs. 5.2-5.5), the release profiles corresponding to the nanoparticle polymeric groups I-IV (Table 5.1) were predicted using the Geno-Mechanistic model. Figure 5.4f illustrates the predicted values and the experimental data of cumulative release of the protein associated with different designs of nanoparticles. The coefficient of determination of 0.98 indicates a very good agreement between experimental data and predicted values (Fig. 5.4g) where the mean prediction error

(MPE) is less than 5% and the residual of errors exhibits a random distribution that indicates unbiased predictability of the Geno-Mechanistic model (Fig. 5.4h). High coefficient of determination, low MPE and random distribution of residual of errors indicate that the model can successfully predict the zero order kinetics of the PLGA nanoparticles (Group I) and the time-delayed release pattern of the bi-layer nanoparticles of groups II-IV. Figure 5.4i illustrates the variation of the volume-averaged MW of the nanoparticles during the release. The PLGA nanoparticles (Group I) undergo 50% and 90% of the polymer degradation within 12 and 40 days, respectively (Fig. 5.4i). The PLGA degradation profile that was predicted by the Geno-Mechanistic model in terms of temporal changes in fractional MW was consistent with the datasets reported by Batycky et al. (1997) [23], Wang et al. (2006) [24] and Xi et al. (2010) [25]. In contrast, the MW of the bi-layer nanoparticles exhibit two-phase degradation profiles where MW decreases by ~13% within 25, 30 and 32 days for Groups II, III and IV, respectively, followed by a relatively sharp MW reduction (Fig. 5.4i). The trend of the MW degradation of the bi-layer nanoparticles is generally consistent with the experimental data reported by Xu et. al (2013) [26]. The fact that PLLA is a weaker hydrophilic polymer than PLGA suggests that PLLA undergoes a slow hydrolysis which reduces the overall degradation rate of the bi-layer polymeric nanoparticles associated with the first degradation phase. As a result, with increasing PLLA/PLGA mass ratio from 1 to 3, the first degradation phase becomes longer for the nanoparticles in Groups II to IV, respectively (Fig. 5.4.i). The sharp reduction in MW in the second phase of degradation can be attributed to PLGA degradation. Since PLGA is more hydrophilic and degrades faster than PLLA, the acidic degradation products from PLGA hydrolysis catalyze PLLA degradation that results in a steep MW reduction of the bi-layer nanoparticles in Groups II-IV (Fig. 5.4i). Despite the consistency in the trend, the discrepancy

between the predicted values and the reported data [26] can be attributed to the assumption of pseudo bi-layer nanoparticles in the GA-Mechanistic model. Also, since the reported data [26] are associated with microparticles, rather than nanoparticles, the mass transfer resistance associated with the larger particle size contributes to slower polymer erosion that can delay the bulk degradation of microparticles, compared to that of nanoparticles.

Table 5.3 presents the volume averaged values of the major release transport and degradation parameters involved in release mechanism of the nanoparticles corresponding to the experimental groups. The initial effective diffusivity of 3.24×10^{-17} m^2s^{-1} that was estimated by the Geno-Mechanistic model was consistent with the value of 9.4×10^{-17} m^2s^{-1} suggested by the regression analysis in literature [20]. The difference between the effective diffusivity values can be attributed to the lower hydrophilicity associated with L:G ratio of 75:25 of PLGA nanoparticles in this study compared to L:G ratio of 50:50 that provides a higher hydrophilicity [20]. The higher hydrophilicity enhances hydrolytic PLGA degradation rate that contributes to increase the effective diffusivity. In addition, since the regression analysis [20] was based on the data of microparticles, there might be an error originated from the extrapolation of the regression equation to estimate the average effective diffusivity of the nanoparticles. The volume-averaged initial effective diffusivity (D_i) of the bi-layer nanoparticles was significantly lower than that of the single polymer nanoparticles. Notably, the effective diffusivity decreases with PLLA/PLGA mass ratio, indicating that the shell thickness may have a significant influence on reducing the volume-averaged diffusivity of the bi-layer nanoparticles (Table 5.3). The average degradation rate constant of 0.064 day^{-1} that was estimated for PLGA nanoparticles by the Geno-Mechanistic model was consistent with the reported values of the average degradation rate constants (K_{deg}) of 0.068 day^{-1} [22], 0.05 day^{-1} [27], and 0.056 day^{-1} [28]. Moreover, the estimated degradation rate

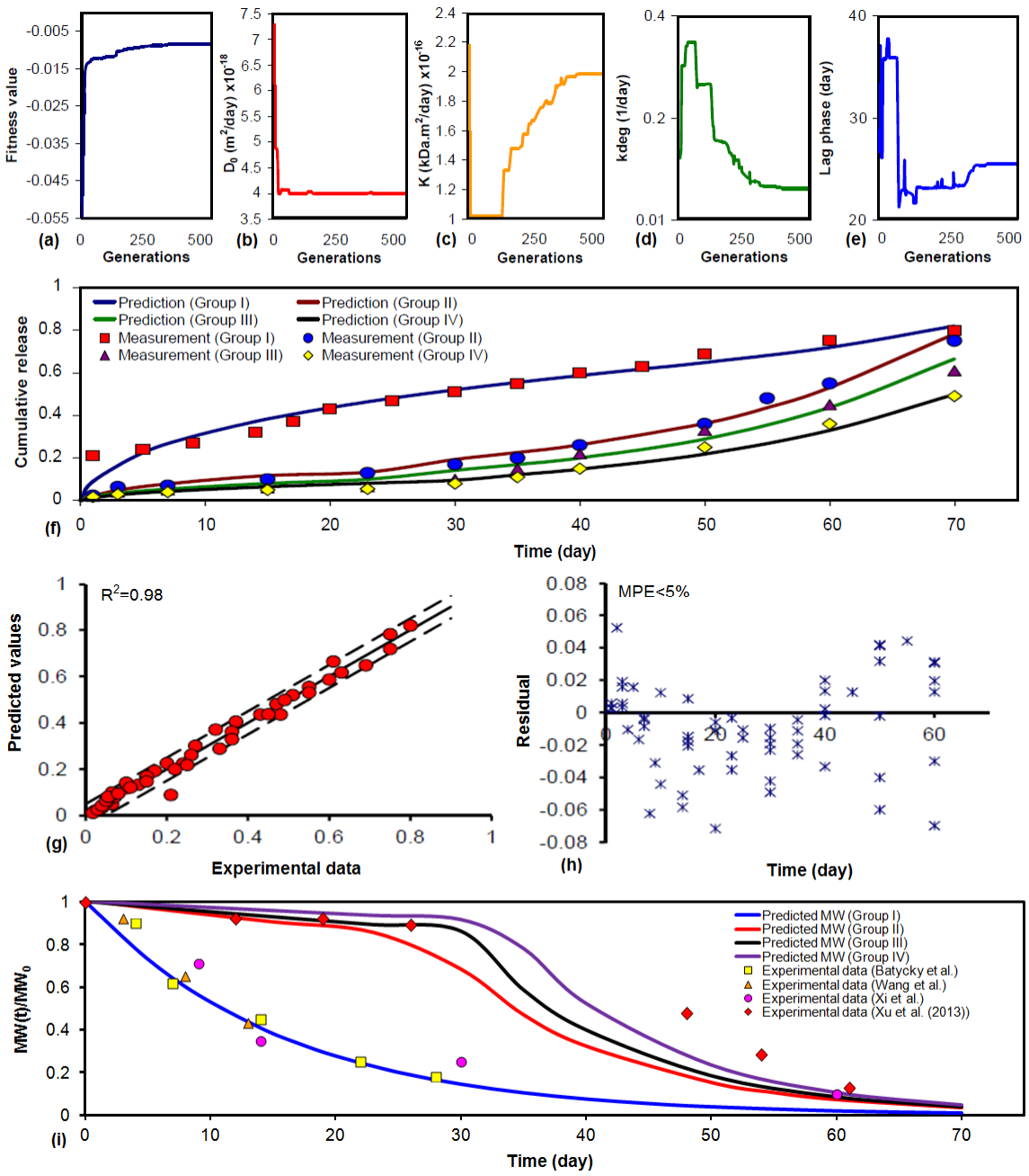

Figure 5.4. (a-e) the variations of the fitness value and the evolved genes over 500 generations, (f, g) agreement between experimental data and simulation results of protein release, (h) the distribution of the residual of prediction errors associated with the Geno-Mechanistic model; (i) the temporal changes in the volume-averaged MW predicted by the Geno-Mechanistic model compared to the reported values in literatures.

Table 5.3. Volume averaged values of major release parameters of the nanoparticles estimated by the Geno-Mechanistic model.

Release parameter	Nanoparticle experimental Group			
	I	II	III	IV
D_i ($m^2 day^{-1}$) $\times 10^{-17}$	3.24	0.41	0.22	0.10
K_{deg} (day^{-1})	0.064	0.075	0.077	0.080
T_d (day)	0.1	27	30	33
X_b	0.27	0.05	0.04	0.03
K_0 (day^{-1})	0.91	0.52	0.43	0.21
$\bar{\tau}$ (day)	21.8	28.2	26.7	23.2
$\sqrt{\sigma^2}$ (day)	3.6	3.2	3.3	3.4
K ($m^2 day^{-1}$ kDa) $\times 10^{-17}$	2.11	19.7	75.3	68.0

constant of PLGA nanoparticles (Group I) is lower than that of bi-layer nanoparticles. This may be explained by the influence of the PLLA shell on the internal build-up of acidic degradation products catalyzing the degradation of core and shell. In a PLGA nanoparticle, the acidic degradation products can more easily diffuse and be released into the releasing medium; however, in bi-layered nanoparticles the PLLA external layer contributes to the accumulation of the acidic products in the core catalyzing the matrix degradation. By increasing the thickness of the shell, the accumulation of the acidic degradation products in the core may be improved so that the matrix degradation rate constant increases with PLLA/PLGA mass ratio. The Geno-Mechanistic model also suggests that the degradation rate constant increases from 0.075 to 0.077 and 0.08 with PLLA/PLGA mass ratios corresponding to Groups II-IV (Table 5.3).

The lag phase of release increases with PLLA/PLGA mass ratio from 27 to 33 days that may be explained by the effect of the shell thickness on controlling the protein release from the core. Moreover, the bi-layer nanoparticles provide an initial burst release (X_b) of <6% which remains significantly lower than 27% associated with PLGA nanoparticles (Table 5.3). The model also suggests that the volumetric mean time of pore formation ($\bar{\tau}$) of bi-layer nanoparticles is significantly higher than that of PLGA nanoparticles (Table 5.3), while the mean time of pore formation decreases with PLLA/PLGA mass ratio of bi-layer nanoparticles (Table 5.3).

5.4.3. 3D-simulation of controlled release from bi-layer nanoparticles using LVA approach

Figure 5.5a illustrates the time course of the protein spatial distribution across a bi-layer nanoparticle at PLLA/PLGA ratio of 1 over 70 days. The protein is initially confined in the core, and notably the diffusion across the shell remains so slow over 35 days (Fig. 5.5a). Over time, the protein diffusion across the shell is enhanced so that the core reaches a uniform protein concentration and the mass transfer is controlled by the concentration gradient across the shell by 50 days of release. The time course of the protein distribution across the bi-layer nanoparticles (Fig. 5.5a) is consistent with the release kinetics of the bi-layer nanoparticles depicted in Fig. 5.5b. The cumulative release remains very limited within 30 days of release but gradually increases with time (Fig. 5.5b). Moreover, a very good agreement between the predicted values from the LVA-based 3D mechanistic model and experimental data can be noted in Fig. 5.5b. The MPE of <5% and the coefficient of determination of 0.98 between predicted and experimental results indicate a very good predictability of the model (Fig. 5.5c). Furthermore, the random distribution of the residual errors of predictions suggests unbiased predictability of the model (Fig. 5.5d). Figure 5.5e illustrates the spatiotemporal protein concentration across the core and shell of a bi- layer nanoparticle at PLLA/PLGA mass ratio of 1. Initially the protein is uniformly

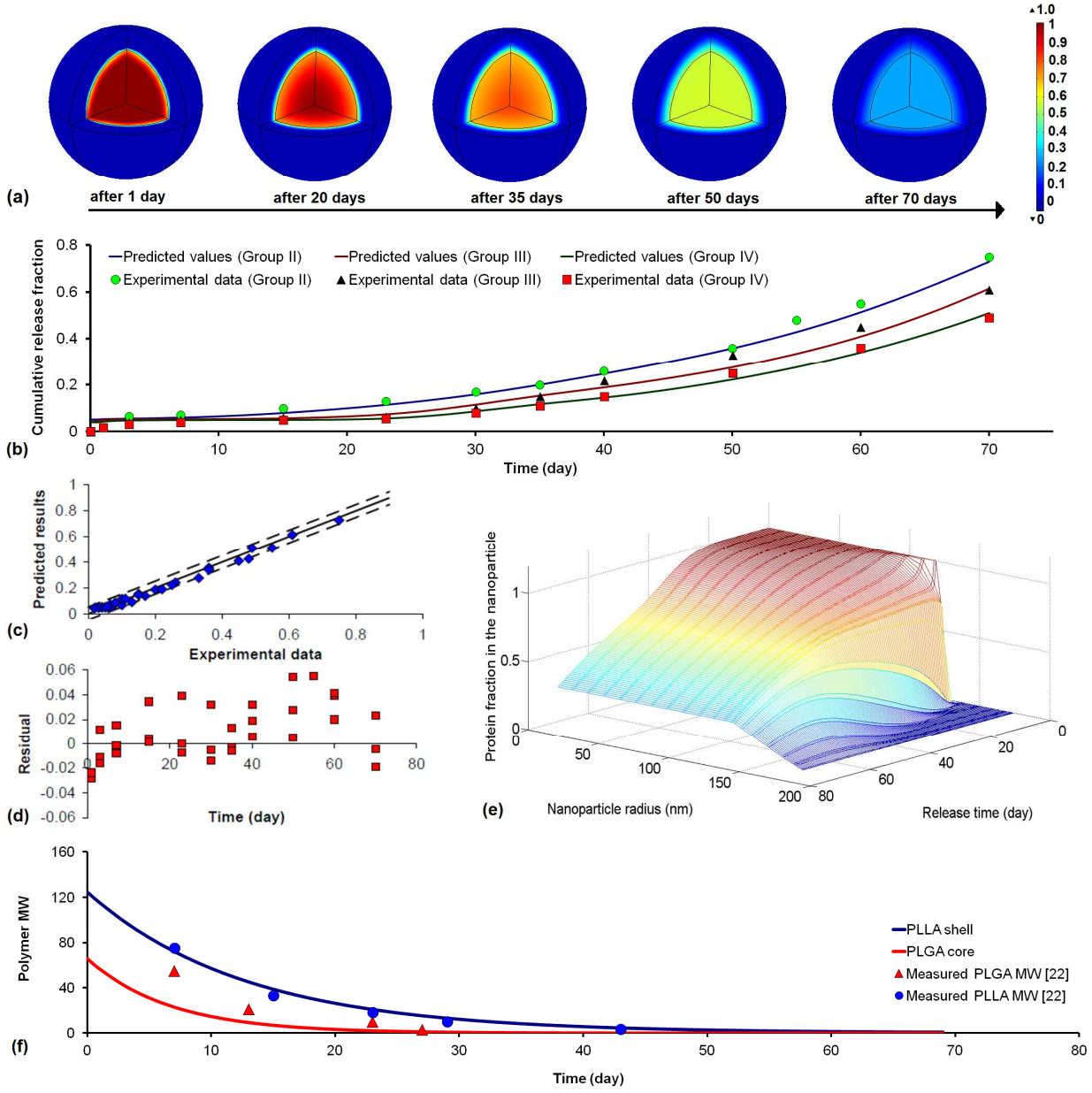

Figure 5.5. (a) Spatiotemporal variation of the encapsulated protein in a bi-layer nanoparticle (Group II) predicted by LVA-based 3D mechanistic model over 70 days; (b, c) the agreement between experimental data and simulation results, (d) random distribution of prediction errors with a MPE of <5%; (e) variation of protein concentration with time and position across a bi-layer nanoparticle at PLLA/PLGA mass ratio of 1; (f) predicted MW variation of PLGA core and PLLA shell compared to the values in the literature.

distributed and confined in the core by the PLLA shell. Due to a large reduction (>50%) in MW of PLGA core within 10 days (Fig. 5.5f), the effective diffusivity of the core relatively increases and subsequently allows for the protein diffusion into the core-shell interface (Fig. 5.5e). At the same time, the protein concentration at the interfacial region of the shell gradually increases but the diffusion rate remains very limited due to the low effective diffusivity of the shell that is attributed to the relatively low degradation rate of PLLA shell (Table 5.4). The protein concentration in the shell begins to increase after 20 days (Fig. 5.5e) and subsequently reduce the interfacial concentration gradient. Despite a significant improvement in PLGA core diffusivity, which is attributed to a sufficiently high polymer degradation rate by 30 days (Fig. 5.5f), the shell predominantly limits the mass transfer from the core-shell interface to the nanoparticle surface (Fig. 5.5e). Further reduction in PLLA shell MW after 40 days improves the shell effective diffusivity (Eq. 5.3) that facilitates the mass transfer across the shell (Fig. 5.5e). After 45 days of release, PLGA MW is so low (Fig. 5.5f) that the effective diffusivity is no longer a limiting factor in the core, and a relatively uniform protein concentration in the core together with a linear concentration gradient across the shell provides a steady diffusional mass transfer (Fig. 5.5e) that results in zero order release kinetics (Fig. 5.5b). The protein concentration continues to linearly decline across the nanoparticles for the rest of the release period. As shown in Fig. 5.5f, there is a good agreement between the simulation results of temporal MW changes of PLLA shell and PLGA core and the experimental data reported by Wu and Wang (2001) [22]. The discrepancy between simulated and experimental data of PLGA MW within the first 10 days can be associated with the acidic degradation products in the core that accelerate PLGA degradation, while the reported experimental data [22] have been collected at pH>5.

Table 5.4. Core and shell averaged transport and degradation properties estimated by LVA-based 3D model compared to the volume-averaged values estimated by the Geno-Mechanistic model.

	PLLA/PLGA mass ratio of bi-layered nanoparticles								
	1:1			2:1			3:1		
	Hybrid model	3D model		Hybrid model	3D model		Hybrid model	3D model	
Properties	Volume-averaged	Core	Shell	Volume-averaged	Core	Shell	Volume-averaged	Core	Shell
[a]d (nm)	340	120	50	490	172	73	680	216	124
MW_0 (kDa)	95	60	130	95	60	130	95	60	130
D_{eff} ($\times 10^{-16}$) ($m^2 day^{-1}$)	0.041	28.3	0.25	0.022	430	0.061	0.010	432	0.052
K_d (day^{-1})	0.075	0.150	0.078	0.077	0.199	0.085	0.080	0.219	0.089

[a]Particle diameter, core radius and shell thickness.

5.4.4. A comparison between Geno-Mechanistic model and LVA-based 3D simulation

Table 5.4 presents the transport and degradation properties of the core and shell of bi-layered nanoparticles corresponding to the size and core-shell polymer mass ratios compared to those estimated by the hybrid (Geno-Mechanistic) model. For all levels of PLLA/PLGA mass ratios and particle size, the averaged effective diffusivity of shell is significantly smaller than that of the core (Table 5.4), indicating that PLLA shell performs as a rate-limiting layer controlling the time-delayed release. Furthermore, the volume-averaged values of the effective diffusivity that were estimated by the Geno-Mechanistic (hybrid) model are similar to the values of shell effective diffusivity predicted by LVA-based 3D model (Table 5.4). This comparison suggests that PLLA shell transport properties pre-dominantly control the overall mass transfer behaviour that is described by the governing equations of the Geno-Mechanistic model (Table 5.4). Being

consistent with the fact that PLLA is less hydrophilic than PLGA, the polymer degradation rate constant of the core is predicted to be larger than that of the shell for all levels of PLLA/PLGA ratios (Table 5.4). Furthermore, the values of the volume-averaged degradation rate constant, which was estimated by the Geno-Mechanistic model, is very close to the values of the shell degradation rate constant for all levels of PLLA/PLGA ratios, indicating that overall degradation of a bi-layer nanoparticle may be approximated by the degradation rate of PLLA shell. The estimated values of PLLA shell and PLGA core degradation rate constants (Table 5.4) are consistent with the measured values ranging from 0.04 to 0.09 day^{-1} reported by Wu and Wang (2001) [22].

5.5. Conclusions

This paper presents a study on the development of models to represent the controlled-release of bioactive agents from nanoparticles for tissue engineering applications. A porous media approach based on LVA was applied to a bi-layer nanoparticle composed of PLGA core and PLLA shell, resulting the mechanistic model; while the Geno-Mechanistic model consisting of a system of governing equations of controlled release coupled with GA was developed to predict the release patterns and to estimate the fittest values of mechanistic parameters involved in protein release. Both models were set for describing the mechanism of release from bi-layer nanoparticles by predicting the transport and degradation parameters. The Geno-Mechanistic model takes into account the transport and degradation properties that are averaged over the entire nanoparticle, while the LVA-based mechanistic model is based on local volume averaged properties and mass transfer governing equations of the shell and core to predict the release behaviour of the bi-layer nanoparticles. A very good agreement between predicted values and experimental data ($r2>0.98$, MPE<5%) was observed for both models, indicating the reliability

of the models for predicting the release behaviours. The estimated values of release parameters including effective diffusivity and degradation rate constants were consistent with the corresponding measured values reported in literatures. A comparison between the mechanistic model and the Geno-Mechanistic model revealed that the transport and degradation properties of PLLA shell predominantly control the time-delayed release from the bi-layer nanoparticles. Based on the estimated degradation and transport parameters, the mechanistic model suggests a rapid degradation of PLGA core within a time course of ~35 days. Moreover, the mechanistic model suggests that all three formulations of the bi-layer nanoparticles exhibit similar PLGA core and PLLA shell erosion despite different PLLA/PLGA mass ratios. In contrast, the Geno-Mechanistic model predicted two-phase (gradual and rapid) polymer degradation and a single-phase degradation for the bi-layer and PLGA nanoparticles, respectively, which were consistent with experimental data reported in literatures.

The models developed in this study provide a better insight on the release mechanism and offer great potentials for designing and optimization of PLGA and bi-layer nanoparticles in a broad range of applications of tissue engineering. Specifically, since controlled release of multiple growth factors is an important issue for development of bio-functional tissue engineered constructs, the developed models can be employed for designing and optimizing growth factor-loaded PLGA and bi-layer nanoparticles to provide simultaneous and sequential release of bio-active agents.

References

[1] Izadifar M, Haddadi A, Chen XB, Kelly ME 2015 Rate-programming of nano-particulate delivery systems for smart bioactive scaffolds in tissue engineering. Nanotechnology **26** 012001.

[2]] Izadifar M, Kelly ME, Chen XB. Characterization of double-layered nanoparticles for time-delayed release of growth factors in cardiovascular tissue engineering, The 37th International Conference of Engineering in Medicine and Biology, Milan, Italy, Aug. 24-30 (2015).

[3] Dong A, Seidel C, Snell D, Ekawardhani S, Ahlskog JKJ, Baumann M, Shen J, Iwase T, Tian J 2014 Antagonism of PDGF-BB suppresses subretinal neovascularization and enhances the effects of blocking VEGF-A. Angiogenesis **17** 553-562.

[4] Fredenberg S, Wahlgren M, Reslow M, Axelsson A 2011 Themechanismsofdrug release inpoly(lactic-co-glycolicacid)-baseddrugdeliverysystems-areview, Int. J. Pharm. **415** 34–52.

[5] Lao LL, Peppas NA, Boey FYC, Venkatraman SS 2011 Modeling of drug release from bulk-degrading polymers, Int. J. Pharm. **418** 28–41.

[6] Corrigan OI, Li X 2009 Quantifying drug release from PLGA nanoparticulates. Eur. J. Pharm. Sci. **37** 477–485.

[7] Perale G, Casalini T, Barri V, Müller M, Maccagnan S, Masi M. 2010 Lidocaine release from polycaprolactone threads. J. Appl. Polym. Sci. **117** 3610–3614.

[8] Rothstein SN, Federspiel WJ, Little SR 2009 A unified mathematical model for the prediction of controlled release from surface and bulk eroding polymermatrices. Biomaterials **30** 1657–1664.

[9] Zhang M, Yang Z, Chow LL 2003 Wang CH Simulation of drug release from biodegradable polymeric microspheres with bulk and surface erosions, J. Pharm. Sci. **92** 2040–2056.

[10] Lao LL, Venkatraman SS, Peppas NA 2008 Modeling of drug release from biodegradable polymer blends. Eur. J. Pharm. Biopharm. **70** 796–803.

[11] Lao LL, Venkatraman SS, Peppas NA 2008 A novel model and experimental analysis of hydrophilic and hydrophobic agent release from biodegradable polymers. J. Biomed. Mater. Res. Part A **90** 1054–1065.

[12] Siepmann J, Faisant N, Benoit JP 2002 A new mathematical model quantifying drug release from bioerodible microparticles using Monte Carlo simulations. Pharm. Res. **19** 1885–1893.

[13] Danhier F, Ansorena E, Silva JM, Coco R, Le-Breton A, Préat V 2012 PLGA-based nanoparticles: An overview of biomedical applications. J. Control. Release **161** 505–522.

[14] Izadifar M 2013 Biomanufacturing versus superficial cell seeding: simulation of chondrocyte proliferation in a cylindrical cartilage scaffold. Int. J. Tissue Eng. **2013** 1-9.

[15] Izadifar M. A Porous Media Approach for Physiological Modeling, LAP LAMBERT Academic Publishing, Germany, 2013.

[16] Hines **DJ**, Kaplan **DL** 2013 Poly (lactic-co-glycolic acid) controlled release systems: experimental and modeling insights. Crit. Rev. Ther. Drug Carrier Syst. **30** 257-276.

[17] Ferrage F, Zoonens M, Warschawski DE, Popot JL, Bodenhausen G 2003 Slow diffusion of macromolecular assemblies by a new pulsed field gradient NMR method. J. Am. Chem. Soc. **125** 2541-2545.

[18] Burkersroda F, Schedl L, Gopferich A 2002 Why degradable polymers undergo surface erosion or bulk erosion. Biomaterials **23** 4221–4231.

[19] Izadifar M, Kelly ME, Haddadi A, Chen XB 2015 Optimization of Nanoparticles for Cardiovascular Tissue Engineering. Nanotechnology **26** 235301.

[20] Rothstein SN, Federspielabce WJ, Little SR 2008 A simple model framework for the prediction of controlled release from bulk eroding polymer matrices. J. Mater. Chem. **18** 1873–1880.

[21] Izadifar M, Zolghadri Jahromi M 2007 Application of genetic algorithm for optimization of vegetable oil hydrogenation process. J. Food Eng. **78** 1–8.

[22] Wu XS, Wang N 2001 Synthesis, characterization, biodegradation, and drug delivery application of biodegradable lactic/ glycolic acid polymers Part II: Biodegradation. J. Biomater. Sci. Polymer Edn. **12** 21–34.

[23] Batycky RP, Hanes J, Langer R, Edwards DA 1997 A theoretical model of erosion and macromolecular drug release from biodegrading microspheres. J Pharm Sci. **86** 1464-77.

[24] Wang XT, Venkatraman SS, Boey FYC, Loo JSC, Tan LP 2006 Controlled release of sirolimus from a multilayered PLGA stent matrix. Biomaterials **27** 5588–5595.

[25] Xi T, Gao R, Xu B, Chen L, Luo T, Liu J, Wei Y, Zhong S 2010 In vitro and in vivo changes to PLGA/sirolimus coating on drug eluting stents. Biomaterials **31** 5151–5158.

[26] Xu Q, Chin SE, Wang CH, Pack DW 2013 Mechanism of drug release from double-walled PDLLA(PLGA) microspheres. Biomaterials **34** 3902-3911.

[27] Blanco MD, Sastre RL, Teijon C, Olmo R, Teijon JM 2006 Degradation behaviour of microspheres prepared by spray-drying poly(d,l-lactide) and poly(d,l-lactide-*co*-glycolide) polymers. Int. J. Pharm. **326** 139–147.

[28] Engineer C, Parikh J, Raval A 2010 Hydrolytic Degradation Behavior of 50/50 Poly Lactide-co-Glycolide from Drug Eluting Stents. Trends Biomater. Artif. Organs **24** 131-138.

CHAPTER 6

LOW-DOSE PROPAGATION-BASED PHASE CONTRAST COMPUTED TOMOGRAPGY FOR NON-INVASIVE QUANTITATIVE ASSESSMENT OF IMPLANTED DUAL-COMPONENT CARDIAC PATCH

"This chapter has been submitted as "M. Izadifar, P. Babyn, M. Kelly, and X. B. Chen, 2016, Low Dose Synchrotron-based Phase Contrast Computed Tomography for Quantitative Assessment of Implanted Tissue Engineered Cardiac Patch, *Journal of Cardiovascular Computed Tomography*, (Under Review)" According to the Copyright Agreement, "the authors retain the right to include the journal article, in full or in part, in a thesis or dissertation".

6.1 Abstract

Due to low density and weak X-ray attenuation coefficient of engineered patches for cardiac tissue engineering, conventional radiography and micro-computed tomography are unable to visualize these patches upon their implantation. In this paper, we present the development of a non-invasive imaging technique based on the synchrotron X-ray propagation-based phase contrast imaging computed tomography (PCI-CT), for the visualization and quantitative assessment of the cardiac patch implanted in a rat heart model. The cardiac patches were fabricated from alginate strands created by three-dimensional (3D) printing, with the pores filled out by fibrin; these so-called "dual-component" patches were then surgically implanted on rat hearts induced with myocardial infarction. A week after surgery, the hearts including patches were excised and embedded in a soft tissue-mimicking gel for imaging by using PCI-CT at a X-ray energy of 25 keV. During imaging, the sample-to-detector distances, CT-scan time, and regions of interest (ROI) were varied and examined for their effects on both imaging quality and

radiation dose received by the samples. Our results illustrated that the sample-to-detector distance was critical to the imaging quality and one value was thus identified for subsequent imaging of the implanted patch. Our results also illustrated that in the phase-retrieved PCI-CT images, the dual component of alginate strands and fibrin-filled pores could be clearly distinguished from each other, thus providing a means to characterize the microstructural features of implanted patches. Furthermore, our phase-retrieved PCI-CT images provided visible structural details for quantitative assessment of the patch, which, however, were not seen from the images by means of phase non-retrieved PCI-CT and a 3T clinical magnetic resonance imaging. By reducing the total CT-scan time per slice and ROI, PCI-CT was examined for lowering the effective dose (<100 mSv), meanwhile without much loss of imaging quality for quantitative assessment of the implanted patch. The microstructural features of patch evaluated from the lowered-dose PCI-CT were in agreement with the ones identified from the stereomicroscope images. Taken together, we illustrate the PCI-CT is of great potential for non-invasive and quantitative assessment of microstructural features of the dual-component patch at the low dose allowed in clinical use.

6.2. Introduction

Myocardial infarction (MI) is the major cause of heart failure associated with cardiovascular disease. Due to the limited regeneration capacity of cardiomyocytes, the injured myocardium is unable to regenerate on its own. Cardiac tissue engineering aims to develop implantable engineered constructs such as cardiac patches to re-establish functional myocardium and associated vasculature following myocardial infarction. A cardiac patch is a soft biomaterial platform that provides physical and biochemical cues to allow for cell attachment, migration, differentiation and organization in order to support new tissue formation on the MI territory.

Hydrogels have been extensively used in the development of functional cardiac constructs in cardiovascular tissue engineering because of their ability to support cell adhesion, retention and growth [1-6], and provide tunable mechanical properties to support cardiomyocytes for secretion of extracellular matrix as they degrade [8, 9]. Moreover, hydrogels can be micro-patterned by using three-dimensional (3D) bioprinting techniques to stimulate vascularization and/or direct the alignment of the cardiomyocytes for a functional cardiac construct [3].

The visualization of hydrogel-based cardiac constructs, once implanted in animal models, is essential for longitudinal studies of cardiac tissue regeneration. However, examination using conventional histological and imaging methods is destructive and demands invasive procedures, for which the animal must be euthanized. The development of non-invasive, quantitative and longitudinal imaging methods for visualization and assessment of 3D microstructures of the implanted cardiac constructs is a strategic priority in cardiac tissue engineering. Magnetic resonance imaging (MRI) is a well-known non-invasive imaging technique for soft tissue imaging but is limited by poor spatial resolution. Ultrasound is limited by access and penetration depth especially if a high spatial resolution is required. Microcomputed tomography (μCT) is an X-ray absorption-based imaging technique that possesses high spatial resolution with deep tissue penetration for non-invasive and quantitative imaging but it only relies on X-ray absorption contrast. Since hydrogels are low density biomaterials with weak X-ray attenuation coefficients, conventional μCT provides little or no information on microstructural properties of the hydrogel-based tissue constructs.

Unlike X-ray absorption-based imaging methods, phase contrast imaging (PCI) techniques have shown promise for soft tissue imaging without contrast agents [7]. Propagation-based PCI, also known as in-line PCI, is an X-ray phase-sensitive imaging technique based on X-ray refraction

rather than absorption index of soft tissues. As the X-ray travels through an object, the X-ray wave field is distorted at the interface between soft tissues. The transmitted wave filed propagates in free space after the object before its intensity is captured by the detector. The phase contrast is accentuated by propagation and results in edge enhancement corresponding to the projected soft tissue interfaces on the image. The advantages of X-ray PCI over absorption-based imaging stem from the fact that soft tissue refractive index variations are typically greater than the X-ray absorption coefficient variations by orders of magnitude [10]. With ever improving high resolution X-ray detectors, highly brilliant and coherent synchrotron X-ray PCI offers great promise for visualization and non-invasive assessment of hydrogel-based tissue engineered constructs and soft tissues that possess very similar X-ray absorption coefficients.

Several groups have applied X-ray in-line PCI for visualization of tissue engineered constructs such as polyethylene glycol in water [11], poly(glycolic acid)- polyethylene glycol *in-vitro* [12], poly(α-hydroxy-ester) in water [13], implanted polyglycolic acid scaffold for spinal cord injury [14], poly(L-lactide) (PLLA) and chitosan scaffold in the air and water [15] and polycaprolactone-alginate *in-vitro* [16]. Although the potential of PCI for visualization of soft tissue has shown promise by these previous studies, little has been published in the hydrogel-based cardiac tissue engineering. In addition, most of the studies have investigated planar PCI for visualization of soft biomaterials. The imaging performance of planar PCI dramatically declines with increasing thickness and complexity of the sample. Combined with computed tomography, PCI-CT may overcome the limitations for visualization of microstructural features of implanted hydrogel-based cardiac constructs and anatomical characteristics of the myocardium. However, PCI-CT requires much longer total scan times for numerous planar images, which subsequently increases the delivered dose. Therefore, the PCI-CT imaging parameters need to be rigorously

adjusted and optimized to provide reasonably high quality images at low absorbed dose, thus allowing for potential application of this imaging technique to live animal studies and possibly human trials in cardiac tissue engineering. To the best knowledge of us, there is no prior report on low-dose propagation-based PCI-CT for visualization of implanted soft cardiac constructs. As inspired, this study aimed to develop non-invasive, quantitative, three dimensional (3D) and longitudinal imaging technique based on in-line PCI-CT to visualize the dual-component fibrin/alginate cardiac patch implanted in a rat model at the low dose allowed in clinical use. The reason of using fibrin, along with alginate, in the patch stems from the fact that fibrin gel has the ability to enhance angiogenesis; particularly when it is incorporated with angiogenic factor-loaded nanoparticles [17]. Our previous study has shown that nanoparticle-incorporated fibrin hydrogels significantly improves sprouting angiogenesis for cardiac tissue engineering [17]; however, the non-invasive quantitative visualization of the fibrin hydrogel as well as alginate in the patch remains a challenge which is addressed in this study.

6.3. Materials and methods

6.3.1. Fabrication of dual-component cardiac patch

Using a 3D-bioplotter fabrication system (Envisiontec GmbH, Gladbeck, Germany) (Fig. 6.1a), sodium alginate (Sigma-Aldrich Co., Saint Louis, MO, USA) (2.5% w/v) solution in sterile de-ionized water was printed layer-by-layer into polyethyleneimine- (PEI) coated culture plate wells (Fig. 6.1b) filled with 50 mM calcium chloride as the cross-linking solution and 0.1% w/v PEI (Sigma-Aldrich). By this way, 3D constructs were fabricated with an overall size of 8 mm × 8 mm × 2.5 mm (W×L×H) with 0/90° perpendicular pattern of strands (Figs. 6.1c-e). The 3D plotting was performed at a dispensing head speed of 8 mm/s under a pneumatic pressure of 0.1 bar through a plastic cone tip dispensing needle (Fig. 6.1b) of 250 μm (EFD Nordson, Westlake,

OH, USA). The clearance between centers of two succeeding strands of each layer was set at 700 μm. The printed micro-construct in the cross-linking solution was incubated for 30 min before being transferred to a sterile saline solution. Sterile fibrinogen (8 mg/ml) and thrombin (2 U/ml) (Baxter Healthcare Co., Westlake Village, CA) were mixed by pipetting in a vial and quickly infused into the pores of the 3D construct before the fibrin gel set (Fig. 6.1f), forming the so-called “dual-component" patches for the subsequent studies.

6.3.2. Surgical procedure and implantation of cardiac patch

Male Lewis rats (~200 g) were anesthetised with a mixture of oxygen and isoflurane (2.5%), intubated, and mechanically ventilated at 70 breath per minute and 2 ml tidal volume using a Physiosuit ventilator (Kent Scientific Corporation, Torrington, CT). Following an anterior thoracotomy through the fourth intercostal space, the heart was exposed, pericardium was carefully removed and the proximal left anterior descending (LAD) coronary artery at ~4 mm below the junction of the left atrium and pulmonary artery was ligated with a 7-0 silk suture under a surgical microscope. The alginate-fibrin patch was then implanted on the myocardium proximally below the LAD ligature using surgical fibrin glue which was prepared at a final fibrinogen concentration of 1 mg/ml (Fig. 6.1g-i).

The intercostal space and then the skin were closed using a 4-0 silk and 4-0 prolene sutures, respectively. After recovery, the rat was housed under standard conditions in the laboratory of animal study unit vivarium for 7 days before being euthanatized prior to synchrotron PCI-CT imaging. Shortly before performing the imaging, the animal was euthanized in a carbon dioxide euthanasia chamber.The experiments were conducted in compliance with the guidelines and ethics set by Canadian Council on Animal Care and the animal use protocol approved by the Animal Research Ethics board if the University of Saskatchewan.

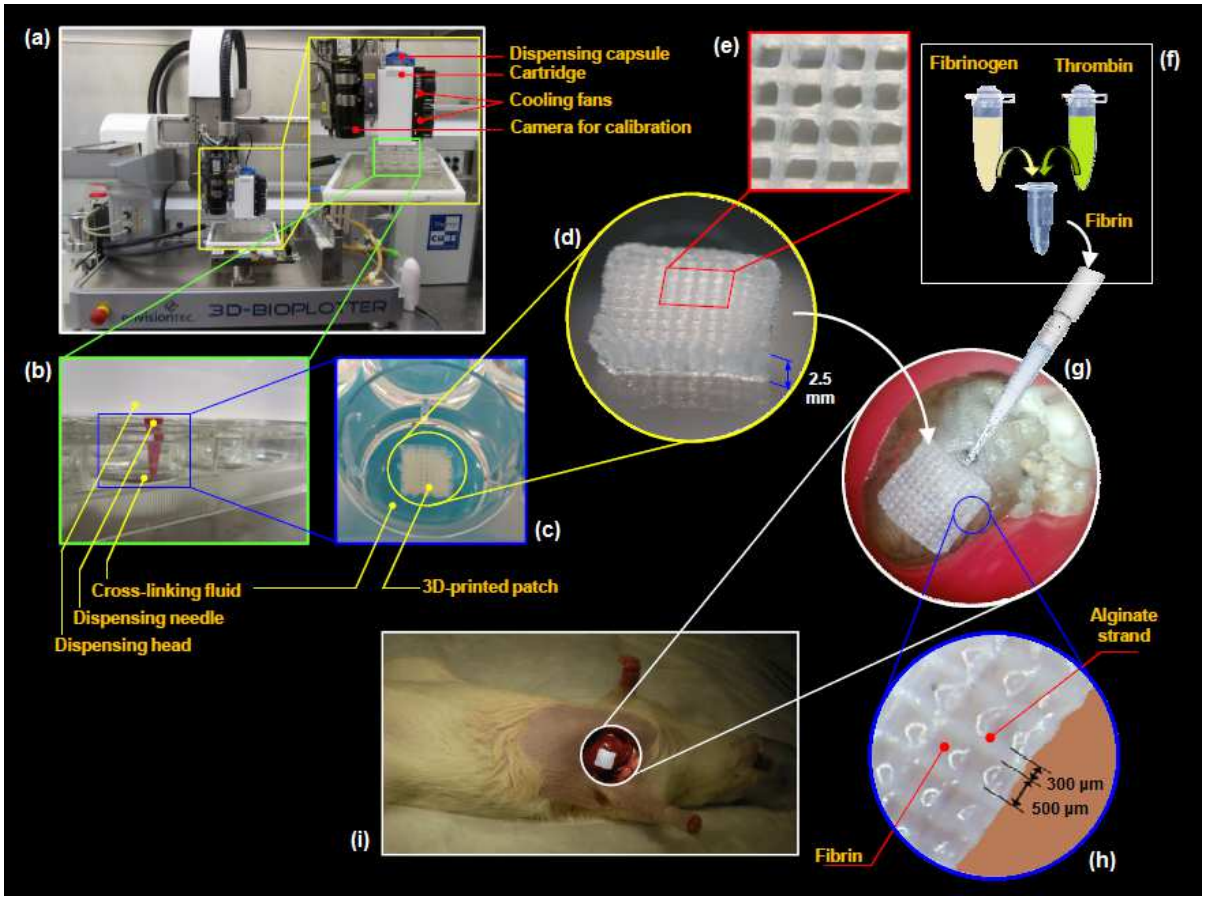

Figure 6.1. Fabrication of an implantable dual-material cardiac patch composed of 3D-printed porous alginate filled with fibrin. Using a 3D-bioplotter (a) alginate (2.5%) strands are plotted layer by layer into the crosslinking solution (b) where the hydrogel construct is set (c) and results in a porous 3D structure (d) with strand size and orientation of ~300 µm and 0/90° pattern (e). The fibrin matrix (f) is infused into the 3D patch pores (g) before the fibrin gel sets resulting in the dual-component patch (h) that is implanted on the rat heart (i) prior to PCI-CT.

6.3.3. Synchrotron X-ray PCI-CT of the implanted cardiac patch

6.3.3.1. Sample preparation for imaging

After cutting the ribs, the thorax cavity was exposed followed by the clipping the vena cava, pulmonary vein and artery and aorta in order to avoid trapping air bubbles in the heart chambers during the excision of the heart. Agar gel that exhibits absorption and scattering characteristics similar to soft tissues was used as the soft tissue mimicking medium [18] fully embedding the heart in a plastics sample holder tube. The heart was carefully excised and immediately laid on the surface of the agar gel inside the sample holder in such a way the cardiac patch was facing upward. Clips were removed and the tube was carefully filled with low melting point agar (Sigma-Aldrich) solution (1% w/v) at 39-40°C, ensuring no trapped bubbles around the patch and the surrounding tissue. The agar was allowed to set for 15 min on ice and then the tube was positioned on the CT imaging stage for PCI-CT imaging.

6.3.3.2. Propagation-based PCI-CT set-up and parameters

PCI-CT was performed under ambient conditions at Biomedical Imaging and Therapy bending magnet (BMIT-BM) beam-line, Canadian Light Source (CLS), Canada. Figure 6.2 illustrates the schematic diagram of the PCI-CT set-up at BMIT-BM. Upstream of the imaging stage, the white beam, was shaped using fully absorbing slits to provide sufficient horizontal beam width. Filtered through an aluminum filter, a highly collimated monochromatic X-ray beam at 25 keV was picked using a Si (2, 2, 0) double crystal Monochromator (Fig. 6.2). Passing through the ion chamber, the X-ray beam illuminates the sample at a beam width and height of 25.56 mm and 4.04 mm, respectively. The X-ray was collected at a Hamamatsu ORCA detector, with an effective pixel size of 12.48 μm, after travelling over a propagation distance, which was optimised by displacing the sample towards or away from the detector (Fig. 6.2). For examining

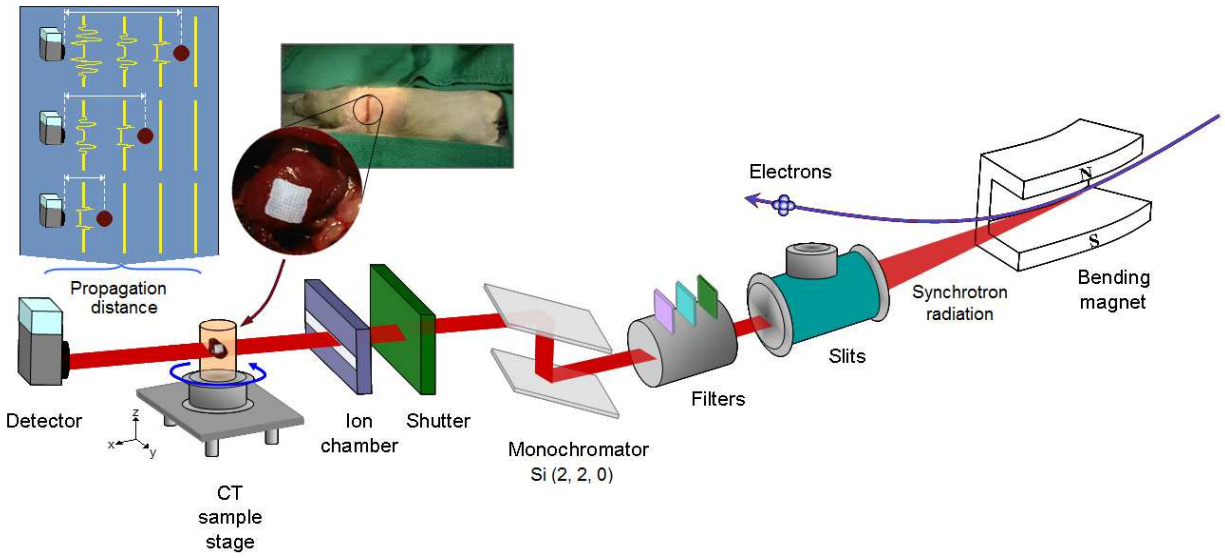

Figure 6.2. Schematic diagram of the synchrotron PCI-CT imaging set-up with adjusted phase propagation distance at BMIT bending magnet beam-line. The deflection of the electron trajectory at the bending magnet provides synchrotron light so called 'white beam' that is shaped by fully absorbing slits and filtered. The double crystal monochromator provides monochromatic X-ray beam (25 keV) that passes through the shutter and ion chamber to used for imaging. The collimitated monochromatic X-ray beam travels through the sample holder containing the heart and implanted patch embedded in the tissue mimicking gel. The small phase shifts attributed to the structural features are developed in free propagation distance after the sample and the accentuated phase contrast is recorded by the detector at three sample-to-detector distances. PCI-CT Tomography projections are collected by rotating the sample in the beam.

the effect of the propagation distance on the imaging quality, in this study PCI-CT was performed at three distinct phase propagation distances of 22 cm, 76 cm and 147 cm. Since the FOV was restricted by the beam height, a full scan of the heart needed multiple vertical scanning.

Unlike conventional CT in a clinic, where the patient is still and X-ray source and detectors are rotated, for synchrotron X-ray in-line PCI-CT, the source of X-ray beam is still while the sample stage is rotated. The rotational increments of the sample stage were set as 0.06, 0.12, 0.18 and 0.24 degrees, which resulted in four levels of CT-acquisition time per slice of the sample over 180 degrees in a step-shoot fashion. The collected planar X-ray projections at different distances of phase propagation, CT-acquisition times and the area of the region of interest (ROI), which can be adjusted by the fully absorbing slits, were normalized over flat and dark images. The background corrected images were then used for phase-retrieval and CT image reconstruction.

6.3.4. Retrieving phase information of PCI-CT images

While X-ray phase-sensitive imaging CT relies on phase shift rather than attenuation information, the collected imaging signals on the detector (Fig. 6.2) are combinations of X-ray absorption and phase information. Phase-retrieval was performed to extract phase information allowing for edge-enhanced visualization of the boundaries of the object features. In this study, phase-attenuation duality Born Algorithm (PAD-BA) that utilizes single propagation distance for objects with weak X-ray absorption and phase-attenuation duality was used for phase retrieval [16, 18-21]. PAD-BA was implemented by using phase-sensitive X-ray image processing and tomography reconstruction (PITRE) software to retrieve phase information as reported in [22]:

$$\begin{cases} \chi = \pi\lambda Z\left(\xi^2 + \eta^2\right) \\ \phi_\theta(x,y) = F^{-1}\left\{ \dfrac{F\left[I_{z,\theta} - 1\right]/2}{(\cos\chi + \sin\chi)/(\alpha/\beta)} \right\} \end{cases} \tag{6.1}$$

where F denote the Fourier transform, λ is the wavelength, Z is the sample-to-detector propagation distance, ξ and η are the spatial frequencies in the Fourier space corresponding to the coordinates of x and y in the real space, α and β are the X-ray refractive and absorption

indices, θ is the tomography rotation angle, I is the photon intensity and $\phi_\theta(x,y)$ is the phase corresponding to the image coordinates of *x* and *y* at the tomography angel of θ.

Given that PAD-BA in PITRE assumes a constant value for α/β, a sensitivity analysis was performed to approximate α/β of the sample. Considering that myocardium is a soft tissue and the implanted cardiac patch is largely composed of water, an initial α/β value of 2180 corresponding to the absorption and refractive indices of water (α=0.14×10^{-6}, β=0.0658×10^{-9}) was used for assessing the width of the fringes at the boundaries with respect to α/β ranging from 1500 to 4000. The best α/β value was determined based on a sensitivity analysis of the frindge size at the myocardium and patch boundaries and then applied to the phase-retrieval algorithm and CT-image reconstruction in PITRE. Applying filtered back projection algorithm, the dual phase-absorption images (non-phase retrieved images) and phase-retrieved images were reconstructed. The signal intensities of the phase-retrieved and dual phase-absorption (non-phase retrieved) CT reconstructed images were corresponding to apparent refractive index ($\bar{\alpha}$) and apparent attenuation coefficient ($\bar{\mu}$), respectively. PAD modified Bronnikov Algorithm (PAD-MBA) was also applied for phase-retrieval of single planar PCI of the myocardium and the implanted patch compared to PAD-BA.

6.3.5. Magnetic resonance imaging (MRI) of the heart and cardiac patch

Following synchrotron PCI-CT experiments, the sample of heart with cardiac patch embedded in agar was imaged by a clinical MRI at Royal University Hospital, Saskatoon, Canada. MRI was performed on a 3T Siemens MAGNETOM Skyra scanner (Erlangen, Germany) equipped with a XQ gradient system capable of 45 mT/m maximum strength. The heart sample-containing tube was stabilized in a MRI-compatible wrist holder for planar scanning along the patch longitudinal axis. T2 measurements were performed at 25°C with a T1 weighted SWI sequence (TE_1=7.01

ms, TE_2=20 ms) at TR of 28 ms, number of echo images of 2, FOV of 50 mm × 50 mm, slice thickness of 0.4 mm, and resolution of 128×128×44 μm^3. Relaxation data were analyzed with the VE11A software.

6.3.6. X-ray radiation dose assessment

The synchrotron radiation dose rate is typically measured using a calibrated ion chamber at BMIT-BM [23]. To determine the dose rate variations over the CT scan during which the storage ring current changes, a multiple regression equation that relates dose rate to the storage ring current (150-250 mA) and photon energy (20-35 keV) was developed:

$$\vartheta^{\bullet} = 198.103 - 10.87E + 0.163\Theta + 0.13E^2 \tag{6.2}$$

where E is X-ray energy (keV), Θ is the storage ring current (mA) and $\vartheta^{\bullet}$ is the dose rate (mGy/s). For X-ray energy of 25 keV at which the dose rate only depends on the storage ring current, Eq. (6.2) results in a mean prediction error of 4% and coefficient of determination of 0.995, where the variation of dose rate with time during PCI-CT scan can be described as:

$$\frac{\partial \vartheta^{\bullet}}{\partial t} = \frac{\partial \vartheta^{\bullet}}{\partial \Theta} \cdot \frac{\partial \Theta}{\partial t} \tag{6.3}$$

Evaluating Eq. (6.3) based on the first derivative of Eq. (6.2), recorded data of storage ring current during the PCI-CT scan and taking the integral of Eq. (6.3) results in:

$$\vartheta^{\bullet} = \vartheta_0^{\bullet} - 0.5008\tau \tag{6.4}$$

where $\vartheta_0^{\bullet}$ is the initial value of the dose rate corresponding to the ring current at the beginning of the PCI-CT scan, and τ is the total exposure time, which is defined by:

$$\tau = (\tau_c + \tau_r)N \tag{6.5}$$

where τ_c is the time for signal capturing of the detector per tomography projection, τ_r is time for the angular rotation step of the CT imaging stage, and N is the total number of tomography

projections. Applying the normalized dose rate (dose rate divided by the area of the beam), the total X-ray radiation dose of the PCI-CT was evaluated as:

$$D = N(\tau_c + \tau_r) S_{ROI}\, \overline{\vartheta}^{\bullet} \tag{6.6}$$

where S_{ROI} is the area of ROI (mm^2), $\overline{\vartheta}^{\bullet}$ is the normalized dose rate (mGy/mm^2 s), and D is the total absorbed dose (mGy). To provide clinically interpretable evaluation of the radiation dose, the absorbed dose was weighted with respect to radiobiological risks of the exposed tissue to evaluate the effective dose equivalent in Sievert (Sv) as:

$$Sv = DW_r W_t \tag{6.7}$$

where W_r and W_t are radiation weighting factor, that is equal to 1 for X-ray photons [24] and the tissue radiosensitivity weighting factor, respectively. A cardiac tissue radiosensitivity weighting factor of 0.12 [25] was used in this study.

6.3.7. Low-dose PCI-CT for quantitative assessment of the implanted cardiac patch

CT- acquisition time per slice, the area of ROI, X-ray energy and dose rate are the main factors affecting the total delivered dose. At the dose rate assigned by the picked X-ray energy (25 keV) and the storage ring current, the total delivered dose was investigated at three levels of the area of region of interest (ROI) (~100, 6, 3 mm^2) and four levels of CT-scan time corresponding to tomography projections of 3000, 1500, 1000 and 750. The beam dimension, which can be adjusted using fully X-ray absorbing slits, was adjusted to provide reduced ROI for visualization and quantitative assessment of the implanted patch. Also, the orientation of the heart with respect to the beam incident was adjusted horizontally to reduce the cardiac tissue exposure to the beam. The combination of decreased CT scan time and reduced ROI was analysed with the associated image quality criteria to identify optimum imaging parameters for an effective low-dose PCI-CT.

6.3.8. Qualitative and quantitative criteria for assessing image quality

The image quality criteria of image correlation coefficient (r), peak of signal to noise ratio (PSNR), contrast to noise ratio (CNR) and structural similarity (SSIM) index [26] were used to compare CT images of the heart and implanted patch associated with different levels of delivered dose. The image quality criteria per unit delivered dose per pixel were defined as:

$$\overline{SSIM} = \frac{(P_{xy})^2(2\mu_{ROI}\mu_b + C_1)(2\sigma_{ROIb} + C_2)}{DS_{ROI}(\mu_b^2 + \mu_{ROI}^2 + C_1)(\sigma_b^2 + \sigma_{ROI}^2 + C_2)} \tag{6.8}$$

$$\overline{CNR} = \frac{(P_{xy})^2\sigma_{ROI}}{DS_{ROI}\sigma_b} \tag{6.9}$$

where $\overline{SSIM}$ and $\overline{CNR}$ are the normalized SSIM index and CNR per unit absorbed dose per image pixel, μ_{ROI} and μ_b are the mean intensity of image signals of ROI and background, respectively, σ_{ROI} and σ_b are intensity standard deviations of image signals of the object ROI and background with equal surface area, respectively, σ_{ROIb} is the inner product of the standard deviations, C_1 and C_2 are stability constants [26], and P_{xy} is the pixel size (mm). The apparent refractive index profiles across the ROI of the implanted cardiac patch were used to identify the boundaries between fibrin-filled pores and alginate strands and quantitatively evaluate the features of the patch compared to the actual values measured from stereomicroscope images.

6.4. Results

6.4.1. Effect of the phase propagation distance of the PCI-CT

A sensitivity analysis of the phase retrieval revealed that the width of phase contrast fringes at the boundaries between myocardium and implanted patch decreased as α/β was increased from 1500 to 3500. Further increase in α/β resulted in no significant improvement in the width of the fringes; thus, α/β of 3500 was applied to PAD-BA for the phase retrieval in the study.

Figure 6.3 depicts the axial and coronal slices associated with phase-attenuation duality (phase non-retrieved) and phase-retrieved images of the implanted patch on the myocardium at three phase propagation distances. The edge illumination is clearly enhanced with propagation distance (Figs. 6.3a-c, g-i). As the phase propagation distance increases from 22 cm to 147 cm, the edge illumination at interface between alginate strands and fibrin-filled spaces (yellow arrows) and between patch and the myocardium (black arrows) significantly improves. At the distance of 147 cm, the phase retrieved images clearly depict the structural and morphological

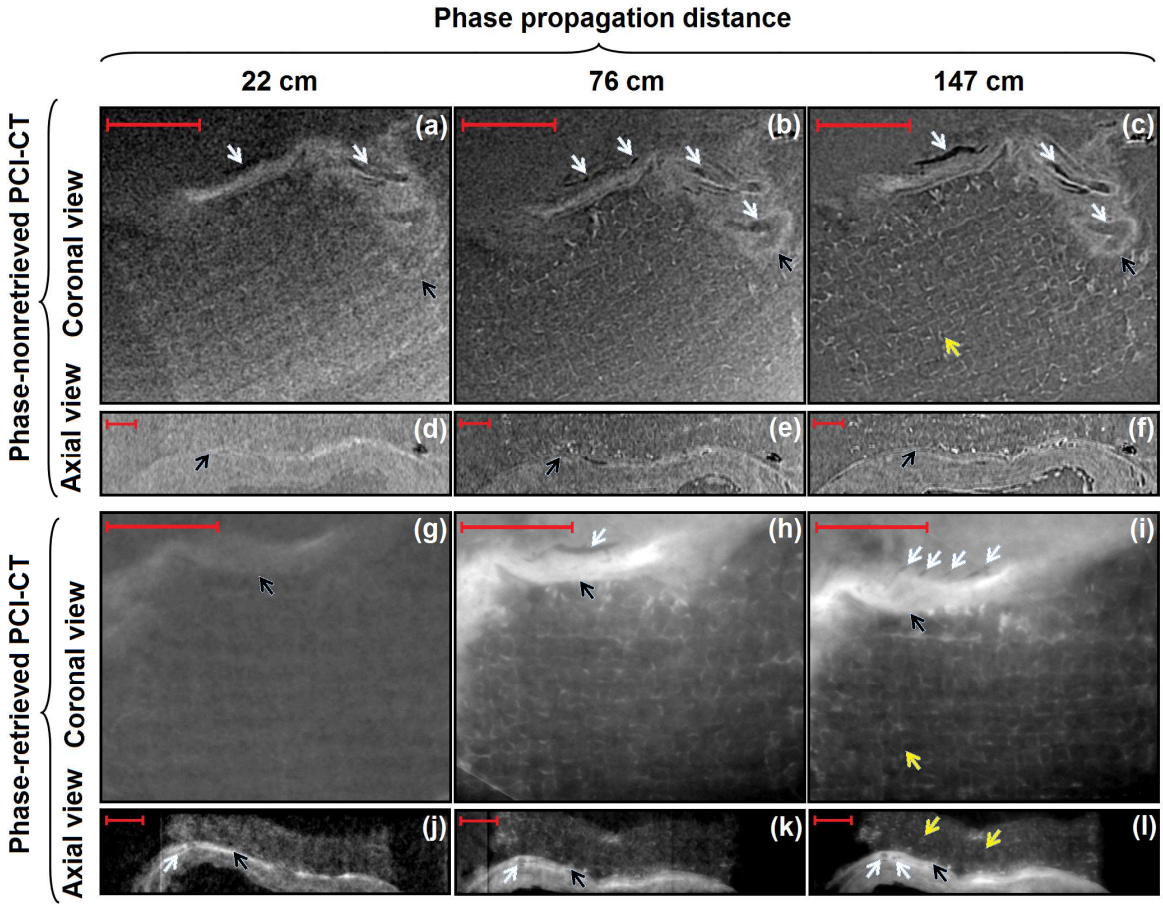

Figure 6.3. Phase-nonretrieved and phase-retrieved PCI-CT images of coronal (a-c, g-i, scale bar=2 mm) and axial (d-f, j-l, scale bar=1 mm) slices of the dual component patch implanted on the rat myocardium at three phase propagation distances of 22 cm, 75 cm and 147 cm.

information of the patch (Fig. 6.3i) including the vertically assembled alginate strands that demonstrate circular cross-sections (yellow arrows) (Fig. 6.3l). Moreover, the microvessels (yellow arrows) can be clearly identified from the coronal views at the propagation distance of147 cm (Figs. 6.3c, i).

Figures 6.4a and 6.4b depict the structural details of the 3D-printed alginate construct and the alginate-fibrin patch, respectively. As the propagation distance increases from 22 cm (Fig. 6.4c) to 76 cm (Fig. 6.4d) and 147 cm (Fig. 6.4e), the edge illumination so improved that the

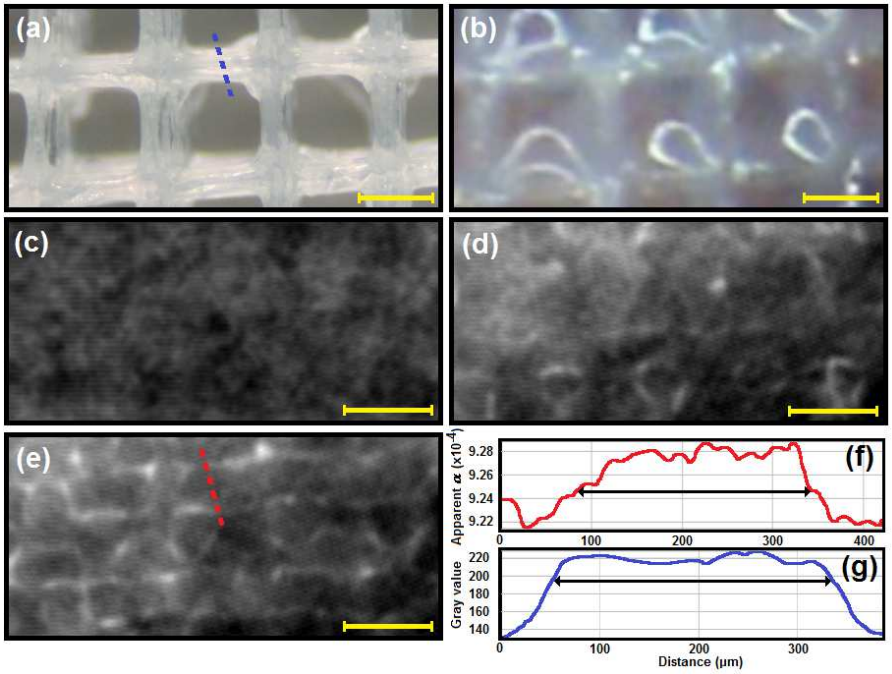

Figure 6.4. Comparison of structural similarity between stereomicroscope images of the 3D-printed alginate strands (a), dual component alginate-fibrin structure (b), and the coronal slice of the phase-retrieved images from PCI-CT at the phase propagation distances of 22 cm (c), 76 (cm) and 147 cm (e) at α/β=3500; a quantitative comparison of the alginate strand thickness evaluated from the PCI-CT at the phase propagation distance of 147 cm (f) and the corresponding measured value from the stereomicroscope image (g) (scale bar=500 μm).

boundaries between alginate and fibrin can be clearly identified and the thickness of the strands can be characterized from the PCI-CT slice (Fig. 6.4e). Figure 6.4f illustrates the apparent refractive index profile across the alginate strand (Fig. 6.4e), indicating an strand thickness of ~300 μm (Fig. 6.4f) which is in agreement with the strand thickness (Fig. 6.4g) evaluated from the intensity profile of the stereomicroscope image (Fig. 6.4a). It is noted that there is an approximately 20% increase in the strand thickness (~300 μm) as compared to the internal diameter of the dispensing needle (250 μm) used for printing the strands of cardiac patch, which is mainly due to the spreading or stretching of strands during their cross-linking process.

6.4.2. Planar PCI to assess the patch implantation

Figures 6.5a-c show the sample holder orientation on the imaging stage with respect to the beam monitoring Scintillator for sagittal and axial planar PCI (single projections) at the phase propagation distance of 147 cm. Figures 6.5d and j depict the sagittal and axial phase-absorption duality planar images where the myocardium (yellow arrows) and part of the aorta (blue arrows) boundaries can be identified (Figs. 6.5d, j). The edges of the left atrium appendage (green arrow) can be distinguished (Fig. 6.5d); however, the profiles of the apparent attenuation coefficient across the region of the patch implantation show no significant contrast for locating the implanted patch (Figs. 6.5e, k). In contrast, the phase retrieved planar images from PAD-MBA (Figs. 6.5f, l) and PAD-BA (Figs. 6.5h, n) can depict boundaries attributed to the edge enhancement of the myocardium (yellow arrows), patch (red arrows), appendage (green arrow) and the aorta (blue arrow). Notably, PAD-BA results in better phase contrast of the implanted patch (Figs. 6.5h, i) compared to PAD-MBA (Figs. 6.5f, g), although both algorithms can retrieve phase contrast of the myocardium (yellow arrows) from the planar PCI (Figs. 6.5l-o).

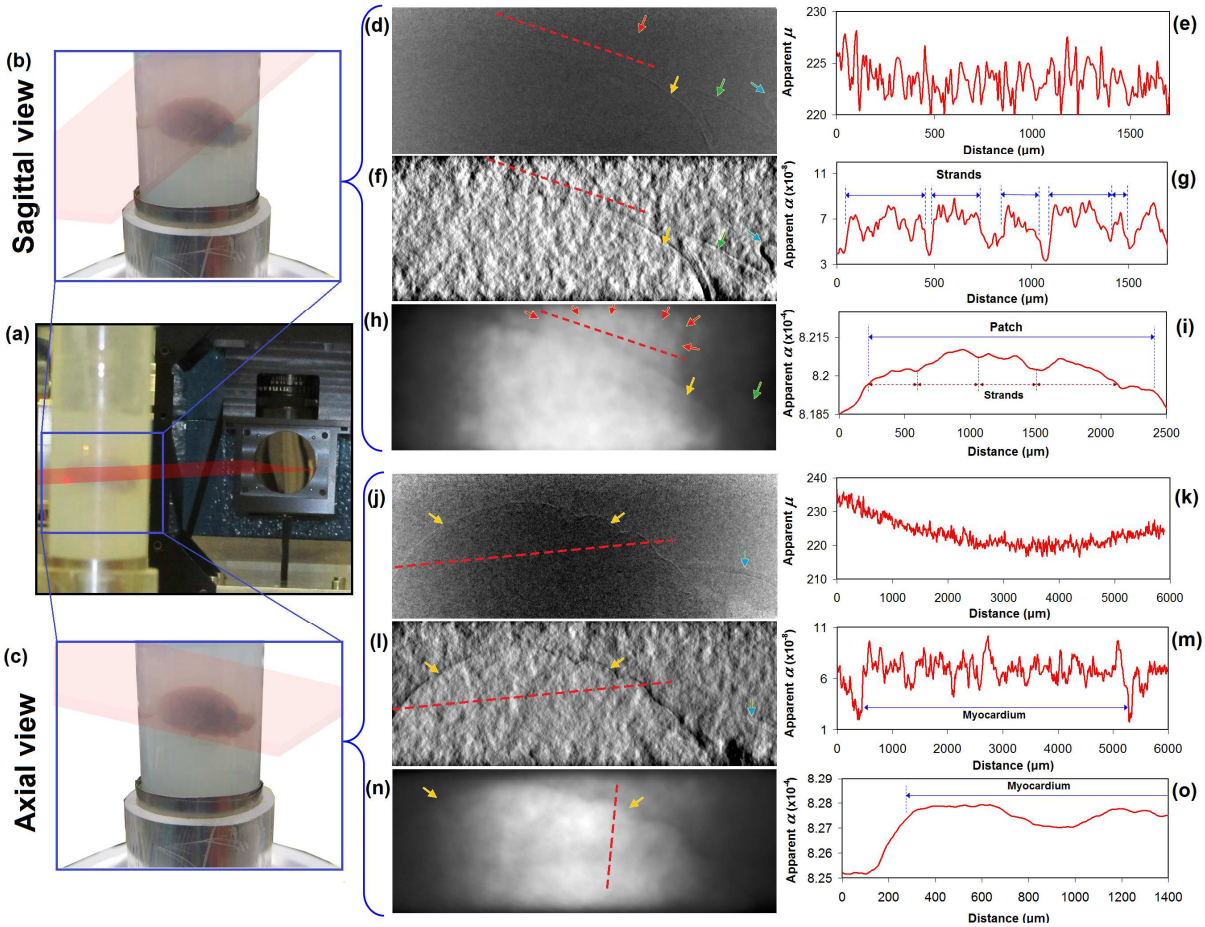

Figure 6.5. The sample-beam monitor orientation in the imaging stage (a) for single projection-based phase contrast imaging of the sagittal (b) and axial (c) views associated with phase non-retrieved (d, j) and phase retrieved images from PAD-MBA (f, l) and PAD-BA (h, n) of the myocardium and the implanted patch, and the intensity profiles of the apparent attenuation coefficient (e, k) and refractive index (g, i, m, o) across the myocardium and the implanted patch.

6.4.3. PCI-CT imaging performance compared to the clinical MRI

The MRI images provide no detailed information of the patch but only indicate the region of patch implantation (Figs. 6.6a, b). As seen in Fig. 6.6c, the MRI horizontal long axis plane is so poor that even chambers are unidentifiable. The magnetic resonance signal intensity profile

across the patch suggests that MRI may only provide sufficient contrast only for locating the implantation landmark but no details of the patch structure (Fig. 6.6d). The axial slice from phase-absorption duality PCI-CT of the patch clearly depicts the patch size and the strand nodes of the patch (Fig. 6.6e). Moreover, the apparent attenuation coefficient profile across the patch and myocardium provides relatively sufficient contrast to identify alginate strands but hardly the exact boundary between the myocardium and the patch (Figs. 6.6f, h). Also, the four chamber long axial plane from phase non-retrieved slices reveals some anatomical details that include left and right ventricles (red arrows), aorta (yellow arrow) and the right atrium (green arrow) (Fig.6.6g). The axial slice of the phase- retrieved images not only provides the size, geometry

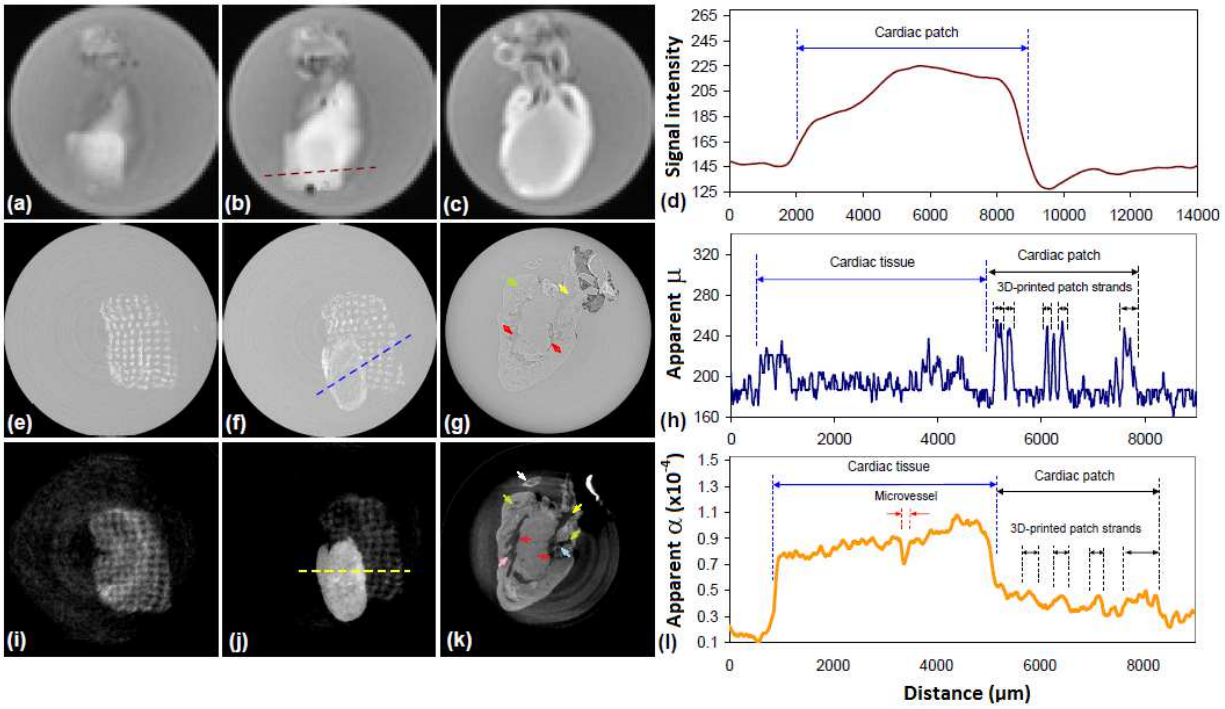

Figure 6.6. Coronal slices and signal intensity profile from MRI images (a-d) compared to the corresponding slices from phase non-retrieved (e-h) and phase retrieved PCI-CT images (i-l) of the heart and the implanted patch.

and the strand nods but clearly visualizes the thickness and orientation of the strands with quantifiable fibrin-filled pores (Fig. 6.6i). Unlike MRI and the phase-absorption duality PCI-CT images, the phase retrieval significantly improves the contrast between myocardium and implanted patch, thus being able to assess the patch attachment to the myocardium post implantation (Fig. 6.6j). Notably, the apparent refractive index profile across the patch and myocardium clearly shows the contrast between the implanted patch and the native myocardium, as well as the information associated with the myocardium microvessel and patch strands (Fig. 6.6l). Furthermore, the axial plane reveals anatomical details of the interior heart such as atriums (green arrows), mitral valve (blue arrow), tendinous cords of the tricuspid valve (pink arrow), left and right ventricles (red arrows), aorta (yellow arrow) and the left atrium appendage (white arrow) (Fig. 6.6k).

The patch microstructure (Fig. 6.7a) and the associated periodic 'hill-valley' pattern of the apparent refractive index profile associated with the fibrin-alginate periodic structure (Fig. 6.7b) can be seen in the axial slice of the phase-retrieved PCI-CT image. The size of the fibrin-filled pores and alginate strands can be approximated from the apparent refractive index profile (Fig. 6.7b), with their values of ~256 and 400 μm, respectively. Notably, these identified values are in agreement with those measured from stereomicroscope images, i.e., ~300 and ~500 μm. Compared to the phase-retrieved image, the axial plane (Fig. 6.7c) and the associated apparent absorption coefficient profile (Fig. 6.7d) from the phase-absorption duality PCI-CT suffers from insufficient contrast, making it very difficult to morphologically and quantitatively assess the patch microstructure.

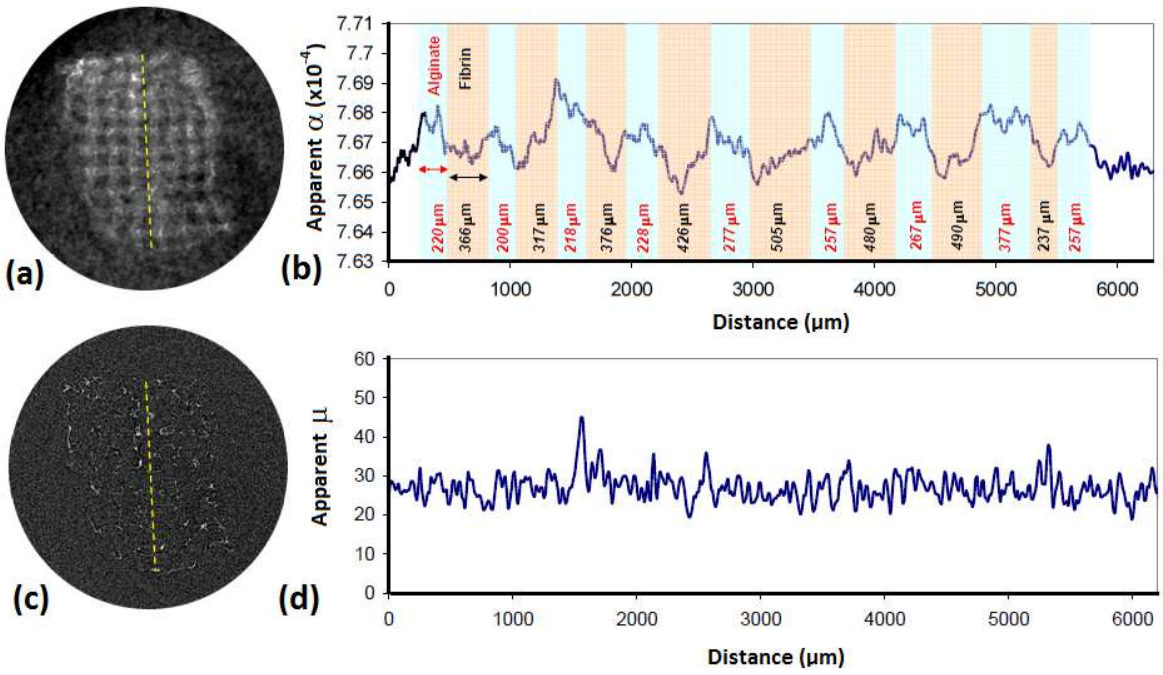

Figure 6.7. Quantitative assessment of the dual component implanted alginate-fibrin patch using phase retrieved (a, b) and phases non-retrieved horizontal long axis slice from the PCI-CT at the phase propagation distance of 147 cm and α/β of 3500.

6.4.4. Low dose PCI-CT imaging

Figures 6.8a-h depict the volume rendered images utilizing 3000, 1500, 1000 and 750 tomography projections, respectively. The patch microstructural features such as patch volume, dimensions, and the strands and pores, and anatomical details including the left atrium appendage (yellow arrow), microvessel branches (red arrows) and the ligature (suture) (blue arrow) can be seen in the images using 3000 projections (Figs. 6.8a, e). The anatomical and structural features remain relatively distinguishable when the number of tomography projections is reduced by 50% (1500 projections) (Figs. 6.8b, f). At 1000 tomography projections, it becomes difficult to identify the microvessels although the patch microstructure can be

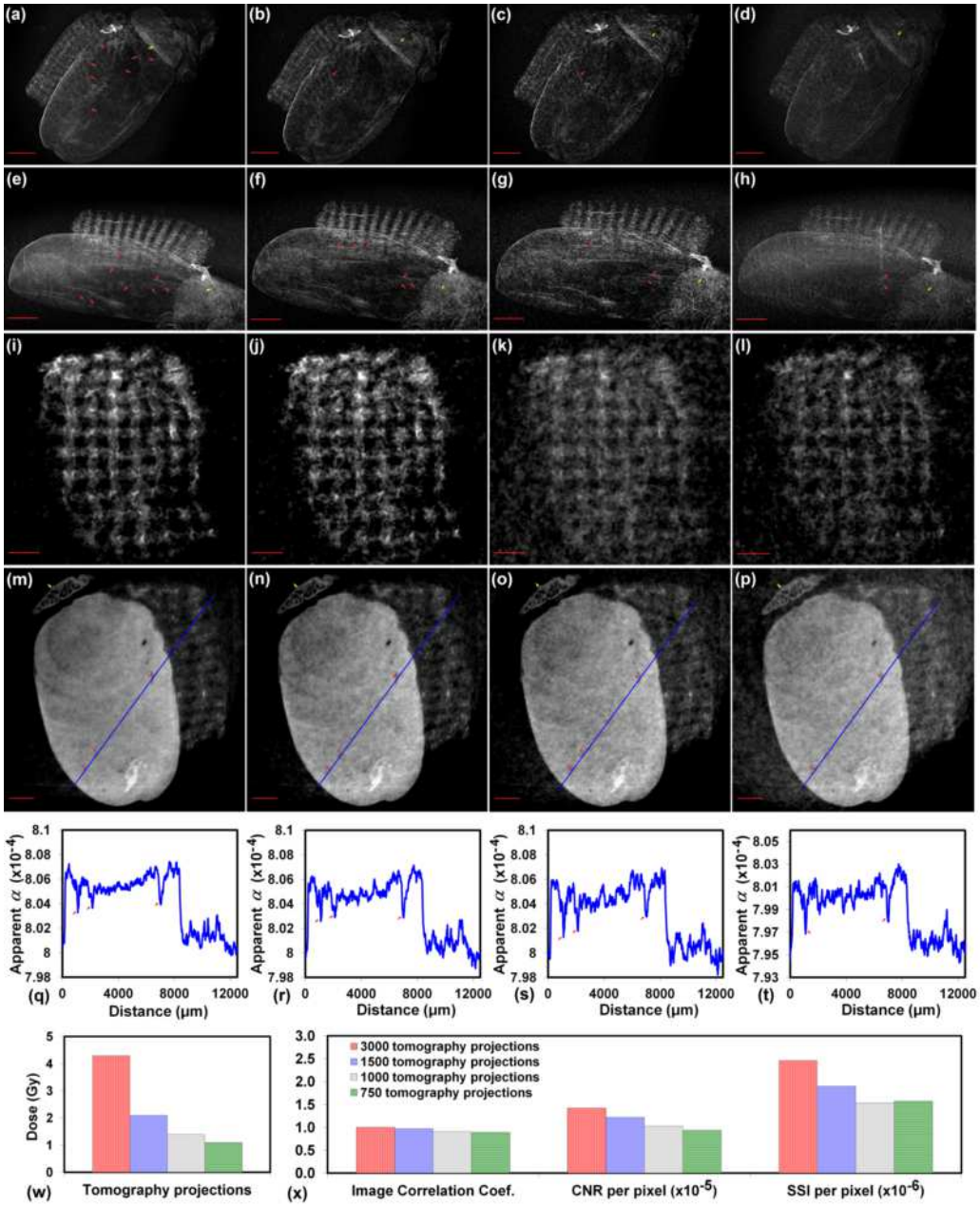

Figure 6.8. Coronal (a-d) and sagittal (e-h) views of the volume rendered PCI-CT images of the heart and implanted cardiac patch, and the horizontal long axial plane of the patch (i-l) attached to the myocardium (m-p) with the associated apparent refractive index profiles (q-t) at tomography projections of 3000 (a, e, i, m, q), 1500 (b, f, j, n, r), 1000 (c, g, k, o, s) and 750 (d, h, l, t) to assess image quality criteria (w) for a low dose PCI-CT (x) (scale bar=1 mm).

visualized (Figs. 6.8c, g). Despite the poor resolution provided by 750 tomography projections, the suture (blue arrow), appendage (yellow arrow) and a few microvessels (red arrows) are identifiable (Fig. 6.8h) and the patch volume, the area of the implantation, the size of strands and pores can be approximated (Fig. 6.8d, h).

A comparison between axial slices of the patch corresponding to full dataset and the reduced tomography projections suggests that the key structural features of the patch remain identifiable at the reduced number of tomography projections despite the decreased resolution (Figs. 6.8i-l). The anatomical features such as the internal structure of the appendage (yellow arrow) and microvessels (red arrows) can be also distinguished from the surrounding tissue at the lower CT scan times corresponding to the reduced number of tomography projections compared to the standard PCI-CT (Figs. 6.8m-p).

The associated apparent refractive index profiles indicate that the phase contrasts of the anatomical features are sufficient to distinguish myocardium anatomical features and the patch at the reduced tomography projections (Figs. 6.8q-t). Although two microvessels (red arrows) out of three can be located from the apparent refractive index profile associated with 750 tomography projections (Fig. 6.8t), 1500 and 1000 tomography projections provide sufficient phase contrast to identify the three microvessels (red arrows) (Figs. 6.8r, s).

Compared to the standard PCI-CT, the total delivered dose significantly declines when the tomography projections are decreased (Fig. 6.8w) but notably, the image correlation coefficient and CNR per pixel are not significantly affected (Fig. 6.8x). Although SSI per image pixel is significantly decreased as a result of the reduced tomography projections, no significant difference in SSI can be noted among the images associated with 1500, 1000 and 750 tomography projections (Fig. 6.8x).

Figures 6.9a, b illustrates the variation of the effective dose (mSv) with tomography projections, photon energy and the area of ROI, as described by Eqs. (6.2), (6.4)-(6.7). The effective dose exponentially decreases with increasing energy for all levels of tomography projections so that low effective dose (<100 mSv) may be achieved at higher energies under the reduced number of tomography projections (e.g. 750-1000) (Fig. 6.9a). Although higher energies could be applied to reduce the dose, the trade-off assessment associated with the higher flux, sufficient penetration depth, and preliminary evaluation of alginate-fibrin phase contrast led to selection of 25 keV picked for this study. At 25 keV, the effective dose can be dramatically reduced from ~2200 mSv for ROI of 20 mm^2 to <100 mSv for ROI of 3 mm^2 corresponding to 3000 and 750 tomography projections, respectively (Fig. 6.9b).

Figures 6.9c-f depict the axial slices of the implanted patch for ROI of 3 mm^2. Notably, the alginate strands of the patch remains identifiable and measurable from the images when the effective dose is reduced from 246 mSv to 123, 82 and 62 mSv corresponding to of 3000, 1500, 1000 and 750 tomography projections, respectively (Figs. 6.9c-f). The refractive index profiles associated with the patch strands reveals the periodic 'hill-valley' patterns attributed to the edge illumination of the alginate strands, which can be used for approximation of the strand thickness (Figs. 6.9g-j).

Table 6.1 presents the image quality criteria evaluated for different levels of PCI-CT doses. Obviously the image correlation coefficient decreases at the lower dose but the correlation coefficient generally remains above 0.8 with no significant change in PSNR except for the image at ROI of 3 mm^2 and 750 tomography projections (Table 6.1). $\overline{CNR}$ and $\overline{SSIM}$ increase despite significant reductions in the effective dose, indicating that the image quality can be largely preserved at the lower doses (Table 6.1). The average strand thickness (d_s) and fibrin-filled pore

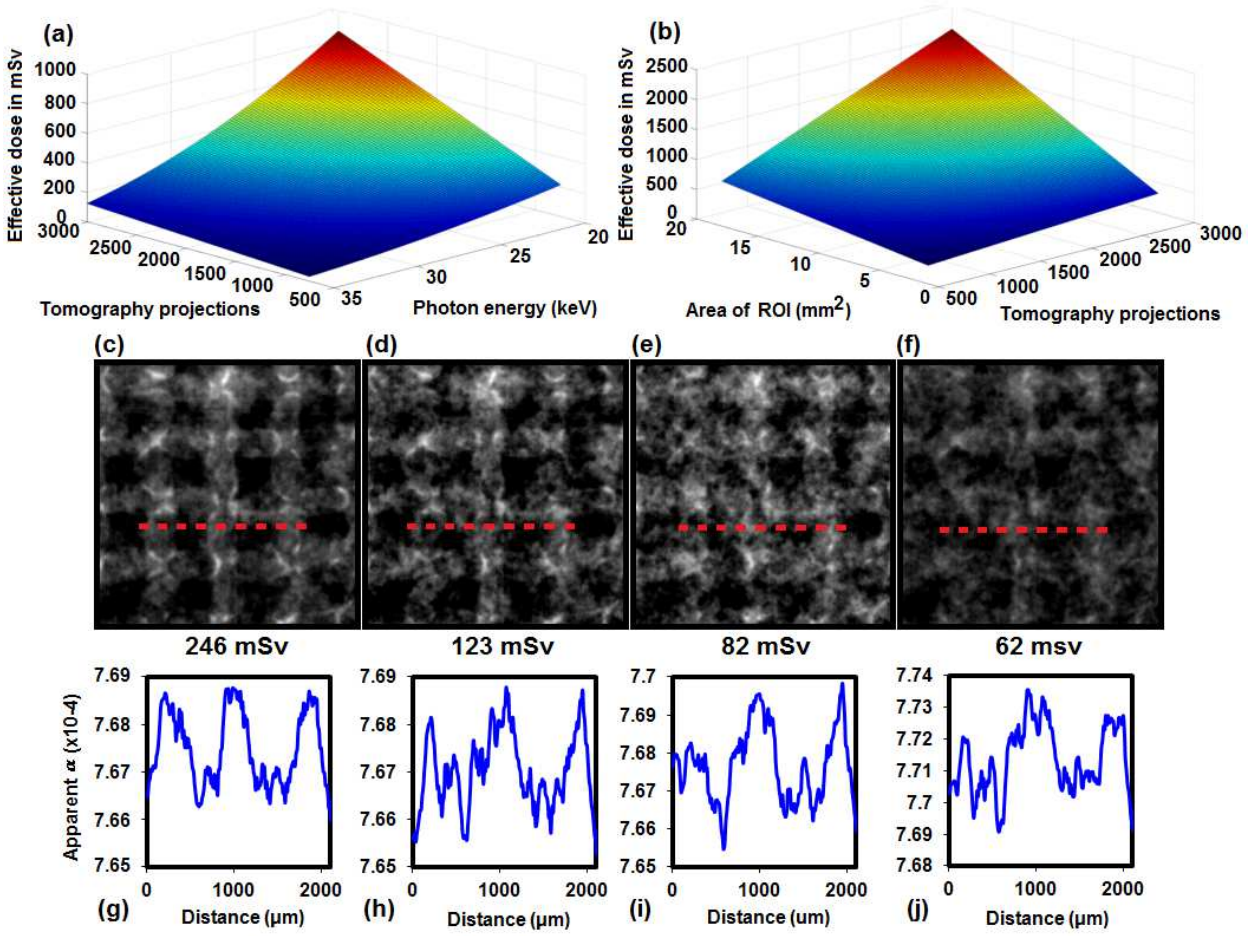

Figure 6.9. Variation of the effective dose with tomography projections and photon energy (a) and area of ROI and tomography projections at 25 keV (b), and the patch structural feature assessment using low dose PCI-CT based on the combined effect of the reduced ROI (3 mm^2) at tomography projections of 3000 (c), 1500 (d), 1000 (e) and 750 (f) to quantitatively evaluate the size of strands and pores from the apparent refractive index profiles across the patch (g-j).

size (d_f), which were evaluated from the phase-retrieved PCI-CT images, are generally consistent with measured values from stereomicroscope imaging (Figs.6.4a, b), suggesting that the low dose PCI-CT may be implemented for quantitative assessment of the implanted cardiac patch.

Table 6.1. Quantitative criteria for image quality assessment and patch structural feature evaluation using low dose PCI-CT at two levels of ROI and four levels of tomography projections.

[a]S_{ROI} (mm^2)	N	[b]D (Gy)	mSv	r	$PSNR$	$\overline{CNR}$ ($\times10^{-6}$)	$\overline{SSIM}$ ($\times10^{-6}$)	[c]d_s (μm)	[d]d_f (μm)
1×6	3000	4.1	492	1	[e]n/a	1.10	0.88	358	459
	1500	2.1	246	0.95	24.5	1.98	1.50	360	401
	1000	1.4	164	0.93	20.5	2.92	1.72	420	348
	750	1.0	123	0.83	20.7	3.71	2.37	442	332
1×3	3000	2.1	246	1	[e]n/a	12.51	1.18	319	433
	1500	1.0	123	0.89	23.0	21.63	2.37	351	436
	1000	0.7	82	0.80	20.4	30.84	3.55	413	358
	750	0.5	62	0.76	12.4	40.30	4.74	415	402

[a]Beam height×width; [b]Total dose at $\overline{\vartheta^{\bullet}}$ of 3.08×10^{-7} mGy/μm^{2}s; [c]Average alginate strand thickness of the implanted patch measured from PCI-CT image; [d]Average size of the fibrin filling spaces between alginate strands of the patch; [e]The reference for evaluation of *PSNR*, *r* and *SSIM*.

6.5. Discussion

It has been shown that cardiomyocyte encapsulation efficiency of alginate is of great [3-6, 27] and that angiogenesis can be improved by means of fibrin [3, 4, 28-17]. Inspired by these findings, it is rationale to develop micro-patterned alginate-fibrin cardiac patches for cardiac tissue engineering. However, the ability to non-invasively and quantitatively visualize the alginate and fibrin is one of the key challenges. For this, the phase propagation distance has been shown critical and been optimised for achieving desirable phase contrast to depict microstructural features of the implanted cardiac patch, as illustrated in this study. It should be

noted that both alginate and fibrin are made of more than 95% water, which provide very low density to the patch microstructure. As such, the patch microstructural features associated with the interface between the alginate strands and fibrin-filled pores produce very small phase shifts as the X-ray travels through the implanted patch, which is also true for the surrounding soft tissues such as microvessels. In the synchrotron-based PCI-CT, the small phase shifts associated with microstructural features are magnified over the free propagation distance, thus being able to produce sufficient phase contrast on the detector. Ideally, the phase propagation distance should allow the phase shift being developed as large as one pixel size. If the phase distortion development is smaller than the pixel size, phase shifts of multiple features are integrated within one pixel, making the projected boundaries fuzzy on the detector (Figs. 6.3g, 6.4c). As the free propagation distance increases, the phase contrast of the edges can be enhanced (Figs. 6.3h,4d). In this study, we illustrated that the best phase propagation distance for edge illumination of alginate-fibrin interface of the patch was 147 cm among the three distance examined for the effective pixel size of 12.48 μm at BMIT-BM. Likewise, microvessel features illuminated at the phase propagation distance of 76 cm and measurable (~25 μm) (Fig. 6.4i) at sample-to-detector distance of 147 cm. Although a longer free propagation distance might improve the phase contrast of the microstructural features, it should be noted that projected boundaries become blurry if the phase shift developments become larger than one pixel size, which can be occurred over a propagation distance longer than the optimum value.

At the optimum phase propagation distance, phase-retrieval of the planar PCI provided sufficient contrast to identify the boundaries of the implanted patch distinguishable from the surrounding soft tissues (Figs. 6.5h, i). This PCI capability, coupled with the extremely low delivered dose (~1.5 mSv), offers a great potential for serial monitoring of the implanted patch, for example, to

visualize degradation and to ensure that the patch is not detached or dislocated after surgery in a live animal study.

The phase retrieved axial slice of the patch depicted no gap at the interface between the myocardium and the implanted patch, a non-invasive qualitative assessment of a successful implantation procedure. Furthermore, phase retrieved PCI-CT slices enabled non-invasive quantitative assessment of the thickness of the alginate strands and the size of fibrin-filled pores which were consistent with the measured values from stereomicroscope.

In addition to the qualitative and quantitative information of the patch, the phase retrieved slices of the heart revealed descriptive anatomical features including the atrium appendage internal structure, mitral valve, tricuspid valve cords, aorta and myocardium microvessels. Notably, these microstructural and anatomical features of the patch and heart were achieved without the usage of any contrast agent, suggesting that the PCI-CT is of great potential for non-invasive assessment of the patch structural changes, myocardium regeneration and vascularization in live animal studies for cardiac tissue engineering.

Application of the PCI-CT technique to live animal studies relies on not only the image quality but also the total radiation dose. For a given storage ring current and the chosen photon energy, the total CT-acquisition time and the area of ROI are the main factors to be optimized in order to reduce the radiation dose. The standard PCI-CT (3000 tomography projections) at a reduced ROI of 1mm×6 mm (Height×Width) delivered an effective dose of 492 mSv, which is within the range of the annual dose limit (500 mSv) suggested by the International Commission on Radiological Protection (ICRP) for skin [30]. However, a recommendation from ICRP indicates that no tissue undergoes clinically relevant functional deterioration at the absorbed X-ray doses up to ~100 mSv [30]. The reduced CT scan time corresponding to 1000 tomography projections

at ROI of 6 mm^2, which covers a large area of the implanted patch, decreased the effective dose to 164 mSv with no significant changes in image quality criteria. Further reductions in ROI (3 mm^2), which can be considered as a representative volume of the implanted patch (Figs. 6.9c-f) reduced the effective dose as low as 123 and 82 mSv corresponding to 1500 and 1000 tomography projections, respectively. Effective dose can be further reduced by use of higher X-ray energies (e.g. 26-30 keV) and/or lower resolution of imaging (e.g. binning 2×2). In the future, a multi-objective optimization of the low dose PCI-CT needs to be investigated to minimize the delivered effective dose but maintain PCI-CT capability to visualize critical features of the patch and the surrounding tissues.

Taken together, the PCI-CT developed in this study offers a great potential for non-invasive qualitative and quantitative assessment of microstructural features of the implanted alginate-fibrin cardiac patch at reduced effective dose consistent with the ICRP recommended dose limits, especially for live animal studies and possible human trials in the future.

6.6. Conclusion

In this study, a low dose synchrotron propagation-based PCI-CT demonstrated promise for qualitative and quantitative assessments of implanted 3D-printed dual-component cardiac patch on the rat heart without usage of contrast agent. The microstructural features of fibrin and alginate, which are low-density (>97% water) constituents of the patch, were clearly visualized and quantitatively characterized from the phase-retrieved PCI-CT slices of the implanted patch. The PCI-CT technique provided anatomical details including the microvessels surrounding the implanted patch. Owing to the notable phase contrast at the optimized phase propagation distance, no contrast agent was needed for quantitative assessments of the patch and myocardium. By decreasing CT scan time and ROI, the effective dose was considerably reduced

without significant changes in the image quality for assessing the anatomical and microstructural features of the implanted alginate-fibrin patch. The evaluated thickness of alginate strands and fibrin-filled pores at the reduced effective dose within the dose limit recommended by ICRP were in agreement with the measured values from stereomicroscope. Findings from this study pave the road for applying the low dose PCI-CT for *in-vivo* studies of patch-based cardiac tissue regeneration therapy.

In future experiments, the PCI-CT at the imaging parameters identified in this study will be applied to the imaging of implanted cardiac patch in a freshly euthanized rat allowing further refinement of the imaging parameters for the development of a robust gated PCI-CT for *in-vivo* live animal studies.

References

[1] Pedron S, van Lierop S, Horstman P, Penterman R, Broer DJ, Peeters E 2011 Stimuli responsive delivery vehicles for cardiac microtissue transplantation. Adv. Funct. Mater. **21** 1624.

[2] Camci-Unal G, Nichol JW, Bae H, Tekin H, Bischoff J, Khademhosseini A 2013 Hydrogel surfaces to promote attachment and spreading of endothelial progenitor cells. J. Tissue Eng. Regen. Med. **7** 337.

[3] Izadifar M, Kelly ME, Chen XB 2014 Engineering Angiogenesis for Myocardial Infarction Repair: Recent Developments, Challenges, and Future Directions. Cardiovasc. Eng. Technol. **5** 281.

[4] Izadifar M, Haddadi A, Chen XB, Kelly M 2014 Rate-Programming of Nano-Particulate Delivery Systems for Smart Bioactive Scaffolds in Tissue Engineering. Nanotechnology **26** 012001.

[5] Fang R, Qiao SP, Liu Y, Meng QY, Chen XB, Song B, Hou XL, Tian, WM 2015 Sustained co-delivery of BIO and IGF-1 by a novel hybrid hydrogel system to stimulate endogenous cardiac repair in myocardial infarcted rat hearts. Int. J. Nanomedicine **10** 4691.

[6] Bai XP, Fang R, Zhang S, Shi SL, Wang ZL, Chen XB, Yang JY, Hou XL, Nie YZ, Li Y, Tian WM 2013 Self-Cross-Linkable Hydrogels Composed of Partially Oxidized Alginate and Gelatin for Myocardial Infarction Repair. J Bioact. Compat. POL. **28** 123.

[7] Izadifar Z., Honaramooz A, Wiebe S, Belev G, Chen XB, Chapman D 2016 Low-Dose Phase-based X-ray Imaging Techniques for In Situ Soft Tissue Engineering Assessments. Biomaterials **82** 151.

[8] Li ZQ, Guan JJ 2011 Hydrogels for cardiac tissue engineering. Polymers **3**, 740.

[9] Hofmann M, Wollert KC, Meyer GP, Menke A, Arseniev L, Hertenstein B, Ganser A, Knapp WH, Drexler H 2005 Monitoring of bone marrow cell homing into the infarcted human myocardium. Circulation **111** 2198.

[10] Lewis RA 2004 Medical phase contrast x-ray imaging: current status and future prospects. Phys. Med. Biol. **49** 3573.

[11] Brey EM, Appel A, Chiu YC, Zhong Z, Cheng MH, Engel H, Anastasio MA 2010 X-ray imaging of poly(ethyleneglycol) hydrogels without contrast agents. Tissue Eng Part C Methods **16** 1597.

[12] Albertini G, Giuliani A, Komlev V, Moroncini F, Pugnaloni A, Pennesi G, Belicchi M, Rubini C, Rustichelli F, Tasso R, Torrente Y 2009 Organization of extracellular matrix fibers within polyglycolic acid-polylactic acid scaffolds analyzed using X-ray synchrotron-radiation phasecontrast micro computed tomography. Tissue Eng Part C Methods **15**, 403.

[13] Appel AA, Larson JC, Somo S, Zhong Z, Spicer PP, Kasper FK, Garson AB, Zysk AM, Mikos AG, Anastasio MA, Brey EM 2012 Imaging of poly(α-hydroxy-ester) scaffolds with X-ray phase-contrast microcomputed tomography. Tissue Eng Part C Methods. **18** 859.

[14] Takashima K, Hoshino M, Uesugi K, Yagi N, Matsuda S, Nakahira A, Osumi N, Kohzuki M, Onodera H 2015 X-ray phase-contrast computed tomography visualizes the microstructure and degradation profile of implanted biodegradable scaffolds after spinal cord injury. J. Synchrotron Rad. **22** 136.

[15] Zhu N, Chapman D, Cooper D, Schreyer DJ, Chen XB 2011 X-Ray Diffraction Enhanced Imaging as a Novel Method to Visualize Low-Density Scaffolds in Soft Tissue Engineering. Tissue Eng Part C Methods **17** 1071.

[16] Olubamiji AD, Izadifar Z, Zhu N, Chang T, Chen XB, Eames BF 2016 Using synchrotron radiation inline phase-contrast imaging computed tomography to visualize three-dimensional printed hybrid constructs for cartilage tissue engineering. J. Synchrotron Rad. **23** 802.

[17] Izadifar M, Kelly ME, Chen XB 2016 Regulation of sequential release of growth factors using bi-layer polymeric nanoparticles for cardiac tissue engineering. Nanomedicine (Under Review).

[18] Liliana AL, Eugenio TG, Rigoberto OP 2014 Biological Tissue Modeling with Agar Gel Phantom for Radiation Dosimetry of 99mTc. OJRad **4** 44.

[19] Gureyev TE, Davis TJ, Pogany A, Mayo SC, Wilkins SW 2004 Optical phase retrieval by use of first born- and rytov-type approximations. Appl. Opt. **43** 2418e2430.

[20] Chen RC, Rigon L, Longo R 2013 Comparison of single distance phase retrieval algorithms by considering different object composition and the effect of statistical and structural noise. Opt. Express **21** 7384.

[21] Wu X, Liu H, Yan A 2005 X-ray phase-attenuation duality and phase retrieval. Opt. Lett. **30** 379e38.

[22] Chen RC, Dreossi D, Mancini L, Menk R, Rigon L, Xiao TQ, et al 2012 PITRE: software for phase-sensitive X-ray image processing and tomography reconstruction. J. Synchrotron Radiat. **19**, 836e845.

[23] Canadian Light Source 2015 BMIT-BM quality assurance for cycle 21. Rev. A **26.5.1.5** 6.

[24] The 2007 recommendations of the international commission on radiological protection. ICRP publication 103, Ann. ICRP **37** 1e332.

[25] SCENIHR. Health effects of security scanners for passenger screening (based on X-ray technology). European Union, 22-27, 2012.

[26] Wang Z, Bovik AC 2004 Image Quality Assessment: From Error Visibility to Structural Similarity. IEEE T. Image Process. **13** 1.

[27] Lim GB 2015 Alginate-hydrogel in chronic HF. Nat. Rev. Cardiol. **12** 443

[28] Hadjipanayi E, Kuhn PH, Moog P, Bauer AT, Kuekrek H, Mirzoyan L, Hummel A, Kirchhoff K, Salgin B, Isenburg S, Dornseifer U, NinkovicM, Machens HG, Schilling AF 2015 The Fibrin Matrix Regulates Angiogenic Responses within the Hemostatic Microenvironment through Biochemical Control. PLoS One. **10**, e0135618,

[29] Lovett M, Lee K, Edwards A, Kaplan DL 2009 Vascularization Strategies for Tissue Engineering. Tissue Eng Part B Rev. **15**, 353.

[30] Wrixon AD 2008 New ICRP recommendations. J. Radiol. Prot. **28**, 161e168.

CHAPTER 7

CONCLUSIONS AND FUTURE RESEARCH

7.1. Conclusions drawn from the development of rate-modulating nanoparticles

Engineering cardiac constructs aims to provide physical and biochemical cues for myocardium regeneration. Spatiotemporal control of growth factor (GF) release is of critical importance for bio-functional engineered cardiac constructs to guide myocardium regeneration and revascularization at the injured territory of the heart. Widely used GF immobilization and encapsulation techniques suffer from limited control over the release rate and the possible loss of GF bioactivity due to covalent bonding and cleaving reactions during the immobilization and release processes. Polymeric particulate delivery systems have shown a lot of promise to overcome these limitations. Especially, engineered PLLA- and PLGA-based nanoparticles have attracted attentions due to their biocompatibility, biodegradability and approval for use by FDA. Furthermore, through adjusting release characteristics of PLGA/PLLA nanoparticles, it will be increasingly possible to modulate GF release rate, a process so called ‘rate-programming’ of the nanoparticles. However, there are some challenges that need to be overcome to achieve rate-modulated nanoparticles for controlled release of the GFs. Some of important properties of the nanoparticles such as size, polydispersity, loading capacity, zeta potential and morphology, which are essential to system functions, are regulated by fabrication variables in a complicated manner. This raises a great need to optimize fabrication process variables to ensure the desired nanoparticle characteristics.

In the first section of this Ph.D. thesis, a comprehensive experimental study was conducted on this matter, along with a novel method, the so-called Geno-Neural approach, to analyze, predict and optimize fabrication variables for desired nanoparticle characteristics. The experimental

results revealed that the polymer and the external aqueous phase concentrations and their interactions with other fabrication parameters were the most significant variables to affect the size, polydispersity index, zeta potential, loading capacity and initial burst release of the nanoparticles. By means of the verified Geno-Neural model, optimum conditions to achieve low polydispersity index, higher negative zeta potential and higher loading capacity were identified for desired particle sizes of 150, 200, 250 and 300 nm, respectively. Electron microscopy images of the nanoparticles showed their spherical geometries with no sign of large pores or cracks on their surfaces. Furthermore, Circular dichroism (CD) spectroscopy unveiled the structural integrity of a releasing protein model from the nanoparticles designed at the optimum fabrication conditions proposed by the Geno-Neural model. Findings from this part of the thesis would greatly contribute to the design of PLGA nanoparticles for prolonged release patterns of GFs in an engineered cardiac construct for myocardium tissue engineering.

Although the PLGA nanoparticles can provide prolonged release of GFs, generally, the use of single polymer nanoparticles/microparticles are undermined by some limitations including the initial burst effect and lack of time-delayed release pattern, which is essential for GF sequential release in cardiac constructs. Moreover, the controlled release of multiple GFs demands rate-modulated nanoparticles to provide simultaneous and/or sequential release patterns for guided vascularization and myocardium regeneration. In the second part of this thesis, Bi-layer polymeric nanoparticles composed of a GF-encapsulating core surrounded by an adjustable shell thickness have been developed for sequential GF release. The bi-layer nanoparticles featured low burst effect, structural integrity of the encapsulated protein and time-delayed release patterns. Allowing for adjusting the timing of release, preconditioned nanoparticles demonstrated bioactive in the context of angiogenesis. The bi-layer nanoparticles successfully regulated

sequential release of platelet-derived GF following co-release of vascular endothelial GF and basic fibroblast GF, and significantly promoted angiogenesis in fibrin matrix, which is considered as an outstanding bio-component of cardiac constructs. Moreover, a novel Geno-Neural model was developed and validated for rate-programming of the nanoparticles. By means of the proposed model, various GF release patterns can be pre-programmed by adjusting the polymeric characteristics of the nanoparticles such as polymer concentration, molecular weight, PLLA/PLGA mass ratio, carboxyl/ester terminal group, lactide:glycolide ratio and the nanoparticle size. In addition, a representative mathematical relationship was presented so that the Geno-Neural model may be easily implemented in a spreadsheet program by various users with different backgrounds. The mathematical relationship was successfully tested on two sets of experimental data, offering a great potential for the rate-modulation of PLLA/PLGA nanoparticles for different tissue engineering applications.

Besides, the release behavior of the nanoparticles relies on the physical and chemical properties of the nanoparticles, which may be optimized for achieving desired release profiles. Mathematical models are powerful and efficient tools that facilitate the development and optimization of the GF delivery systems. Furthermore, mechanistic modeling combined with precise experimental evaluation of the nano-particulate delivery systems improves the understanding of the mechanisms of GF release, and thus help to determine crucial parameters that regulate the release rate. Also, predictive models can reduce and even eliminate the need for experiments, thus saving time and the associated costs. Despite numerous models for controlled release, there is no report on mechanistic models to elucidate governing mechanism and provide predictive means on release behavior and parameters for bi-layer polymeric nanoparticles. In the third part of this thesis, two novel modeling approaches based on local volume averaging (LVA)

and Geno-Mechanistic modeling to represent the controlled-release of bioactive agents from bi-layer polymeric nanoparticles were presented. From a porous media perspective, differential mass transfer governing equations based on LVA method were derived and numerically solved to provide the insight on the transport and degradation properties of the nanoparticles. In contrast, a system of analytical governing equations of release of pseudo bi-layer nanoparticles was coupled with genetic algorithm to provide a hybrid model, so called 'Geno-Mechanistic' model, to predict volume-averaged release properties of the nanoparticles at various conditions. A very good agreement between predicted values and experimental data (r^2>0.98, MPE<5%) was observed for both models, indicating the reliability of the models for predicting the release behaviors. Moreover, the estimated values of release parameters including effective diffusivity and degradation rate constants were consistent with the corresponding measured values reported in literatures. Predictions from both models indicated that the transport and degradation properties of the shell of bi-layer nanoparticles predominantly control the release rate. The Geno-Mechanistic model predicted two-phase (gradual and rapid) polymer degradation and a single phase degradation for the bi-layer and PLGA nanoparticles, respectively, which were consistent with experimental data reported in literatures. The developed models will be powerful, effective and efficient tools to predict and optimize the controlled release of bioactive agents from polymeric nanoparticles for many tissue engineering applications.

7.2. Conclusions drawn from the development of synchrotron phase contract-based assessment techniques

Hydrogels have been extensively used for development of functional cardiac constructs in cardiovascular tissue engineering because of their ability to support cell adhesion, retention and growth. Micro-patterning of hydrogel-based cardiac constructs enables spatial control over

microstructural characteristics of the patch. Moreover, different hydrogels combined with rate-modulating nanoparticles can be precisely assigned to the structure of the patch by use of 3D-bioprinting techniques. By optimizing dispensing speed, extrusion rate, and strand thickness, a dual-component 3D-printed cardiac patch was successfully created from alginate (the micro-construct framework), with pores filled out by fibrin. Overall structural and morphological assessemnt of the 3D-printed dual-component constructs showed the feasibility of micro-patterning of very soft hydrogel (e.g alginate containing 97.5% water). Also, the patch demonstrated good attachment post implantation on the rat heart using surgical fibrin glue. Synchrotron in-line phase contrast tomography was optimized and successfully implemented to visualize and quantitatively assess the details of the implanted patch microstructure through an *ex-vivo* study. Results illustrated that in the phase retrieval of the PCI-CT images, alginate strands could be distinguished from fibrin-filled pores, thus being able to characterize the microstructural features of implanted patches and surrounding microvessels and ligature in the myocardium. Furthermore, the phase-retrieved PCI-CT images provided clear structural details for quantitative assessment of the patch as compared to the images from phase non-retrieved PCI-CT and a 3T clinical magnetic resonance imaging. By reducing the total CT-acquisition time per slice and ROI, PCI-CT was examined for lowering the effective dose (<100 mSv), meanwhile it was illustrated that there were no significant changes in imaging quality for quantitative assessment of the implanted patch microstructure. The features of the patch evaluated from the low dose PCI-CT were in agreement with the measured values from stereomicroscope images. Taken together, it has been illustrated that the PCI-CT is of great potential for non-invasive qualitative and quantitative assessment of microstructural features of the implanted alginate/fibrin cardiac patch at the low dose allowed in clinical use.

7.3. Future research

One of the challenges that smart bioactive cardiac patches are facing to is spatiotemporal control of GF release to facilitate cellular fate regulation in situ. Development of such scaffolds requires precise design and optimization of structural, architectural and physicochemical characteristics of the GF-loaded nanoparticles for pre-programmed GF release profiles within the scaffolds. Precise 3D printing technique can be used to fabricate customized cardiac patch constructs with the ability of spatiotemporal control of release of multiple GFs. The development of the rate-modulated nanoparticles and the 3D-printed dual-component patch as discussed in this dissertation can greatly contribute to achieve the fabrication of pre-programmed bioactive cardiac patches. With the predictive models proposed in this thesis, the nanoparticles can be designed, rate-programmed and prepared. Each design of the nanoparticles is then assigned to particular layer in the patch microstructure through 3D printing of the nanoparticle-incorporated alginate and fibrin, as disscused earlier. Thus, spatiotemporal control of GF release will be achieved across the patch microstructure to guide vascularization and myocardium regeneration. Another challenge is attributed to weak mechanical properties of hydrogel-based micro-fabricated cardiac patches. To address this issue, further research and assessments are required to improve structural properties of micro-patterned hydrogel-based cardiac patches. The PCI-CT imaging technique that was developed in this research for visualization of the implanted 3D-printed cardiac patch will be eventually used for monitoring the cardiac patch degradation, tissue regeneration and vascularization *in-situ* after surgery. The optimum imaging parameters that were identified and discussed in this dissertation may be refined for the development of a robust gated PCI-CT for *in-vivo* live animal study in the future.

Appendix A: Matrices and vectors for evaluation of Eq. (3.4)

$$\overline{\overline{\mathbf{M}}} = \begin{bmatrix} -0.6699 & 0.2258 & -1.0658 & -0.9678 & 0.1380 & 0.1491 \\ 1.0619 & -0.6035 & 0.0128 & 0.3509 & 0.2597 & -0.0382 \\ 0.0480 & -0.3500 & 0.6355 & -2.5142 & 0.0636 & -0.2020 \\ 0.7223 & 1.3019 & -0.3550 & 0.0484 & -0.2684 & 0.0684 \\ 1.8385 & 0.2109 & 0.2897 & -0.2768 & -0.2215 & 0.0801 \\ 0.2512 & 0.2104 & -0.2818 & 2.0524 & -0.1823 & 0.0675 \end{bmatrix}$$

$$\overline{\overline{\mathbf{N}}} = \begin{bmatrix} 0.2394 & -1.5171 & 0.1288 & -0.2091 & 0.3206 & 0.4019 \\ 0.9412 & -1.0848 & 0.8325 & -0.0472 & 0.1851 & 1.4429 \\ 0.4070 & -0.1053 & -0.4718 & -0.7704 & 1.2096 & 0.1426 \\ -0.3795 & 0.0225 & 0.2445 & -0.7825 & 0.3029 & 0.3418 \end{bmatrix}$$

$$\overline{\mathbf{q}} = \begin{bmatrix} 0.5984 \\ 0.8215 \\ 0.1779 \\ 0.0338 \\ 0.0057 \\ 0.5326 \end{bmatrix}, \quad \overline{\mathbf{r}} = \begin{bmatrix} 0.1365 \\ -0.3708 \\ -0.0734 \\ -0.1138 \end{bmatrix}$$

Appendix B: The neural network synaptic weights associated with Eq. (4.3)

$$\overline{\mathbf{M}} = \begin{bmatrix} 0.2066 & -0.1556 & -0.0977 & 0.0184 & 0.4615 & 0.0825 & 0.2840 & -0.5668 \\ 0.7418 & 0.0795 & 0.0798 & 0.2060 & -0.1059 & 0.1105 & 0.3364 & -1.5058 \\ -0.7418 & -0.0048 & 0.2705 & 0.0332 & -0.3645 & 0.0778 & -0.2959 & 0.0057 \\ -0.3067 & -0.0621 & -0.2979 & -0.3234 & 0.1040 & -0.2980 & -0.3141 & 1.8461 \end{bmatrix}$$

$$\overline{\mathbf{q}} = \begin{bmatrix} 0.5194 \\ -0.1056 \\ -0.0892 \\ -0.1318 \end{bmatrix}$$

$$\overline{\mathbf{N}} = \begin{bmatrix} -0.7205 & -1.6768 & -0.3748 & -0.9719 \\ -0.0069 & -0.0038 & 1.1765 & -0.0086 \end{bmatrix}$$

$$\overline{\mathbf{r}} = \begin{bmatrix} 0.0972 \\ -0.0496 \end{bmatrix}$$